

**Fundamental Studies of AC/DC Electrokinetic Phenomena for
the Realization of Microchip Capillary Electrophoresis for
Single-Cell Analysis**

A Thesis

Submitted to the Faculty

of

Drexel University

by

Doh-Hyoung Lee

in partial fulfillment of the
requirements for the degree

of

Doctor of Philosophy

March 2011

© Copyright 2011

Doh-Hyoung Lee. All Rights Reserved

ACKNOWLEDGEMENTS

I would like to acknowledge the support and help of numerous people, without whom this thesis would not have been possible.

I would like to express my deepest gratitude to my two advisers, Dr. Hongseok (Moses) Noh, and Dr. Bakhtier Farouk for their invaluable guidance and support throughout this research work. I am also grateful to Dr. Young I. Cho, Dr. Joe Foley, and Dr. Elisabeth Papazoglou for serving on my thesis committee and for their many helpful comments.

I would like to thank my graduate student friends for their help, friendship and support: Temitope Sodunke, Jorge Capurro, Rob Hart, Jonghyun Oh, Joseph Cirillo, Kewei Liu, Chengjie Yu, and many others.

Finally a special thanks to my parents, wife Soyoung and son Benjamin for their love and support.

TABLE OF CONTENTS

ACKNOWLEDGEMENTS.....	iii
TABLE OF CONTENTS.....	iv
ABSTRACT.....	ix
CHAPTER 1. INTRODUCTION & MOTIVATION.....	1
1.1 . Motivation.....	1
1.1.1. Needs for Single Cell Analysis.....	1
1.1.2. Challenges in Single-cell Analysis.....	3
1.1.3. Current Techniques for Single-cell Analysis.....	4
1.1.4. Challenges of Microchip Capillary Electrophoresis.....	8
1.1.5. AC/DC Electrokinetic Phenomena for Single-cell Analysis Microchips.....	9
1.2 . Research Objectives.....	10
1.3 . Outline of the Thesis.....	16
1.4 . Summary.....	19
CHAPTER 2. BACKGROUND.....	21
2.1 . Microfluidics, BioMEMS and Lab-On-A-Chip.....	21
2.2 . Microfabrication Techniques.....	23
2.3 . DC Electrokinetics Theory.....	29
2.3.1. Electrophoresis.....	29

2.3.2. Electroosmosis	30
2.4 . AC Electrokinetics Theory.....	34
2.4.1. AC Electroosmosis.....	34
2.4.2. Dielectrophoresis	37
2.4.3. Electrothermal Flow.....	40
2.5 . Cell Manipulation in Microchannels.....	44
2.6 . Cell Lysis in Microchannels.....	53
2.6.1. Chemical Lysis.....	53
2.6.2. Mechanical Lysis	55
2.6.3. Electrical Lysis (irreversible electroporation).....	56
2.6.4. Osmotic Lysis	60
2.6.5. Other Cell Lysis Methods	61
2.7 . Sample Concentration Techniques.....	62
2.8 . Separation Methods.....	68
2.9 . Detection Methods	75
CHAPTER 3. INTERACTION BETWEEN DC AND AC ELECTROKINETICS.....	81
3.1 . Introduction.....	81
3.2 . Microfabrication Method: PDMS Replica Molding	83
3.3 . Experiment Procedure.....	84
3.4 . Measurement of DC Electroosmotic Mobility	84

3.5 . Numerical Methods: AC Electroosmosis.....	85
3.5.1. Geometry and Boundary Conditions.....	86
3.5.2. Electrostatics Simulation	86
3.5.3. Incompressible Navier-Stokes Simulation.....	87
3.6 . Experimental Results	87
3.6.1. AC and DC Electroosmotic Flow Interaction.....	87
3.6.2. Dielectrophoresis under DC Electroosmotic Flow	88
3.7 . Numerical Simulation Results.....	89
3.8 . Conclusions.....	92
CHAPTER 4. DIELECTROPHORETIC PARTICLE-PARTICLE INTERACTION UNDER AC ELECTROHYDRODYNAMIC FLOW CONDITIONS	93
4.1 . Introduction.....	93
4.2 . Theory	95
4.2.1. Dielectrophoresis	95
4.2.2. AC Electroosmosis.....	97
4.2.3. Electrothermal Flow.....	98
4.2.4. Van der Waals Force and Double Layer Interaction.....	99
4.3 . Experimental Method.....	100
4.3.1. Device Fabrication and Materials	100
4.3.2. Experimental Procedure.....	102
4.4 . Simulation Method.....	103

4.5 . Results and Discussion.....	106
4.5.1. Particle Behaviors under ACEO Flows	106
4.5.2. Particle Behaviors under Electrothermal Flows.....	112
4.6 . Conclusions.....	116
CHAPTER 5. 3-D SIMULATION OF ELECTROSMOTIC SAMPLE INJECTION AND MIGRAION IN MICROCHANNELS : EFFECTS OF NON-RECTANGULAR CROSS SECTION.....	118
5.1 . Introduction.....	118
5.2 . Problems Considered	120
5.2.1. Effects of Non-rectangular Cross Section.....	120
5.3 . Governing Equations.....	124
5.4 . Numerical Methods: DC Electrokinetics	125
5.5 . Model Validation	128
5.6 . Effects of Non-rectangular Cross Section.....	129
5.6.1. 3-D Characteristics in Sample Loading	129
5.6.2. 3-D Characteristics in Sample Dispensing.....	132
5.6.3. 3-D Characteristics of Sample Dispersion during migration in a Straight Migration Channel.....	138
5.6.4. Numerical Inaccuracy due to Sharp Corners at the Intersection.....	140
5.7 . Conclusions.....	142

CHAPTER 6. 3-D SIMULATION OF ELECTROOSMOTIC SAMPLE MIGRAION IN MICROCHANNELS: EFFECTS OF SURFACE AND SOLUTION PROPERTY VARIATIONS	144
6.1 . Introduction.....	144
6.2 . Problems Considered	148
6.3 . Numerical Methods & Governing equations	153
6.4 . Results and Discussion.....	155
6.5 . Conclusions.....	175
CHAPTER 7. CELL LYSIS AND SINGLE CELL ANALYSIS	177
7.1 . Introduction.....	177
7.2 . Microfabrication Method: Glass Microchip Fabrication.....	180
7.3 . Microchip Electrophoresis: Pinched Injection	181
7.4 . Continuous Cell Lysis	184
7.5 . Single Red Blood Cell Analysis.....	186
7.6 . Conclusions.....	187
CHAPTER 8. CONCLUSIONS & FUTURE WORK.....	189
8.1 . Achievement of Aims	190
8.2 . Future Work	194
REFERENCES.....	198
APPENDIX – PROTOCOLS	208

ABSTRACT

Fundamental Studies of AC/DC Electrokinetic Phenomena for the Realization of Microchip Capillary Electrophoresis for Single-Cell Analysis

Doh-Hyoung Lee

Hongseok (Moses) Noh, Ph. D. and Bakhtier Farouk, Ph. D.

The goal of this research was to investigate AC and DC electrokinetic phenomena to better understand their individual and combined effects on particle and fluid motions in microchannels in order to realize microchip capillary electrophoresis for single cell analysis. AC-DC electroosmotic flow interaction was studied by observing the motions of polystyrene microbeads suspended in deionized water in a microchannel as the main AC and DC electrokinetics parameters were varied. Particle-particle interactive dielectrophoretic (DEP) force under electrohydrodynamic flow conditions was studied by performing experiments on a microchannel - microelectrode system containing polystyrene beads and comparing the experimental results with numerical simulation results using the Maxwell stress tensor calculation. Efficient sample injection and separation is another key to successful microchip CE. Accurate numerical studies were performed for understanding 3-D characteristics of the dispersion of sample species that is injected and carried by electroosmotic flow in diverse microchannel geometries. The following three cases were investigated; 1) non-rectangular cross section of microchannels, 2) different zeta potential for the top and bottom microchannel substrates, and 3) development of internal pressure gradient by variation of electric or electrokinetic properties along the channel direction. The results of the numerical study for the aforementioned 3 cases showed that 3-D modeling is crucial for accurate predictions of sample injection and migration in microchip electrophoresis system. Finally, continuous cell lysis in microchip CE devices was investigated experimentally by adopting a

combination of electrical and osmotic cell lysis methods. The concept of continuous single cell lysis and CE was proven by analysis of single red blood cells labeled with FITC.

CHAPTER 1. INTRODUCTION & MOTIVATION

1.1 . MOTIVATION

1.1.1. Needs for Single Cell Analysis

Understanding the behavior, composition and metabolism of cells is very important in advancing medical sciences and related fields because cells control the metabolism and activities of all living organisms. Also, many fatal diseases such as cancers and diabetes are related to cell malfunction or infection. The analysis of cells will lead us to better understand cells and to find ways to treat cellular diseases. The need for single-cell analysis originates from the heterogeneity of cells, and the purposes of single-cell analysis can be classified into the following two categories.

- *Medical diagnosis; Early detection of disease*

In the diagnosis of diseases, analysis of tissue or blood samples taken from a patient is complex because they consist of both normal and diseased cells. Single-cell studies of tumor biopsies have shown that the majority of cells within a tumor may be normal and that significant heterogeneity exists even among the abnormal cells [1, 2]. Thus, the conventional diagnosis techniques that provide averaged data from numerous cells may lead to inaccurate medical diagnosis. Especially if rare abnormal cells need to be detected at an early disease stage, single cell analysis may be the only option. For example, molecular heterogeneity of gene expression in Hodgkin's disease was studied through single-cell analysis [3], which may be the only option for detecting this disease at a very early stage. Abnormal gene expression of T cells was also studied

through single-cell analyses to reveal the molecular mechanism of autoimmune diseases [4, 5] and possibly find early-diagnostic or curing methods.

•Biological studies and drug screening

Most traditional cell-based biochemical assays have analyzed bulk cell samples and provided averaged data in order to attempt to understand the molecular mechanisms of cellular functions. However, it has been reported that individual cells differ in many characteristics even though they may look identical [6-10]. For example, Huang et al. [7] showed that Ca^{2+} responses of rat aortic endothelial cells to a fixed concentration of either acetylcholine or histamine differ by two orders of magnitude. The transcription events in mammalian cells are observed to be subject to random fluctuations, leading to large variations in mRNA copy numbers [11, 12]. In a clonal population of mouse multipotent progenitor cells, the cell-cell heterogeneity is found to be connected with cell-fate decisions [13]. Due to this heterogeneity of cells, the bulk averaged biochemical assays may overlook the rich information available when single cells are studied (Figure 1-1). The seemingly identical cells are also quite heterogeneous in their responses to drugs or external stimuli [9, 14, 15]. The understanding of such variability can lead to better drug design and control of side effects.



Figure 1-1. Average sample analysis vs. single cell analysis. In a population average, it is not possible to distinguish between the left state in which all cells have an intermediate phenotype (orange cells) and the right state in which half are on (red cells), half are off (yellow cells).

1.1.2. Challenges in Single-cell Analysis

Many researchers have worked on single-cell analysis ever since the first study on chemical components of single cells was performed in the 1960's [16]. However, the progress in the field of single cell analysis has been rather slow due to several technical challenges as follows.

1. The chemical species of interest in a cell exist in extremely small amounts (eukaryotic cells are generally on the order of 5–20 μm in diameter and therefore have volumes of only 0.1–8 pL [17]) and at low concentrations (total number of molecules of each receptor protein in a cell is less than 100 while signaling enzymes are in the range of 1000–10,000 molecules [18]) which makes detection of the target materials very difficult. Particularly, proteins and most non-DNA analytes cannot be readily amplified, so that their detection is even more difficult.
2. The cellular constituents exist in a complex cytoplasmic environment or tied to lipid membranes. This complex state of constituents often requires employment of purification or separation strategies prior to analysis, but doing so with minimal loss or dilution of the sample remains a challenge in the chemical analysis of individual cells. For example, a detergent such as sodium dodecyl sulfate (SDS) can be added to dissolve cell membranes.
3. The mixed hydrophobic-hydrophilic nature of many biological macromolecules may lead to their adsorption to a variety of surfaces, resulting in significant loss of target cells during manipulation or in device malfunction. For example, when two or more kinds of proteins are present in solution, such as in blood plasma, the adsorption is the result of the competition between the time scale to reach the surface and the strength of the surface–protein interaction (Vroman sequence) [19, 20]. Cells themselves may stick to the non-natural surfaces of LOC devices; the vast majority of mammalian cells grow adherent to a surface and may undergo

- apoptosis (programmed cell death) when detached from their growth surface for more than a few minutes [21]. This behavior may result in losing target cells during manipulation or in device clogging.
4. Intracellular changes related to perturbations or membrane damage during cell sampling are also a potential pitfall of analysis performed on live cells. Biological molecules are in a constant state of flux and changes in the cell's environment, such as pH, ionic strength, and temperature, can lead to variation in the intracellular concentrations of many molecular species. Ion concentration and protein phosphorylation can vary dramatically on the sub-second timescale, whereas RNA and protein concentrations can change over minutes to hours [22].
 5. Single-cell studies may need to analyze enormous numbers of individual target cells especially when applied for the clinical purpose or the statistical study of samples in a cell population. As a result, it will require high throughput and fast procedures of cell delivery, cell lysis and sample analysis. For example, one micro liter of blood contains about 5 million red blood cells [23] and it takes 289 days to assay this number of cells with the highest throughput single cell analysis method reported so far (12 cells/min) [24]. The cell preparation and sequential delivery of cells will be very challenging to increase throughput of single-cell analysis up to the level of flow cytometry (100,000 cells/s).

1.1.3. Current Techniques for Single-cell Analysis

(1) *Flow cytometry*

Flow cytometry is a well-established technique for analysis of the physical and chemical characteristics of single cells in a stream of fluid with a high throughput up to 100,000 cells s⁻¹.

The technique uses one or more focused laser beams directed at the stream of cells and the fluorescent flow emanating from the cells is analyzed (Figure 1-2). Despite the throughput capabilities of flow cytometry, it has a critical drawback. This technique is restricted to materials that must be labeled with a fluorophore, and, therefore, there must be differentiation between spectra from different species since there is no other basis for distinction besides spectroscopy.

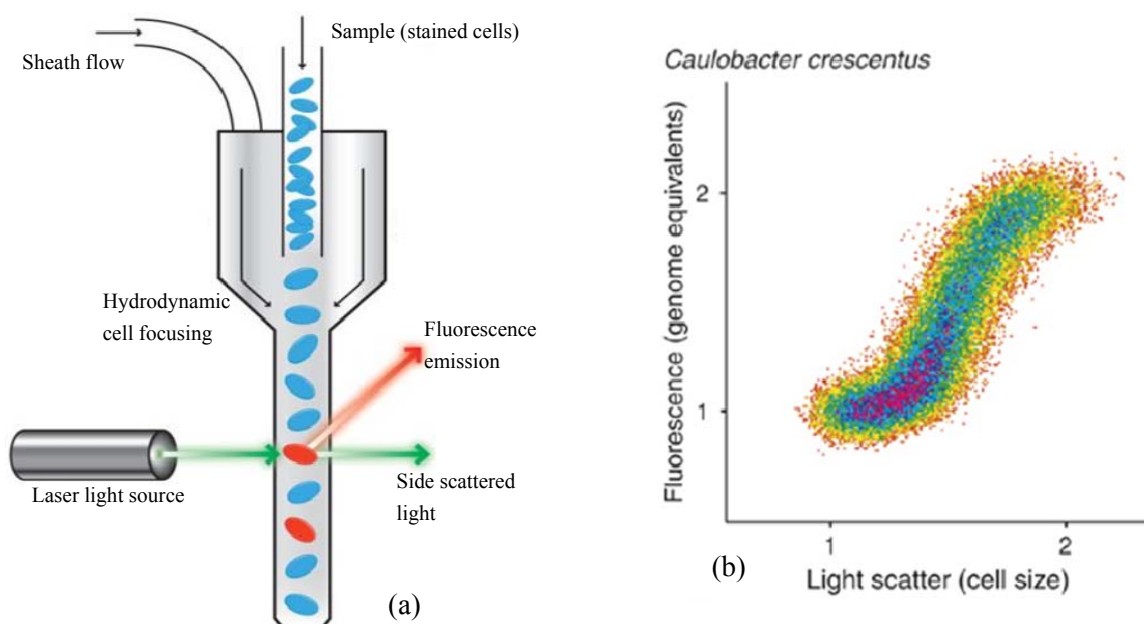


Figure 1-2. A schematic of flow cytometry (a) and flow cytometry analysis of chromosome replication (b)[25].

(2) *Capillary electrophoresis*

Electrophoresis is the motion of charged particles under an electric field due to Coulombic force. The Coulombic force is balanced with friction force in the electrophoretic separation. The force balance makes a group of the same type of sample species travel at a constant velocity. The certainty and uniqueness of the electrophoretic mobility of a species makes it possible to separate the species in a mixture by applying an electric field (Figure 1-3). This

technique is called electrophoretic separation. More detailed discussion of various electrophoretic separation techniques is provided in Section 2.7. Contrary to slab gel electrophoresis, the capillary electrophoresis spatially confines the sample volume as small as target cells. This spatial confinement makes the capillary electrophoresis suitable for single cell analysis. Combined with fluorescence-based detection, capillary electrophoresis is sensitive enough to detect small amounts of bio-molecules from a cell [26]. Ever since capillary electrophoretic separation of single cell constituents was first achieved by Kennedy et al. [27] using neuron cells from sea snails, many researchers have performed the measurement of various analytes from single cells. These analyses include DNA, RNA, proteins, protein activity, and metabolites. However, the conventional capillary electrophoresis has some disadvantages for single cell analysis such as intensive labor and low throughput.

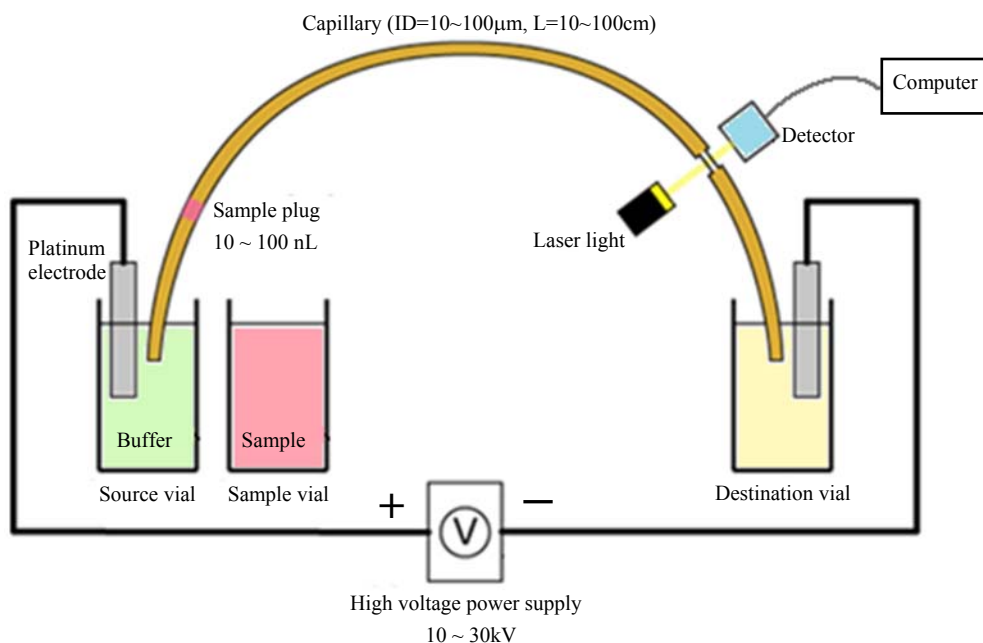


Figure 1-3. Schematic of capillary zone electrophoresis system.

(3) Microchip Capillary Electrophoresis

Since Manz proposed the potential of microfabrication in chemistry and life science field in the early 80's, many groups have developed miniaturized capillary electrophoresis systems on a single chip. Such microchip capillary electrophoresis has many advantages over conventional capillary electrophoresis. Microfabrication allows for accurate on-chip sample injection techniques, producing faster separation performance with much shorter channels. This results in a great reduction in the overall analysis time for capillary electrophoresis. In addition, multiple channels can be readily integrated on a single chip, realizing parallel analysis. Another important aspect of microchip capillary electrophoresis is that other microfluidic components such as cell manipulation can be integrated with the system. For these reasons, the microchip concept of capillary electrophoresis system has drawn attention since the early 1990's and has shown enough capability to achieve high-throughput total analysis of single cells. Microchip capillary electrophoresis has shown a great enhancement of analysis speeds compared to conventional capillary electrophoresis, with a throughput of 38 cells/min reported by Xu and Ying [28]. This enhancement of throughput was mainly due to the faster exchange of buffer around the cell prior to lysis and the use of shorter separation channels with relatively higher electric field. Serial separations of multiple cells within a channel also provided additional speed enhancements. Although it is in the early stages of development, microchip electrophoretic separation of single-cell contents may enable increased adoption of this powerful technique by providing a tool for automated, high-throughput separations.

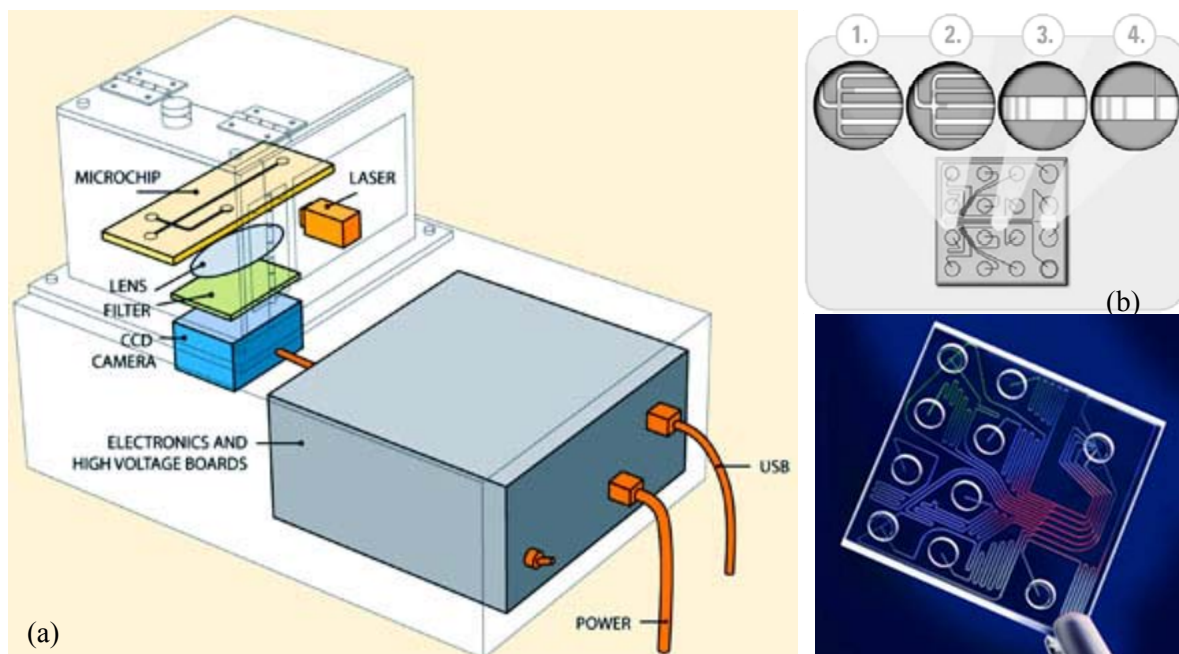


Figure 1-4. Schematic of a portable microchip CE-LIF system [29] (a) and a capillary electrophoresis microchip developed by Agilent (b).

1.1.4. Challenges of Microchip Capillary Electrophoresis

Microchip capillary electrophoresis has been shown to provide a great enhancement of analysis speed compared to conventional capillary electrophoresis, with a throughput of 38 cells/min [28]. However, several technical improvements are still needed for reliable single-cell analysis. The cellular perturbation during cell manipulation needs to be minimized by reducing duration of cell manipulation and selecting proper treatments with reagents. Additional upstream cell processing steps such as loading reagents and labeling may be required for detection of a variety of cellular constituents. An automatic and high-throughput system requires a well functioning cell manipulation system. In order to analyze rare species from a cell, the separation efficiency and detection method may need to be improved. Separation efficiency depends not only on the separation method but also on the lysis technique so that both efficient lysis and

separation methods need to be co-developed. The biological issues arising during the single-cell analysis can be addressed through a proper interpretation of biological phenomena.

1.1.5. AC/DC Electrokinetic Phenomena for Single-cell Analysis Microchips

Electroosmosis is the motion of liquid induced by an applied electric field along a solid surface due to interaction between electric double layer on the surface and the applied electric field. The thinness of the electric double layer in typical microchannels makes the induced bulk flow behave like a wall-driven flow that has a uniform velocity profile [30]. The uniform velocity profile makes the electroosmotic flow very attractive in separation science because dynamic dispersion and band broadening effects can be minimized with such a velocity profile, compared to the parabolic velocity profile of pressure-driven flows. This velocity profile also makes this phenomenon available as a micro pump without involving significant pressure drop. Electrophoresis is the motion of charged particles (or ion species) under electric field due to Coulombic force. The electrophoretic force has also been used for particle manipulation [31]. Efficient and effective fluid or particle manipulation by DC electrokinetics can be designed through accurate analysis of these phenomena. However, because of relatively recent development of computational power and biased-efforts on developing new devices through experimental methods, computational methods of these phenomena still need to be improved. For example, 3-D characteristics of AC electroosmotic sample injection and migration in microchannels were not previously studied.

AC electrokinetic phenomena, such as dielectrophoresis (DEP), AC electroosmosis (ACEO), and electrothermal flow (ETF), have drawn much attention in the microfluidics and lab-on-a-chip communities because of their potential for effective manipulation of small particles and fluids in microchannel environments. The ease of implementation and the versatility in

application make AC electrokinetic techniques very attractive in microfluidics and lab-on-a-chip applications. Diverse particle manipulation techniques based on DEP have been reported for the past two decades [32-44]. More recently, AC electrohydrodynamic phenomena, such as ACEO and ETF, have also been discovered [45-47] and some of their applications have been explored [48-50]. In spite of the versatility of AC electrokinetic techniques, their use in particle manipulation in biochips still need to be explored further because the particle behavior under AC electrokinetic conditions was not fully understood. In other words, a complete and exact force analysis on micro particles under AC electrokinetics has not been achieved yet. For example, interaction between AC and DC electrokinetic phenomena has not been investigated in previous research. Also, the most rigorous analysis method of dielectrophoretic force, Maxwell stress tensor method, which has been rarely applied for the characterization of particles, will help reveal the mechanism of interesting particle behaviors.

1.2 . RESEARCH OBJECTIVES

The ultimate objective of the lab-on-a-chip research will be to realize high-throughput single cell analysis system. A possible proposed idea to realize a high-throughput single cell analysis system is continuous cell delivery, lysis and separation as shown in Figure 1-5. This proposed system contains many challenging ideas whose feasibility should be verified.

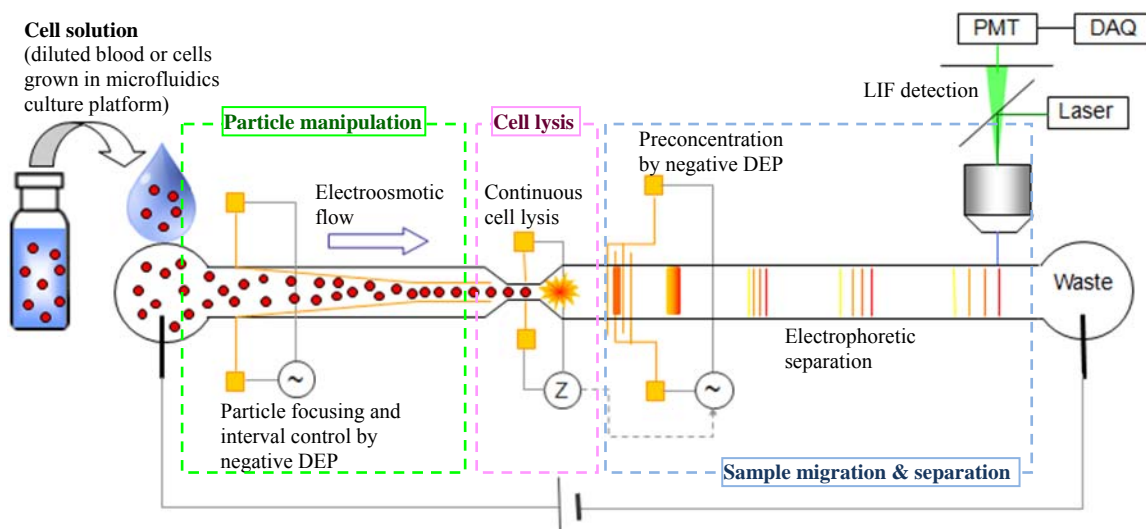


Figure 1-5. Schematic of a proposed microchip capillary electrophoresis for high-throughput single cell analysis.

The objective of the current thesis study is to verify some of those challenging components by performing fundamental studies of AC and DC Electrokinetic phenomena to better understand them in order to apply for the realization of microchip capillary electrophoresis for single cell analysis. The proposed specific aims are:

1. *To investigate AC electrokinetic particle manipulation in a microchannel through experimental and numerical studies.*

In order to build an automatic and high throughput single-cell analysis system, well functioning cell delivery and manipulation system is the first thing to be achieved. This corresponds to the particle manipulation component in Figure 1-5. Individual cells need to be separated from other cells and sequentially delivered to the capillary electrophoresis module for high-throughput analysis. AC electrokinetic phenomena such as dielectrophoresis, AC electroosmosis, and electrothermal flow have drawn much attention in the microfluidics and lab-

on-a-chip communities since those techniques have a great potential for effective manipulation of small particles and fluids in microchannel environments. AC electrokinetic particle manipulation is readily achieved in a microchannel via non-uniform electric fields generated by microfabricated planar electrodes. High electric fields required for particle motion ($10^4\sim 10^6$ V/m) can be easily achieved with only a few volts since the electrode gap is of the order of micro- or nanoscale. The electrolysis of water can be significantly reduced since AC power is used. Moreover, each of the electrokinetic and electrohydrodynamic forces has fairly distinct characteristics, and as a result, various types of particle motion can be achieved by simply varying operational conditions [51]. This convenience and versatility make AC electrokinetics the most suitable particle manipulation technique for microfluidic devices compared with other options such as optical tweezers [52, 53], ultrasonic techniques [54], and magnetic techniques [55-57].

It is likely that AC electrokinetics will be combined with DC electrokinetics in the same space; AC electrokinetics can be integrated in a microchip capillary electrophoresis for the purpose of sample preparation. However one concern is raised about the possibility that the characteristics of DC and AC electrokinetics can be affected by each other. Understanding the interactive effects between DC and AC electrokinetic phenomena will help to develop stable microfluidic devices based on the combination of these two techniques. The interaction between AC electrokinetic phenomena and DC electroosmotic flows are investigated by experimental and numerical methods (Chapter 3) as illustrated in Figure 1-6.

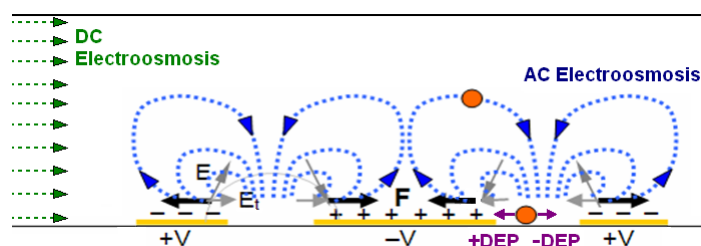


Figure 1-6. Schematic of the case of combination of DC and AC electrokinetics.

When particles are present in the fluid under AC electrohydrodynamic flow (ACEO or ETF) conditions, the particles experience Stokes drag force and DEP force. DEP force is magnified when particles approach each other or another solid surface. The previous works show the magnified DEP effect when particles come close to each other. However, the dielectrophoretic particle-particle interactions under AC electrohydrodynamic flow conditions and the subsequent behaviors of particles under ACEO and ETF have not been thoroughly investigated. The dielectrophoretic particle-particle and particle-electrode surface interactions under AC electrohydrodynamic flow condition are investigated through both experimental and numerical studies. The problem case is illustrated in Figure 1-7.

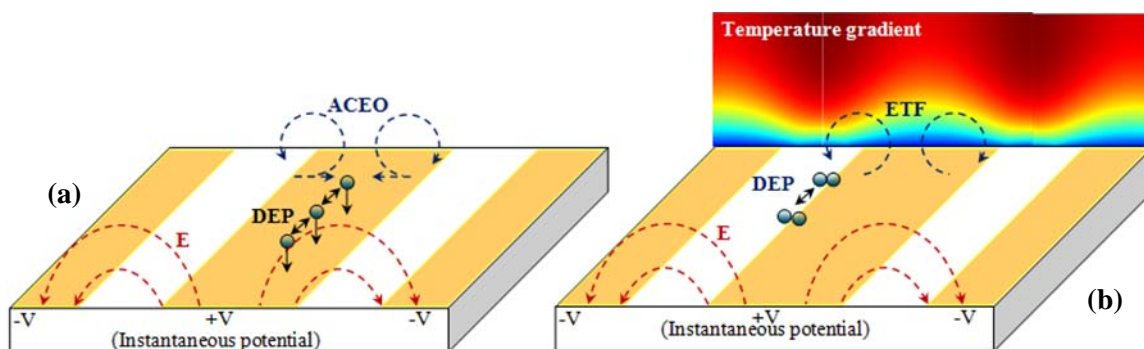


Figure 1-7. Schematic of the forces that affect particle motions under AC electrohydrodynamic conditions: (a) AC electroosmosis-dominant case and (b) electrothermal flow-dominant case.

2. *To investigate 3-D characteristics of electroosmotic sample injection and migration through 3-D accurate numerical studies.*

The previous numerical simulations of electrokinetically driven flows [30, 58-67] employed many approximations in deriving the governing equations. For example, the thin velocity boundary layer and the consequent uniform velocity profile of electroosmotic flow has served as the basis for many previous studies, which employed a 2-D [30, 59, 61, 68, 69] or even an 1-D [70-72] approximation for electroosmosis numerical simulations. 1-D approximation has been usually considered for the simulation of traditional capillary electrophoresis systems while 2-D approximation has been used for the simulation of pinched injection-based microchip capillary electrophoresis systems that have multiple branch channels. These lower dimensional (1-D and 2-D) approximations are valid if there is no variation in any critical parameters in the eliminated dimensions. However, the approximations lose their validity when 3-D features are present in the device resulting in non-trivial variation of critical parameters. Numerical studies are performed on the electroosmotic sample injection and migration for three cases where the consideration of 3-D characteristics is crucial for an accurate prediction of sample distribution: 1) a non-rectangular microchannel cross section (Figure1-8a), 2) different zeta potentials on channel surfaces (Figure1-8b), and 3) the development of internal pressure gradients due to the variation of surface and solution properties along the channel length (Figure1-8c).

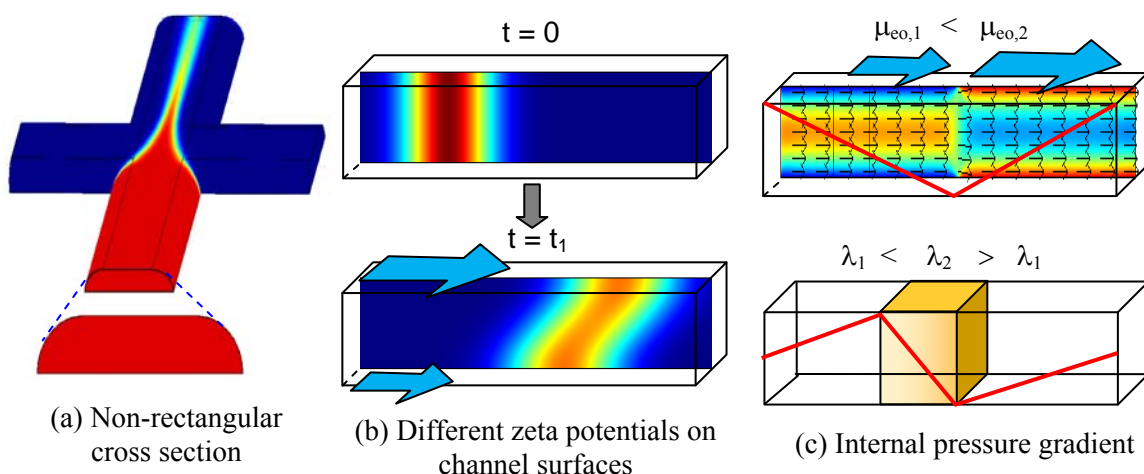


Figure 1-8. Three cases where the 3-D characteristics of electroosmotic flow become significant. (a) A pinched injection system with non-rectangular cross section, (b) a straight channel with different zeta potentials on channel surfaces, and (c) an internal pressure gradient developed by zeta potential or chemical concentration variation.

3. *To investigate continuous cell lysis methods and to identify optimal design and operational parameters for a rapid and effective cell lysis.*

The analysis of intracellular constituents through separation necessitates cell lysis. Initial sample injection is a key element that determines the separation efficiency of capillary electrophoresis. Therefore, the cell lysis must be done in such a way that the released intracellular components may have a very narrow initial band. The intracellular biochemical reaction due to external stimuli should also be minimized through a rapid cell lysis. Combination of electrical and osmotic cell lysis method is developed for a continuous and high-throughput single-cell analysis and for rapid and effective cell lysis. Blood cells are considered the first target objects since blood can be taken easily from patients and it contains a massive amount of information about the functioning of all tissues and organs in the body [73].

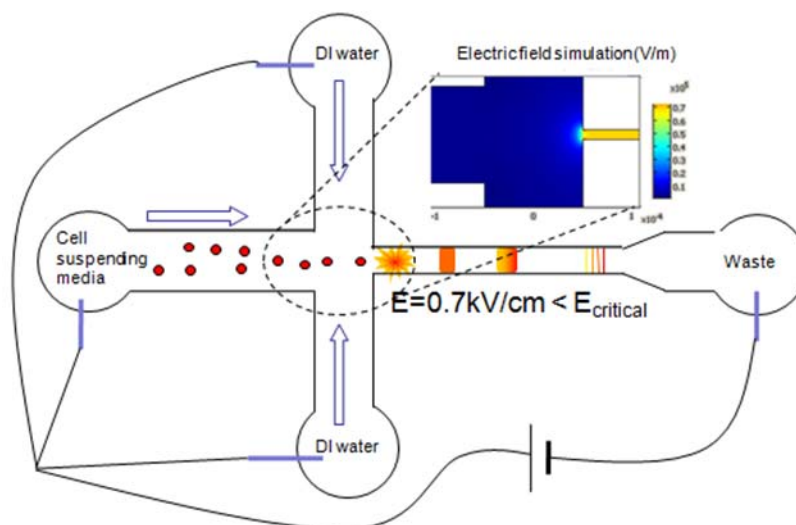


Figure 1-9. Combination of electric and osmotic cell lysis method to achieve longer separation channel and high throughput continuous cell lysis.

1.3 . OUTLINE OF THE THESIS

Following Introduction in chapter 1 and Background in chapter 2, each chapter represents an individual publication. The final chapter (8) provides a conclusion to the thesis work.

Chapter 1 (Introduction & Motivation) provides an introduction to this thesis which includes the research motivation, research objective and specific aims. The motivation explains the importance of single biological cell analysis and microchip capillary electrophoresis. Three specific aims are provided; 1) Investigation of AC electrokinetic manipulation, 2) Accurate 3-D simulation of electrokinetic sample injection and migration, and 3) Experimental studies on rapid and effective cell lysis.

Chapter 2 (Background) provides background knowledge related to microchip capillary electrophoresis for single cell analysis and AC/DC electrokinetics. Fundamentals of microfluidics are explained first and then microfabrication techniques popularly used in the field of bioMEMS

are provided. The theory behind AC/DC electrokinetic phenomena is explained next. Finally, each component of single cell analysis system is discussed in the sequence of cell manipulation, cell lysis, sample concentration, separation and detection.

Chapter 3 (Interaction between DC and AC Electrokinetics) presents experimental and numerical studies on the interaction between AC electrokinetic phenomena and DC electroosmotic flows. The motions of polystyrene microbeads suspended in deionized water in a microchannel were studied as the main AC and DC electrokinetics parameters were varied. Numerical simulations of flow field were performed using COMSOL Multiphysics software. The numerical simulation results showed good agreement with experimental data. This study intends to contribute to the understanding of the interactions between DC and AC electrokinetic phenomena and thus help researchers develop more efficient cell manipulation tools.

Chapter 4 (Dielectrophoretic Particle-particle Interaction under AC Electrohydrodynamic flow conditions) is focused on understanding particle-particle interactive DEP force under AC electroosmosis and electrothermal flow conditions by performing experiments on a microchannel - microelectrode system containing polystyrene beads and comparing the experimental results with numerical simulation results using the Maxwell stress tensor calculation. It was revealed that the attraction of particles to the electrode surface is attributed to the strong interactive DEP between particles and electrode surface. The Maxwell stress tensor analysis demonstrated how the DEP force on a particle was affected when neighboring particles were closer. It also explained the experimentally-observed attraction and repulsion of particles. This study intends to contribute to the understanding of the role of DEP

force under AC electrohydrodynamic flow dominant conditions and thus help researchers develop more efficient cell manipulation tools along with the study in Chapter 3.

Chapter 5 (3-D Simulation of Electroosmotic Injection and Migration in Microchannels: Effects of Non-rectangular Cross Section) presents a numerical study of the 3-D characteristics of electroosmotic injection and migration of sample species in microchip capillary electrophoresis systems. In particular, the effect of a non-rectangular cross section commonly found in isotropically-etched microchannels is thoroughly investigated through 3-D numerical simulations. A non-rectangular cross section resulted in a vertically non-uniform sample plug during the loading stage. Conventional 2-D simulation approach can result in up to a 40 % error in the calculation of injection qualities. It was also found that the 2-D simulation using a proper channel width shows good agreement with the 3-D simulation data. This study provides quantitative assessment of 2-D approximations compared to accurate 3-D simulation data in order to determine the optimal design and operation conditions of microchip capillary electrophoresis systems.

Chapter 6 (3-D Simulations of Electroosmotic Sample Migration in Microchannels: Effects of Surface and Solution Property Variations) presents a numerical study on the effects of variation of surface and solution properties in microchannels on sample dispersion during electroosmotic migration. Zeta potential variations across and along the microchannel generated a shear flow that increases the rate of dispersion of a sample plug. The electrical conductivity variation due to the presence of a sample plug resulted in a complicated distortion of the sample plug due to the interaction between flow fields, electric potential, and species concentration. A study on the appropriateness of the 1-D Taylor dispersion method in microchip capillary

electrophoresis modeling was also carried out. Along with the study in Chapter 5, this study provides a quantitative basis for judging the accuracy of the conventional 1-D or 2-D simulation of sample plug distribution during electroosmotic injection and migration compared to the complete 3-D simulation.

Chapter 7 presents an experimental investigation of cell lysis methods to identify optimal design and operational parameters for a rapid and effective cell lysis. Using a glass microchip, a pinched injection separation is successfully demonstrated. A continuous cell lysis method using combination of the electrical and osmotic lysis methods is also successfully demonstrated. To analyze the electric field condition, a numerical simulation with Comsol Multiphysics was performed. With the help of additional osmotic effect, cells were lysed below the critical electric field. The single cell analysis with red blood cells was performed. The result also confirms cell lysis.

Chapter 8 concludes the main body of the thesis. It also includes a discussion of the achievement of specific aims suggested in Chapter 1 in this Thesis. Finally, some relevant future work is discussed.

1.4 . SUMMARY

Single-cell analysis is a very useful method to understand the molecular mechanisms in a cell or to diagnose cell disease. There are several technical challenges for accomplishing single cell analysis. The small amount and low concentrations of the cellular constituents of interest cause significant difficulty for detection. Intracellular changes related to perturbations or membrane damage during cell sampling are also a potential pitfall for analyses performed on live

cells. These problems in single-cell analysis require high speed and high sensitivity analysis, which can be achieved by employing microchip capillary electrophoresis combined with laser-induced fluorescence detection. The advent of microengineering especially makes it possible to build automatic cell handling and cellular material analysis systems on a small chip which enables high-throughput analysis. The development of a microchip capillary electrophoresis system for high-throughput, sequential single cell analysis is proposed through comprehensive experimental and numerical studies. In order to build an automatic and high-throughput single-cell analysis system, an efficient cell delivery system must be achieved first. The development of a reliable sequential cell delivery system can be achieved via experimental and numerical studies on AC electrokinetic cell manipulation. Initial sample injection is a key element that determines the separation efficiency of capillary electrophoresis. The cell lysis must be done in such a way that the released intracellular components have a very narrow initial band and that the intracellular biochemical reactions due to external disturbances are minimized. The second task of this research is to perform an experimental investigation of cell lysis methods and to identify optimal design and operational parameters for rapid and effective cell lysis. Since capillary electrophoresis is activated by an electrokinetic mechanism, a characterization of electrokinetic phenomena is important to optimize the flow field in a microchannel to achieve the best separation efficiency.

CHAPTER 2. BACKGROUND

2.1 . MICROFLUIDICS, BIOMEMS AND LAB-ON-A-CHIP

Microfluidics is the science of very small volumes of fluid, ranging from a few microliters to volumes as low as femtoliters. The behavior of fluids at the microscale can differ from conventional macroscale fluid mechanics, having strong effects of surface tension, energy/molecule dissipation, fluid viscosity, and molecular level interfacial interaction. For example, low Reynolds number in microfluidic systems prohibits chemical mixing in the traditional sense; molecular transport must be through molecular diffusion. Microfluidics studies how these behaviors change, and how they can be applied for new uses [74].

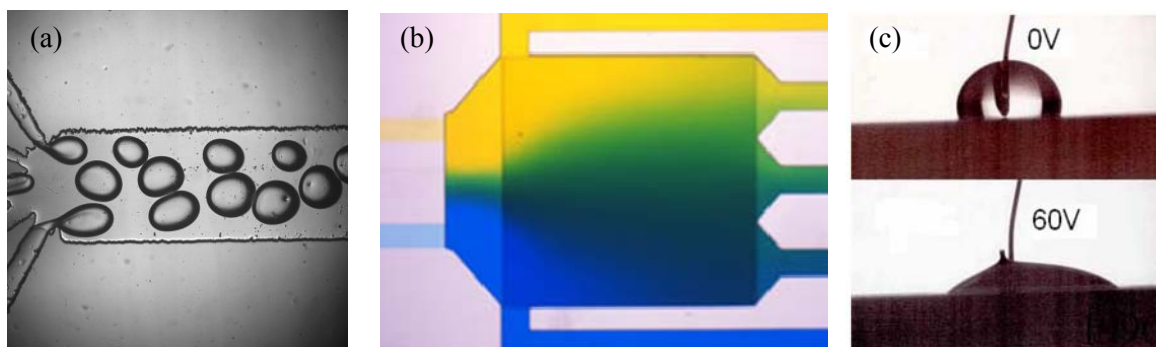


Figure 2-1. Examples of microfluidics phenomena. (a) Droplet formation by surface tension, (b) laminar diffusion and (c) electrowetting.

Recently, significant research has been performed for the application of microfluidics for the development of various industrial products. To date, the most successful commercial application of microfluidics is the inkjet print head. However, considering that biological metabolisms are mostly microfluidic phenomena, one can easily surmise that the biomedical area will be the biggest application area of microfluidics. Advances in microfluidics technology are

revolutionizing molecular biology procedures for biochemical material (enzyme, DNA and protein) analysis.

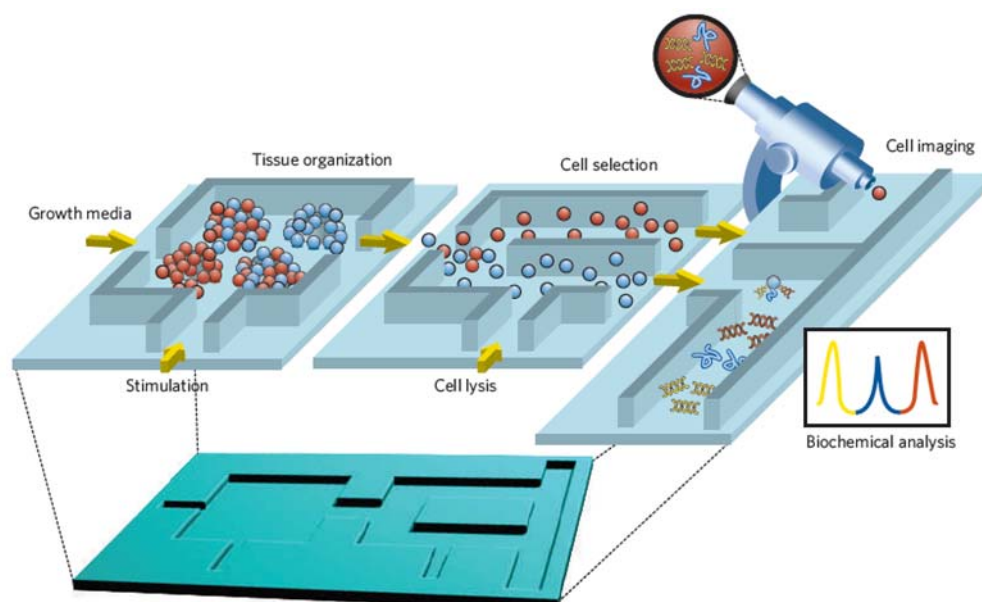


Figure 2-2. A conceptual schematic of a lab-on-a-chip device. This conceptual device contains many different components such as cell preparation, cell lysis and single cell analysis.[75]

Use of microfluidics phenomena often depends on the development of microscale devices, also known as micro electro mechanical systems (MEMS). The microfabrication techniques are described in Section 2.10. Micro systems for biomedical applications, called ‘BioMEMS’, are utilized to manipulate biological matter to analyze its activity or to perform planned functions. One of the biggest advantages of using microsystems is that many assay operations can be integrated into a chip because the geometric limitation of conventional assay tools is no longer present in microscale systems. This advantage of bioMEMS devices entices people to attempt to integrate assay operations such as detection, as well as sample pre-treatment and sample preparation on one chip. The idea of integration of biochemical assay operations on a chip is called ‘lab-on-a-chip’ or micro total analysis systems (μ TAS). One of the emerging

application areas for biochips is clinical pathology, especially the immediate point-of-care diagnosis of diseases. In addition, microfluidics-based devices, capable of continuous sampling and real-time testing of air/water samples for biochemical toxins and other dangerous pathogens, can serve as a continual alarm system for early warning.

2.2 . MICROFABRICATION TECHNIQUES

1. Photolithography

Photolithography is the process of transferring 2-D patterns from a photomask onto the surface of a substrate by using the chemical structure change of a photosensitive polymer (photoresist) under light exposure and subsequent selective removal of the polymer film. The 2-D pattern of the final polymer film with controlled thickness of the film may serve as a 3-D microstructure. Or a series of chemical treatments either etch away from, or deposit a new material on, the exposed substrate to form a final microstructure. Therefore the photolithography is usually an indispensable step in microfabrication procedures.

There are two types of photoresist: positive and negative. Exposure to the UV light breaks down polymer chains or changes functional groups in a positive photoresist to make the light-exposed polymer more soluble in a specific developer solution while exposure to the UV light causes a negative resist to become further polymerized, and more difficult to dissolve in the negative resist's developer. Table 2-1 provides brief photolithography recipes for some popular photoresists used for MEMS device fabrication.

Table 2-1. Photolithography recipes for some popular photoresists used for MEMS device fabrication.

PR name	SU8-2035	SC-1827	NR7-1500PY
Polarity	Negative	Positive	Negative
Thickness (controllable)	40 μm	2.5 μm	1.5 μm
Spin speed	3000 rpm	3000 rpm	3000 rpm
Soft bake	6 min @ 95 °C	2 min @ 100 °C	1 min @ 150 °C
UV exposure dose (365 nm)	160 mJ/cm ²	150 mJ/cm ²	585 mJ/cm ²
Post-exposure bake	6 min @ 95°C	-	1 min @ 100°C
Develop time	5 min	30 sec	12 s
Usage	Thick microstructure	Pattern transfer	Lift-off

2. Etching

Etching is the process of cutting into the unprotected parts of a substrate to create incising patterns. The two fundamental types of etching methods are liquid-phase etching (wet etching) and plasma-phase (dry etching).

The wet etching method uses a strong acid (etchant) to remove exposed patterns. The substrate is usually immersed in a bath of etchant and agitated to achieve good process control. For example, hydrofluoric acid (HF) is used commonly to etch silicon dioxide in an isotropic way. The etch rate of borofloat glass in a mixture of 49%HF, Nitric acid and DI water with the volume ratio of 20:17:79 is about 0.5 micron/min.

One of the most popular dry etching methods for MEMS fabrication is the deep reactive-ion etching (DRIE) technique, which is a highly anisotropic etch process used to create deep holes or trenches in substrates, with aspect ratios of 20:1 or more. The Bosch process alternates

repeatedly between two modes to achieve nearly vertical structures; 1. deposition of a chemically inert passivation layer (Teflon-like polymer) and 2. a standard, nearly isotropic plasma etch.

3. Deposition

Physical vapor deposition (PVD) is a general term used to describe any of a variety of methods to deposit thin films by the condensation of a vaporized form of a material onto various substrates. The coating method involves purely physical processes such as high temperature vacuum evaporation (thermal evaporation), electron beam bombardment (e-beam evaporation) or plasma sputter bombardment (sputtering). Parylene coating method can also be categorized into PVD.

Chemical vapor deposition (CVD) is a chemical process used to deposit high-purity, high-performance solid films on substrates. In a typical CVD process, a substrate is exposed to one or more volatile precursors, which react and/or decompose on the substrate surface to produce the desired deposit. For example, polycrystalline silicon is deposited from silane (SiH_4), using the following reaction: $\text{SiH}_4 \rightarrow \text{Si} + 2 \text{H}_2$

4. Soft lithography

Soft lithography refers to a family of techniques for replicating structures using stamps or molds. It is called "soft" because this method uses elastomeric materials. Soft lithography techniques are practical methods for fabricating structures as small as 30 nm in organic polymers with accuracy in vertical dimension of 5 nm. It is also eligible for mass production.

One of the most popular microfabrication methods in these days is the PDMS replica molding. In replica modeling, the master mold is replicated by casting and curing the pre-polymer. A micro-mold master is usually fabricated by using photolithography (one popular

photoresist is SU-8). After a mold master is prepared, a PDMS mixture (10:1 ratio of base resin to curing agent) was then poured onto the mold pattern as shown in Figure 2-3. After 30 minutes of degassing in a vacuum desiccator, putting the PDMS mixture in an oven at 80°C for 2 hours completely cures it. After baking, the fully-cured PDMS is peeled off and cut into individual devices. A PDMS trench can be placed on top of a flat substrate to make an enclosed channel.

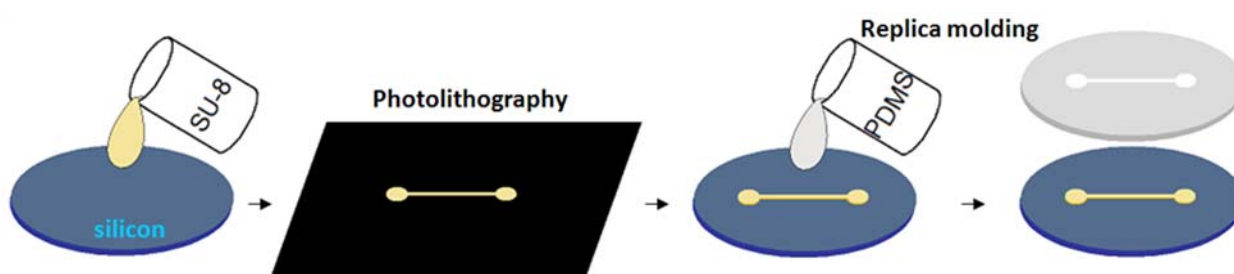


Figure 2-3. Schematic of fabrication procedures for a PDMS microchannel. The first step is to make an SU-8 mold master using photolithography and the next step is PDMS replica molding.

Hot Embossing is a technique of imprinting microstructures on a polymer substrate by placing the substrate on a stamp (mold master) and raising the temperature of the polymer just above its glass transition temperature. The stamp used to define the pattern in the polymer may be made in a variety of ways including wet etching on a silicon or glass plate, LIGA, micromachining using a mini mill, and even photolithography for SU-8 structure. A wide variety of polymers have been successfully hot embossed with micron-scale (and below) size features, including polycarbonate and PMMA. The benefits of this method are the ability to take advantage of the wide range of properties of polymers, as well as the potential to economically mass produce parts with micron-scale features.

Micro-contact printing (or μ CP) uses the PDMS rubber stamp to form patterns of self-assembled monolayers (SAMs) of ink on the surface of a substrate by covalent chemical reactions. This technique is popularly used in cell biology.

5. Other micro fabrication methods

Stereolithography is an additive manufacturing process using liquid UV-curable photopolymer resin and a UV laser to build parts a layer at a time. On each layer, the laser beam traces the cross-section pattern on the surface of the liquid resin. Exposure to the UV laser light cures, solidifies the pattern traced on the resin and adheres it to the layer below. After a pattern has been traced, the SLA's elevator platform descends by a single layer thickness, typically 0.05 mm to 0.15 mm. Then, a resin-filled blade sweeps across the part cross section, re-coating it with fresh material. On this new liquid surface, the subsequent layer pattern is traced, adhering to the previous layer. A complete 3-D part is formed by this process. After building, parts are cleaned of excess resin by immersion in a chemical bath and then cured in a UV oven.

A high-power and short-wavelength laser can be used to ablate a substrate to make relatively large dimension ($> 1 \mu\text{m}$) micro structures. The advantages are: 1) no solvents needed (environmentally friendly), 2) easy automation, 3) low running cost (although high equipment cost), 4) gentler process than abrasive techniques and 5) minimal heating of the target.

A high-resolution micromill can be used to make a relatively rough surface ($>1 \mu\text{m}$) with relatively large dimensions ($\sim 1\text{mm}$ or above).

6. Bonding

Most additive or reductive microfabrication techniques described above except the stereolithography produce open channels (trench). Then an open microchannel probably needs to

be bonded with another plate to serve as a complete microfluidics device. There are many different bonding methods available depending on the material type.

Thermal bonding

Any two clean plates of the same type can be bonded if their temperature is raised above the glass transition temperature. This bonding method, called thermal bonding, is the most fundamental bonding technique. Two plastic plates can be bonded by the hot embossing technique while glass plates can be thermally bonded in a furnace after perfect cleaning with Piranha and RCA solutions. Disadvantages of the pure thermal bonding method include high temperature deforming the shape and ruining parts of the device. For example, gold electrodes deposited on a glass substrate will be easily burned during the thermal glass-glass bonding process. In order to decrease the bonding temperature, alternative methods were developed.

In anodic bonding, one glass and one silicon substrate can be bonded at elevated temperatures (~ 400 °C) by placing the substrates between metal electrodes and applying a high DC potential (up to >1 kV). Sodium ions are displaced from the bonding surface of the glass by the applied electrical field and the elevated temperature. The depletion of sodium ions near the surface of the glass makes the surface highly reactive with the silicon surface of the other substrate forming a solid chemical bond.

In fusion bonding, two Si substrates are first forced into intimate contact by applying a high contact force. Once in contact, the substrates hold together due to atomic attraction forces (van der Waal), which are strong enough to allow the bonded substrates to be handled. The substrates are then placed in a furnace and annealed at high temperature, after which a solid bond is formed between the substrates.

Plasma bonding

A PDMS substrate can be sealed with a glass, a PMMA or another PDMS plate by means of oxygen plasma treatment. Exposure to oxygen plasma gas causes the oxidation of the surface layer which increases the concentration of hydroxyl groups and this leads to the formation of strong intermolecular bonds. This bonding method is becoming very popular, as the usage of PDMS in the bioMEMS field is growing.

2.3 . DC ELECTROKINETICS THEORY

The electrokinetic phenomena are movement of charged particles or liquid medium under imposed electric field. Electrokinetic phenomena are a family of several different effects that occur in heterogeneous fluids or in porous bodies filled with fluid. The term heterogeneous here means a fluid containing particles. Particles can be solid, liquid or gas bubbles with sizes on the scale of a micrometer or nanometer.

2.3.1. Electrophoresis

Electrophoresis is the movement of electrically-charged particles relative to the surrounding liquid under applied electric field. The rise of net electric charge in a particle is due to electron exchange between the particle and the surrounding medium (mostly water-based electrolyte). The size of particles varies from as small as a molecule to as big as a micro particle (a bulk body). The electrophoresis of a micro particle should be involved with formation of an electric double layer on the particle surface. The electrophoretic mobility is the ratio of the equilibrium velocity of the particle to the applied electric field. The equilibrium speed is established from the balance between the electric driving force (Coulombic force) and the viscous drag force (Stokes force).

For example, a spherical micro particle (radius r) with electric charge q will have the following force balance and thus electrophoretic mobility (μ_{ep}).

$$6\pi\eta r V_{ep} = qE, \quad \mu_{ep} = \frac{V_{ep}}{E} = \frac{q}{6\pi\eta r} \quad (2-1)$$

where E is the applied electric field, η is the viscosity of medium and V_{ep} is electrophoretic velocity. In general, the electrophoretic mobility of any particle or species is a function of the solution's viscosity and the electric charge and shape of the particle. The certainty and uniqueness of the electrophoretic mobility of a species makes it possible to separate the chemical species in a sample mixture by applying an electric field.

2.3.2. Electroosmosis

Electroosmosis is the motion of aqueous liquid along a solid surface induced by migration of ions collected near the surface in the form of an electrical double layer (EDL). When a solid substrate is immersed in an electrolyte, the surface can carry a net charge resulting from dissociation of the substrate ions or preferential ion attraction to the substrate surface. For example, when a glass substrate contacts an electrolyte with pH higher than 2, a proton dissociates from each silanol group (SiOH) on the glass surface, making the surface negatively charged (SiO⁻). As a result, positively charged counter ions in the bulk solution are attracted toward the surface, forming an EDL. Under a DC electric field, the positive counter ions of the EDL move toward the cathode, inducing bulk fluid motion. The region of the electric double layer in typical running media is limited to only a few nano meters from the wall which is much smaller than the dimension of the typical microchannels in over-micron size. The thin thickness

of the electric double layer makes the induced bulk flow behave like the wall-slipping flow. The slipping-like flow results in a uniform velocity profile across the channel as shown in Figure 2-4. The uniform velocity profile makes the electroosmotic flow very attractive in separation science because dynamic dispersion and band broadening effect can be minimized with such a velocity profile, compared to the parabolic velocity profile of pressure-driven flows.

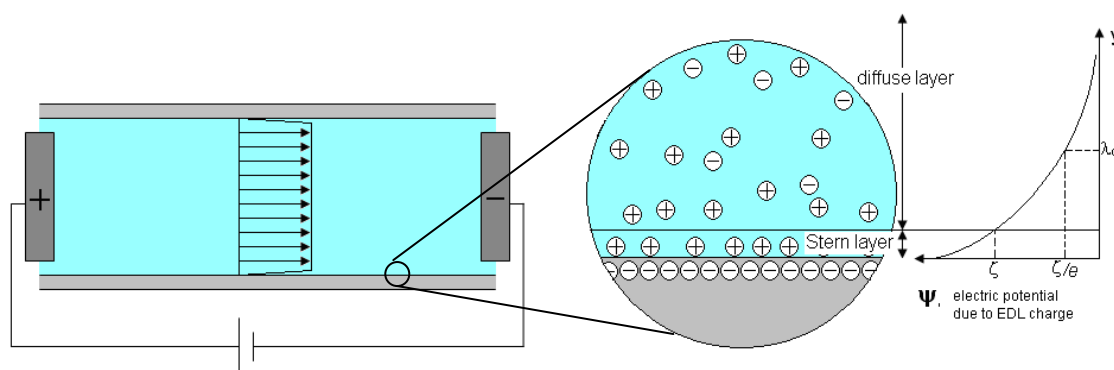


Figure 2-4. Electroosmotic velocity and electric double layer schematic. The zeta potential (ζ) is the electric potential at the interface between the Stern and diffuse layers. The Debye length (λ_d) is the distance from the wall to the point where the potential decreases to ζ/e .

The electroosmotic flow can be a useful delivery tool for biochemical separation systems because its uniform velocity profile suppresses the dynamic diffusion present in pressure driven flows. In this lab, the author is going to observe electroosmotic flow in microchannels generated by high DC electric field and measure the proportionality between electric field and flow velocity, called electroosmotic mobility, via the current monitoring method.

Electroosmotic mobility and zeta potential

The governing equation of dynamics of electroosmotic flow in microchannels is obtained by adding the electric body force to the incompressible Navier-Stokes equation as follows.

$$\rho \frac{D\vec{V}}{Dt} = -\nabla p + \mu \nabla^2 \vec{V} + \rho_e \vec{E} \quad (2-2)$$

where ρ_e is the electric charge density and \vec{E} is the electric field.

The electric charge density, ρ_e , is proportional to the divergence of the electric field (the Gauss's law). Noting that the electric charge arises from the double layer, the electric charge density is purely related to the electric potential due to the double layer as follows.

$$\rho_e = -\varepsilon \nabla^2 \psi \quad (2-3)$$

where ε is the permittivity of the solution and ψ is the electric potential due to the double layer.

Substituting Eq. (2-3), Eq. (2-2) becomes

$$\rho \frac{D\vec{V}}{Dt} = -\nabla p + \mu \nabla^2 \vec{V} - \varepsilon \nabla^2 \psi \vec{E} \quad (2-4)$$

When the flow is steady and constant along the streamline direction or convective acceleration is negligible compared with other forces ($Re \ll 1$), the left hand side is dropped and the momentum equation becomes a linear differential equation (Stokes flow). After decomposing the velocity into a pressure driven part and an electroosmosis-driven part, the electroosmotic velocity (excluding pressure gradient) is expressed as

$$\nabla^2(\mu\vec{V}_{eo} - \varepsilon\vec{E}\psi) = 0 \quad (2-5)$$

The solution for Eq. (2-5) can be expressed as

$$\mu\vec{V}_{eo} = \varepsilon\vec{E}\psi + \beta \quad (2-6)$$

where β is the solution of the Laplace equation, Eq.(2-5), obtained by imposing no slip velocity and zeta potential boundary conditions. Note that β becomes constant when the zeta potential is uniform all around the channel walls. After imposing boundary conditions, the final velocity and Eq.(2-6) is expressed as

$$\vec{V}_{eo} = \frac{\varepsilon\vec{E}}{\mu}(\psi - \zeta) \quad (2-7)$$

Analyzing the ion distribution, the function ψ is solved to be near zero in almost the entire domain except very near the wall in typical microchannels. Thus the following velocity expression is also valid for nearly the entire flow field.

$$\vec{V}_{eo} = -\frac{\varepsilon\zeta}{\mu}\vec{E} \quad (2-8)$$

The proportionality between velocity and electric field, $-\varepsilon\zeta/\mu$, is defined as electroosmotic mobility, μ_{eo} . The zeta potential (thus electroosmotic mobility) is dependent upon

the solid surface property and the solution properties (pH and ionic strength) as shown in Figure 2-5.

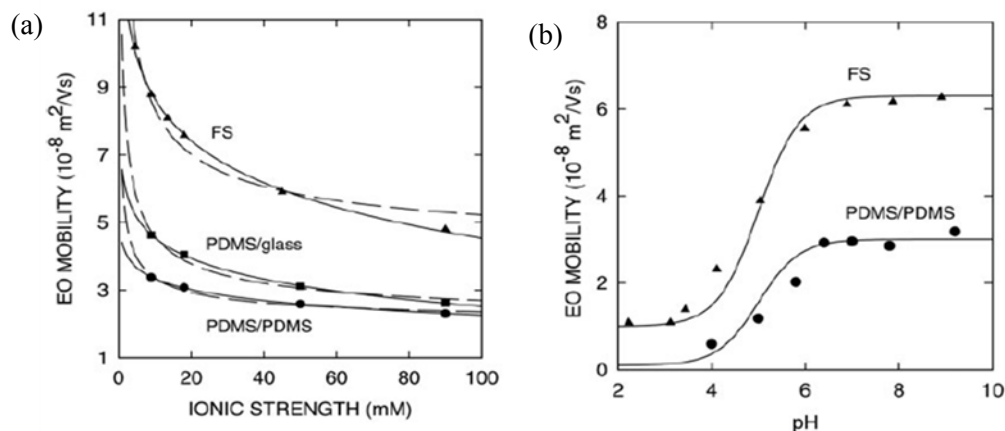


Figure 2-5. Electroosmotic mobility as a function of (a) ionic strength and (b) pH. FS represents the fused silica (glass).[76]

2.4 . AC ELECTROKINETICS THEORY

AC electrokinetics refers to the movement of fluids or particles driven by AC electric fields. Depending on applied frequency and medium conductivity, there are various AC electrokinetic phenomena such as dielectrophoresis, AC electroosmosis, and electrothermal flows. These AC electrokinetic phenomena have drawn much attention in the microfluidics and lab-on-a-chip communities since these techniques have a great potential for effective manipulation of small particles [35-43] and fluids in microchannel environments [48-50]. The simplicity in manufacturing and the versatility in application of AC electrokinetic techniques further enhances the popularity in the application of microfluidics and lab-on-a-chip.

2.4.1. AC Electroosmosis

When an AC electric field is applied to planar microelectrodes immersed in a liquid electrolyte, mobile counter ions are attracted to the microelectrode surfaces by the applied electric potential, and an electric double layer (EDL) is formed (Figure 2-6). Since the electric field has a tangential component due to the planar electrode geometry, the counter ions are pulled along the tangential component of the applied electric field (from the edge to the middle of the electrode). The direction of movement does not change with the polarity change of the AC voltage because the polarity of the induced counter ions is switched as well. The motion of the ions drags the bulk fluid along the surface. That fluid motion is called AC electroosmosis. ACEO can only exist in low conductivity media such as DI water. High conductivity media such as isotonic buffer results in a tightly bound and immovable electric double layer.

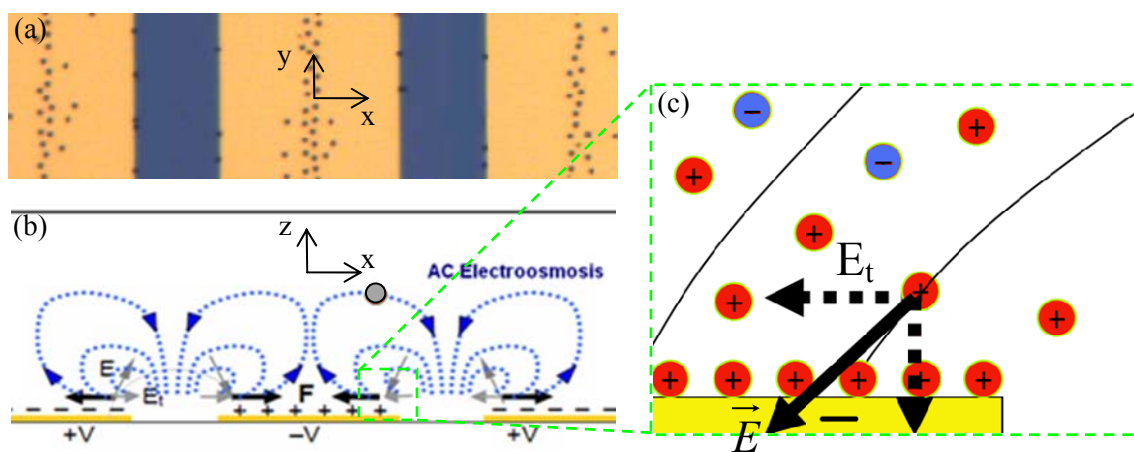


Figure 2-6. Mechanism of ACEO flow. (a) Microbeads collection by ACEO, (b) schematic of ACEO generation and (c) zoomed-in schematic; electric double layer is formed by applied electric potential.

In a set of interdigitated electrodes, these charges move from the edges of the electrode towards the center. The bulk movement of these charges induces fluid flow due to viscous drag effects. The induced bulk motion of fluid is swirling pattern. The time-averaged AC

electroosmotic slip velocity on two parallel electrodes was derived by Ramos *et al* [32-34] by assuming a linear relationship between the surface charge and electric potential, neglecting the stern layer and assuming two wide electrodes with a very narrow gap in between. The simplified ACEO velocity expression is as follows:

$$V_{ACEO} = \left(\frac{\varepsilon \varphi_0^2 \Omega^2}{8\eta x (1 + \Omega^2)^2} \right) \quad (2-9)$$

$$\Omega = \frac{1}{2} \pi \kappa x \left(\frac{\varepsilon_m}{\sigma_m} \right) \omega \quad (2-10)$$

where φ_o is the applied electric potential, Ω is a non-dimensional frequency defined as above, η is the dynamic viscosity, x is the horizontal location starting from the center of the gap between the electrodes and κ is the reciprocal of the Debye length. Figure 2-7 plots the AC electroosmotic velocity as a function of frequency and position on an electrode using Eq.(2-9). The velocity is always greatest at the edge and decreases as the center is approached. The velocity also is zero at low and high frequencies and reaches a maximum at mid-range frequencies. However this simulation is not very accurate (the difference between prediction by Eq.(2-9) and experimental observation was by a factor of 4 [45]) because of employed approximations.

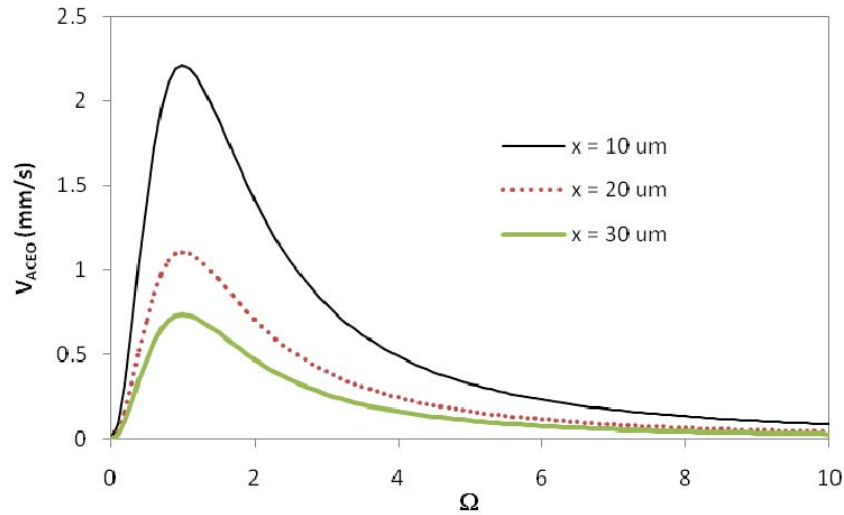


Figure 2-7. Analytical solution of AC electroosmotic velocity as a function of non-dimensional frequency using Eq. (2-9)

2.4.2. Dielectrophoresis

When a dielectric particle is suspended in a liquid media of different polarizability (electric permittivity) and subjected to a non-uniform electric field, the particle experiences a net force (dielectrophoresis, DEP) and is either attracted to (positive DEP) or pushed away from (negative DEP) a high electric field region [77]. By employing a dipolar approximation of a particle and neglecting the influence of particle volume on the near field of the particle, the simplest formula for the DEP force for a solid particle can be derived as follows:

$$\vec{F}_{DEP} = 2\pi a^3 \epsilon_m \operatorname{Re}[CM] \nabla |\vec{E}|^2 \quad (2-11)$$

where

$$CM = \left(\frac{\tilde{\epsilon}_p - \tilde{\epsilon}_m}{\tilde{\epsilon}_p + 2\tilde{\epsilon}_m} \right) \text{ and } \tilde{\epsilon} = \epsilon - j \frac{\sigma}{\omega} \quad (2-12)$$

where ε , E , σ , ω and j indicate permittivity, electric field, electric conductivity, the frequency of applied electric field and the imaginary unit, respectively. Subscripts, m and p , indicate properties of the media and particle. Clausius–Mossotti factor via Eq. (2-12) is a function of frequency through the complex permittivity of the particle and the media and it ranges from -0.5 to 1 [35-37]. In general, the CM factor is determined by the particle geometry, the electric properties of the particle and medium, and the frequency of applied electric field. In most cases of complicated biological objects it is difficult to find an exact analytical expression. Instead, the function must be obtained experimentally. This factor affects not only the magnitude of the force, but also its polarity. When this factor is positive, DEP is positive. When this factor is negative, DEP is also negative. Figure 2-8 shows how the CM factor varies as a function of frequency and media conductivity for both a solid sphere and for a shell structure.

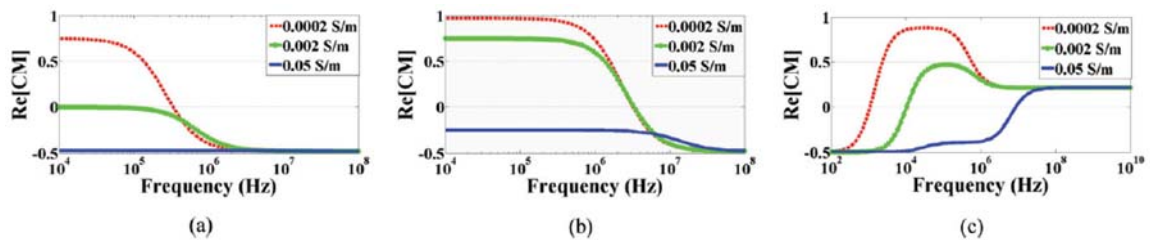


Figure 2-8. Clausius–Mossotti factor as a function of frequency for polystyrene spheres (particle permittivity = $2.5 \varepsilon_0$) with (a) 2 μm and (b) 200 nm diameter, and (c) a shell structure modeled on *Chlorella sp.* (surface capacitance = 12.4 mS, radius = 3.29 μm , inside conductivity = 8 mS /m, inside permittivity = $150 \varepsilon_0$). $\varepsilon_p = 80.2 \varepsilon_0$

When the near field influence becomes significant, such as when particles are close to each other or another solid surface, the dipole approximation of DEP becomes inaccurate [78]. In Benselama’s simulation, as a particle approaches the top or bottom wall, the DEP calculation via point-dipole approximation deviates from the accurate calculation results as shown in Figure 2-9.

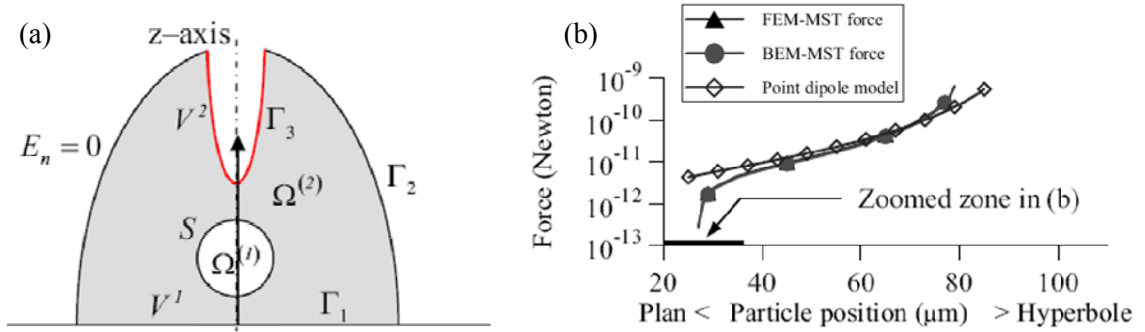


Figure 2-9. Comparison between point dipole method and Maxwell stress tensor (MST) method for DEP on a latex particle immersed in Mannitol at 10 Hz (radius = 20 μm) [78]. (a) Computational domain and (b) DEP force calculation via FEM/BEM MST and point dipole methods with varying particle position (z).

The most accurate calculation of the DEP force can be made by integrating Maxwell stress tensor (\vec{T}) over a closed body as follows:

$$\vec{F}_{DEP} = \oint (\vec{T} \cdot \vec{n}) dA \quad (2-13)$$

where \vec{n} is the unit vector normal to the control surface (A). This is a direct calculation of the electric force over any control volume, making it the most rigorous calculation of dielectrophoresis.

The Maxwell stress tensor with neglecting magnetic field is defined as

$$T_{ij} = \epsilon_m \left(E_i E_j - \frac{1}{2} \delta_{ij} E_k E_k \right) \quad (2-14)$$

where ε_m is the media permittivity and δ_{ij} is Kronecker's delta. The average DEP force of AC oscillation can be obtained by the complex variable analysis as follows:

$$\langle \vec{F}_{DEP} \rangle = \oint \left(\langle \vec{T} \rangle \cdot \vec{n} \right) dA \quad (2-15)$$

$$\langle T_{ij} \rangle = \frac{\text{Re}(\varepsilon_m)}{4} (E_i E_j^* + E_i^* E_j - \delta_{ij} E_k E_k^*) \quad (2-16)$$

where $\langle \rangle$, $\text{Re}(\)$ and $*$ indicate the time average, real and complex conjugate parts respectively. Note that the electric field should be obtained in the media region (not in the particle region). For example, the x-component of the DEP force is calculated by

$$\begin{aligned} \langle \vec{F}_{DEP,x} \rangle &= \oint \left(\langle T_{xx} \rangle \cdot n_x + \langle T_{xy} \rangle \cdot n_y + \langle T_{xz} \rangle \cdot n_z \right) dA \\ &= \frac{\text{Re}(\varepsilon_m)}{4} \oint \left(\left(2|E_x|^2 - |\vec{E}|^2 \right) \cdot n_x + 2 \text{Re}(E_x E_y^*) \cdot n_y + 2 \text{Re}(E_x E_z^*) \cdot n_z \right) dA \end{aligned} \quad (2-17)$$

2.4.3. Electrothermal Flow

Non-uniform Joule heating or cooling in an electrical system generates a spatial temperature gradient according to the following heat transfer formula:

$$\begin{aligned} k \nabla^2 T + \sigma E^2 &= \rho c_p \vec{V} \cdot \nabla T \quad \text{or} \\ k \nabla^2 T + \sigma E_{rms}^2 &= \rho c_p \vec{V} \cdot \nabla T \quad \text{for an AC system} \end{aligned} \quad (2-18)$$

The temperature gradient also creates variation in the electrical conductivity and permittivity of the media, and assuming small temperature variation, the following equations may define the linear relationships between temperature and electrical parameter variations [79].

$$\alpha = \left(\frac{1}{\varepsilon} \right) \left(\frac{\Delta \varepsilon}{\Delta T} \right) = -0.004 \text{ K}^{-1} \quad (2-19)$$

$$\beta = \left(\frac{1}{\sigma} \right) \left(\frac{\Delta \sigma}{\Delta T} \right) = 0.02 \text{ K}^{-1} \quad (2-20)$$

This electrical property gradient generates free charges and thus, the electric body force, called electrothermal force. The derivation of electrothermal force starts with a general expression for the electrical force per volume as follows,

$$\vec{f}_E = \rho_q \vec{E} - \frac{1}{2} |\vec{E}|^2 \nabla \varepsilon + \frac{1}{2} \nabla \left(\rho \frac{\partial \varepsilon}{\partial \rho} |\vec{E}|^2 \right) \quad (2-21)$$

where ρ_q is the electric charge density. For an incompressible fluid, the last term in this equation vanishes. Assuming that the deviations of the electric properties are small, the electrical field can be written as the sum of two components $\vec{E} = \vec{E}_0 + \vec{E}_1$, where \vec{E}_1 is the perturbation by thermal gradient and \vec{E}_0 is the sinusoidally oscillating electric field when there is no thermal perturbation. Then the electric charge due to thermal gradient is derived via Gauss's law as follow,

$$\rho_q = \nabla \cdot (\varepsilon \vec{E}) = \nabla \varepsilon \cdot \vec{E}_0 + \varepsilon \nabla \cdot \vec{E}_1 \quad (2-22)$$

The time-dependent electric charge conservation equation is obtained as

$$\partial \rho_q / \partial t + \nabla \cdot (\sigma \vec{E} + \rho_q \vec{V}) = 0 \quad (2-23)$$

where the convection term can be neglected via order of magnitude analysis. Combining Eqs. (2-22) and (2-23) and a complex variable method results in

$$\nabla \cdot \vec{E}_1 = \frac{-(\nabla \sigma + j\omega \nabla \varepsilon) \cdot \vec{E}_0}{\sigma + j\omega \varepsilon} \quad (2-24)$$

Substituting Eqs. (2-22) and (2-24) into Eq. (2-21) and taking time average, the final form of electrothermal force is derived as follows,

$$\begin{aligned} \langle \vec{f}_{ETF} \rangle &= \left\langle \rho_q \vec{E} - \frac{1}{2} |\vec{E}|^2 \nabla \varepsilon \right\rangle = \left\langle (\nabla \varepsilon \cdot \vec{E}_0 + \varepsilon \nabla \cdot \vec{E}_1) \vec{E} - \frac{1}{2} |\vec{E}|^2 \nabla \varepsilon \right\rangle \quad (\vec{E} \approx \vec{E}_0) \\ &\approx \frac{1}{2} \text{Re} \left[\left(\frac{(\sigma \nabla \varepsilon - \varepsilon \nabla \sigma) \cdot \vec{E}_0}{\sigma + j\omega \varepsilon} \right) \vec{E}_0^* - \frac{1}{2} |\vec{E}_0|^2 \nabla \varepsilon \right] \quad (\vec{E}_0^* = \vec{E}_0 \text{ are real}) \\ &= -\frac{1}{2} \left[\left(\frac{\nabla \sigma}{\sigma} - \frac{\nabla \varepsilon}{\varepsilon} \right) \cdot \vec{E}_0 \frac{\varepsilon \vec{E}_0}{1 + (\omega \varepsilon / \sigma)^2} + \frac{1}{2} |\vec{E}_0|^2 \nabla \varepsilon \right] \end{aligned} \quad (2-25)$$

Note that \vec{E}_0 is real value everywhere if boundary conditions are all real. For electrothermal flow simulation, the electrothermal force, Eq. (2-25) is added into the Navier-Stokes equation as a body force. Like ACEO, electrothermal flow is an electrohydrodynamic phenomenon. Assuming that the gap between the electrodes is much smaller than the width of the

electrodes, the temperature gradient becomes parallel to the electric field and an analytical solution of electrothermal force can be derived as [32],

$$\langle \vec{f}_{ETF} \rangle = \frac{2}{\pi^3 k} \frac{\varepsilon \varphi_0^2}{r^3} \left(1 - \frac{2\theta}{\pi} \right) \sigma \Pi \hat{\theta} \quad \Pi(\omega, \sigma) = \left(\frac{\alpha - \beta}{1 + (\omega\tau)^2} - \frac{\alpha}{2} \right) \quad (2-26)$$

where τ is the charge relaxation time (ε/σ). Π (plotted in Figure 2-10a) determines the direction of the force and also plays a role in determining its magnitude.

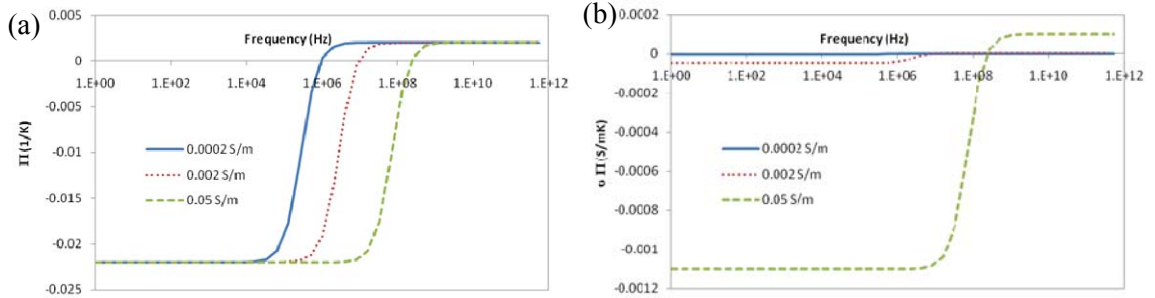


Figure 2-10. Π and $\sigma\Pi$ as functions of frequency with three different conductivities.

Electrodes deposited on highly-conductive substrate such as a silicon wafer can serve well as heat sinks. This, together with the non-uniform electric field, causes there to be strong temperature gradients. Electrothermal flow also usually requires high conductivity media to generate stronger Joule heating effects. Also the electrothermal flow requires higher field strengths than ACEO to generate useful flow velocities. However, velocity increases much more dramatically with an increase in voltage because the relationship is a fourth power one, so that doubling the voltage results in a 16 times increase in fluid velocity. Generally, when the frequency of the applied voltage and the media conductivity are high ($f > 80$ kHz, $\sigma > 100$

$\mu\text{S/cm}$), ACEO diminishes, and ETF becomes dominant. As shown in Figure 2-11, the swirling flow pattern of ETF in interdigitated electrode cases is somewhat similar to that of ACEO.

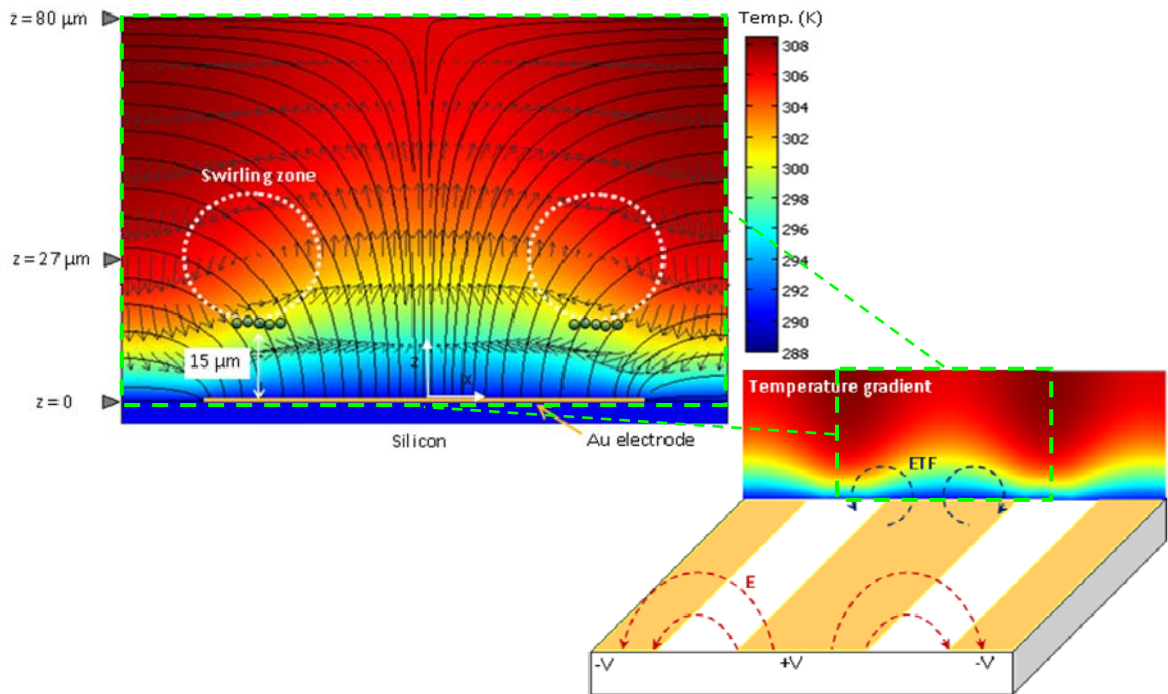


Figure 2-11. Electrothermal flow 2-D simulation result. The contour colors, the streamlines and the arrows represent temperature profile, electric field lines and electrothermal flow velocity, respectively. ($\sigma_m = 1.77 \text{ S/m}$, $f = 200 \text{ kHz}$ and $V_{\text{rms}} = 7 \text{ V}$). Detailed discussion about this simulation is provided in Chapter 4.

2.5 . CELL MANIPULATION IN MICROCHANNELS

The first critical process of microchip single-cell analysis system is to separate and deliver each cell to the place where the cell is lysed. When a sequential single-cell analysis is pursued, an automatic cell delivering system is desired. Methods suitable for parallel delivery are also desired to achieve a high throughput. Various cell manipulation techniques for the purpose of

microchip single-cell analysis have been previously developed by employing various physics or devices; hydrodynamics, [80], micro-valves [81, 82], micro-droplets [83], geometric trapping, electrophoresis[84], dielectrophoresis, magnetophoresis, ultrasound, centrifugation, gravitation, optical tweezers, etc. Particle manipulation methods can be categorized into active or passive methods. Active methods use an external field to precisely manipulate and separate particles while passive methods use the channel geometry and the intrinsic hydrodynamic fluid forces (inertia, shear and pressure) to separate microparticles mostly based on their size.

Hydrodynamic particle manipulation (passive method)

The hydrodynamic method is a passive particle manipulation method by using the effects of laminar fluid flow combined with geometrical features of microchannels. The hydrodynamic cell focusing uses the laminar characteristics of microfluidic flow to focus cells into a narrow stream. The sheath flow narrows down the main flow containing cells in a stable laminar way. This hydrodynamic method has been widely adopted for focusing cells in flow cytometry and very high throughput up to 100,000 cells/s was achieved in that area. McClain et al. [24] employed a hydrodynamic cell focusing method and achieved up to 12 cells/min throughput. Inertial lift force was also used to sort microparticles [85, 86]. Inertial lift force is a hydrodynamic force generated by shear flow in a laminar microchannel flow. Segre [87] first observed that particles in laminar channel flows moved to certain radial locations depending on the particle size and flow conditions as they flow. This phenomenon, later named inertial lift force, is due to the balance between shear-induced inertial lift force pushing away from the center and wall-effect-induced inertial lift force pushing away from the wall as illustrated in Figure 2-12a. If a particle is close to the center line, the fluid velocity relative to the sphere is larger on the wall side than on the centerline side. The asymmetry of fluid velocity results in a lower pressure on the wall side

(higher velocity) than on the centerline side, leading the sphere to migrate away from the centerline (shear-induced inertial lift force, Figure 2-12b. If a particle is close to the wall, the streamlines around the sphere are altered as shown in Figure 2-12c. The change of streamlines induces the higher pressure on the wall side than the centerline side.

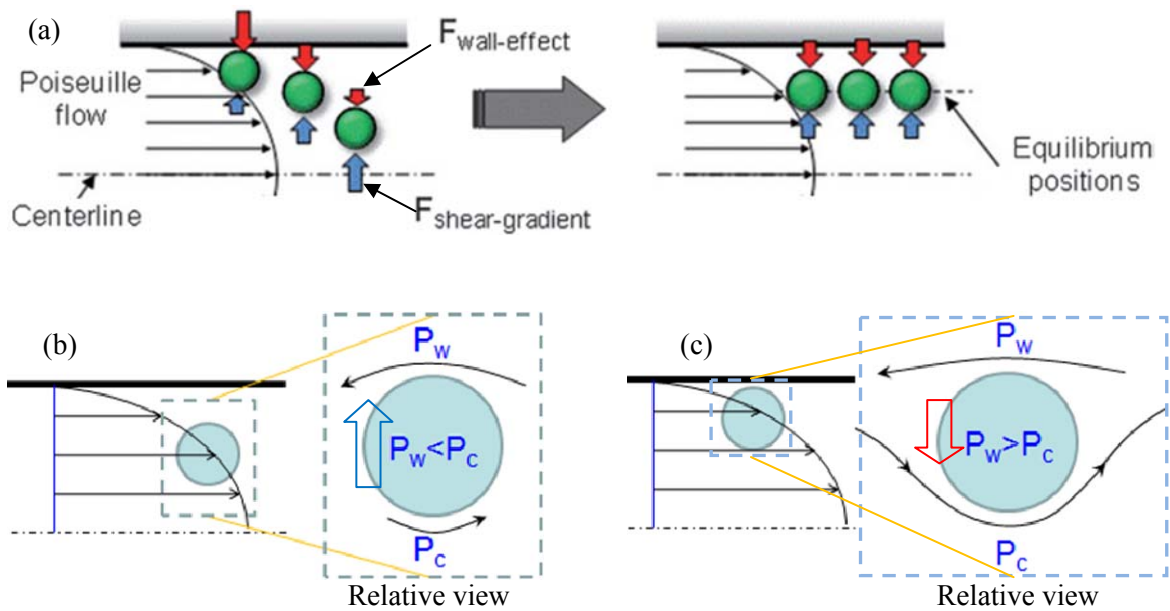


Figure 2-12. The mechanism of inertial lift force. (a) Particles move to the balance location between shear-induced inertial lift force and wall-effect-induced inertial lift force. The mechanisms of (b) shear-induced inertial lift force and (c) wall-effect-induced inertial lift force.

Dean vortices are a pair of secondary circulations generated in a curved channel. These vortices are generated by the variation of centrifugal force due to the flow variation in a Poiseuille flow. Combination of inertial lift force and Dean vortices was also used for particle separation [86]. Figure 2-13 shows examples of continuous particle separation results.

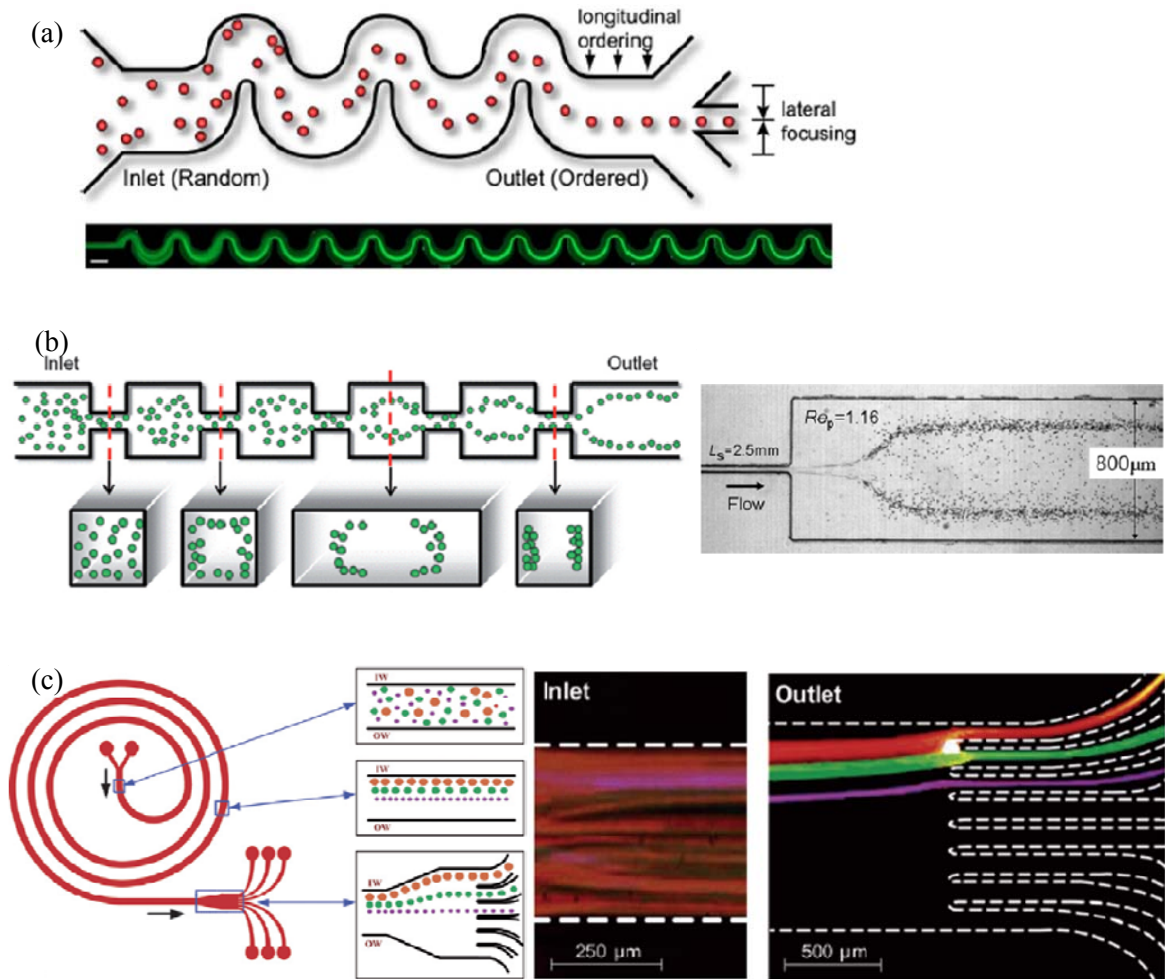


Figure 2-13. Continuous particle sorting or focusing using inertial lift force (hydrodynamic method). Continuous particle focusing (a: [88], b:[89]) and (c) continuous particle separation using combination of inertial lift force and Dean vortices[86].

Electric and magnetic field methods

Electric field-based manipulation is well suited for micro systems because of the ease in generating a high electric field by applying a voltage of several volts between micro electrodes which can also be easily fabricated through MEMS techniques.

In traditional methods, dielectrophoresis has been applied to separate cells by using castellated or interdigitated planar electrodes. DEP was often adopted for binary separation where

a mixture is separated into two subpopulations by DEP force. DEP was also used to stop particle flow [90]. When the DEP was actuated, all the cells were held above the electrodes against the flow. Being coupled with antibody recognition technique, targeted cells were bound with the antibodies when cells were stopped. When the DEP was deactivated, the unbound cells flow away, leaving the targeted cells separated in the channel. Some drawbacks of this positive DEP method are that cells are often permanently trapped and high applied voltage can damage cells. While the cells trapped by pDEP seemed to stay viable, an anomalous protein was released [90]. Hydrodynamic forces have also been coupled to dielectrophoresis to produce continuous particle separation. This technique uses electrodes to levitate particles to different heights depending on their dielectric properties. The addition of a parabolic flow allows the particles to be dragged away at different velocities. Separation of erythrocytes and latex beads was performed by Rousselet et al. [91] Separation of different types of leucocytes was reported with a purity after separation up to 98% [92]. Choi and Park [93] proposed a trapezoidal planar electrode array providing a specific electric field geometry in a microchannel. Li and Kaler [94] reported an ingenious 'isomotive' electrode arrangement for continuous-flow separation. This geometry provides a better separation of species, based only on their dielectric properties. The use of dielectrophoretic barriers has also been widely and successfully demonstrated where electrodes were mounted at the top and bottom of a microchannel. DEP force deflects particles from the direction of fluid flow. Leu et al. [95] fabricated a device where a mixture of particles was separated in a single particle stream with a combination of DEP forces and hydrodynamic forces in a funnel-like channel. In Figure 2-14, electrodes are mounted at the top and bottom of the microchannel. When the electric field was applied, cells were diverted from their natural path and reacted with the reagent.

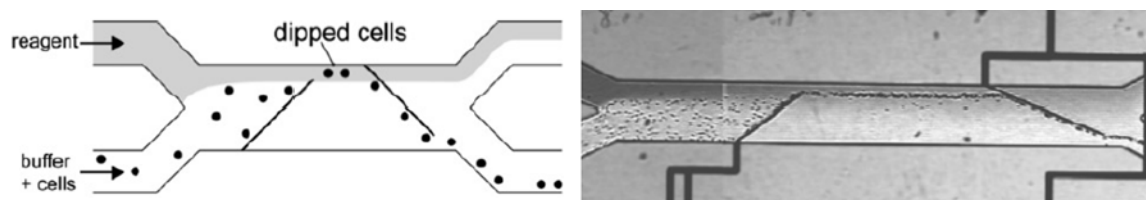


Figure 2-14. DEP barriers for cell dipping. [95] Cells are guided to the reagent and returned from the reagent back to the buffer when electric field is on.

In the magnetic separation method, sorted particles have either intrinsic magnetic properties or are labeled with magnetic beads. A magnet is placed in the vicinity of a column containing the cells to be separated. Magnetically-labeled cells are retained in the column, whereas non-labeled cells will be flushed with the buffer. The use of permanent magnets allows for portable (no electric connection) and autonomous devices while electromagnets have the advantage to be easily switched on and off. A technique called ‘on-chip free-flow magnetophoresis’ was demonstrated by Pamme et al.[96] In this example, a mixture of different magnetic particles and non-magnetic particles is aligned along the wall of a microchannel. A micromagnet placed upon the channel provides a non-homogeneous magnetic field gradient transverse to the laminar flow. Depending on their size and magnetic properties, particles are deflected more or less from their path. The addition of spacers allows the collection of particles in separated outlets as shown in Figure 2-15a. In another type of continuous magnetic, some ferromagnetic strips fabricated in a microchannel provide an array-like magnetic field pattern at a given angle to flow direction [97]. Cells selectively tagged with magnetic nanoparticles deflect from the flow path to follow the strips. This technique convincingly demonstrates the separation of white blood cells (WBCs) from human blood as shown in Figure 2-15b.

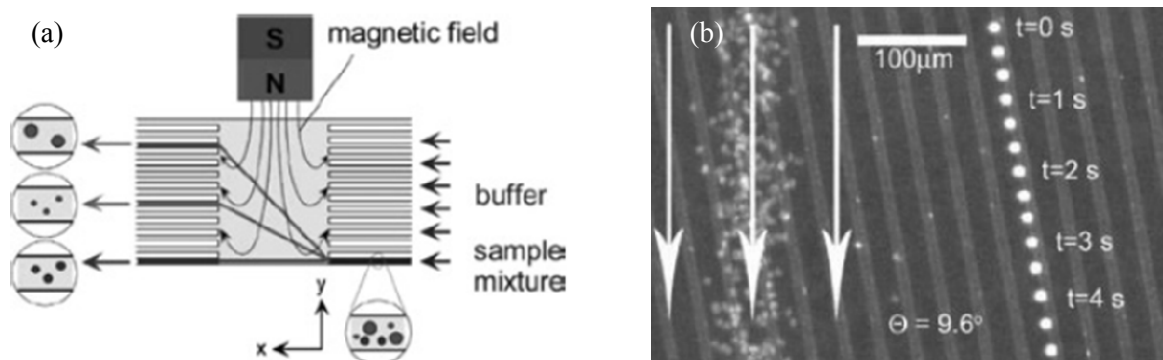


Figure 2-15. Particle manipulation by magnetic field. (a) Separation of magnetic and non-magnetic particles, based on particle size and magnetic properties [96]. (b) Separation of red blood cells from white cells with magnetic strips [97].

Kim and Soh [98] reported an integrated DEP–Magnetic Activated Cell Sorter (iDMACS) where an integrated platform combined two different force fields in a single microfluidic device for highly efficient multi-target separation as illustrated in Figure 2-16. The target cells are sequentially sorted dielectrophoretically and magnetically, and eluted through independent outlets. They showed about 900-fold enrichment of multiple bacterial target cell types with over 95% purity after a single round of separation with this device.

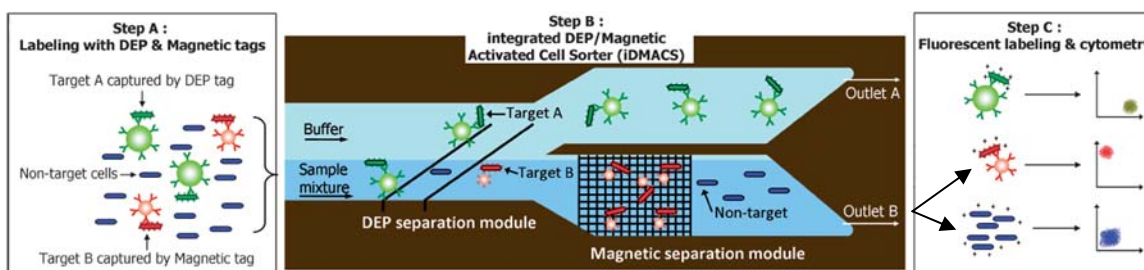


Figure 2-16. Multi-target bacterial cell sorting via iDMACS. The target cells are sequentially sorted dielectrophoretically and magnetically, and eluted through independent outlets. [98]

Optical methods

Optical tweezers are capable of manipulating nanometer- and micrometer-sized dielectric particles via a highly focused laser beam. The narrowest point of the focused beam has a very strong electric field gradient. Dielectric particles are attracted along the gradient to the region of strongest electric field. The laser light also tends to apply a force on particles in the beam along the direction of beam propagation. Optical tweezers have been widely used to trap single particles in microfluidic systems [99, 100]. In optical fractionation, an optical gradient force is generated to deflect particles from their natural pathway according to their size or properties [101]. Particles experiencing sufficient optical force are kinetically locked in arrays of optical tweezers, whereas other particles flow along the natural stream, as shown in Figure 2-17.

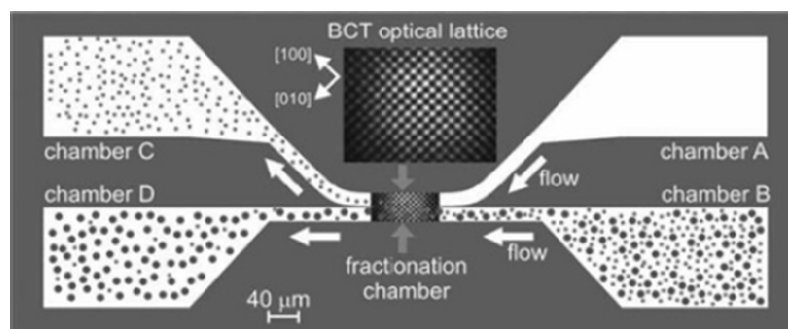


Figure 2-17. Optical fractionation.[101] 3D optical lattice is introduced in the shared part of the chambers A, B, C and D allowing the separation of species according to their size or optical properties.

Droplet, valve and other methods

He et al. have developed a device which generates pL and fL aqueous droplets in microfluidic device as shown in Figure 2-18a [83]. The aqueous droplets containing single cell is delivered to next analysis place by being surrounded by non-aqueous media. The elastomeric

characteristics of PDMS enable it to be valves which can be used to isolate single cells by controlling flow [102]. Figure 2-18b,c shows that the PDMS valve is actuated by another PDMS channel. Cell manipulation by various trapping methods has also been studied by many groups. Cells can be repetitively trapped and released for the capture, treatment or analysis of single cells by geometries. Cells were trapped between weirs at a T-intersection [103] (Figure 2-18c) or through the precise control of flow hydrodynamic flows at such intersections (Figure 2-18c) [104].

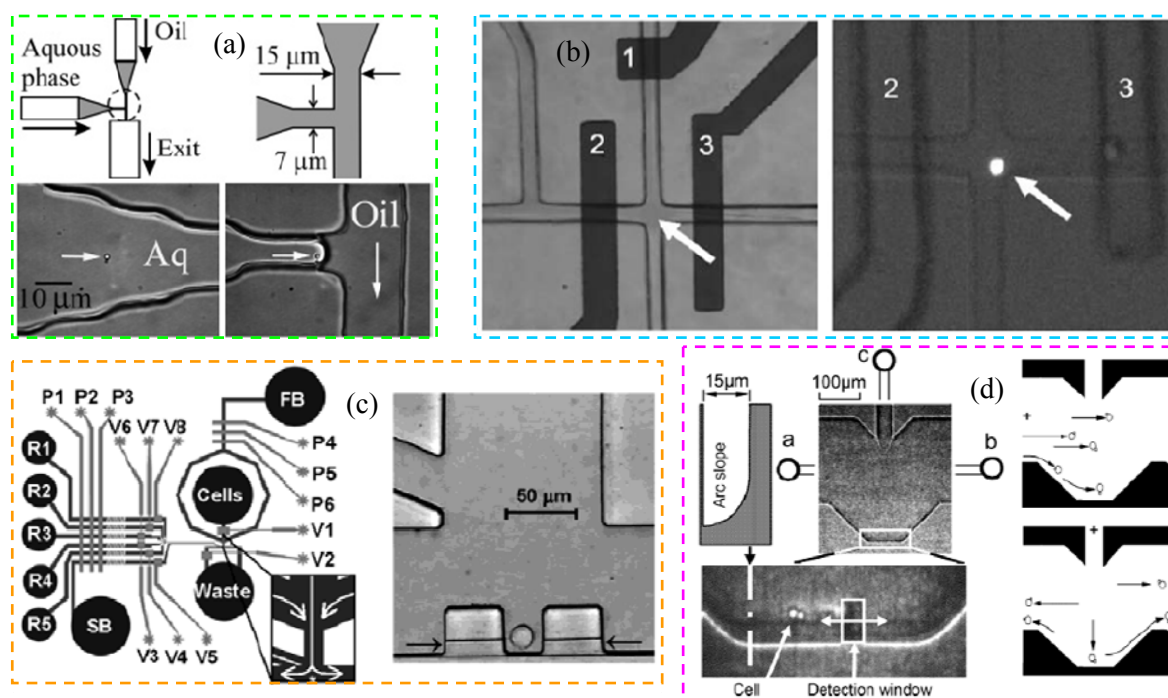


Figure 2-18. Various cell manipulation methods. (a) Cell delivery by micro droplets, (b) cell control by PDMS valve, (c) cell trap by weirs and, (d) cell trap via precise 3-D flow control.

2.6 . CELL LYSIS IN MICROCHANNELS

Single cell analysis indicates that the constituents of each single cell are examined. Thus, a cell must be lysed before analysis of cell ingredients. The lysis of cells can be classified by the lysis mechanism into chemical, physical, mechanical and electrical methods. Chemical methods use chemicals to disrupt cell membrane. Physical methods use osmotic pressure to rupture cells. Mechanical methods use shear stress to tear up cells. Electrical methods use applying strong electric field across cells to make irreversible holes on them. Depending on assay requirements, different methods of on chip cell lysis have been utilized. For protein extraction from a cell, detergents such as sodium dodecyl sulfate (SDS) and Triton X-100 have been successfully used for lysis. However, this method needs complex devices including injection channels and mixing to homogenize samples. In addition, detergents will often interfere with downstream assays and sometimes are not strong enough to activate lysis. For DNA analysis, thermal methods are often used since heaters are already equipped for polymerase chain reaction (PCR). Lysis caused by irreversible electroporation has also been reported and successfully shown at the single cell level. The use of electroporation as an alternative to other mechanical lysis methods has been motivated by its ability to achieve high local fields using integrated microelectrodes.

2.6.1. Chemical Lysis

Chemical lysis uses non-ionic, less denaturing detergents delivered from reservoirs or generated on chip for cell lysis. Detergents disrupt the lipid membrane surrounding cells by disrupting lipid-lipid, lipid-protein and protein-protein interactions. A microfluidic lysis device that deals with erythrocyte removal at nearly the single-cell level was fabricated and evaluated for rapid chemical lysis of erythrocytes [105]. Single-cell capture and chemical lysis inside a 50-pL closed volume was performed in a microfluidic device designed by Irimia et al. [106] (Figure 2-

19). In this device, cells and fluids were independently isolated in two microchambers of 25- μl volumes using the geometry of the microchannels and the coordinated action of four on-chip thermopneumatic actuators. Zeringue et al. [107] reported the removal of zona pellucida from mammalian embryos in a PDMS microfluidic chip using chemical treatments. A microfluidic chip was developed for on-chip cell lysis based on local hydroxide electro-generation and evaluated by lysis of red blood cells, human tumor line and Chinese hamster ovary cell lines. Chemical lysis with Triton X-100 and denaturation with sodium dodecyl sulphate have both proven effective [108]. The disadvantages of chemical lysis are that the lysis time is relatively long, the sample is diluted by the detergents and it requires additional injection, mixing and purification steps.

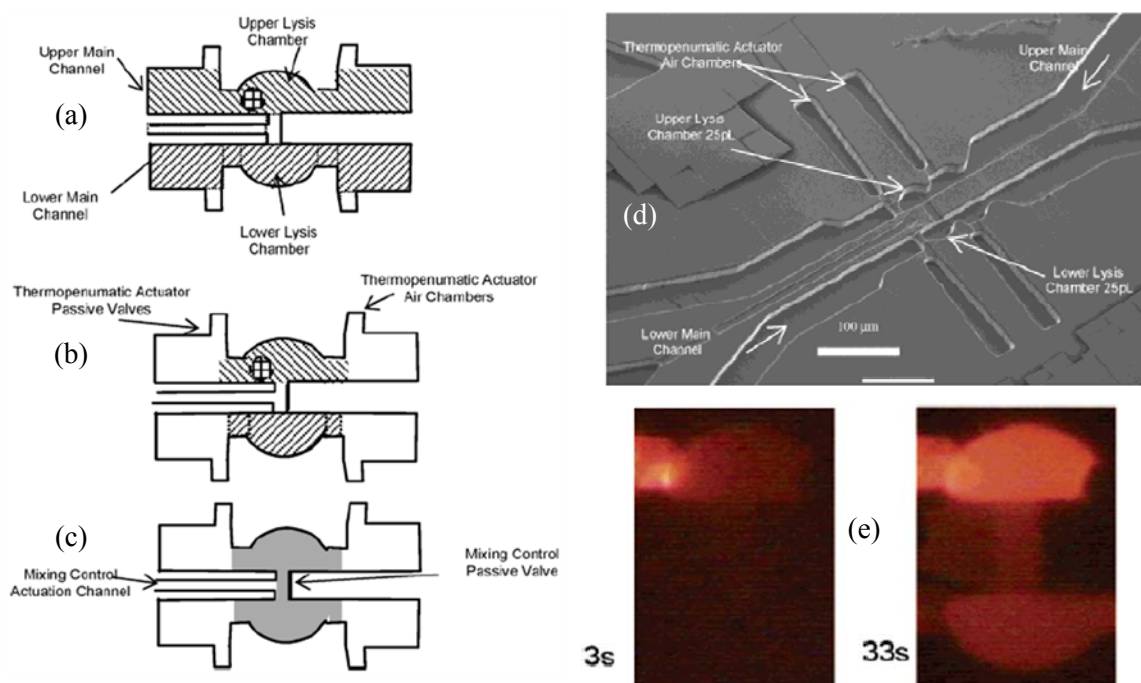


Figure 2-19. A chemical cell lysis device [106]. (a) One cell is introduced with the fluid in the upper main channel and captured by a dam-like structure. (b) Closed volume fluid compartments are formed by the coordinated action of the four thermopneumatic actuators. (c) Cell lysis is

achieved by removing air from the mixing channel. (d) Scanning electron micrograph of the PDMS device. (e) Serial fluorescence images of the dye diffusing throughout the two compartments after the single-cell lysis. (0.2 % SDS used)

2.6.2. Mechanical Lysis

Kim et al. [109] developed a microfluidic CD platform for cell lysis. The rimming flow established inside a partially solid-liquid mixture-filled annular chamber when the microfluidic CD rotated around a horizontal axis of rotation could be employed for cell lysis. However, the cell lysis method they employed is not proper for single cell lysis but rather suitable for lysis of bunches of cells. Carlo et al. [110] lysed cells by forcing them through nanoscale barbs which were fabricated using DRIE process (Figure 2-20). Taylor et al. [111] demonstrated cell disruptions using ultrasonic energy (typically 20 ~ 50 kHz) transmitted through a flexible interface into a liquid region and measured the released nucleic acid. While the efficiency of lysis is high, mechanical lysis does not provide the discrimination needed for organelle analysis. [112]

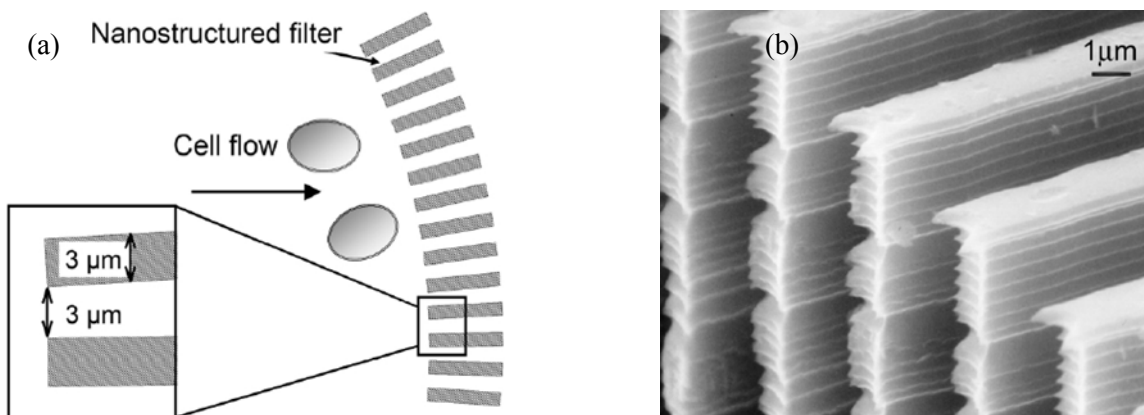


Figure 2-20. Nano barbs for mechanical cell lysis. (a) schematic and (b) SEM image. [110]

2.6.3. Electrical Lysis (irreversible electroporation)

Electrical cell lysis has gained substantial popularity in microfluidics community due to its fast speed and reagentless procedure. Easy fabrication of microelectrodes with MEMS techniques is another benefit of using this method. Electrical cell lysis is based on electroporation. Electroporation is a common method for creating holes in cell membranes to deliver genetic materials or molecular therapeutic drugs. When a cell is exposed to an external electric field, a transmembrane potential, $\Delta\phi$, is induced as shown in Figure 2-21a. The external electric fields, which cause sufficient transmembrane potential ($>0.5V$), generate micro-pores on the cell membrane. The micro-pores are resealable in a moment if the electric excitation is small ($<1V$). If the transmembrane potential is higher than about 1 V, the cell membranes is permanently disrupted ($>1V$); holes on the cell membranes are sustained, and intracellular materials are released. For a spherical cell of radius a , the transmembrane potential can be expressed as [113]

$$\Delta\phi = 1.5 a E \cos\theta$$

where E is the applied electric field strength, θ is the angle between the field line and the normal to the point of interest in the membrane as shown in Figure 2-21a .

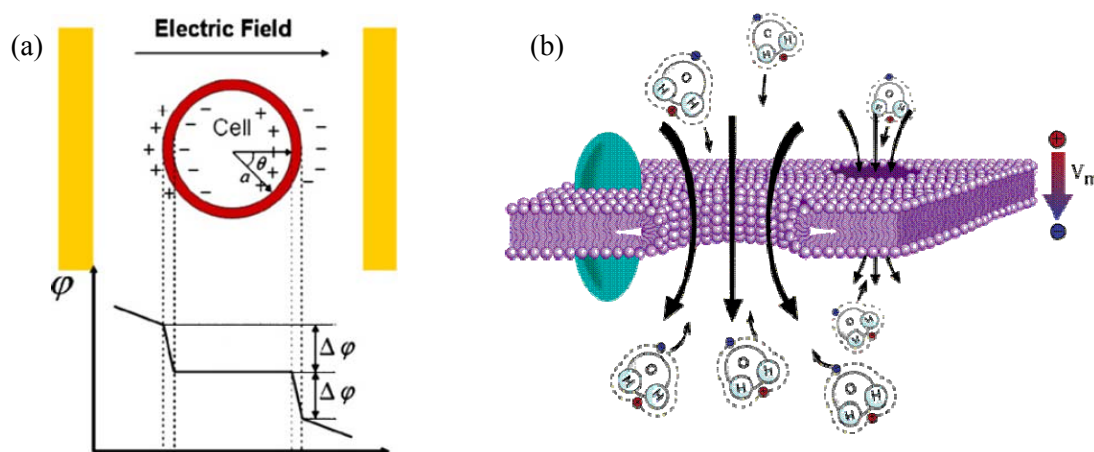


Figure-2-21. (a) Induction of a transmembrane potential $\Delta\phi$ in a cell and (b) hole generation by electroporation.

The mechanism of electroporation is not fully understood. The most widely accepted model for electroporation is the electromechanical compression of the cell membrane [114, 115]. The attraction of opposite charges induced on the inner and outer membrane generates compression pressure, which makes the membrane thinner. If the electric field strength exceeds a critical value, the cell membrane becomes permeable to the medium. The critical value corresponds to a transmembrane potential of approximately 1 V (normal transmembrane potential is about 70 mV). The poration of the cell membrane can be reversible or irreversible depending on the electric field strength and duration of pulse. The irreversible breakdown of the membrane causes cell membranes to burst open, or as the osmotic pressure of the cytosol and the external medium become unbalanced and the cells swell, the membrane is torn as a result of the over-swelling.

Electrical lysis contains many advantages including its simple structure and rapidity. It can greatly reduce purification steps for preparing bio-samples required in chemical method. The disruption time is as low as 33ms, which is about eight times faster than lysis by SDS. A proper

intensity of electric field may need to be applied in order to selectively disrupt the cell membrane while keeping the transorganelle membrane safe. An obvious choice for selective electroporation is by a direct current (DC) electric field since the cell membrane would experience the largest applied transmembrane potential. However, the high DC electric field required for cell lysis also results in water electrolysis and severe Joule heating, creating hydrogen and oxygen gas bubbles and causing extreme pH conditions near the electrodes. The water electrolysis can be suppressed by adopting a high frequency AC electric field. The required AC field conditions for several biological cells were investigated (Table 2-2) [116].

Table 2-2. AC electrical lysis conditions for various cells. [116]

	AC (sinusoidal)	Square pulse	Size (μm)	DC based on Eq. to have $\Delta\phi_{\text{lysis}}$ (1V)
Chinese cabbage protoplasts	590V/cm at 1 MHz	1.5 kV/cm at 1 ms	30	0.22 kV/cm
Radish protoplasts	880 V/cm at 1 MHz	1.75kV/cm at 1 ms	35	0.19 kV/cm
Yeast protoplasts	Not observed up to 21 kV/cm at 2 MHz	10 kV/cm at 0.1 ms	3	2.2 kV/cm
E. coli	Not observed up to 21 kV/cm at 2 MHz	7 kV/cm at 0.5 ms	1	6.67 kV/cm

The simplest fabrication method of microelectrodes would be deposition of planar electrodes. Although, simple in fabrication, the electric field generated by planar electrodes decays exponentially, resulting in rather non-uniform forces on the cell membrane [117]. In order to avoid this problem, various techniques have been developed to fabricate three dimensional electrode structures as illustrated in Figure 2-22. In Figure 2-22a,b, the cells are introduced into the lysis channel by hydrodynamic force and then dielectrophoretic force under an AC electric

field attracts the cells to the sharp point of the electrode. The cells are lysed when they reach the high electric field region near the sharp point of the electrode. [112]

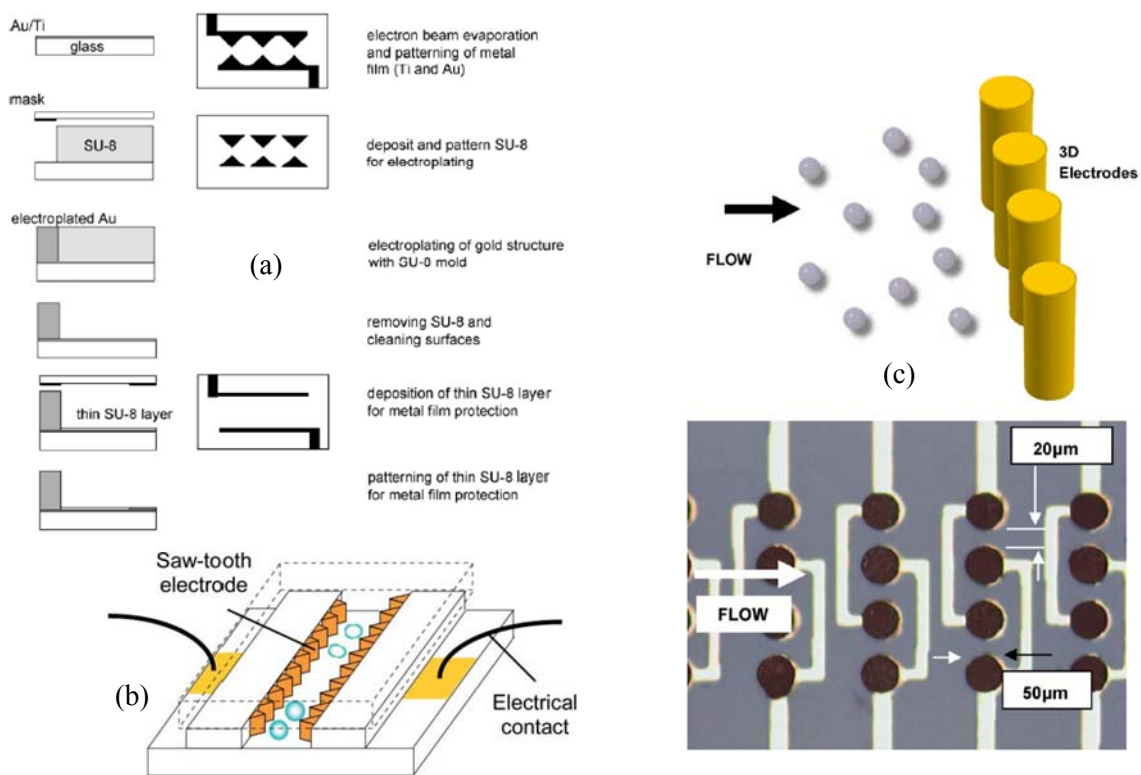


Figure 2-22. Three-dimensional electrical cell lysis devices. (a) Microfabrication of 3-D electrodes, (b) schematic of saw-tooth electrodes [112] and, 3-D cylindrical electrodes [117].

Continuous cell lysis devices were also developed by varying the channel cross section as illustrated in Figure 2-23 [118]. The serial geometry will be suitable for continual high-throughput CE system by placing a separation channel downstream. From electric current conservation, the following electric field is obtained.

$$I = J_c A_c = \sigma E_c A_c = J_t A_t = \sigma E_t A_t$$

where subscripts c and t denote ‘channel’ and ‘throat’ regions, respectively. For a uniform height channel geometry, this equation becomes

$$E_c W_c = E_t W_t$$

where W is the channel width at a local position. In other words, the local electric field is inversely proportional to the local channel width. One advantage of this geometry is that the severe Joule heating at the throat region can be effectively discharged because that region is small. Lee and Cho [118] reported that 100% red blood cells were lysed in their device with $E_t=1.2$ kV/cm.

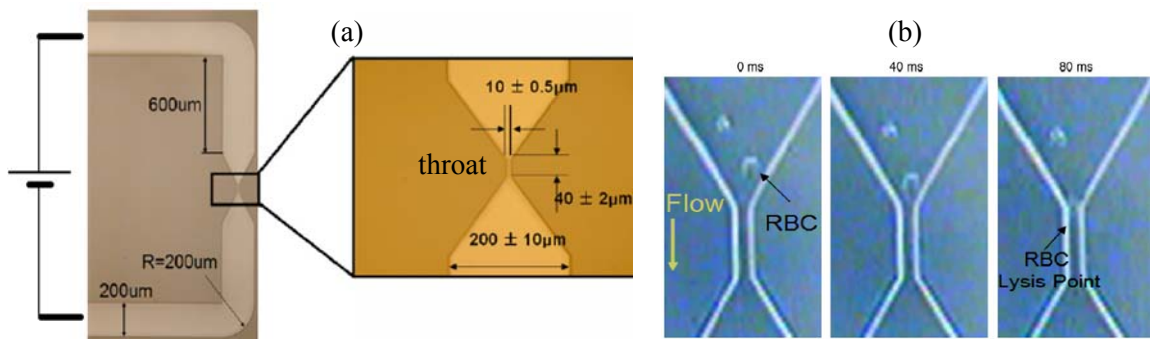


Figure 2-23. Continuous electrical cell lysis. (a) Top view of cell lysis device and (b) RBC lysis at the entrance of the throat ($E_t=1.2$ kV/cm) [118].

2.6.4. Osmotic Lysis

Osmotic lysis occurs when a cell bursts due to an osmotic imbalance that has caused excess water to move into the cell. It occurs in a hypotonic environment, where water diffuses into the cell and causes its volume to increase. If the volume of water exceeds the cell membrane's capacity, the cell will burst. Lillard et al.[74] used the osmotic lysis method for red

blood cell single-cell electrophoresis. They introduced single cells to 50mM H_3PO_4 solution, which has a lower ionic strength than isotonic condition. Thus, the osmotic pressure inside the cell caused cell lysis when the buffer solution was drawn over the cell. Prinz et al. [119] used osmotic pressure to lyse E. coli cells. Lysis of the cells was achieved by rapid diffusional mixing of deionized water with the osmotically vulnerable cells. The peptidoglycan layer in E. coli enables the cell to withstand osmotic pressure. Therefore the cells were pretreated with lysozyme to break down the layer. The lysozyme-treated cells absorbed water, swelled and finally burst.

2.6.5. Other Cell Lysis Methods

Heating disrupts the cell membrane and the intracellular materials are released. The heater can be easily accommodated for DNA analysis chip since DNA analysis often utilizes PCR amplification which already requires a heating device [120]. However, this method may not be suitable for protein analysis because protein molecules denature easily in the course of heating.

Sonication involves the use of ultrasonic waves to generate localized areas of high pressure resulting in cavitation that can shear apart cells. Sonication has several limitations that keep it from being widely used for single-cell lysis including the requirement of more than 50 s for the lysis of cells such as lymphocytes, which can result in significant heating and thus denaturing of proteins, and excessive diffusion of the cell contents that can lead to difficulties in downstream detection [121-123]. However, when used after first treating the cell with a weak detergent such as digitonin, sonication can lyse cells within 3 s, allowing efficient separation of cell contents [122, 123].

Pulsed laser cell lysis involves directing a nanosecond pulse from a 532 nm laser through a high numerical aperture objective lens and thus focused down to a small spot where localized plasma formation occurs. This results in the generation of a shock wave, followed by generation

of a cavitation bubble that expands and contracts within a matter of microseconds [124, 125]. The cells located near the center of the targeted area have been shown to lyse either during the expansion of the cavitation bubble (less than 1 μs after pulse) when the focal point of the laser pulse is directed near the cells (approx. 10 μm above), or during bubble collapse, when a liquid jet is directed downwards onto the slide (approx. 30 μs after pulse) when it is focused significantly higher (approx. 400 μm).

2.7 . SAMPLE CONCENTRATION TECHNIQUES

A key challenge yet to be addressed by miniaturized bioanalytical devices is the detection of analytes with very low (nanomolar or lower) initial concentrations in very small (one microliter or less) volumes. Sensitivity to low analyte concentrations is a crucial challenge towards the development of robust miniaturized bioanalytical devices. Researchers have developed several sample concentration techniques to increase the sample concentration and thus signal. Most concentration methods use spatial gradient of physical properties. The sample concentration techniques described in this section are mostly placed before the electrophoretic separation part or occur with separation at the same time.

The sample concentration is generally achieved by varying analyte migration speed along the channel. If the front of the sample plug migrates slower or the rear of the plug moves faster than the body of the sample plug, the sample plug is condensed.

1. Field amplified sample stacking

Field amplified sample stacking (FASS) uses gradients in electrolyte conductivity to subject sample ions to non-uniform electric fields (Figure 2-24). Sample ions are dissolved in a

lower conductivity electrolyte than the surrounding running buffer. The lower conductivity in the sample results in larger electric field and, therefore, larger local electrophoretic velocity. Sample ions stack as they move from high electric field and high velocity region to the low field and low velocity regions.

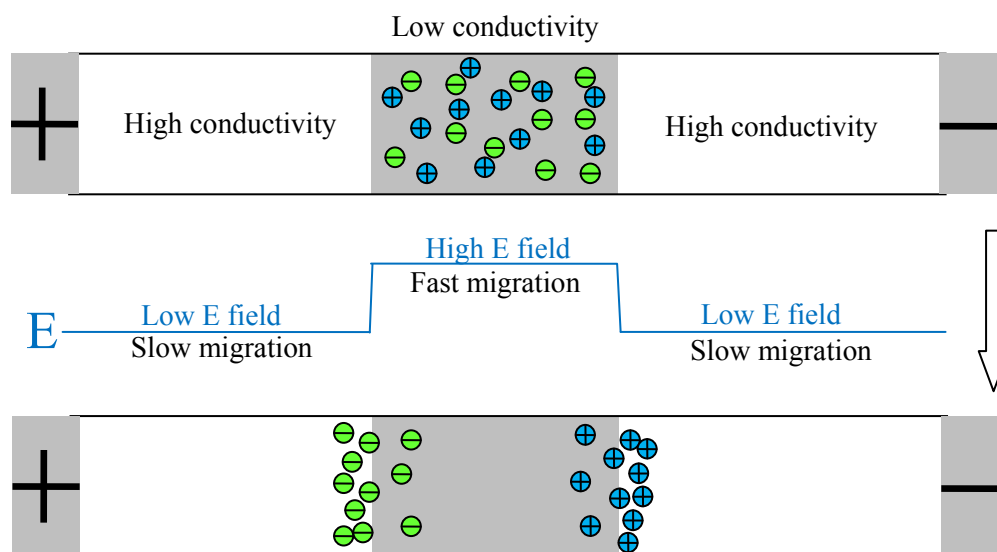


Figure 2-24. Schematic of field amplified sample stacking showing sample ions stacking as they exit the low conductivity region and enter the high conductivity regions. Buffer ions (not shown) maintain electroneutrality in each zone.

Some microchips having a component of FASS preconcentration can be found in [126-128]. Figure 2-25 shows schematic of an example of FASS microchip. They used a photoinitiated porous polymer structure to facilitate sample injection and flow control for high-gradient FASS [128]. This porous polymer structure provides a region of high flow resistance that allows the electromigration of sample ions. 0.4% methylcellulose solution was coated on the channel and was contained in buffers also to suppress electroosmotic flow. Electropherogram signal was increased by a factor of 1100 in electrophoretic separations with this device.

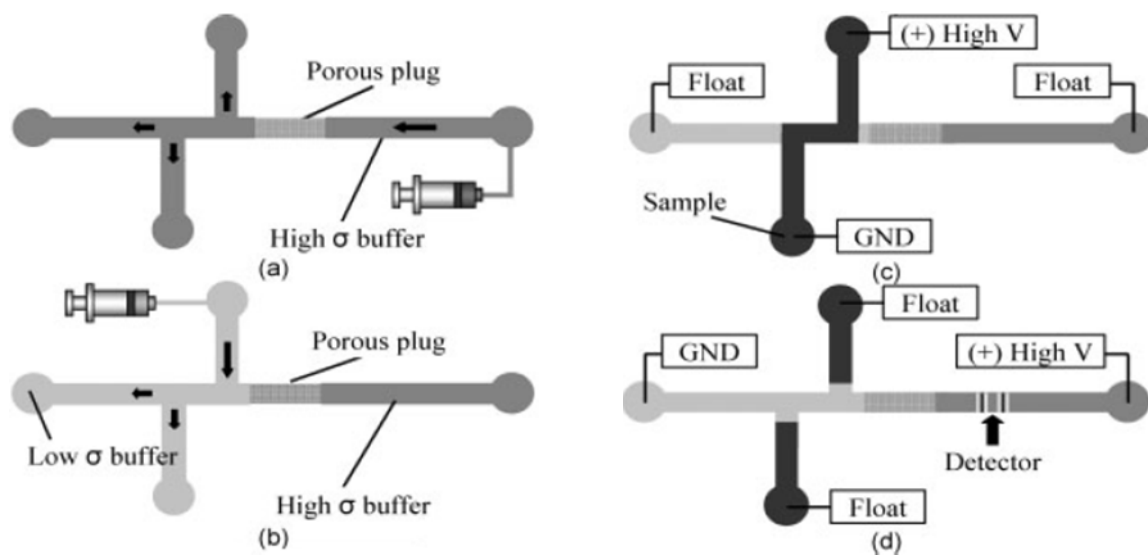


Figure 2-25. Schematic of FASS-CE assay protocol. (a) High-conductivity buffer injection, (b) low-conductivity buffer injection, (c) electrokinetic sample loading and (d) a series of stacking, separation, and detection.

2. Isotachopheresis

Isotachopheresis (ITP) uses various ion mobilities to create zones of relatively purified sample ions in a microchannel. First, two solutions are created: a leading electrolyte (LE) with relatively high mobility ions and a trailing electrolyte (TE) with low mobility ions (Figure 2-26). The sample can be dissolved in the TE electrolyte solution. In isotachopheresis the sample is introduced between a fast leading electrolyte and a slow terminating electrolyte. After application of an electric potential a low electrical field is created in the leading electrolyte and a high electrical field in the trailing electrolyte. In the first stage the sample constituents migrate at different speeds and start to separate from each other. The faster constituents will create a lower electrical field in the leading part of the sample zone and vice versa.

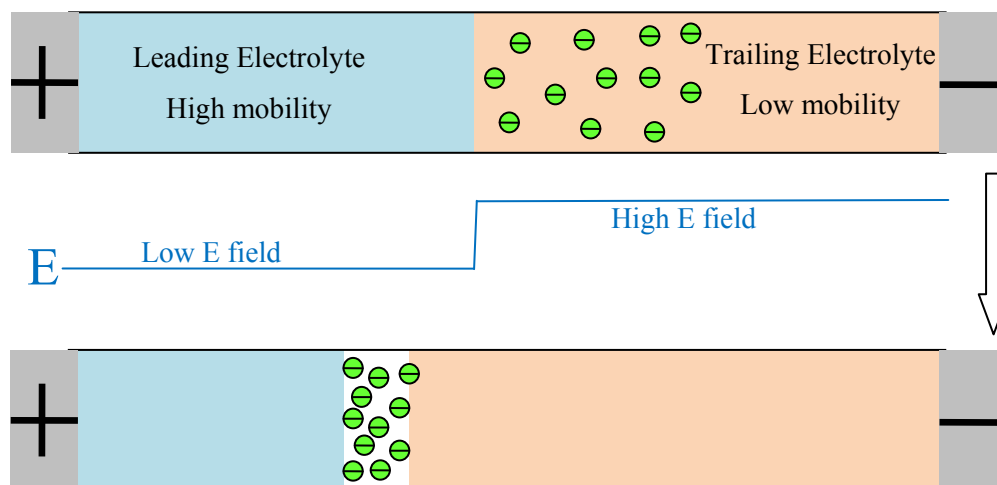


Figure 2-26. Schematic of an ITP sample stacking process. Counterions (not shown) maintain electroneutrality in each zone. In the trailing ion region, sample ions overspeed trailing ions and race ahead. Sample ions cannot race ahead of leading electrolyte ions and so segregate and focus into a narrow region of purified sample (and counter ion).

Some examples of isotachopheresis microchip can be found in [129-132]. An example of isotachopheresis-gel electrophoresis microchip is illustrated in Figure 2-27 [132]. All channels and reservoirs LEB and W were first filled with leading electrolytes and reservoirs TEB and S were filled with the terminating electrolytes and sample, respectively. The sample and terminating electrolytes were then withdrawn from the reservoirs into the channels by the syringe pump to form the sandwiched sequence of buffers as shown in Figure 2-27a. Compared to conventional microchip GE, the sensitivity of microchip ITP-GE was estimated to increase by one to two orders of magnitude based on the dilution factor of the injected sample and the S/N ratio detected from the electropherogram.

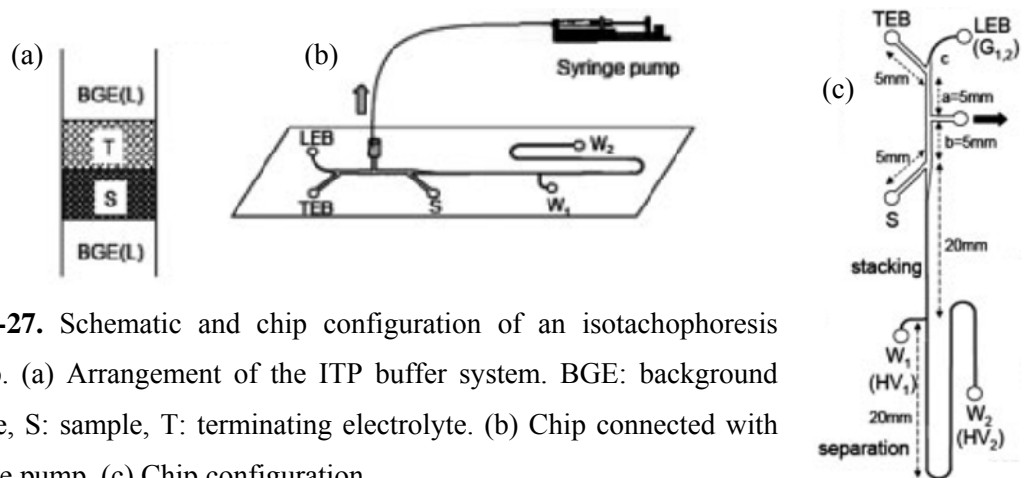


Figure 2-27. Schematic and chip configuration of an isotachopheresis microchip. (a) Arrangement of the ITP buffer system. BGE: background electrolyte, S: sample, T: terminating electrolyte. (b) Chip connected with the syringe pump. (c) Chip configuration.

3. Isoelectric focusing

In isoelectric focusing, charged molecules or particles move within a pH gradient via electrophoresis. The method is applied particularly often in the study of proteins, which separate based on their relative content of acidic and basic residues, whose value is represented by the pI. A protein that is in a pH region below its isoelectric point (pI) will be positively charged and so will migrate towards the cathode (Figure 2-28). As it migrates through a gradient of increasing pH, however, the protein's overall charge will decrease until the protein reaches the pH region that corresponds to its pI. At this point (isoelectric point), it has no net charge and so migration ceases (as there is no electrical attraction towards either electrode). As a result, the proteins become focused into sharp stationary bands with each protein positioned at a point in the pH gradient corresponding to its pI. Some examples of microchips having isoelectric focusing can be found in [133-136]

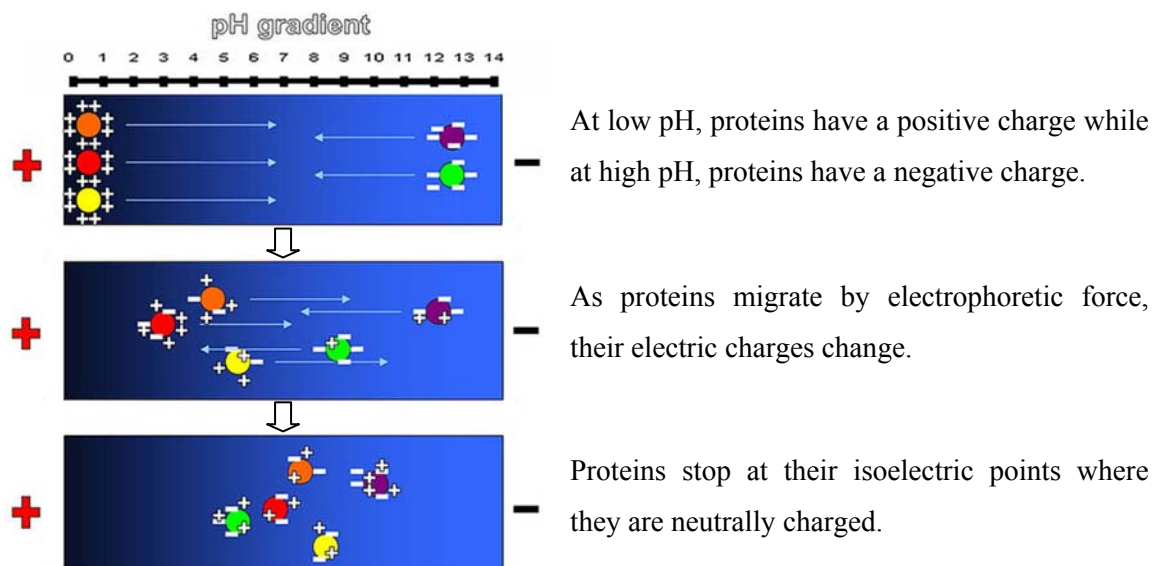


Figure 2-28. Schematic of isoelectric migration of proteins.

4. Temperature gradient focusing

Temperature gradient focusing (TGF) involves application of a temperature gradient across a microchannel. The required temperature gradient can be produced either by external heating/cooling equipment or inherent Joule heating that is resulted from applied electric field. Compared to the external heating mode, the Joule heating mode involves less bulky equipment [137]. A higher temperature in an electrolyte results in a lower viscosity and thus higher electric conductivity and electrophoretic mobility. Assuming constant current, a higher conductivity induces a lower electric field. If the effects on the electric field and the electrophoretic mobility are equal and opposite, the electrophoretic velocity, a product of the mobility and the field, will be unaffected by temperature changes. Most commonly used TGF would be implemented with a buffer having strong temperature dependence on its electric conductivity and analytes having negligible temperature dependence on their electrophoretic mobility. By balancing the electrophoretic velocity against the bulk flow of a temperature dependent buffer, sample species

will then be stationary and concentrated at a unique point where the total velocity sums to zero (Figure 2-29). Some examples of microchips having temperature gradient focusing can be found in [137-139].

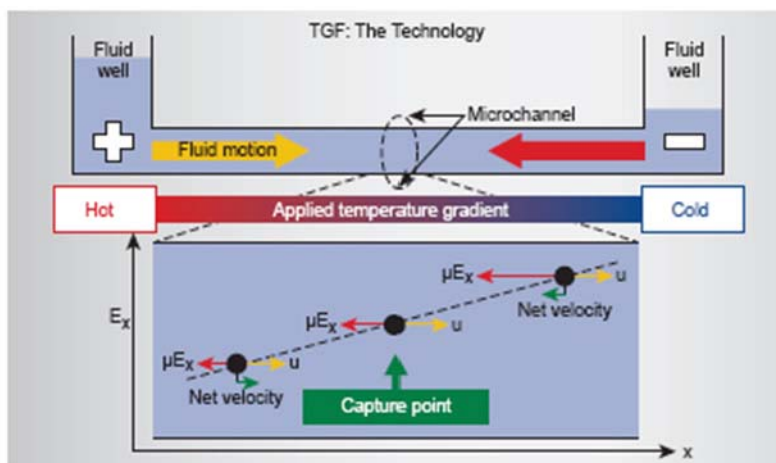


Figure 2-29. Schematic of temperature gradient focusing. Bulk fluid motion (yellow arrow) is balanced by an opposing electrophoretic velocity (red arrow) to capture analytes at a unique spatial location within a specific electrophoretic mobility range.

2.8 . SEPARATION METHODS

Single cell analysis or other sample analysis usually requires a separation process of (bio) chemical composition in sample. In general, the separation of sample can be achieved by many different techniques; electrophoresis, chromatography, mass spectrometry, etc. However, the most appropriate method for the biological single cell analysis is electrophoresis.

(Microchip) Capillary zone electrophoresis

Capillary zone electrophoresis (CZE) is used to separate ionic species by the ratio of their electric charge to viscous frictional force in liquid media. Introduced in the 1960s, the technique

of capillary electrophoresis (CE) was designed to separate species based on their size to charge ratio in a small capillary filled with an electrolyte. The migration of the analytes is initiated by an electric field that is applied between the source and destination vials and is supplied to the electrodes by the high-voltage power supply (Figure 1-3). It is important to note that all ions, positive or negative, are pulled through the capillary in the same direction because electroosmotic flow usually dominates over electrophoretic migration. The electrophoretic mobility is a function of medium viscosity and the electric charge and shape/size of particles as discussed in Section 2.3. The certainty and uniqueness of the electrophoretic mobility of a species makes it possible to separate the species from a mixture during electrophoretic migration. The separated analytes are then detected near the outlet end of the capillary. The output signal of the detector is sent to a data output and handling device such as an integrator or computer. The data is then displayed as an electropherogram, which reports detector response as a function of time. Separated chemical compounds appear as peaks with different retention times in an electropherogram.

Microchip capillary electrophoresis has many advantages over conventional capillary electrophoresis. Microfabrication allows for accurate on-chip sample injection techniques, producing faster separation performance with much shorter channels. Microchip capillary electrophoresis has also shown a great enhancement of analysis speeds compared to conventional capillary electrophoresis, with a throughput of 38 cells/min [28]. This enhancement of throughput was mainly due to the faster exchange of buffer around the cell prior to lysis and the use of shorter separation channels with more intensive electric fields. Serial separations of multiple cells within a channel also provided additional speed enhancements.

Examples of microchip capillary zone electrophoresis can be found in many published reports for either the pinched injection analysis of sample mixture [49, 61, 140-143] or the single cell analysis [24, 144]. Figure 2-30 shows schematic of pinched injection by using a cross

channel and a double-T channel. Most microchip CE devices were fabricated with glass substrates via standard photolithographic, wet etching and glass bonding methods due to its stable electroosmotic mobility. Recently researchers [145, 146] have also paid more attention to polymers such as PDMS because polymer microchannels can be manufactured with low cost in non-clean room environment, holding bio-friendly environment.

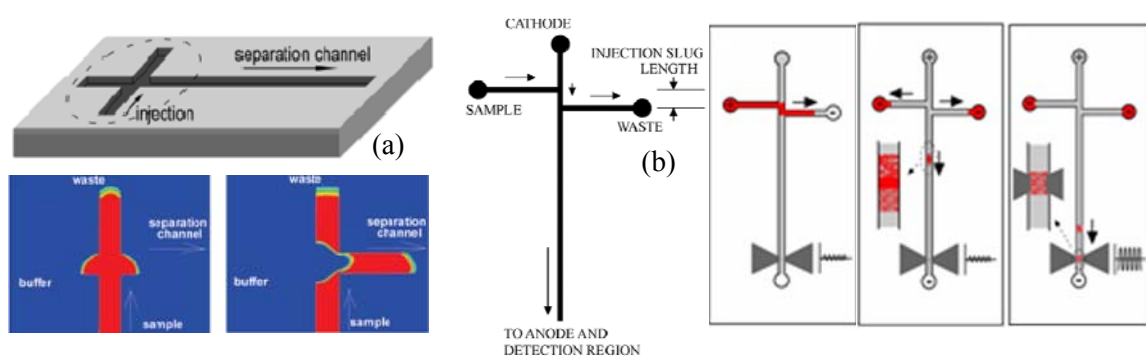


Figure 2-30. Schematic of pinched injection, using (a) a cross channel and (b) a double-T channel.

(Microchip) Capillary gel electrophoresis

As discussed above, separations in a capillary zone electrophoresis system are typically dependent on the analytes having different electrophoretic mobilities. However, some classes of analytes cannot be separated by this effect because they are neutral (uncharged) or because they may not differ significantly in electrophoretic mobility. However, there are several techniques that can help separate such analytes. Adding a surfactant to the electrolyte can facilitate the separation of neutral compounds by micellar electrokinetic chromatography. Charged polymers such as deoxyribonucleic acid (DNA), ribonucleic acid (RNA), or protein molecules can be separated in a gel matrix that retards larger molecules more than smaller molecules. This is called gel electrophoresis.

The most popular application of gel electrophoresis is for DNA analysis. DNA gel electrophoresis is often preceded by amplification of DNA via PCR, and may be used as a preparative technique prior to use of other methods such as mass spectrometry, RFLP (restriction fragment length polymorphism), PCR, cloning, DNA sequencing, or Southern blotting for further characterization. In most cases, the gel is a cross-linked polymer whose composition and porosity is chosen based on the specific weight and composition of the target to be analyzed.

Contrary to slab gel electrophoresis, the capillary gel electrophoresis spatially confines the sample to a micron scale capillary. Thus capillary gel electrophoresis can reduce the volume of sample or reagents and it also reduces the assay time significantly. Microchip gel electrophoresis (MGE) especially enables rapid and sensitive analysis and has potential in clinical diagnosis [147-150]. The MGE system has distinct advantages over the traditional capillary and slab gel electrophoresis with respect to time, resolution and sensitivity, particularly for PCR analysis in molecular biology. At the same time, traditional systems cannot detect the PCR products in a single run.

The clonality in the lymphoid processes in humans has been examined using capillary electrophoresis [151]. The molecular diagnostics of T-cell lymphoma in dogs using PCR with capillary electrophoresis was also reported [152]. Pal et al. [153] designed and tested an integrated genetic analysis device as shown in Figure 2-31. The key components (phase change valves, thermally isolated reaction chambers, gel electrophoresis and pulsed drop motion) are electronically controlled. They demonstrated an identification of sequence for hemagglutinin A subtype for the A/LA/1/87 strain of influenza virus.

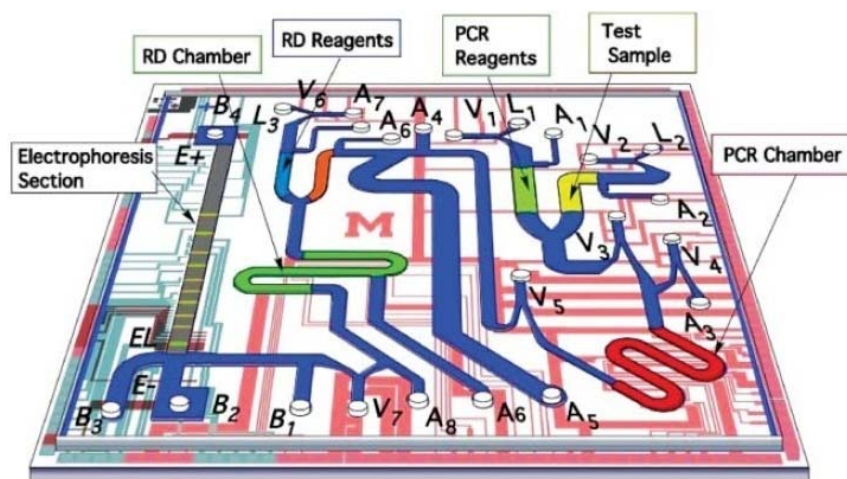


Figure 2-31. Schematic representation of Pal's microfluidic device. There are three liquid entry channels ("L"; sample, PCR reagents and RD reagents), several metering channels, drop mixing intersections, a sealed PCR chamber, an open RD chamber, and an electrophoresis channel. Each valve ("V") is individually and electronically addressable [153].

More examples of microchip CE (either zone or gel electrophoresis) for single cell analysis

Various species of single cells have been successfully analyzed by microchip capillary electrophoresis. For example, fluorescently labeled amino acids were detected by Wu et al. [154] Ros et al. [155] detected proteins linked to a green fluorescent protein in single insect cells. Arrays of channels permitted the separation of many cells in a parallel manner as performed by Munce et al. [156] The incorporation of cell loading strategies and analyte reactions on-chip described by Wu et al. [154] can be expected to provide further speed benefits.

McClain et al. [24] developed a microfluidic chip for single-cell analysis of Jurkat cells as shown in Figure 2-32. The cells were hydrodynamically delivered from the cell-containing reservoir to a lysis region where a square shape AC electric field with DC offset was applied for electric cell lysis. The lysis was claimed to be finished within 33ms. The hydrophobic cellular

debris from the cellular and organelle membranes were prevented from adhering to the wall by an emulsification agent, pluronic P84.

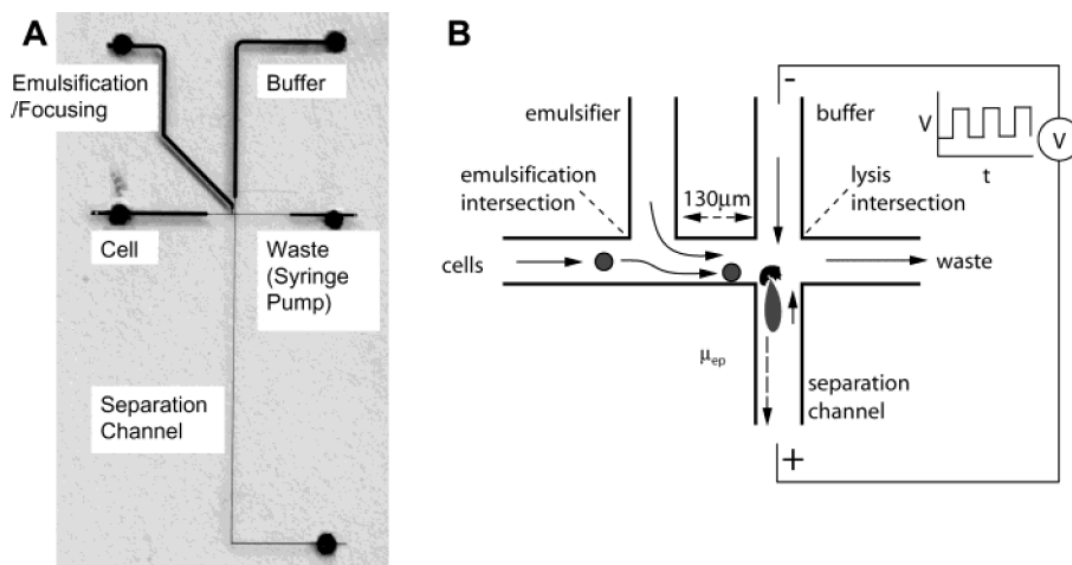


Figure 2-32. (A) Image of microchip used for the cell analysis experiments. (B) Schematic of the emulsification and lysis intersections for the microchip design shown in (A). The solid arrows show the direction of bulk fluid flow and the dashed arrow shows the electrophoretic migration direction of the labeled components in the cell lysate. [24]

Gao et al. [144] developed a microfluidic system for the analysis of single human red blood cells as shown in Figure 2-33. Cells were again hydrodynamically transported and, when a cell was detected in the cross section, a weak electric field was applied to lead the cell towards the detection point and let the cell sediment on the wall. After complete sedimentation of the cell, a sudden strong electric field was applied and the electrokinetic force lysed the cell.

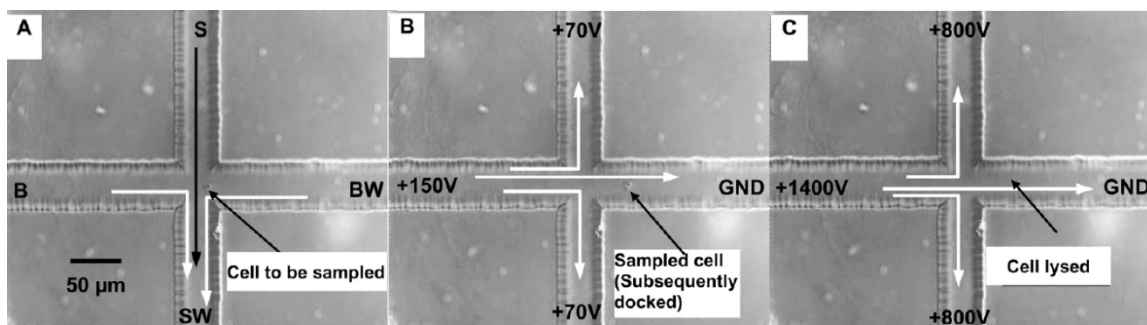


Figure 2-33. CCD images showing a single erythrocyte being transported (A), docked (adhering) (B) and lysed (C) in the micro-channels. Arrows indicate the direction of liquid flow and the black bar shows the scale (50 mm) [144].

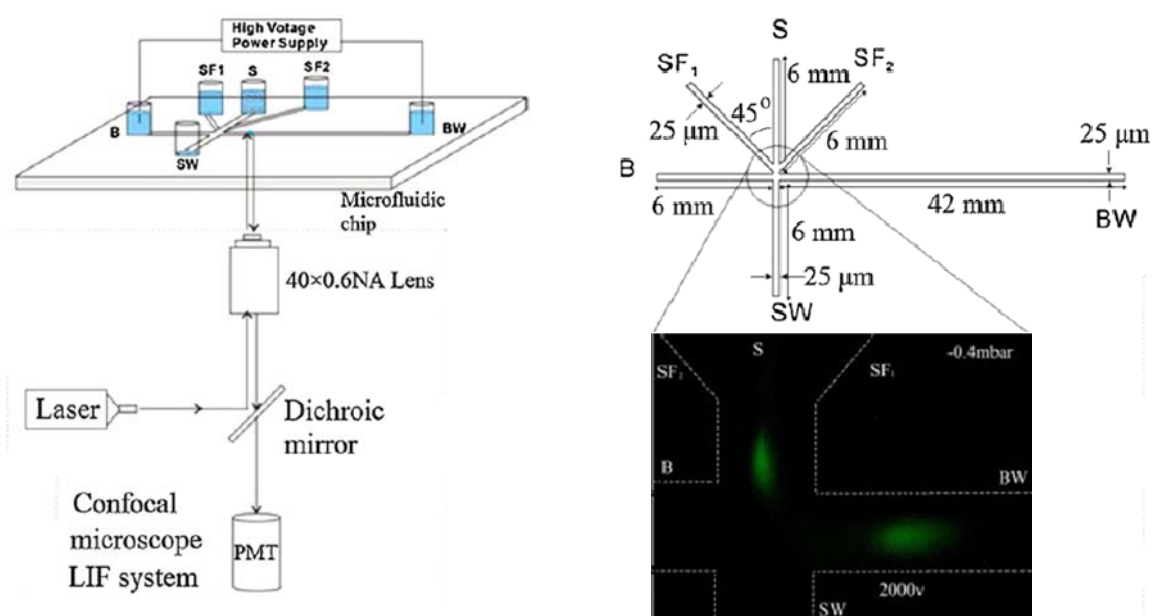


Figure 2-34. Schematic of the experimental setup and channel design of a continuous single cell analysis system. Fluorescent image: lysis of cells labeled with fluorescein diacetate [28].

Xu and Ying [28] recently reported a microchip CE-LIF system with continuous single cell introduction via hydrodynamic focusing by sheath-flow as shown in Figure 2-34. Combined with the electric field applied on the separation channel, the aligned cells were driven into the

separation channel and rapidly lysed within 33ms at the entry of the separation channel by Triton X-100 added in the sheath-flow solution. The introduction of sheath-flow streams also significantly reduced the concentration of phosphate-buffered saline (PBS) injected into the separation channel along with single cells, thus reducing Joule heating during electrophoretic separation. A throughput of 38 cells/min was obtained.

2.9 . DETECTION METHODS

Separation techniques on microchips provide very rapid separation, versatile channel designs, very small sample volumes, and low reagent consumption. One of the consequences of such reductions in size of the microfluidic device will be the resulting demands on the detection system [157]. For example, the sample volume in conventional microchannel devices is less than 1 nL, and the optical path length is as short as several tens of micrometers. Therefore, very highly sensitive detector hardware should be constructed to analyze even modest concentrations of sample solutions in the microfluidic system.

1. Laser-induced fluorescence (LIF)

Among several detection methods available, laser induced fluorescence has been the most popular for microchip CE due to its high sensitivity.[157]

Fluorescence is the emission of light by a substance that has absorbed exciting light energy of a different wavelength. Laser-induced fluorescence (LIF) is a spectroscopic method used for detection of fluorescent chemical species. The species to be examined is excited with a laser (Figure 2-34). The wavelength is often selected to be the one at which the species has its largest cross section. The excited species will then de-excite and emit light at a wavelength

usually larger than the excitation wavelength. The emitted light, fluorescence, is measured by a light sensor such as photomultiplier tube, CCD camera, etc.

Analytes can be naturally fluorescent to a properly equipped optical system (exciting light and optical filter system). Yeung's group [74, 158] analyzed single red blood cells by using the native fluorescence of hemoglobin. 275 nm UV light was used as an excitation source and 365 nm band pass filter was used to selectively detect the emitted light. The problem of native fluorescence is to find and prepare the proper optical conditions and equipment and this task is not always possible. The alternative option is to label the target analytes with fluorescent dyes. For example, Gao et al. [144] labeled Glutathione (GSH) with 2,3-naphthalenedicarboxaldehyde (NDA). NDA-derivatized GSH was detected with 488 nm laser and a 520 nm cutoff filter.

Again, the biggest limitation of LIF technique is that it is only applicable for natively fluorescent samples or samples capable of fluorescent labeling and finding fluorescence is not always available for every analyte.

Following are some other technical issues researchers frequently encounter during fluorescence experiment. Photobleaching is the photochemical destruction of a fluorophore. In microscopy, photobleaching may complicate the observation of fluorescent molecules, since they will eventually be destroyed by the light exposure necessary to stimulate them into fluorescing. Autofluorescence is the fluorescence of other substances than the fluorophore of interest. It increases the background signal. In fluorescence microscopy, wide-spectrum autofluorescence from the device or all other uninteresting chemicals is eliminated by adopting a band pass filter. The autofluorescence in the similar spectrum to the signal of interest interferes with detection of the resulting specific fluorescent signals, especially when the signals of interest are very dim - it causes structures other than those of interest to become visible.

2. Electrochemical detection (EC)

Although LIF is the most widely used detection scheme for its high sensitivity, a conventional LIF detector is sophisticated, expensive, and difficult to be miniaturized. Furthermore, derivatization of the analytes with a fluorophore is often necessary. Electrochemical (EC) detection is ideally suited to miniaturized analytical systems and the sensitivity and selectivity of EC detection are comparable to those of LIF detection [159].

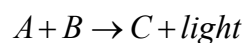
Oxidizable or reducible sample species can be detected by electrochemical detection. As a sample passes, electrochemical detector electrodes get the electrical output results from an electron flow caused by the chemical reaction that takes place at the surface of the electrodes [159]. The detector normally has three electrodes, the working electrode (where the oxidation or reduction takes place), the auxiliary electrode and the reference electrode (which compensates for any change in the electrical conductivity of the mobile phase). There are three general modes of EC detection: amperometry, conductimetry, and potentiometry. Amperometry is the most popular EC detection method to be coupled with microchip CE-based systems. Amperometry is accomplished by applying a constant potential to the working electrode and measuring the current as a function of time. The applied potential facilitates the redox reactions of the analytes, while the current output is proportional to the concentration of the analytes. In CE–EC systems, it is important to isolate the EC detector from the separation voltage when utilizing amperometric detection. Some examples of microchips having an electrochemical detection component can be found in [160].

3. Chemiluminescence detection (CL)

As previously mentioned, despite its high sensitivity, LIF has some critical limitations; difficulty in achieving fluorescence and integration of the whole system on a chip.

Chemiluminescence (CL) detection is also very sensitive detection schemes and has the advantages including simple instrumental setup, low background noise, and low costs for operation and maintenance [161]. This detection technique is well suited for online detection in microchip electrophoresis.

Chemiluminescence is the emission of light as the result of a chemical reaction as follows,



where A can be the analyte, then B is a CL reagent and C is the product. Chemiluminescence detection measures the emission light from this reaction to determine analyte concentration.

Some examples of MCE-CL (microchip capillary electrophoresis with chemiluminescence detection) systems can be found in [161, 162]. Tsukagoshi et al. [161] used their microchip for analysis of isoluminol isothiocyanato (ILITC) by having three processes of immune reaction, electrophoresis, and chemiluminescence detection occurring within the chip. Zhao et al. [162] developed a MCE-CL system (Figure 2-35) for single cell analysis by using human red blood cells to determine intracellular content of glutathione (GSH). GSH was first labeled with diazo-luminol, and then individual cells were injected and electrically lysed (similar to Gao's method [144]). CL detection was based on the oxidation reaction of luminol-labeled GSH with NaBrO.

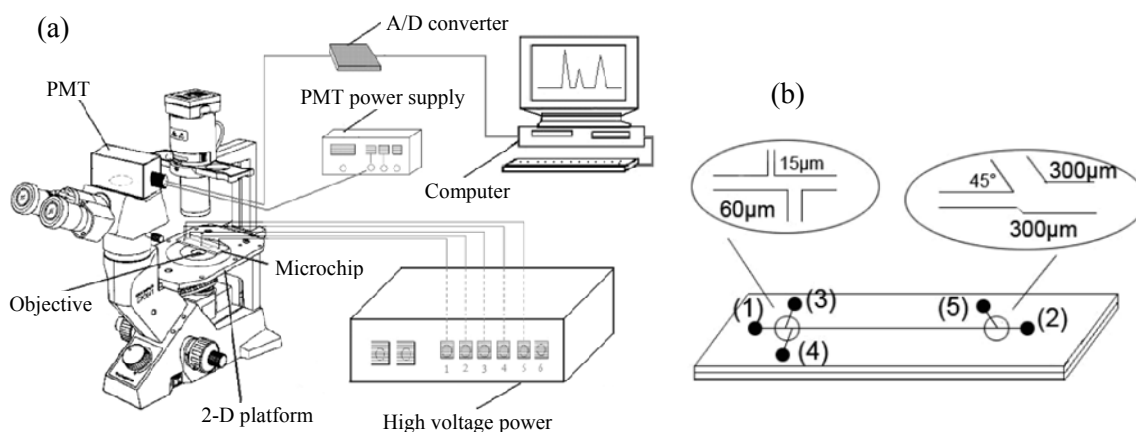


Figure 2-35. Schematic of a MCE-CL system for single cell analysis. (b) The layout and dimensions of the glass microchip: (1) electrophoresis buffer reservoir; (2) electrophoresis buffer waste reservoir; (3) cell suspension sample reservoir; (4) sample waste reservoir; (5) CL reaction buffer solution reservoir. [162]

4. Mass spectrometry (MS)

Mass spectrometry (MS) measures the mass-to-charge ratio of charged particles under electromagnetic fields as illustrated in Figure 2-36a, for determining masses of particles or elucidating the chemical structures of molecules, such as peptides and other chemical compounds. Thus mass spectrometry combined with CE overcomes the limitation of LIF detection, little chemical information necessary for identification of the analytes [163-165].

One detection technique that attracts much interest is electrospray ionization (ESI) coupled with time-of-flight mass spectrometry (TOF-MS), because of its ability to detect large bio-molecules with high sensitivity (Figure 2-36b). Many attempts have been made to devise an interface between chip and ESI-MS [166-169]. For example, Mellors et al.[170] developed an ESI-MS system single red blood cell analysis. Cell lysis occurred at a channel intersection using a combination of rapid buffer exchange and an increase in electric field strength. An electroosmotic pump is incorporated at the end of the electrophoretic separation channel to direct eluent to the integrated electrospray emitter as shown in Figure 2-36b.

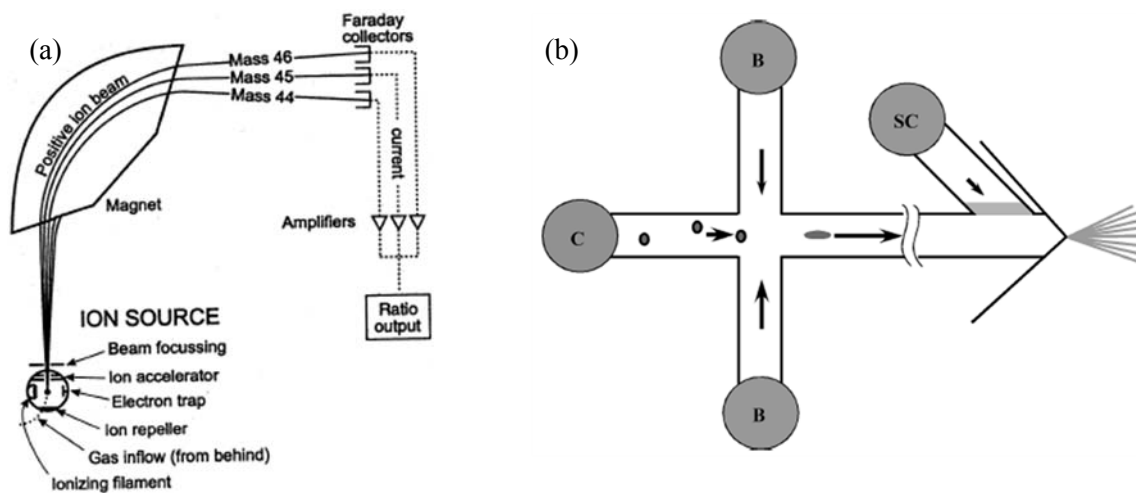


Figure 2-36. (a) Schematics of a simple mass spectrometer with sector type mass analyzer. (b) Electro spray ionization-MS chip for single cell analysis.

CHAPTER 3. INTERACTION BETWEEN DC AND AC ELECTROKINETICS

3.1. INTRODUCTION

AC electrokinetic phenomena such as dielectrophoresis, AC electroosmosis, and electrothermal force have drawn much attention in the microfluidics and lab-on-a-chip communities since those techniques have a great potential for effective manipulation of small particles and fluids in microchannel environments. Since Pohl discovered the phenomena in 1970's [77], dielectrophoresis (DEP) has been explored for the manipulation of micro- and nanoscale particles such as polymer micro/nanospheres [32-34], cells [35-37, 39, 40], bacteria [41], viruses [42], DNA [38], and carbon nanotubes [43]. AC electroosmosis (ACEO) is a relatively recently discovered phenomenon [45-47] and it has been mainly applied for fluid and chemical species mixing applications in low Reynolds number flows in microchannels [48-50]. Electrothermal force (ETF) has also been applied for mixing applications in a microfluidic device [50].

AC electrokinetic particle manipulation is readily achieved in a microchannel via non-uniform electric fields generated by microfabricated planar electrodes. High electric fields required for particle motion ($10^4\sim 10^6$ V/m) can be easily achieved with only a few volts since the electrode gap is of the order of micro- or nanoscale. The electrolysis of water can be significantly reduced since AC power is used. Moreover, each of the electrokinetic and electrohydrodynamic forces has fairly distinct characteristics and as a result various types of particle motion can be achieved by simply varying operational conditions [51]. This convenience and versatility make AC electrokinetics the most suitable particle manipulation technique for microfluidic devices

compared with other techniques such as optical tweezers [52, 53], ultrasonic techniques [54], and magnetic techniques [55-57].

The simplicity in manufacturing and the versatility in application provide a great potential to AC electrokinetic techniques in the field of microfluidics and lab-on-a-chip. It is likely that AC electrokinetics will be combined with various other techniques including DC electrokinetics. For example, AC electrokinetics can be integrated in a microchip capillary electrophoresis for the purpose of sample preparation. However one concern is raised about the possibility that the characteristics of DC and AC electrokinetics can be affected by each other. Understanding the interactive effects between DC and AC electrokinetic phenomena will help to develop stable microfluidic devices based on the combination of these two techniques. This chapter presents experimental and numerical studies on the interaction between AC electrokinetic phenomena and DC electroosmotic flows. The concept of combination of DC and AC electrokinetics is illustrated in Figure 3-1.

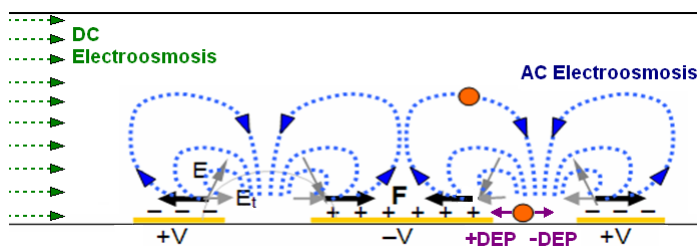


Figure 3-1. Schematic of the current study (combination of DC and AC electrokinetics).

3.2 . MICROFABRICATION METHOD: PDMS REPLICA MOLDING

The devices used in the current experimental studies consist of a glass substrate and a microchannel made of polydimethyl-siloxane (PDMS). The glass substrate contains parallel interdigitated gold electrodes which were fabricated by electron beam evaporation followed by photolithographic patterning and metal etching. 20 nm thick chrome and 200 nm thick gold were deposited on a cleaned glass substrate using an electron beam evaporator. A photoresist pattern (Shipley 1827) was made on the metal surface by photolithography to be used as a masking material during the subsequent etching process. Gold and chrome etching was done with Gold etch-type TFA and Chromium mask respectively (both manufactured by Transene company).

PDMS microchannels were fabricated by replica molding. The molds for replica molding were made on a glass plate using a negative photoresist (SU-8 2035). A PDMS mixture (10:1 of Sylgard 184 base resin to curing agent) was then poured onto the mold pattern. A 30 minute degassing step in a vacuum dessicator, followed by baking at 80°C for 2 hours took place. After baking, the fully cured PDMS was peeled off and cut into individual devices. Holes with approximately 1 mm in diameter were punched into each side of the channel to form an inlet and outlet. The dimension of microchannel was 100 μm in height, 200 μm in width and 18 mm in length. The PDMS channel was placed on top of the electrode substrate and a gentle compression was applied to ensure the adhesion. Electrical connections were made by attaching metal wires to the planar electrodes with an electrically conductive adhesive. 2 μm polystyrene microbeads (Polysciences, Inc.) were added to deionized water to make a colloidal mixture for the experiments (0.05 g/ml). The conductivity of each solution was measured by a conductivity meter (Orion Model 105A+).

3.3 . EXPERIMENT PROCEDURE

The experimental setup consists of a microscope (Nikon Eclipse ME600) equipped with a CCD camera and a function generator (HP 33120A 15MHz), which connects to an assembled device placed on the microscope stage. In order to better visualize particles on electrodes, an external, through-objective light source was used. Platinum wire electrodes were inserted into the reservoir holes and DC electric voltage was applied through the wires by high voltage power supply (Labsmith HVS448). A schematic of the experimental setup is shown in Figure 3-2. Various frequency and voltage settings were supplied by the function generator while the CCD camera recorded the behavior of the particles. The frequencies of 1 kHz, 400 kHz and 900 kHz were selected because it is known that AC electroosmosis, positive DEP and negative DEP becomes dominant at those frequencies, respectively.

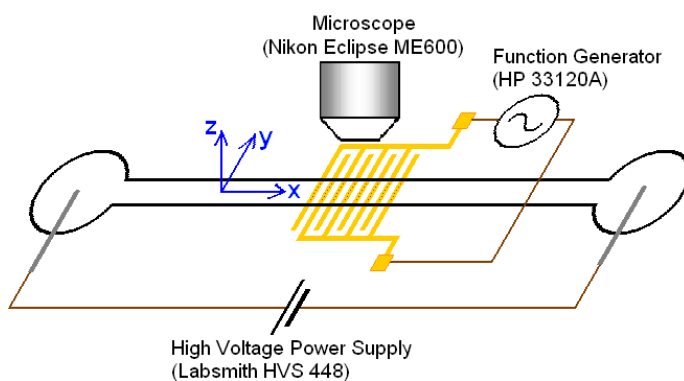


Figure 3-2. Schematic of the experimental setup.

3.4 . MEASUREMENT OF DC ELECTROSMOTIC MOBILITY

Electroosmotic mobility can be measured via several different techniques including a current monitoring method [171], a streaming potential method [172], and direct measurement

from the sample speed [173]. An easy and popular method is the current monitoring method which is based on observation of variation of electric current as the electroosmotic flow propagates through a microchannel. The schematic of the current monitoring method is illustrated in Figure 3-3. Initially the channel and outlet reservoir contain one solution and the inlet contains a solution of different conductivity. As an electric field is applied, fluid from the inlet reservoir will displace the fluid in the microchannel, and the electric resistance of the system will vary. This results in a variation of electric current which we are monitoring. In sum, the migration time of flow can be obtained by monitoring the signal of electric current.

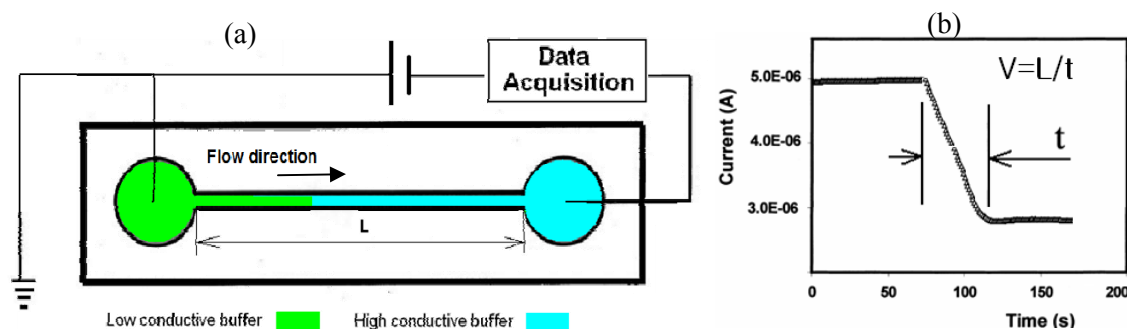


Figure 3-3. Schematic of (a) experimental set-up and (b) an example graph of current vs. time.

3.5 . NUMERICAL METHODS: AC ELECTROOSMOSIS

In general, a problem of AC-DC electrokinetics can be solved by considering three computational modules : an electrostatic simulation, a conduction heat transfer simulation and an incompressible Navier-Stokes simulation as illustrated in Figure 3-4. The geometry and details of each simulation are described below.

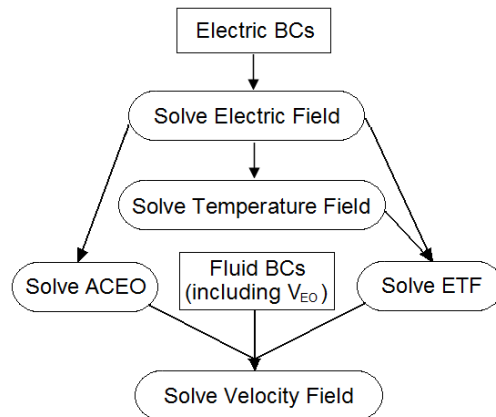


Figure 3-4. The flow chart of AC-DC electrokinetic flow simulation strategy.

3.5.1. Geometry and Boundary Conditions

The 2D numerical simulation was carried out using COMSOL Multiphysics 3.4. A 500 μm wide, 100 μm high chamber was designed with three electrodes on the bottom surface. Each electrode was 200 nm thick and 40 μm wide. The gap between each of the three electrodes was 60 μm . The experimental devices have much more electrodes. It must be noted that in simulating only three electrodes, there would normally be some distortion effects arising from the absence of many more electrodes on either side.

3.5.2. Electrostatics Simulation

A quasi-static potential field was calculated first from the Laplace equation: $\nabla^2 V = 0$ where V is voltage. The boundary conditions are zero charge everywhere except on the electrodes, where voltage condition was applied. The outside electrodes receive a 2 V potential and the center electrode has a -2 V potential. The solved electric field is $\vec{E} = -\nabla V$. The maximum norm value of the electric field is at both edges of the middle electrode. The time-averaged dielectrophoretic force can be calculated with Eq. 2-11 and the CM function for that of a sphere.

3.5.3. Incompressible Navier-Stokes Simulation

The incompressible Navier-Stokes equation is solved, including the effects of ETE and ACEO which are obtained, based on the solutions of the electrostatic and conduction heat transfer simulations. AC electroosmosis slip velocity conditions were applied on the electrodes while DC electroosmotic velocity was applied on the rest top and bottom walls. The calculation of electroosmotic velocity was based on PDMS μ_{eo} ($4 \times 10^{-4} \text{cm}^2/\text{V s}$) from [76]. Zero pressure condition was applied at the inlet and outlet. To determine the velocity at the electrode, the time-averaged equation for electroosmotic velocity is used (Eq. 2-9). This function is used as the slip velocity boundary condition for the surface of each electrode. Since the equation is intended to be centered on an electrode gap, it may easily be applied to a pair of electrodes. However, since three electrodes are used in this simulation, Eq. 2-9 must be used twice - once centered on the right gap and once centered on the left gap.

3.6 . EXPERIMENTAL RESULTS

3.6.1. AC and DC Electroosmotic Flow Interaction

Figure 3-5 shows particle shift on the electrode surface due to the combined effects of ACEO and DCEO. The media conductivity was 0.0002 S/m and the frequency of AC electric field was 1 kHz. Under this condition, AC electroosmosis becomes dominant. Without external DC electric field, the beads were immediately collected in the middle of the electrodes. When DC electric field was applied, the beads shifted toward the direction of DCEO (from right to left) and reached a new location at which the ACEO and DCEO are balanced. As the applied DC field increased, the amount of shift also increased. The higher AC magnitude activates the stronger AC electroosmosis. Thus the particle shift decreases with the applied AC voltage.

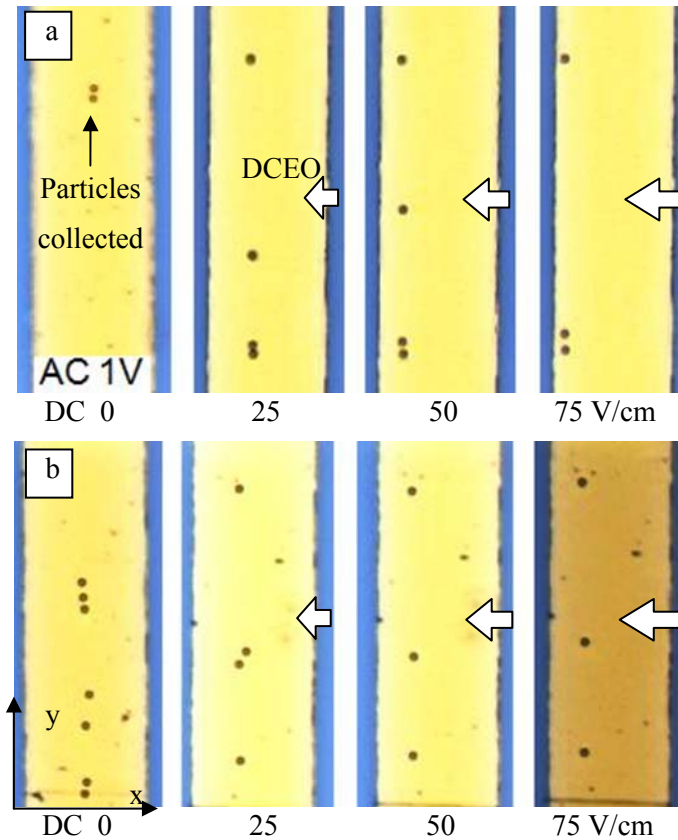


Figure 3-5. Particle shift on the electrode surface due to the combined effects of ACEO and DCEO. The frequency of the applied voltage for ACEO was fixed at 1 kHz and two amplitudes ((a) 1V and (b) 2V) were tested. The media conductivity was 0.0002 S/m. The DC electric field was varied from 0 to 75 V/cm.

3.6.2. Dielectrophoresis under DC Electroosmotic Flow

At higher frequencies (e.g. 400kHz), ACEO dies out and positive DEP becomes dominant. Since particles are more polarizable than the media at these conditions, they are attracted towards high electric field area (near edge) as shown in Figure 3-6(a) [36, 37, 39, 40]. At even higher frequencies (900 kHz), particles experience negative DEP, which propels particles towards regions of low electric field (inter-electrode areas or bulk solution) as shown in Figure 3-

6(b). Both positive and negative DEP forces were not strong enough to hold particles when a DCEO was applied. The beads initially collected by DEP forces were blown away immediately after DC field was applied.

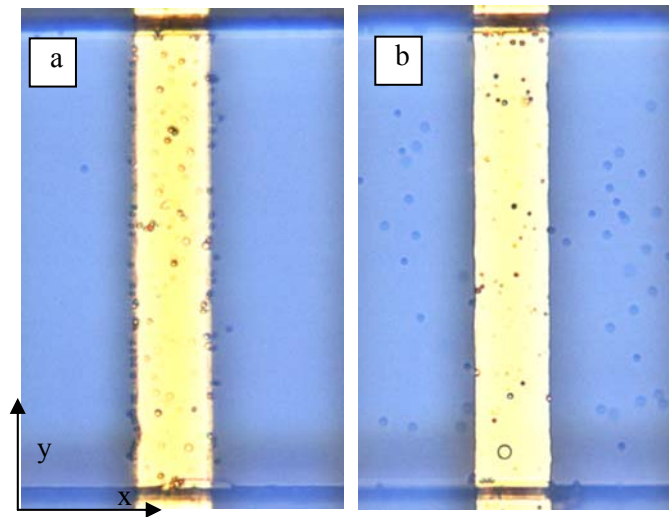


Figure 3-6. (a) Positive dielectrophoresis(400 kHz, 2 V_{pp}) and (b) negative dielectrophoresis (900 kHz, 2 V_{pp}) conductivity was 0.0002 S/m. The DC electric field was varied from 0 to 75

3.7 . NUMERICAL SIMULATION RESULTS

Figure 3-7 shows the simulated 2-D flow field in the presence of both ACEO and DCEO. When DCEO is not applied (Figure 3-7(a)), circulating flow patterns are induced by AC electroosmosis. Since the ACEO forces negated in the middle of the electrodes, the particles are collected there. Figure 3-7(b) shows the perturbation of AC electroosmotic flow field under slight DC field (2.5V/cm). The flow field was dramatically changed by this small amount of external DC perturbation. Figures 3-7(c-e) show how the flow field is changed as DCEO is increased. 2-D velocity profile in the simulation shows a great change in velocity field was induced by DC electroosmotic flows while the shift of beads alignment location in experiments seems to be

somewhat small. This seeming disagreement was further analyzed by comparing the velocity data near the electrode surface ($1\ \mu\text{m}$ above the electrode) where the microbeads are manipulated.

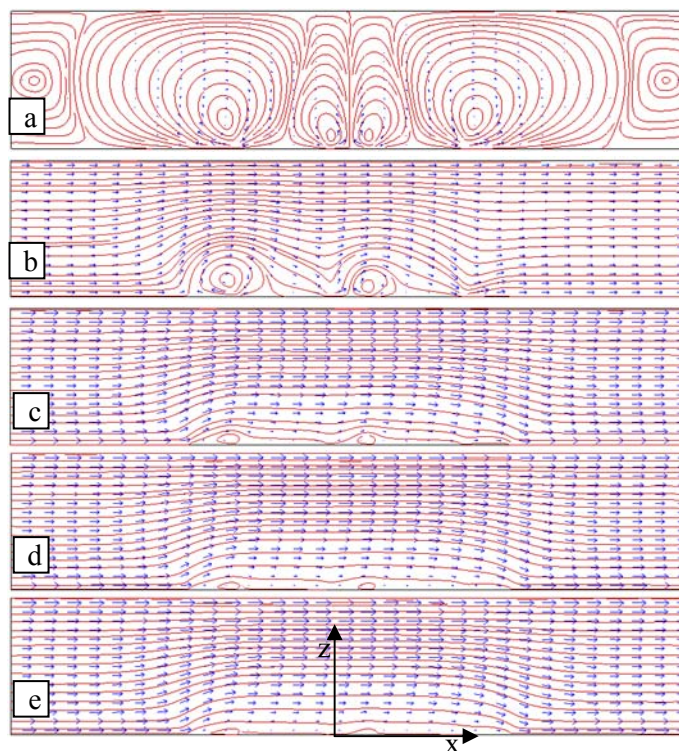


Figure 3-7. 2D AC electroosmotic flow simulation results (1 kHz, 2 V_{pp} and 0.0002 S/m) under the influence of DC electroosmosis. Velocity streamlines and vectors. (a) No DC field applied and (b) DC=2.5V/cm ($\mu_{\text{eo}}=4 \times 10^{-4} \text{cm}^2/\text{V s}$) (c) DC=25 V/cm , (d) DC=50 V/cm and (e) DC=75 V/cm

Figure 3-8 plots x-directional velocity at this location. The graph shows that the location where the velocity becomes zero shifts from the origin as the applied DC field increases. This result agrees with the experimental observation shown in Figure 3-5. Figure 3-9 quantitatively compares the particle shift data obtained from numerical and experimental studies. The shift amount from simulation results is actually larger than that measured in the experiment. It may be

because, in the numerical simulation, the DC electroosmotic flow velocity was not affected by AC electric field while, in reality, DC electroosmotic velocity is also likely to be deteriorated by the AC electric field. This effect should be also studied for further understanding of the interactive mechanism between AC and DC electrokinetics.

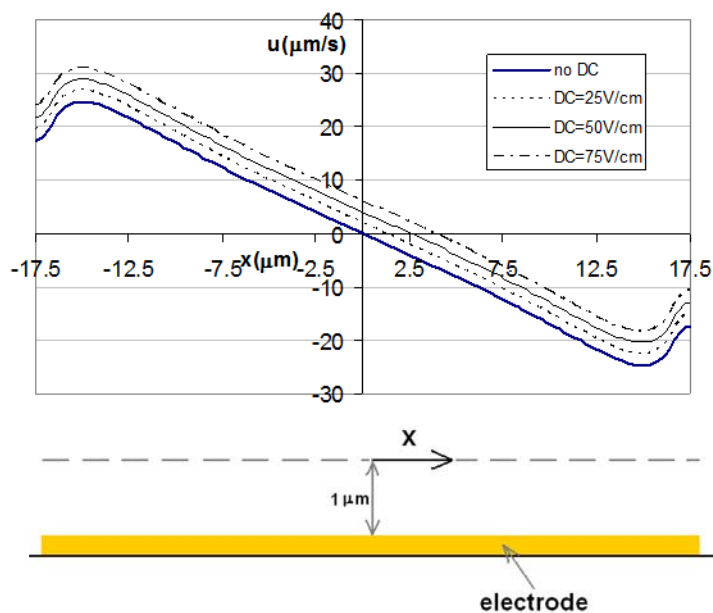


Figure 3-8. u velocity at $1\ \mu\text{m}$ above the electrode.

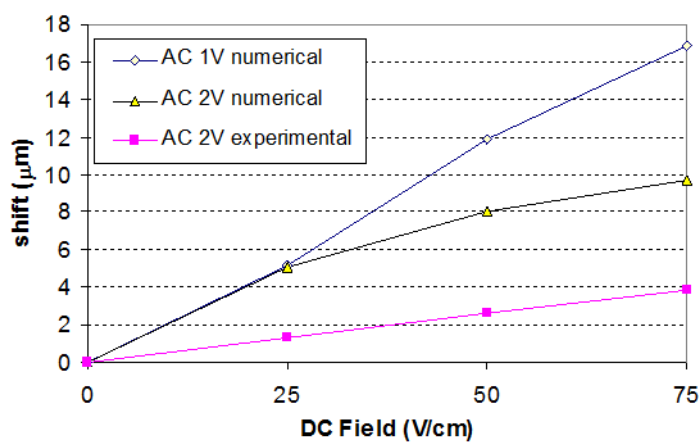


Figure 3-9. Numerical and experimental particle shift data as a function of DC electric field.

3.8. CONCLUSIONS

The effect of DC electroosmotic flow on AC electrokinetic phenomena has been investigated through experimental studies and numerical simulations. The motions of polystyrene microbeads suspended in deionized water in a microchannel were observed as major AC and DC electrokinetics parameters were varied. Numerical simulations of flow field were performed using Comsol Multiphysics. At low frequencies where AC electroosmosis becomes dominant and particles are collected in the middle of the electrodes, shifts of the collected particles were observed due to the force balance between AC electroosmosis and DC electroosmosis. Particle shift increased as DC electroosmosis increased. Flow field were calculated by numerical simulation. The distortion of circulating flow pattern typical for AC electroosmosis was clearly observed as the DC electroosmosis increased. The flow velocity was plotted and the zero velocity location in numerical simulation showed a good agreement with experimental results. At higher frequencies where dielectrophoresis is dominant, particles were almost immediately swept away by DC electroosmotic flows indicating that dielectrophoresis (both positive and negative DEP) is significantly deteriorated by DC electroosmoticl flows. For more accurate simulation, the reverse influence (effect of AC on DC) should also be investigated.

CHAPTER 4. DIELECTROPHORETIC PARTICLE-PARTICLE INTERACTION UNDER AC ELECTROHYDRODYNAMIC FLOW CONDITIONS

4.1. INTRODUCTION

AC electrokinetic phenomena, such as dielectrophoresis (DEP), AC electroosmosis (ACEO), and electrothermal flow (ETF), have drawn much attention in the microfluidics and lab-on-a-chip communities because of their potential for effective manipulation of small particles and fluids in microchannel environments. The ease of implementation and the versatility in application make AC electrokinetic techniques very attractive in microfluidics and lab-on-a-chip applications. Diverse particle manipulation techniques based on DEP have been reported for the past two decades [32-44]. More recently, AC electrohydrodynamic phenomena, such as ACEO and ETF, have also been discovered [45-47] and some of their applications have been explored [48-50]. One of the major applications of the AC electrohydrodynamic phenomena is mixing, which is a challenging task in microchannel laminar flows and miniature biosensor platforms [174, 175].

ACEO flow is generated by the migration of the induced ions on the planar electrode surface due to the tangential component of the applied electric field (Figure 4-1a). In the case of the planar interdigitated electrode, the ACEO flow pattern is rotational and the direction of the flow on the electrode surface is always from the edge to the middle of the electrode with the maximum velocity at the edge. ETF is generated by the temperature gradients due to non-uniform Joule heating or cooling conditions (Figure 4-1b). The flow pattern is quite similar to ACEO flow although the maximum velocity location is slightly off the edge of the electrode. ACEO and ETF play an important role in the particle behaviors at different conditions. ACEO

becomes dominant in low electrical conductivity media ($< 100 \mu\text{S}/\text{cm}$) and at relatively low frequencies ($< 10 \text{ kHz}$) of the applied voltage while ETF becomes dominant in higher electrical conductivity media and at higher frequencies. ETF also requires the electrode substrate to be thermally conductive and even actively cooled to generate a sufficient temperature gradient.

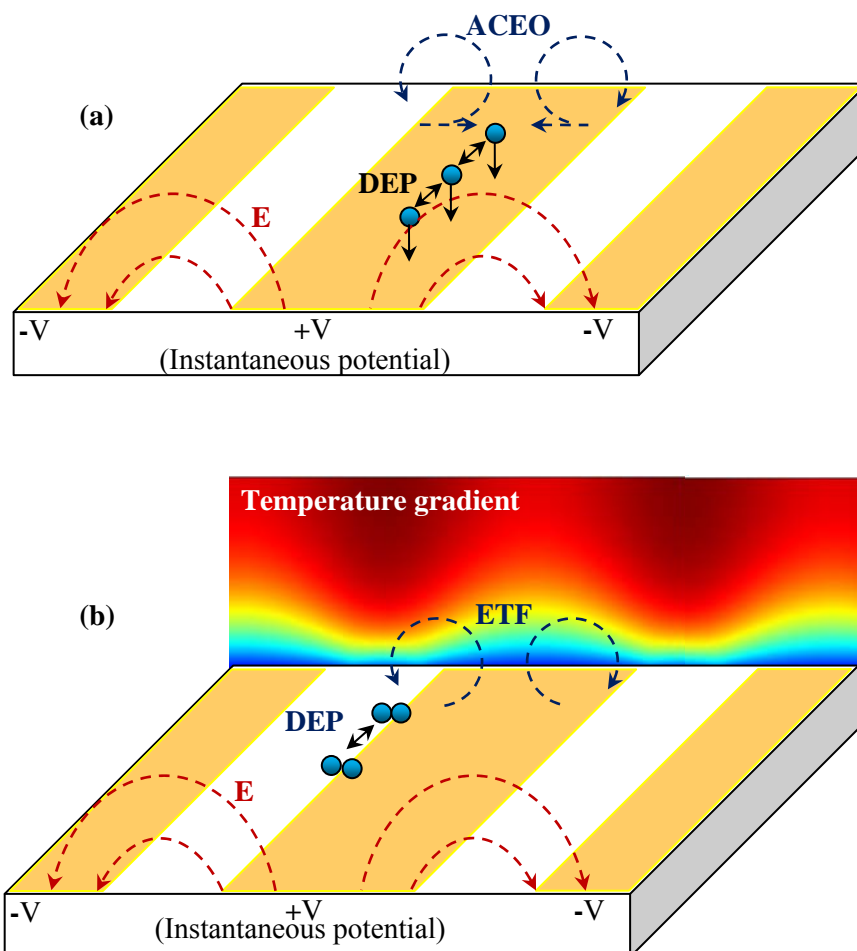


Figure 4-1. Schematic of the forces that affect particle motions under AC electrohydrodynamic conditions: (a) AC electroosmosis-dominated case and (b) electrothermal flow-dominated case.

When particles are present in the fluid under ACEO or ETF dominant conditions, the particles experience Stokes drag force due to the electrohydrodynamic motion as well as DEP force. DEP force is magnified when particles approach each other or another solid surface. Dielectrophoretic particle-particle interactions under no electrohydrodynamic flow have been discussed by others. Giner *et al.* [176] investigated how micro-particles formed chains through interactive DEP force and revealed that the particle chaining style depended on the applied AC frequency. Morgan and Green [35] showed using 2-D model that two particles of the same type experience an attractive force when they are aligned along the applied electric field and they experience a repulsive force when they are aligned perpendicular to the electric field. This attraction or repulsion trend was independent of the DEP polarity (i.e. positive or negative DEP). These previous works show the magnified DEP effect when particles come close to each other. However, the dielectrophoretic particle-particle interactions under AC electrohydrodynamic flow conditions and the subsequent behaviors of particles under ACEO and ETF have not been thoroughly investigated.

This chapter presents, through both experimental and numerical studies, how the dielectrophoretic particle-particle and particle-electrode surface interactions affect the overall particle behaviors under AC electrohydrodynamic flow conditions. DEP forces exerted on individual particles were calculated using Maxwell stress tensor method considering particle-particle and particle-electrode surface interactions and combined with ACEO and ETF effects to discuss the specific particle behaviors observed in experiments.

4.2. THEORY

4.2.1. Dielectrophoresis

When a dielectric particle is suspended in a liquid media of different polarizability and subjected to a non-uniform electric field, the particle experiences a net force (dielectrophoresis, DEP) and is either attracted to (positive DEP) or pushed away from (negative DEP) a high electric field region [77]. By employing a dipolar approximation of a particle and neglecting the influence of particle volume on the near field of the particle, the simplest formula for the DEP force can be derived as follows:

$$\vec{F}_{DEP} = 2\pi r^3 \varepsilon_m \operatorname{Re}[CM] \nabla |\vec{E}|^2 \quad (4-1)$$

where

$$CM = \left(\frac{\tilde{\varepsilon}_p - \tilde{\varepsilon}_m}{\tilde{\varepsilon}_p + 2\tilde{\varepsilon}_m} \right) \text{ and } \tilde{\varepsilon} = \varepsilon - j \frac{\sigma}{\omega} \quad (4-2)$$

where ε , E , σ , ω and j indicate permittivity, electric field, electric conductivity, the frequency of applied electric field and the imaginary unit, respectively. Subscripts, m and p , indicate properties of the media and particle.

When the near field influence becomes significant, such as when particles are close to each other or another solid surface, the above approximation becomes inaccurate [78]. In those cases, the DEP force can be accurately calculated by integrating Maxwell stress tensor (\vec{T}) over a closed body as follow:

$$\vec{F}_{DEP} = \oint (\vec{T} \cdot \vec{n}) dA \quad (4-4)$$

where \vec{n} is the unit vector normal to the control surface (A). This is a direct calculation of the electric force over any control volume, making it the most rigorous calculation of dielectrophoresis. The Maxwell stress tensor that neglects magnetic field is defined as

$$T_{ij} = \varepsilon_m \left(E_i E_j - \frac{1}{2} \delta_{ij} E_k E_k \right) \quad (4-4)$$

where ε_m is the media permittivity and δ_{ij} is Kronecker's delta. The average DEP force of AC oscillation can be obtained by the complex variable analysis as follows:

$$\langle \vec{F}_{DEP} \rangle = \oint \left(\langle \vec{T} \rangle \cdot \vec{n} \right) dA \quad (4-5)$$

$$\langle T_{ij} \rangle = \frac{\text{Re}(\varepsilon_m)}{4} (E_i E_j^* + E_i^* E_j - \delta_{ij} E_k E_k^*) \quad (4-6)$$

where $\langle \rangle$, $\text{Re}(\)$ and $*$ indicate the time average, real and complex conjugate parts respectively. Note that the electric field should be obtained in the media region (not in the particle region). For example, the x -component of the DEP force is calculated by

$$\begin{aligned} \langle \vec{F}_{DEP,x} \rangle &= \oint \left(\langle T_{xx} \rangle \cdot n_x + \langle T_{xy} \rangle \cdot n_y + \langle T_{xz} \rangle \cdot n_z \right) dA \\ &= \frac{\text{Re}(\varepsilon_m)}{4} \oint \left(\left(2|E_x|^2 - |\vec{E}|^2 \right) \cdot n_x + 2\text{Re}(E_x E_y^*) \cdot n_y + 2\text{Re}(E_x E_z^*) \cdot n_z \right) dA \end{aligned} \quad (4-7)$$

4.2.2. AC Electroosmosis

When an AC electric field is applied to interdigitated planar microelectrodes immersed in a liquid electrolyte, mobile counter ions are attracted to the microelectrode surfaces by the applied electric potential, and an electric double layer (EDL) is formed. Since the electric field has a tangential component due to the planar electrode geometry, the counter ions are pulled along the tangential component of the applied electric field (from the edge to the middle of the

electrode). The direction of movement does not change with the polarity change of the AC voltage because the polarity of the induced counter ions is switched as well. The motion of the ions drags the bulk fluid along the surface.

The time-averaged AC electroosmotic slip velocity on two parallel electrodes was derived by Ramos *et al* [32-34] by assuming a linear relationship between the surface charge and electric potential, neglecting the stern layer and assuming two wide electrodes with a very narrow gap in between. The simplified ACEO velocity expression is as follows:

$$V_{ACEO} = \left(\frac{\varepsilon \varphi_0^2 \Omega^2}{8\eta x (1 + \Omega^2)^2} \right) \quad (4-8)$$

$$\Omega = \frac{1}{2} \pi \kappa x \left(\frac{\varepsilon_m}{\sigma_m} \right) \omega \quad (4-9)$$

where φ_0 is the applied electric potential, Ω is a non-dimensional frequency defined as above, η is the dynamic viscosity, x is the horizontal location starting from the center of the gap between the electrodes and κ is the reciprocal of the Debye length.

4.2.3. Electrothermal Flow

Non-uniform Joule heating or cooling in an electrical system generates a spatial temperature gradient according to the following heat transfer formula:

$$k\nabla^2 T + \sigma E^2 = \rho c_p \vec{V} \cdot \nabla T \text{ or}$$

$$k\nabla^2 T + \sigma E_{rms}^2 = \rho c_p \vec{V} \cdot \nabla T \text{ for an AC system (4-10)}$$

The temperature gradient creates variation in the electrical conductivity and permittivity of the media, and assuming small temperature variation, the following equations define the linear relationships between temperature and electrical parameter variations [79].

$$\left(\frac{1}{\varepsilon}\right)\left(\frac{\Delta\varepsilon}{\Delta T}\right) = -0.004 \text{ K}^{-1} \quad (4-11)$$

$$\left(\frac{1}{\sigma}\right)\left(\frac{\Delta\sigma}{\Delta T}\right) = 0.02 \text{ K}^{-1} \quad (4-12)$$

This electrical property gradient results in a body force in the Navier-Stokes equation according to the following formula [35]:

$$\vec{f}_{ETF} = -0.5 \left[\left(\frac{\nabla\sigma}{\sigma} - \frac{\nabla\varepsilon}{\varepsilon} \right) \vec{E} \frac{\varepsilon\vec{E}}{1+(\omega\tau)^2} + 0.5|\vec{E}|^2 \nabla\varepsilon \right] \quad (4-13)$$

where τ is the charge relaxation time (ε/σ). This driving force of fluid motion is called electrothermal force. The fluid velocity can be calculated by using \vec{f}_{ETF} as a body force acting on the liquid once the temperature gradient and electric field are solved. Generally, when the frequency of the applied voltage and the media conductivity are high ($f > 80 \text{ kHz}$, $\sigma > 100 \text{ }\mu\text{S/cm}$), ACEO diminishes and ETF becomes dominant.

4.2.4. Van der Waals Force and Double Layer Interaction

Other than electrokinetic forces acting on particles, there are two more interactive forces between two solid bodies (particle-particle or particle-surface) that need to be considered. One is the van der Waals force, which is an attractive force generated by dipole-dipole interactions and electron fluctuation in two particles. This force is magnified when particles are near each other and can be of the same order as the DEP force [35]. The other force is the double layer interaction. The double layer force between the same type of particles is repulsive because the particles must form the same polarity EDL and, as the two particles approach each other, squashing double layers into a smaller space induce an osmotic pressure [177]. The repulsive double layer force is proportional to $e^{-\kappa y}$ while the attractive van der Waals force is proportional to $1/y^2$, where y is the distance between two sphere surfaces [177]. The combined force graph in DLVO analysis [177] shows that the van der Waals attraction dominates over the repulsive double layer interaction at very small or very large distances (y). In other words, two particles at a long distance from each other experience a weak attractive force and if two particles happen to get very close, they will experience a strong attractive van der Waals force and form a group. An attractive double layer force can be also generated between asymmetric surfaces.

4.3 . EXPERIMENTAL METHOD

4.3.1. Device Fabrication and Materials

The devices used in the current experiments consist of an electrode substrate and a microchannel. The planar interdigitated electrodes were fabricated on glass substrates or silicon wafers with an oxide layer. First, 20 nm thick chrome and 200 nm thick gold layers were deposited on the substrate using thermal evaporation. Then a photoresist pattern (Shipley 1827) was made on the metal surface by photolithography (3000 rpm coating and 120 mJ/cm² dose), and it was used as a masking material during the subsequent etching process. Gold and chrome

etching was done with Gold etchant trifluoroacetic acid (TFA) and Chromium mask etchant, respectively (Transene company). The device with an interdigitated microelectrode is shown in Figure 4-2b. The fingers of the interdigitated electrode had a width of 93 μm and a gap of 33 μm .

Microchannels were made of polydimethylsiloxane (PDMS). PDMS microchannels were fabricated using replica molding technique. First, the master molds were made on a glass plate using a negative photoresist (SU-8 2035). A PDMS mixture (10:1 of Sylgard 184 base resin to curing agent, Dow Corning) was then poured onto the mold pattern. The following steps consisted of degassing in a vacuum dessicator for 30 minutes and baking at 80°C for 2 hours. After baking, the fully cured PDMS was peeled off and cut into individual devices. Dimensions of the channels were 2 mm x 12 mm x 80 μm . Holes with a diameter of approximately 0.3 mm were punched into each end of the channel to form an inlet and outlet. The PDMS channel was then placed on top of the electrode substrate, and gentle compression was applied to ensure adhesion. Electrical connections were made by attaching metal wires to the planar electrodes with an electrically conductive adhesive. The final device assembly is shown in Figure 4-2b. 2 μm polystyrene microbeads (Polysciences, Inc.) were added to water-based media to make a colloidal mixture for the experiments. The electrical conductivity of the solution was controlled by adding KCl. The electric conductivity of each solution was measured by a conductivity meter (Orion Model 105A+).

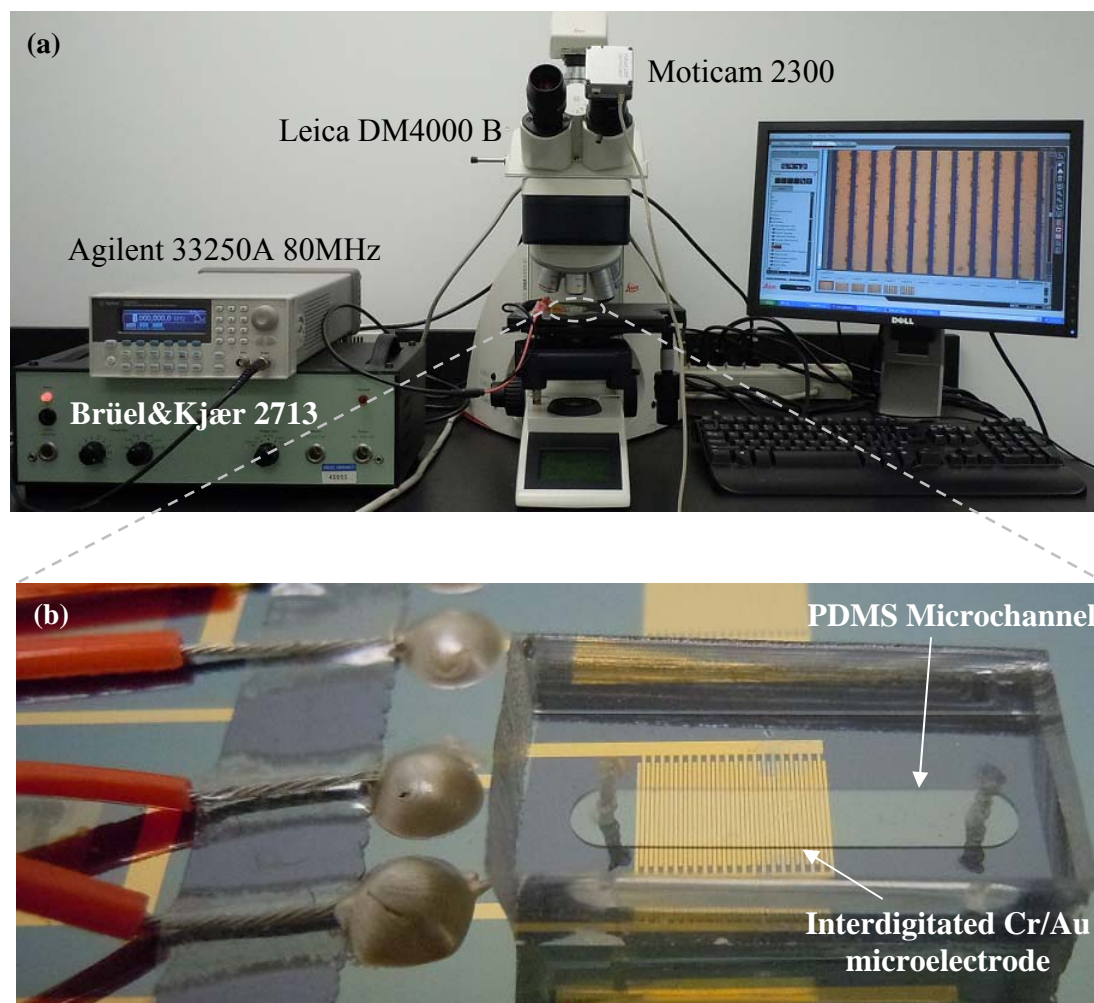


Figure 4-2. Pictures of (a) experimental set-up and (b) a device used in the experiments.

4.3.2. Experimental Procedure

(1) AC Electroosmosis Condition

The experimental setup consisted of a microscope (Leica DM4000 B) equipped with a CCD camera and a function generator (Agilent 33250A 80MHz), which is connected to an assembled device placed on the microscope stage (Figure 4-2a). Microbead-containing solutions were then gently injected into the PDMS channel through an inlet

hole. After confirming the initial random distribution of the microbeads on the electrode surface and no air bubble formation, an AC field of 1 kHz and $4V_{pp}$ was applied using the function generator. The frequency of 1 kHz was selected because ACEO becomes dominant at this frequency [178]. The behavior of the particles were video-taped using the CCD camera.

(2) Electrothermal Flow Condition

The experimental setup consisted of a microscope (Leica DM4000 B) equipped with two CCD cameras (Leica DFC 420C; Moticam 2300), a function generator (Agilent 33250A 80MHz) and a voltage amplifier (Brüel&Kjær Type 2713), which was connected to an assembled device placed on the Peltier cooler (CP-031, TE technology) (Not shown in Figure 4-2a). For these experiments, the voltage was increased incrementally from 3 to 10 V_{rms} in steps of 1 V_{rms} . Although different frequencies were tested in the experiment, a frequency of 200 kHz was the default setting for most of the tests. A Peltier cooler was used to maximize the temperature gradient and thus, enhance the ETF. The experiments were conducted in 1X phosphate buffer solution (PBS) because PBS is widely used in biological assays and is a highly conductive media. The electric conductivity of 1X PBS is 1.77 S/m.

4.4 . SIMULATION METHOD

COMSOL Multiphysics software version 3.5a was used for the simulation of DEP. The software is based on the finite element method. The element shapes were triangular for 2-D geometries and tetrahedral for 3-D geometries considered. The element type used was the quadratic Lagrange element, and the maximum element length was set to 0.2 μm . With the help of complex number analysis, all current simulations fall into stationary problems. DEP force was

calculated by integrating Maxwell stress tensor, Eq. 4-7, over a control surface enclosing a target particle. First, the complex-number electric field was solved with proper boundary conditions, and then the Maxwell stress tensor and DEP force were calculated based on the complex-number electric field solution.

The governing equation for the electric potential of a dielectric system is expressed by

$$\nabla(\varepsilon\nabla V) = 0 \quad (4-14)$$

where ε is the complex permittivity and V is the electric potential. This equation is based on the assumptions of no-net electric charge (negligible ion effect), harmonic oscillation (linear model) and negligible convection effects.

The electrothermal flow is simulated by the sequence of solving the electric (Eq. 4-14), the Navier-Stokes and the convection-conduction equations (Eq. 4-10). The Navier-Stokes equation that includes electrothermal force (Eq. 4-13), is

$$\rho \frac{D\vec{V}}{Dt} = -\nabla p + \eta \nabla^2 \vec{V} + \vec{f}_{ETF} \quad (4-15)$$

The modeling conditions were taken to be similar to the experimental conditions. The computational domain for DEP calculation is illustrated in Figure 4-3a. Long and repeating interdigitated electrodes are represented by the boundary conditions described in the figure. Physical parameters used for computation were $\varepsilon_{m,r} = 80$, $\varepsilon_{p,r} = 2.5$, $\sigma_{p,bulk} = 1\text{e-}16$ S/m and $K_s = 1\text{e-}9$ S. The electric field for ACEO-dominant condition was 1 kHz and 4 V_{pp}. The computational domain of electrothermal flow simulation is illustrated in Figure 4-3b. For the electric field and

flow field equations, region II (silicon substrate) was not included in the simulation. The boundary conditions for the heat transfer equation are shown in the figure. Parameters for this case were $V_{\text{rms}} = 7 \text{ V}$, $c_{p,m} = 4.184 \text{ kJ}/(\text{kg K})$, $k_m = 0.598 \text{ W}/(\text{m K})$, $\sigma_m = 1.77 \text{ S}/\text{m}$, $k_{\text{silicon}} = 149 \text{ W}/(\text{m K})$, $\rho_{\text{silicon}} = 2330 \text{ kg}/\text{m}^3$, and $c_{p,\text{silicon}} = 0.70675 \text{ kJ}/(\text{kg K})$.

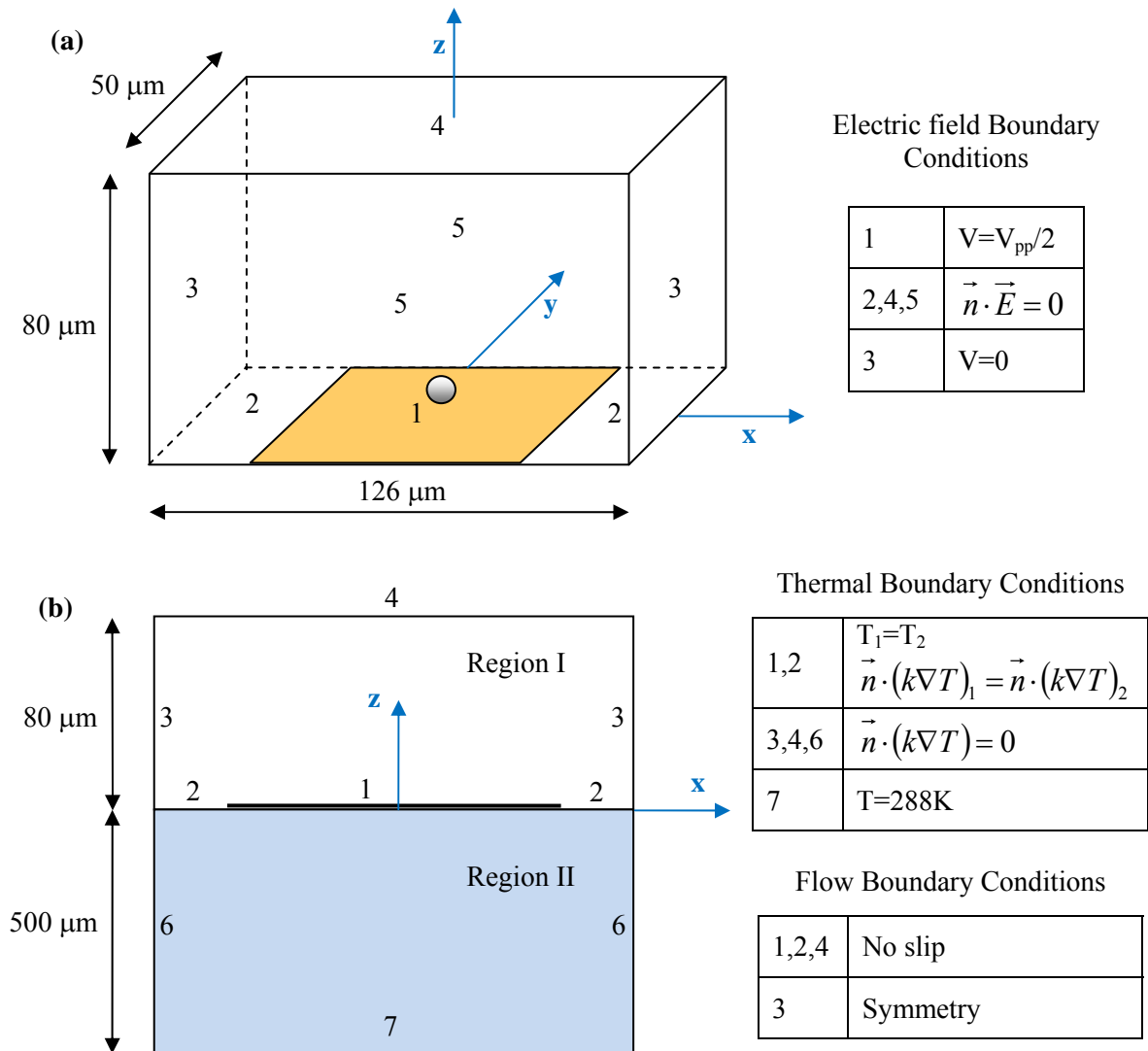


Figure 4-3. Computational domains and boundary conditions. (a) 3-D domain for DEP calculation and (b) 2-D domain for electrothermal flow simulation (Region I: media and region II: silicon). Electric field boundary conditions are common for both (a) and (b) cases. Thermal and flow equations were solved only for case (b).

4.5 . RESULTS AND DISCUSSION

4.5.1. Particle Behaviors under ACEO Flows

At low frequency (< 10 kHz) and in low conductivity media (< 100 $\mu\text{S/cm}$), ACEO is usually dominant over DEP and ETF. However, dielectrophoretic particle-particle interaction also plays an important role in determining particle behaviors. Figure 4-4 shows particle behaviors under an AC field of $4 V_{pp}$ and 1 kHz for three different media conductivities (2 , 20 , and 65 $\mu\text{S/cm}$). For a very low electric conductivity case (2 $\mu\text{S/cm}$), most microbeads were immediately dragged towards the middle of the electrodes due to ACEO and stopped there instead of following the rotational ACEO flow over the electrode surface. A small number of particles were initially in rotational motion but soon came to rest and were collected at the center of the electrode as well. The particles collected in the middle of the electrode did not come in contact but kept a distance (~ 5 μm) from each other.

In order to better understand the particle behavior in this condition, the DEP force acting on a particle was calculated using Maxwell stress tensor method (Eq. 4-5). Figure 4-5a shows the vertical DEP component on a particle with varying particle location (z) above the center of electrode ($x = 0$). z is the distance from the center of the particle to the electrode surface. In this graph a positive value indicates attraction between the particle and the electrode surface while a negative value indicates repulsion. As the particle approaches the electrode surface ($z = 0$), particles experience a strong attraction to the electrode surface ($\text{DEP}_z \gg 0$). This explains why microbead particles stay on the electrode surface instead of following the rotational ACEO flow. Note that the strong DEP attraction of particles to the electrode surface is not shown in the common dipole method simulation (Eq. 4-1). This is because, unlike the Maxwell stress tensor, the dipole method does not consider the perturbation of the electric field as the particles come close to each other or to a solid surface. Except in the vicinity of the electrode surface, Maxwell

stress tensor method and the dipole method show a good agreement ($z > 5 \mu\text{m}$). This validates the current Maxwell stress tensor calculation algorithm.

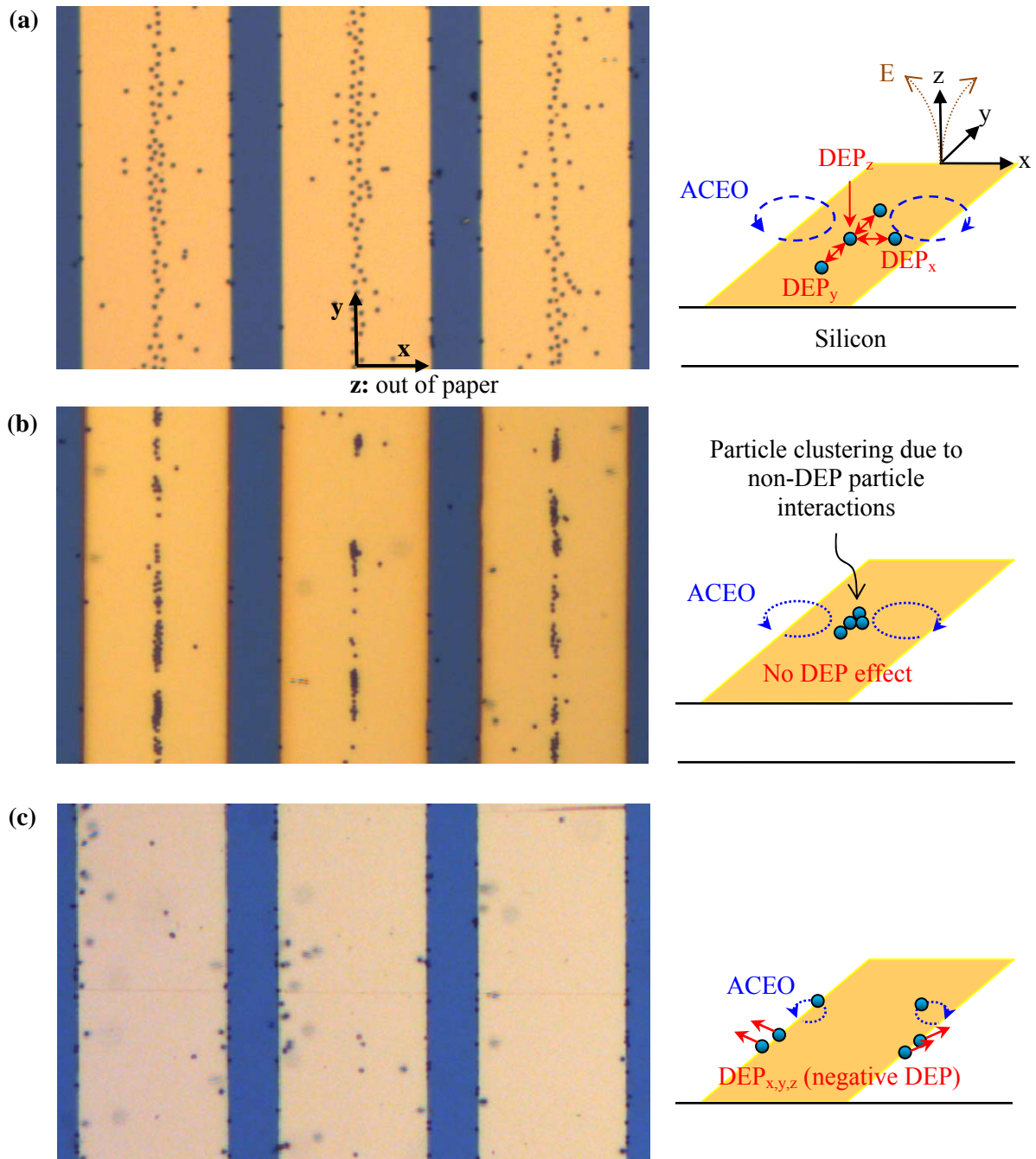


Figure 4-4. Behaviors of polystyrene microbeads for different media conductivities under ACEO flows ($4 V_m$ and 1kHz), (a) $2 \mu\text{S/cm}$ (b) $20 \mu\text{S/cm}$ and (c) $65 \mu\text{S/cm}$.

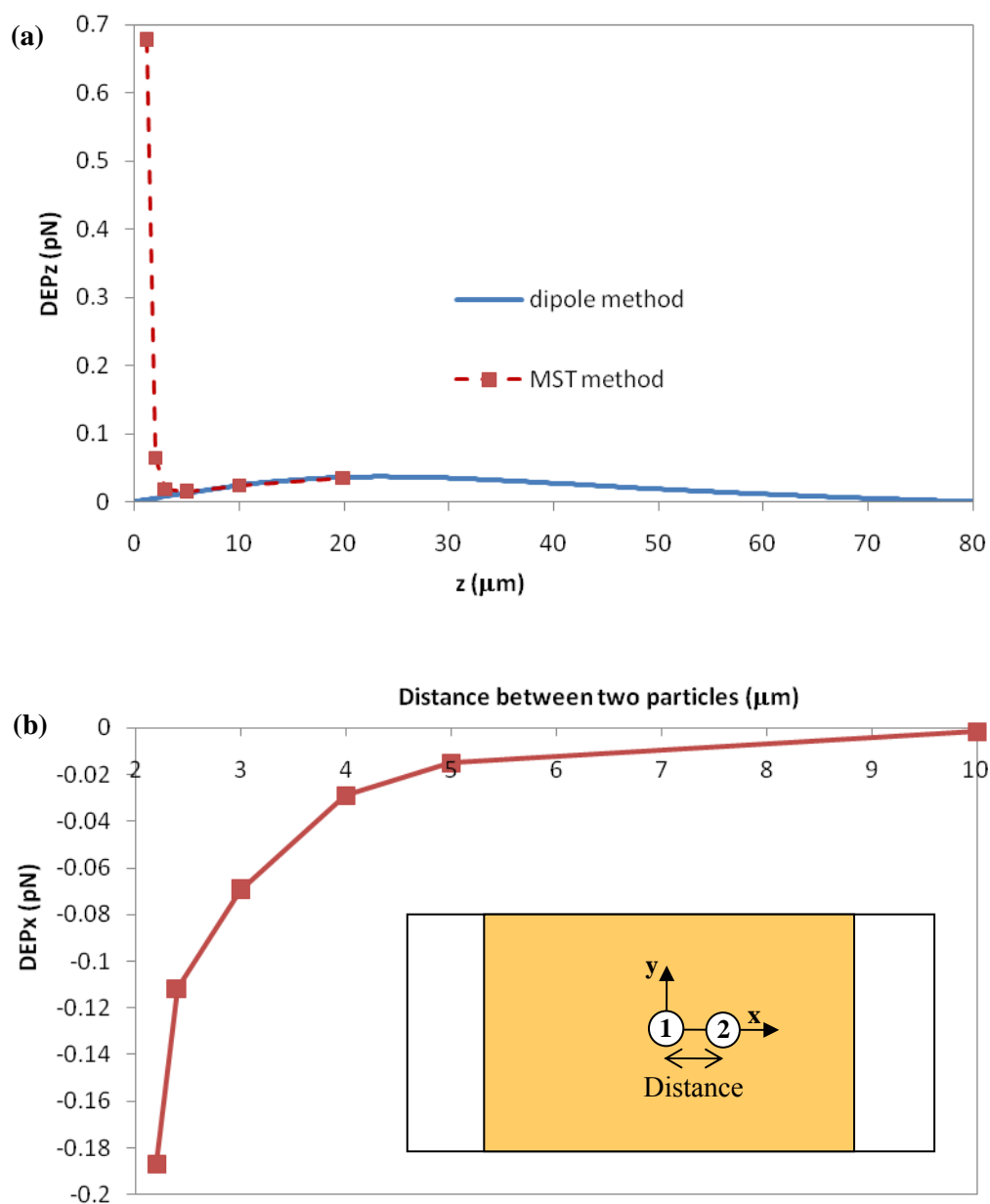


Figure 4-5. Computer simulated DEP force components acting on a particle under an ACEO condition ($\sigma = 2 \mu\text{S}/\text{cm}$, $f = 1 \text{ kHz}$ and $V_{pp} = 4 \text{ V}$). (a) Vertical DEP component with changing particle elevation ($x=0$) and (b) horizontal DEP component on particle 1 due to the presence of the neighboring particle (particle elevation $z = 1.2 \mu\text{m}$).

Dielectrophoretic particle-particle interaction was also investigated by placing two particles on the same horizontal plane (Figure 4-5b). The interval between two particles was changed in a way that the location of particle 1 was fixed while particle 2 was moved in the x direction. Figure 4-5b shows the horizontal DEP force (DEP_x) on particle 1 and a negative value denotes a repulsive force. As particle 2 approaches particle 1, the repulsive force increases significantly. This repulsive DEP explains why microbead particles kept a certain distance ($\sim 5 \mu\text{m}$) with each other in Figure 4-4a. Note that this dielectrophoretic particle-particle interaction cannot be analyzed by the dipole method. Placing two particles in the y direction showed a similar result (data not shown). Particles experience strong repulsive force as they come close. This is because both x and y directions are perpendicular to the electric field direction (z direction at the middle of the electrodes). This simulation data explains why the particles keep similar distance from their neighboring particles in all directions on the surface of the electrode as shown in Figure 4-4a.

For an increased media conductivity case ($20 \mu\text{S/cm}$), the particles were concentrated in the center line of the electrodes, and they clustered with each other (Figure 4-4b). The ACEO flow was still active in this condition although the flow velocity was reduced compared to the $2 \mu\text{S/cm}$ case. Figure 4-6 shows the simulation of DEP force in x and z directions as a function of media conductivity. DEP_x is always a negative value (repulsive force) while DEP_z is always positive (attractive force). This is because the interaction between solid bodies in the direction of the electric field always attract each other while those aligned perpendicular to the electric field repel each other [35]. Note that the amplitudes of DEP_x and DEP_z decrease initially with the increase in media conductivity up to $20 \mu\text{S/cm}$ where DEP forces become zero and then begin to increase again at higher media conductivities. This result agrees with the real part of Clausius-Mossotti (CM) factor calculation shown in Figure 4-6c. The CM factor is positive at low media

conductivities, becomes zero at $20 \mu\text{S}/\text{cm}$, and then becomes negative. In other words, the relative polarizability between media and the particles that induces DEP becomes zero when the media conductivity is $20 \mu\text{S}/\text{cm}$ and thus no significant DEP is observed in any direction. Since the particles do not experience repulsive DEP force on the electrode surface any longer, they can now come close to each other until van der Waals force becomes sufficient to produce particle clusters.

For an even higher media conductivity ($65 \mu\text{S}/\text{cm}$), a very different particle behavior is observed (Figure 4-4c). At the beginning of the application of the electric field, most particles made small rotational motions above the electrode edges, and only a few particles were captured in the middle of the electrode. Most of the rotating particles were then captured at the edges. This is a surprising result because the particles experience negative DEP with such a high media conductivity (Figure 4-6c). ACEO still exists but its effect has become so weak that particles are not pushed to the middle of the electrodes any longer. It seems that magnitudes the negative DEP force and ACEO force are close enough so that the particles are rotating around the electrode edges instead of being completely pushed away from the electrode. It is not clear why these particles adhere to the electrode edges as if they were under positive DEP. This may be due to the attractive electric double layer interaction between two dissimilar surfaces; the electrode and the particles [179, 180].

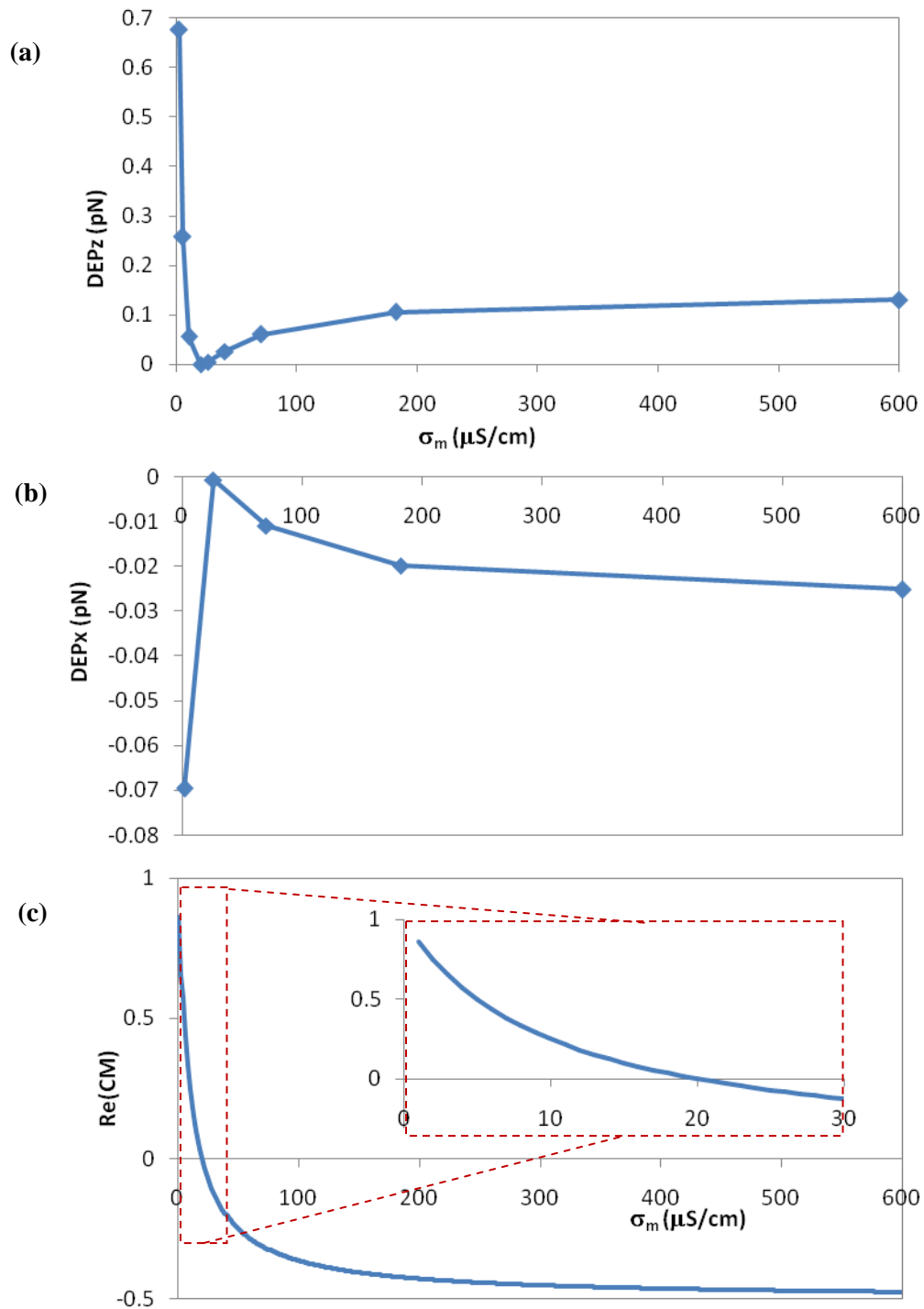


Figure 4-6. Effect of electric conductivity on DEP force (simulation result) acting on a particle under ACEO conditions ($z = 1.2 \mu m$, $x = 0$, $f = 1$ kHz and $V_{pp} = 4$ V). (a) Vertical DEP component, (b) horizontal DEP component on particle 1 due to the presence of neighboring particle (distance between particle centers = $3 \mu m$) and (c) CM factor with varying σ_m .

4.5.2. Particle Behaviors under Electrothermal Flows

Figure 4-7 shows particle behaviors at an AC field of 4 V_{rms} and 200 kHz. ETF is dominant in this condition (ACEO does not exist at such a high frequency). The amplitude of the applied voltage was gradually increased and ETF became noticeable at above 3 V_{rms} when a Peltier cooler was applied. The effect of Peltier cooling of the electrode substrate was clearly observed in the change of fluid and particle velocity. Figure 4-7 is the data obtained using a Peltier cooler. Immediately after applying an electric field, swirling zones above the electrodes edge appeared and most of the particles followed the fluid motion (Figure 4-7a). The direction of rotation was same as that of ACEO flow but the motion was more circular and focused near the electrode edges. In about three seconds after the potential was applied, the particles formed short chains above the electrode edges (Figure 4-7a). The particle chains were perpendicular to the electrode edge when viewed from the top and kept some distance from each other (3~7 μm). These phenomena can be explained by the combination of DEP and ETF forces. At a 200 kHz frequency, particles experienced negative DEP and were repelled from the electrode edges. As they entered the swirling zone of ETF, they experienced circular movement in a plane perpendicular to the electrodes. Particles rotated locally within a certain distance from the electrode edges. In the meantime, particles moved close to each other in the x direction and began to form chains at about 15 μm above the electrodes.

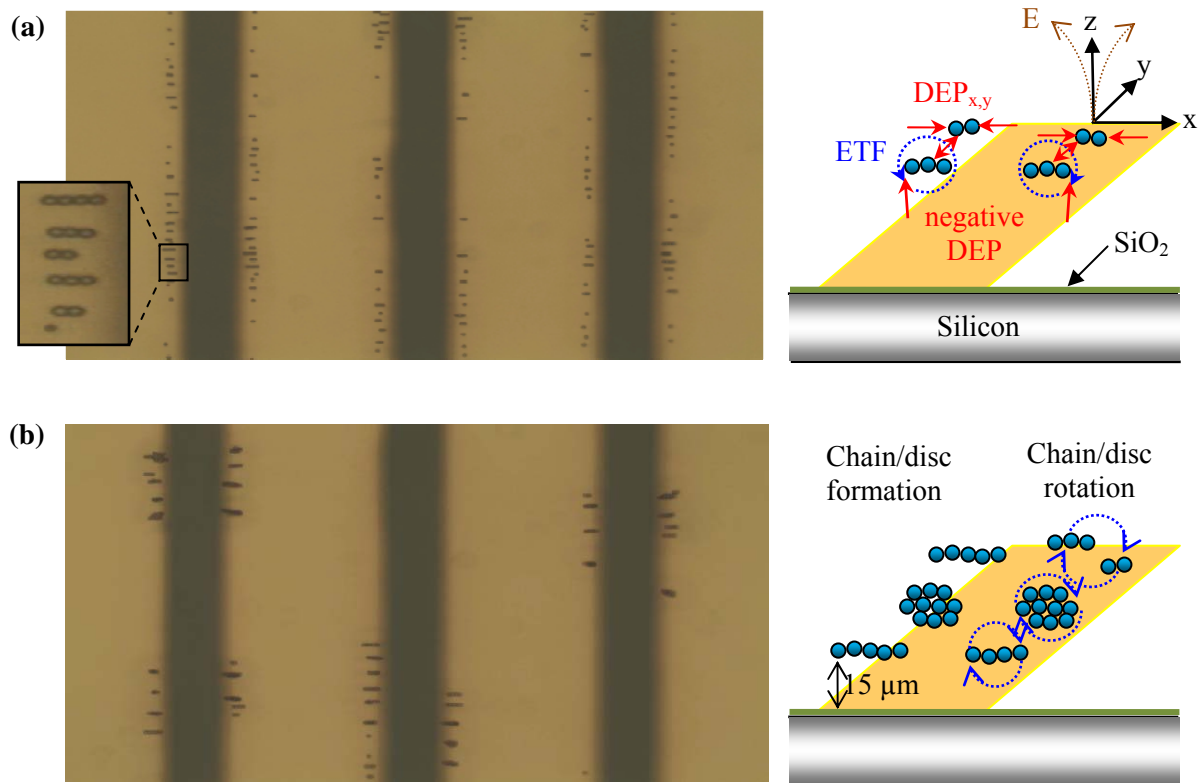


Figure 4-7. Behaviors of polystyrene microbeads under ETF condition (4 V_{rms} and 200 kHz), (a) 3 seconds after an electric field was applied (b) 3 minutes after an electric field was applied.

In order to better understand these phenomena, ETF was solved in a 2-D domain. Figure 4-8 shows the temperature profile contour plot, electric field streamlines and electrothermal flow arrows. Swirling zones were clearly observed and had good agreement with the experimental observation. The center of swirling motion was approximately 27 μm above the electrode ($x = 36$ μm and $z = 27$ μm). The location of particle chains in the experiment was approximately 15 μm above the electrode ($z = 15$ μm), right below the swirling zones. The reason why the particles were located below the swirling center may be due to the effect of gravity. In other words, the particle resting location of $z = 15$ μm seems to be the location where DEP, ETF, and gravity effects were balanced.

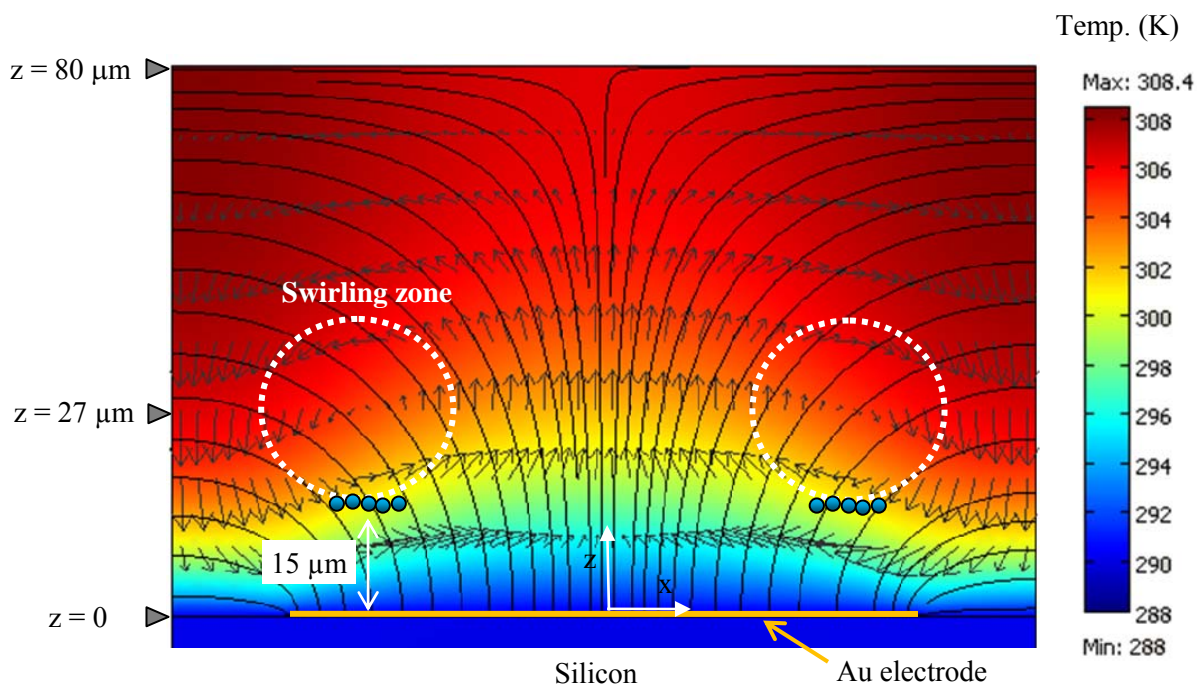


Figure 4-8. Electrothermal flow 2-D simulation result. The contour colors, the streamlines and the arrows represent temperature profile, electric field lines and electrothermal flow velocity, respectively. ($\sigma_m = 1.77$ S/m, $f = 200$ kHz and $V_{rms} = 7$ V)

The particle-particle dielectrophoretic interaction was investigated by placing a subject particle at the swirling center and another particle within a certain distance from the first particle. When the two particles were placed in the electric field direction 45° from the normal direction of the electrode plane, attraction force was experienced by the particles (Figure 4-9a). As the particle distance decreased, the attractive DEP force increased significantly. This result supports the formation of particle chains and their alignment normal to the electrodes. When two particles were positioned in the y direction (perpendicular to the electric field), a repulsive DEP force was generated between them. Figure 4-9b shows how the repulsive DEP force varies with the distance between the two particles in y direction. As two particles get closer, the repulsive force

increases. This result is consistent with the experimental observations that particle chains kept a distance from each other.

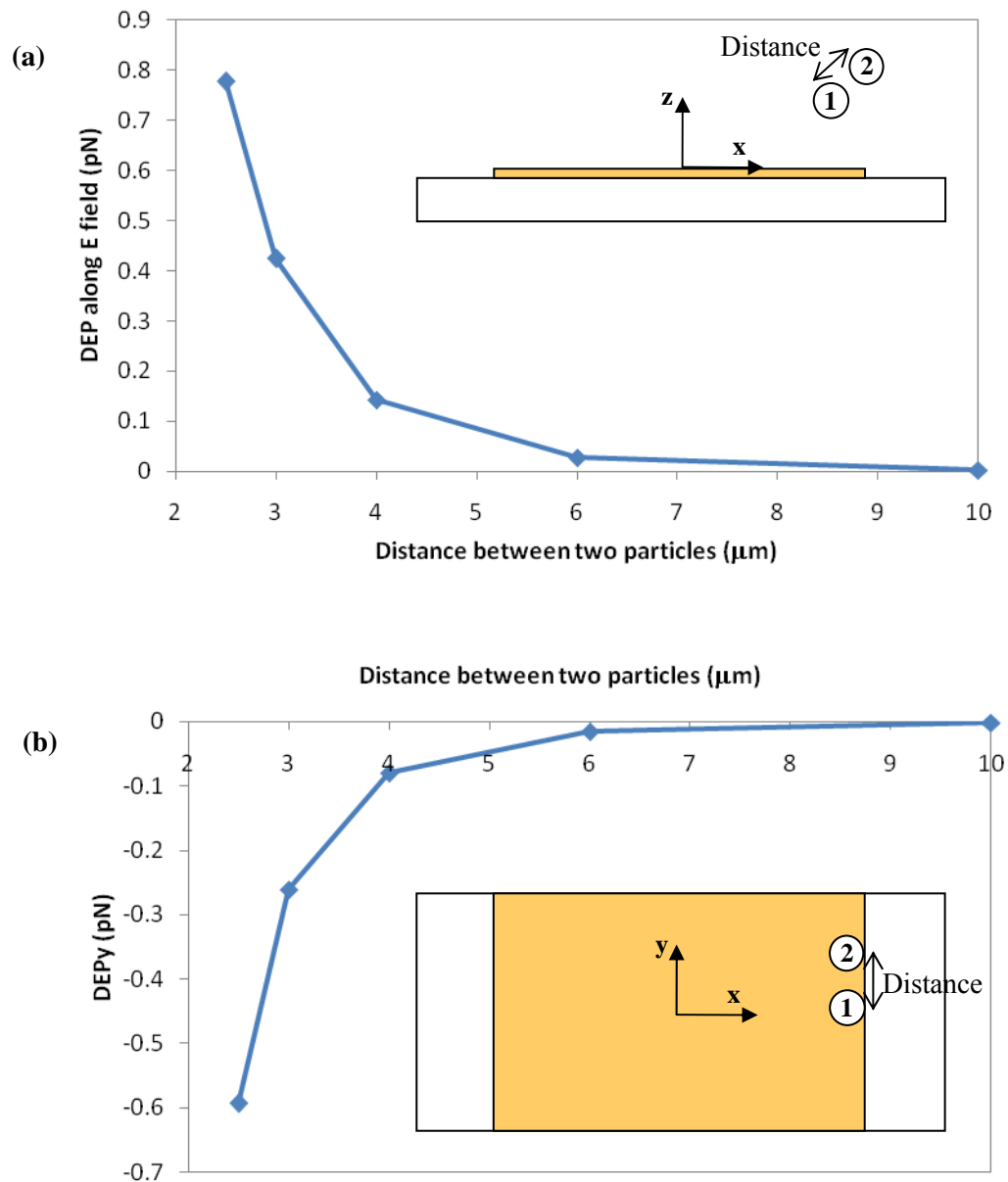


Figure 4-9. Computed DEP force acting on a bead particle under an ETF condition ($\sigma_m = 1.7$ S/m, $f = 200$ kHz and $V_{rms} = 7$ V). The subject particle (particle 1) is located at the swirling center ($x = 36$ μm, $y = 0$ and $z = 27$ μm), the neighboring particle approaches in (a) the parallel and (b) the perpendicular directions to the electric field.

The particle chains became longer with time as they recruited more particles from the surrounding. Moreover, the particle chains formed near the swirling zones continued to rotate. Short chains rotated like a spinning rod while longer chains split into two short chains and switched their locations as shown in the schematic in Figure 4-5b. As time goes on, the chains merged together into larger groups and particle “discs” were formed. It is not clearly understood why the particle chains merged with others forming discs, but it seems that the attractive DEP particle-particle interaction in the electric field direction overcame the repulsive DEP particle-particle interaction in the direction perpendicular to the electric field as the chains became longer.

4.6 . CONCLUSIONS

In this chapter, diverse behaviors of microbead particles subject to AC electroosmosis and electrothermal flow conditions through experimental and numerical studies were investigated. Typical particle behaviors were monitored as the main parameters, such as media conductivity and the frequency of the applied voltage, were varied, and the experimental observations were compared with numerical simulation results. Since the conventional dipole method for DEP calculation does not consider the effect of neighboring particles and other solid surfaces, Maxwell stress tensor method was used in the current numerical study to understand the dielectrophoretic particle-particle interactions. Distinct particle behaviors under ACEO and ETF conditions and diverse particle-particle interactions, such as particle clustering, particles keeping a certain distance from each other, chain formation, and disc formation, have been analyzed and explained based on the numerical simulation results. For instance, ACEO flow conditions at low media conductivity ($\sigma \sim 2 \mu\text{S/cm}$) resulted in repulsive DEP among particles collected in the middle of electrodes while a higher conductivity ($\sigma \sim 20 \mu\text{S/cm}$) caused particle aggregation. The numerical simulation results showed that the repulsive DEP particle-particle interaction is

significant at 2 $\mu\text{S}/\text{cm}$ but diminishes at 20 $\mu\text{S}/\text{cm}$. ETF conditions induced particle chain and disc formation 15 μm above the electrode edge, and they remained in rotational motion. The calculation of the attractive and repulsive DEP particle-particle interaction was performed for this case, and the unique particle behaviors were explained. The improved understanding of particle behaviors in AC electrohydrodynamic flows presented here will enable researchers to design better particle manipulation strategies for lab-on-a-chip applications.

CHAPTER 5. 3-D SIMULATION OF ELECTROSMOTIC SAMPLE INJECTION AND MIGRAION IN MICROCHANNELS : EFFECTS OF NON-RECTANGULAR CROSS SECTION

5.1 . INTRODUCTION

Electroosmosis is the motion of liquid induced by an applied electric field along a capillary tube or microchannel. This bulk fluid flow is due to the migration of ions collected near the channel surface in the form of an electrical double layer (EDL) [181]. The EDL thickness in typical operating liquid media ranges only up to a few nanometers [30, 182, 183] from the channel wall, which is much smaller than the cross-sectional dimensions of typical microchannels. The thinness of electric double layer makes the induced bulk flow behave like a wall-driven flow that has a uniform velocity profile[30]. The uniform velocity profile makes the electroosmotic flow very attractive in separation science because dynamic dispersion and band broadening effects can be minimized with such a velocity profile, compared to the parabolic velocity profile of pressure-driven flows.

The thin velocity boundary layer and the consequent uniform velocity profile of electroosmotic flow has also served as the basis for many previous studies, which employed a 2-D [30, 59, 61, 68, 69] or even an 1-D [70-72] approximation for electroosmosis numerical simulations. 1-D approximation has been usually considered for the simulation of traditional capillary electrophoresis systems while 2-D approximation has been used for the simulation of pinched injection-based microchip capillary electrophoresis systems that have multiple branch channels. These lower dimensional (1-D and 2-D) approximations are valid if there is no

variation in any critical parameters in the eliminated dimensions. However, the approximations lose their validity when 3-D features are present in the device resulting in non-trivial variation of critical parameters. In Chapters 3 and 4, I present numerical simulations of the electroosmotic sample injection and migration for three cases where the consideration of 3-D characteristics is crucial for an accurate prediction of sample distribution as illustrated in Figure 5-1. Case 1 is a non-rectangular microchannel cross section shown in Figure 5-1a. Case 2 is different zeta potentials on channel surfaces shown in Figure 5-1(b). Case 3 is the development of internal pressure gradients due to the variation of surface and solution properties along the channel length shown in Figure 5-1c. Chapter 3 focuses on the first case – the effect of a non-rectangular cross section in 3-D channel geometry – while the other two cases are investigated in Chapter 4.

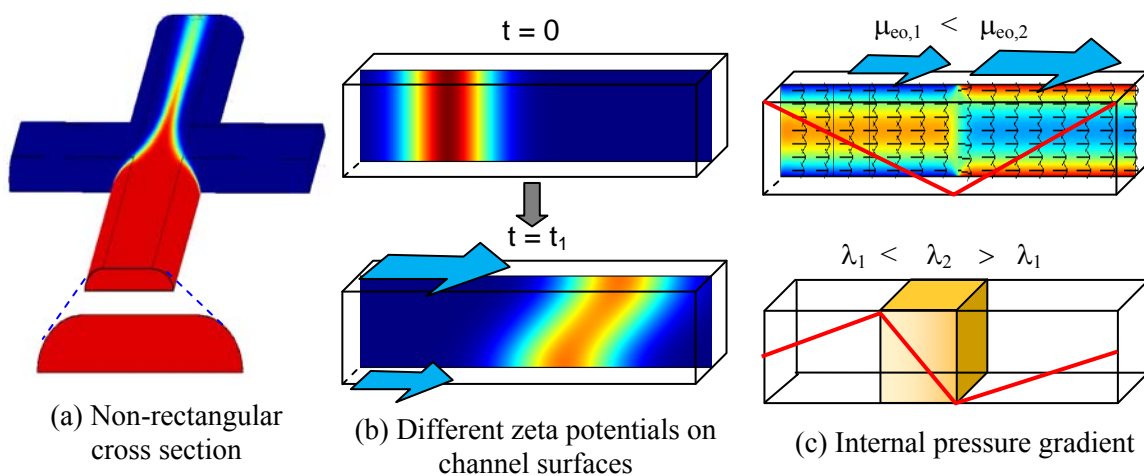


Figure 5-1. Three cases where the 3-D characteristics of electroosmotic flow become significant. (a) A pinched injection system with non-rectangular cross section, (b) a straight channel with different zeta potentials on channel surfaces, and (c) an internal pressure gradient developed by zeta potential or chemical concentration variation. Cases (b) and (c) are considered in Chapter 6.

More specifically, Chapter 3 presents how the 3-D geometry of a channel affects the performance of a pinched injection and species migration. 3-D simulation results are compared with 2-D simulation results to elucidate the significance of considering 3-D characteristics. Most previous simulation studies [30, 59, 61, 68, 69] on pinched injection systems were based on 2-D simulation. Ermakov et al. [30, 59] simulated the sample concentration distribution during focusing and dispensing stages of a pinched injection by applying Helmholtz-Smoluchowski slip velocity condition on a 2-D computational domain to find the optimal operation conditions. Fu et al. [61, 69] used 2-D simulation to compare with their experiments on the performance of capillary electrophoresis microchips. Patankar and Hu [58] used 3-D rectangular channel geometry. However, the emphasis of the study was for investigating the effect of external pressure gradients on the sample focusing behavior. No previous paper has investigated the 3-D characteristics of the electroosmotic pinched injection and quantitatively discussed the significance of 3-D simulation.

5.2 . PROBLEMS CONSIDERED

5.2.1. Effects of Non-rectangular Cross Section

(1) *Sample Loading*

The 3-D characteristics of sample loading in a pinched injection system are investigated by using a non-rectangular, isotropically-etched microchannel as shown in Figure 5-2a. This model geometry represents glass microchannels commonly made by wet etching techniques. The channel is 50 μm wide at the top (W_t), 90 μm wide at the bottom (W_b), and 20 μm high (H). In order to save computational time and memory, only the region around the intersection, instead of the entire microchannel system, is used as a computational domain ($L_s = L_w = L_b = 300 \mu\text{m}$ and L_c

= 1000 μm). Both narrow and wide sample plugs can be produced by controlling the three inlet flows via applied electric fields. The electric field conditions used for sample loading methods are specified in Table 3-1. The subscripts, s, w, b, and c, denote the sample, waste, buffer and collect channels respectively. The cross-sectional distribution of sample species at the intersection was carefully investigated using 3-D simulations. Particularly, the vertical non-uniformity induced by the non-rectangular 3-D channel geometry was investigated.

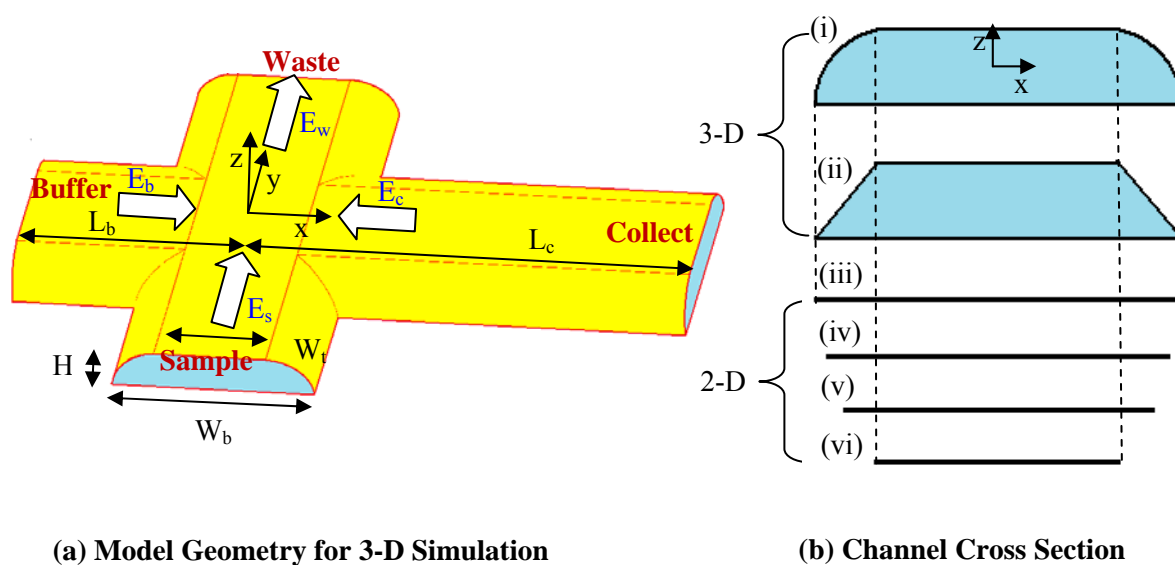


Figure 5-2. A schematic geometry of the 3-D computational domain. (a) Definition of dimensional and operational parameters, and (b) 6 different channel cross sections investigated for the sample dispensing study; i) isotropically-etched cross section (5-D), ii) trapezoidal cross section (5-D), iii-vi) 2-D geometries with various widths (iii: 90 μm (W_b), iv: 81.4 μm (A/H where A is the cross-sectional area of the isotropically etched channel), v: 70 μm ($(W_b + W_t)/2$), vi: 50 μm (W_t)).

Table 3-1. Electric field values at the inlets and outlets for loading and dispensing stages (Loading *Method 1*: narrow loading, *Method 2*: wide loading).

	Loading		Dispensing
	<i>Method 1</i>	<i>Method 2</i>	
E_s	3 kV/m	30 kV/m	-10 kV/m
E_b	10 kV/m	10 kV/m	30 kV/m
E_c	10 kV/m	10 kV/m	-10 kV/m
E_w	-23 kV/m	-50 kV/m	-10 kV/m

(2) *Sample Dispensing*

The 3-D characteristics of sample dispensing of pinched injection were investigated for various cross-sectional geometries as shown in Figure 5-2b. 3-D geometries include isotropically-etched cross section and trapezoidal cross section. For 2-D simulation, several different channel widths were selected for comparison. Note that the channel width used in previous 2-D simulation studies were the top width (W_t) or bottom width (W_b) or average width of the channel ($(W_t + W_b)/2$). The author considered one more channel width that is calculated from the equivalent cross-sectional area and height of the isotropically-etched cross section, i.e. $W = (\pi H^2/2 + W_t H)/H$. The narrow sample loading method (Table 3-1) was selected as the initial condition. The dispensing electric fields were selected to have maximum injection efficiency based on the Ermakov's report [59].

(3) Sample Migration

The effect of 3-D non-rectangular geometry on sample dispersion during electroosmotic migration was also investigated. Since the electroosmotic flow and electrophoretic sample motion are both uniform, they do not affect the dispersion of a sample plug if there is no pressure gradient in the channel. In other words, the dispersion of a sample plug during electroosmotic migration in a straight channel is determined only by the molecular diffusion. If the sample plug has no variation in lateral direction, the problem further simplifies to a trivial 1-D diffusion case and there would be no difference between 3-D and lower dimensional simulations. However, in reality, the sample plug is not laterally uniform but close to a triangular shape after pinched injection as shown in Figure 5-3a. 2-D simulation would be sufficient if the channel is rectangular and the concentration profile is constant in z-direction. But for channels with non-rectangular geometry the lateral dispersion of sample plug will be further perturbed due to the concentration gradient in z-direction developed during sample migration. In order to study this effect, the author selected a simple triangular sample plug as initial condition as shown in Figure 5-3b and performed 2-D and 3-D simulations. The model geometries selected for this study are a 2-D channel with a width of 90 μm and a 3-D isotropically-etched channel ($W_b = 90 \mu\text{m}$ and $H = 20 \mu\text{m}$). The effect of non-rectangular channel geometry on the band broadening was investigated using 3-D simulations.

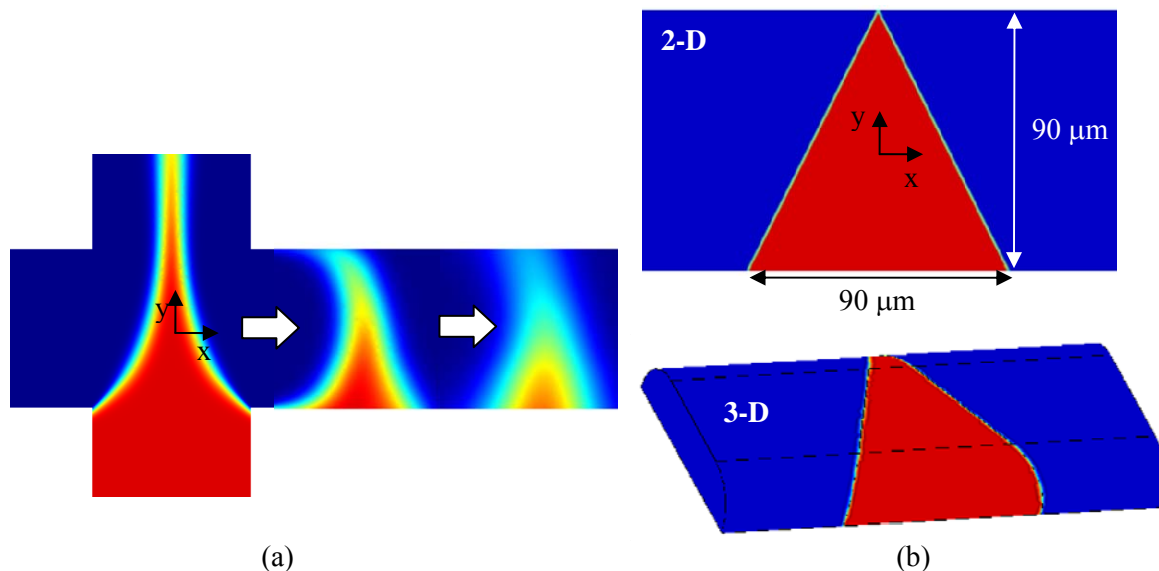


Figure 5-3. (a) Schematic of pinched injection and migration of a sample plug and (b) the initial sample plug used in the electroosmotic migration study.

5.3 . GOVERNING EQUATIONS

The general governing equation for the dynamics of electroosmotic flow is derived by adding the electric body force to the incompressible Navier-Stokes equation and the momentum equation is solved together with the electric potential developed from the ionic distribution in an electric double layer [58]. Since the thin Debye length approximation is employed in this study, the flow problem can be further simplified to a slip velocity problem with the Helmholtz-Smoluchowski electroosmotic velocity [30, 181]. This approximation is well accepted and saves significant computational time and memory by avoiding very fine meshes near the wall for capturing the velocity profile within the electric double layer. Detailed validation and explanation of the Helmholtz-Smoluchowski electroosmotic slip velocity is described in references [30, 181]. The governing equations for the current problem are as follows:

$$\text{Flow continuity equation: } \nabla \cdot \vec{V} = 0 \quad (5-1)$$

$$\text{Flow momentum equation: } \rho \frac{D\vec{V}}{Dt} = -\nabla p + \eta \nabla^2 \vec{V} \quad (5-2)$$

$$\text{Helmholtz-Smoluchowski slip velocity: } \vec{V}_{eo} = \mu_{eo} \vec{E} \quad (5-3)$$

$$\text{Electric potential governing equation: } \nabla^2 \Phi = 0 \quad (5-4)$$

$$\text{Chemical species conservation: } \frac{\partial C}{\partial t} + \nabla \cdot ((\vec{V} + \mu_{ep} \vec{E})C) = D \nabla^2 C \quad (5-5)$$

where \vec{V} is flow velocity, ρ is the density, η is the dynamic viscosity, \vec{E} is the applied electric field, C is sample species concentration, D is the diffusivity of sample species, and μ_{eo} and μ_{ep} are the electroosmotic and electrophoretic mobilities. The complete form of electric potential equation contains the effect of conductivity variation and ion densities. A simpler form, Eq. (5-4), was derived by assuming a constant conductivity and negligible effect of ion distribution on the activation electric field [58]. The governing equation of sample concentration, Eq. (5-5), is a linear equation in terms of the sample concentration, and the sample concentration does not influence other parameters such as \vec{V} or Φ in this simulation. All sample concentration results here are normalized by the sample concentration delivered from the sample reservoir (C_0), denoted by C^* .

5.4 . NUMERICAL METHODS: DC ELECTROKINETICS

COMSOL Multiphysics version 3.5a was used for the simulations in this study. The general parameter values for the current simulations are the electroosmotic mobility (μ_{eo}) = 4×10^{-8} m²/Vs, the electrophoretic mobility of sample (μ_{ep}) = -1×10^{-8} m²/Vs, the diffusivity of sample (D)

$= 1 \times 10^{-10} \text{ m}^2/\text{s}$, the solution density (ρ) = 1000 kg/m^3 , the dynamic viscosity of solution (η) = 0.001 kg/m s . The selected electroosmotic mobility corresponds to a ζ -potential of about 60 mV, which is a typical value for glass or other polymer substrates in standard conditions [172]. This value was also used in previous papers [30, 184]. The selected diffusivity and electrophoretic mobility values match typical values for small proteins or large fluorescent dyes [185, 186]. The COMSOL software has formulated modules for various physics equations in the name of application modes. The author selected three application modes from the COMSOL software, *Conductive Media DC* (for electric potential, Eq. (5-4)), *Incompressible Navier-Stokes* (for fluid flow, Eqs. (5-1) and (5-2)), and *Electrokinetic Flow* (for species concentration, Eq.(5-5)), for the simulations in this study. At the walls, insulation boundary conditions ($\partial\Phi/\partial n = 0$, $\partial C/\partial n = 0$) were imposed for the electric potential and chemical species simulations while Helmholtz-Smoluchowski slip velocity (Eq. (5-3)) was imposed for the flow simulation as the wall boundary condition. The zero pressure boundary condition was imposed at the inlets and outlets, based on the fact that there is no pressure difference between each individual inlet and outlet reservoir and the assumption that pressure gradient along each channel is negligible. This zero pressure boundary condition (also known as periodic boundary condition) has been adopted in some previous reports [58, 184, 187] while others [188, 189] used the zero pressure gradient boundary condition. The author found that there is no more than 0.2 % difference in the velocity field solutions obtained using the two different pressure boundary conditions. The outlet condition for the species conservation (Electrokinetic Flow) assumes that the mass flow through the boundary is dominated by convection. This condition has often been adopted in previous reports [189, 190].

For the simulation of a pinched injection, the loading stage solution is calculated first by using steady-state computation for all three computation modes in the sequence of *Conductive Media DC*, *Incompressible Navier-Stokes* and *Electrokinetic Flow* modes. The solution of sample

concentration at the loading stage is then used as an initial condition for the dispensing stage sample concentration, which is solved with a time-dependent solver. Even for the dispensing stage, the *Conductive Media DC* and *Incompressible Navier-Stokes* equations are solved in steady-state computation, while the *Electrokinetic Flow* equation is solved with time-dependent calculation (0 ~ 3 sec).

The author has observed significant numerical errors when sharp corners exist in the microchannel geometry even with extremely fine mesh around the corners (The numerical inaccuracy will be discussed in Results and Discussion section). A 1- μm radius fillet was applied on the corners for 2-D cases for an accurate simulation. The small fillets applied to the corners did not significantly change the performance of the device, and they relieved the numerical inaccuracy related with the sharp corners.

COMSOL Multiphysics is based on the finite element method. The element shapes were triangular for 2-D geometries and tetrahedral for 3-D geometries considered. The element type used was the quadratic Lagrange element. The maximum element length was set to 4 μm . The grid independence was confirmed by comparing the solution with the solution of a finer element case (maximum element size = 1 μm); the peak value of concentration from those two solutions for a rectangular cross-section channel had a difference less than 0.1%. For the temporal differencing scheme, the backward differentiation (implicit) formula was used. The convergence criterion is controlled in COMSOL by using relative and absolute tolerances; solution is accepted when

$$\left(\frac{1}{N} \sum_i \left(\frac{E_i}{A + R|U_i|} \right)^2 \right)^{1/2} < 1 \quad (5-6)$$

where N = the number of degrees of freedom, E_i = the error of degree of freedom i , A = absolute tolerance, R = relative tolerance and U_i = the solution of degree of freedom i . The author used an

absolute tolerance value 10^{-6} . No artificial diffusion was employed because instability (spurious oscillation) issue of convection-diffusion equation was not observed with a smoothly varying (Gaussian distribution) initial concentration distribution.

5.5. MODEL VALIDATION

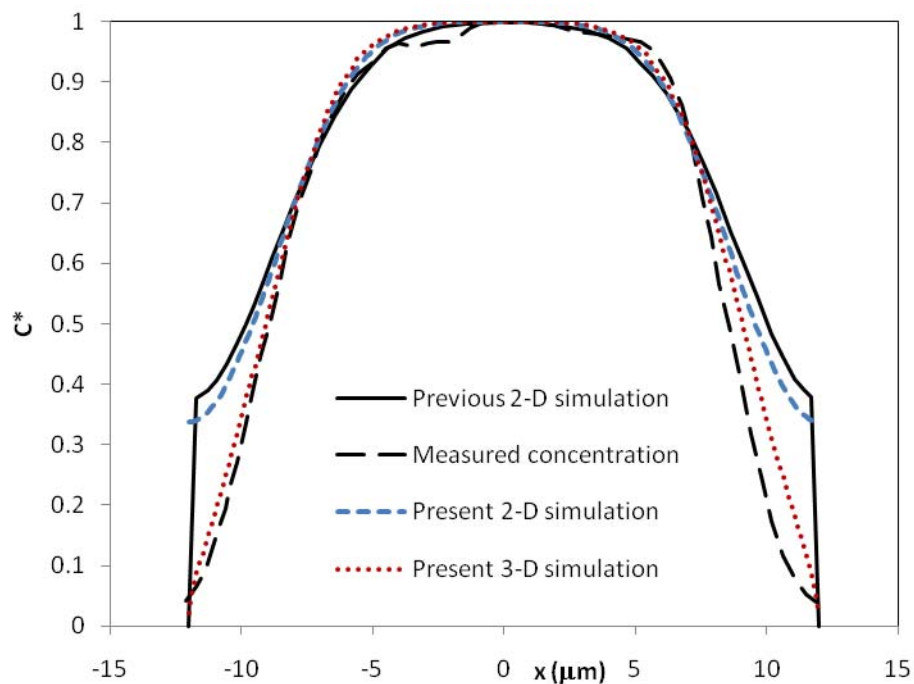


Figure 5-4. Normalized sample concentration profile at 3 μm upstream from the focusing chamber for the present 2-D and 3-D simulations compared with previous 2-D numerical [30] and experimental [143] data.

The current simulation method was first validated by comparing the predictions with previous numerical [30] and experimental [143] data. The channel geometry selected for the present 3-D simulation is an isotropically-etched microchannel with a bottom width of 24 μm and a height of 6.4 μm as described in [143]. The geometry for the 2-D simulation was the same as

the previous simulation described in [30] (channel width = 24 μm) except for having the fillet of radius 0.1 μm at the intersection corners. Figure 5-4 compares the normalized sample concentration profiles at 3 μm upstream ($y = -15 \mu\text{m}$) from the intersection obtained by 2-D and 3-D simulations with experimental data that is an accumulated sample concentration from the top view along the x-axis. The graph shows that the 3-D simulation result has a better agreement with the experimental data compared to the previous and current 2-D simulation results. This result supports that the current 3-D simulation model is valid and accurate.

5.6 . EFFECTS OF NON-RECTANGULAR CROSS SECTION

5.6.1. 3-D Characteristics in Sample Loading

Figures 5-5 and 5-6 show the top and cross-sectional views of the sample concentration profile during sample loading in pinched injection in an isotropically-etched microchannel. The top view represents the sample concentration distribution on the top boundary surface of the 3-D channel geometry, while the cross-sectional views (x-z plane) show the vertical (in z direction) variation in the concentration profile. The narrow loading method (Table 5-1) resulted in a V-shaped concentration profile in the z direction while the broad loading method produced a Δ -shaped concentration profile. In the narrow sample loading, the flows from the buffer and collect channels are higher than the flow from the sample channel so that the sample band becomes narrow and focused at the intersection. This flow is not uniform in the vertical coordinate because of the curved top surface near the corners at the intersection. The lower part of the sample plug ($z < 0$) encounters the strong narrowing flows from the buffer and collect channels first before the upper part does at the intersection because of the isotropically-etched geometry. Therefore the lower part is compressed more than the upper part resulting in a V-shape sample

band. In the case of wide sample loading, the opposite motion occurs. The flows from the buffer and collect channels are lower than that of the sample channel so the sample band becomes wide at the intersection. Now the opposite expanding action is strong in the lower part of the sample plug ($z < 0$), resulting in a Λ -shape sample plug.

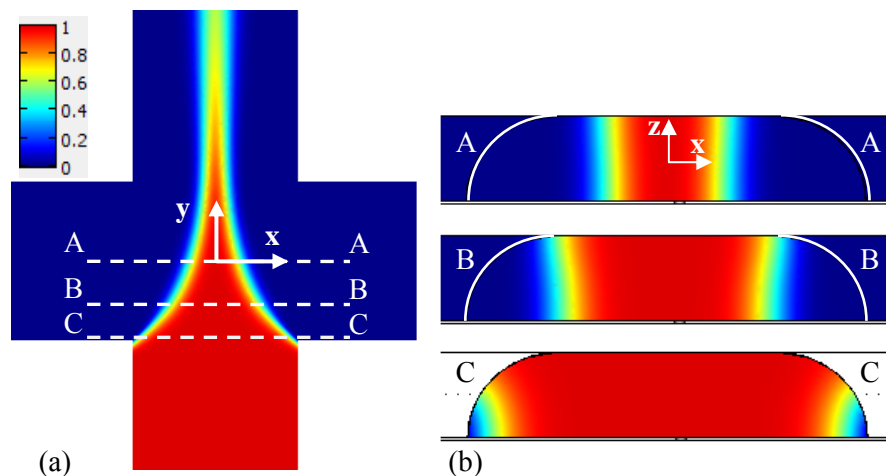


Figure 5-5. Normalized sample concentration distribution during a narrow sample loading in an isotropically-etched microchannel. (a) Top view and (b) cross-sectional views (A-A: $y = 0$, B-B: $y = -25 \mu\text{m}$, and C-C: $y = -45 \mu\text{m}$)

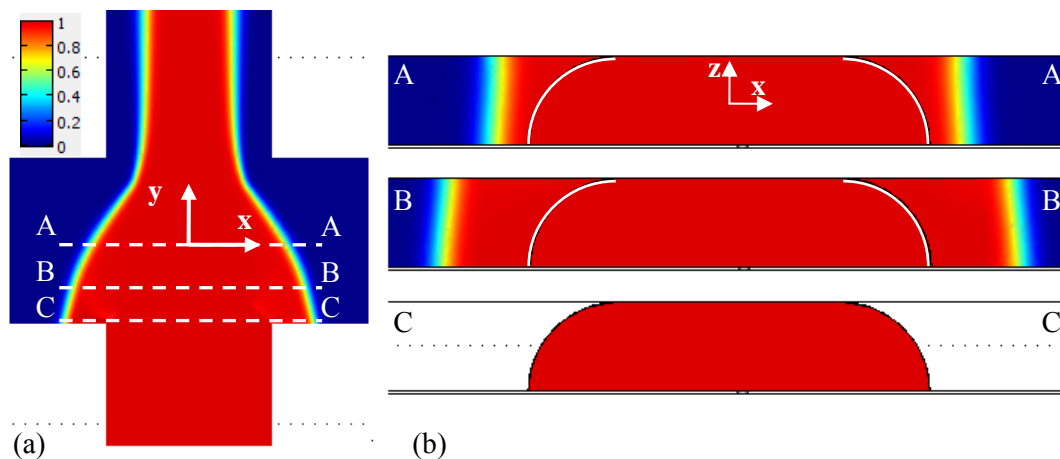


Figure 5-6. Normalized sample concentration distribution during a wide sample loading in an isotropically-etched microchannel. (a) Top view and (b) cross-sectional views (A-A: $y = 0$, B-B: $y = -25 \mu\text{m}$, and C-C: $y = -45 \mu\text{m}$)

Figure 5-7 shows the distribution of the vertical (z -directional) component of flow velocity, w , in a 3-D isotropically-etched channel geometry. In a rectangular microchannel, the vertical velocity component is always zero. However, in a non-rectangular microchannel, the vertical velocity component arises due to the 3-D characteristic of the geometry as shown in Figure 5-7. The vertical velocity component is strong near the corners of channel intersection, where the flow is guided up and down by the curved top surface. The three solid curves (L_1 , L_2 , and L_3) in Figure 5-7 represent flow streamlines passing through the corners of the intersection. The streamline falls down when it passes negative w region, and it rises when it passes positive w region. The maximum elevation along L_2 was $3.4 \mu\text{m}$ which is 17 % of the channel height.

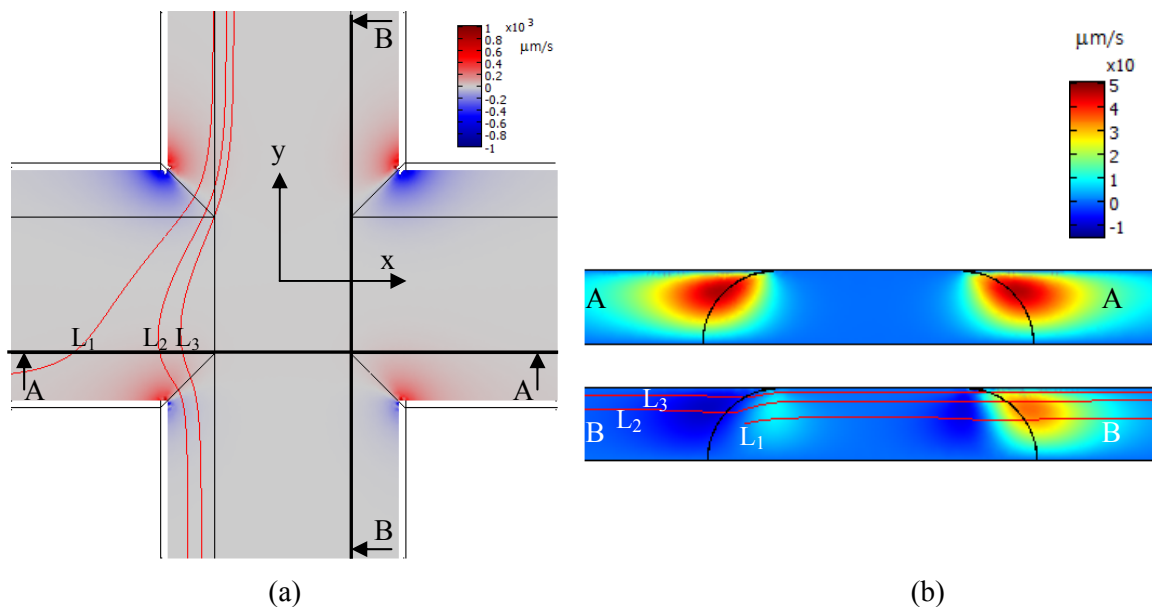


Figure 5-7. The variation of vertical velocity component (w) in an isotropically-etched channel for a wide sample loading case. (a) Vertical velocity distribution at the $z = 0$ plane and (b) cross-sectional views (along A-A: $x = 25 \mu\text{m}$ and along B-B: $y = -25 \mu\text{m}$). Solid lines are streamlines passing through the corners of the intersection at different locations: $(-200 \mu\text{m}, -35 \mu\text{m}, 0 \mu\text{m})$ for L_1 , $(-35 \mu\text{m}, -200 \mu\text{m}, -4 \mu\text{m})$ for L_2 and $(-30 \mu\text{m}, -200 \mu\text{m}, 8 \mu\text{m})$ for L_3 .

5.6.2. 3-D Characteristics in Sample Dispensing

Figure 5-8 shows the variation of sample concentration during the dispensing stage of a pinched injection process (the initial sample plug was loaded using loading method 1 in 3- 1). 3-D simulation results for an isotropically-etched channel is compared with 2-D simulation ($W = 90 \mu\text{m}$). For the 3-D case, the sample concentration is accumulated across the z -direction and normalized by the initial value as follows.

$$C_{accum}^*(x, y) = \frac{\int C(x, y, z) dz}{C_0 H} \quad (5-7)$$

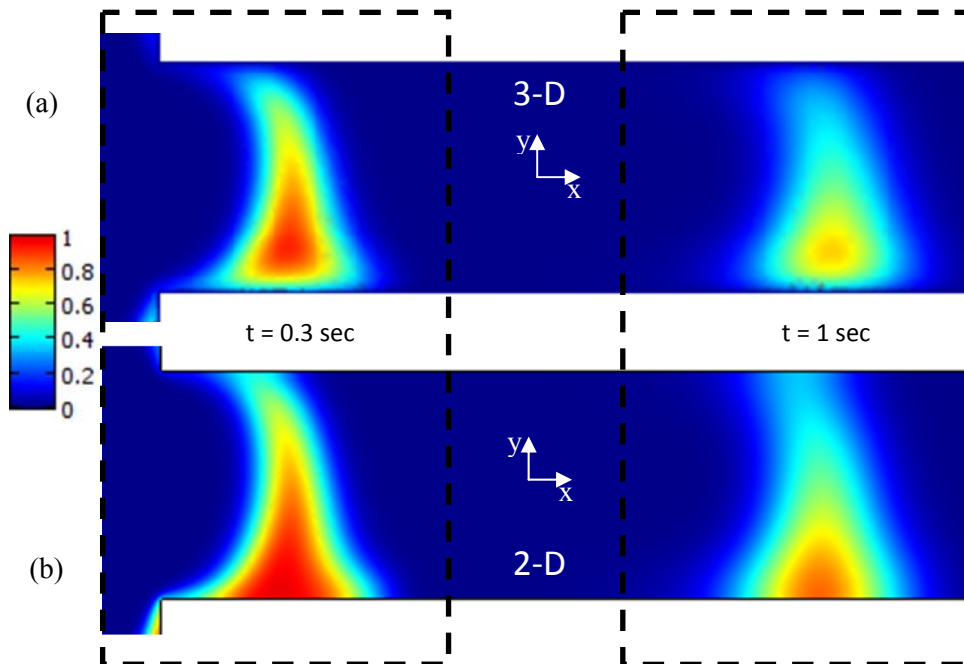


Figure 5-8. Sample dispersion during dispensing of a pinched injection in the collect channel (see Figure 2) with loading method 1: (a) 3-D isotropically-etched channel case and (b) 2-D channel case (width = $90\mu\text{m}$). The plots in the dashed box on the left side are for $t=0.3$ sec and the ones on the right are for $t=1$ sec. For the 3-D case, sample concentration is accumulated from the top view and normalized by the initial value using Eq. (5-7).

The clear difference between 3-D and 2-D sample dispersion is mainly attributed to the non-uniform channel height in the isotropically-etched channel.

For a quantitative and proper comparison between 2-D and 3-D simulation results, the averaged sample concentration data as a function of x (the axis along the migration channel) were obtained by the following equations:

$$C_{average}^*(x) = \frac{\iiint C(x, y, z) dy dz}{C_0 A} \text{ for 3-D and } C_{average}^*(x) = \frac{\int C(x, y) dy}{C_0 W} \text{ for 2-D (5-8)}$$

where A is the cross-sectional area of 3-D channel and W is the cross width of 2-D channel. This averaged concentration along x -axis corresponds to the signal from a detector commonly used in capillary electrophoresis, such as laser induced fluorescence (LIF).

Figure 5-9 shows the averaged concentration distribution at different traveling times ($t = 0, 1, \text{ and } 2 \text{ sec}$) and the variation of peak value with traveling distance (x) for 2-D and 3-D simulations. Since the concentration data were averaged across the transverse cross section (y - z plane), the band width (σ) of the sample concentration profile did not have significant variation among the 3-D and 2-D simulation data at different times. However, there was a quite significant difference in the peak value of the concentration profile and its variation with traveling distance. The 3-D simulation data for the isotropically-etched cross section lies between two cases of 2-D simulation data ($W = 90 \mu\text{m}$ and $W = 70 \mu\text{m}$) while the 3-D simulation data for a trapezoidal cross section lies between the $W = 90 \mu\text{m}$ and $W = 50 \mu\text{m}$ cases. The percent differences of 2-D peak concentrations for the cases of $W = 90 \mu\text{m}$, $81.4 \mu\text{m}$, $70 \mu\text{m}$ and $50 \mu\text{m}$ from the 3-D simulation value (isotropically-etched cross section) at $t = 2 \text{ sec}$ are 5.86 %, -2.28 %, -12.93 % and -34.99 %, respectively. The 3-D simulation data for the isotropically etched cross section and

the trapezoidal cross section were close to the 2-D simulation data of $W = 81.4 \mu\text{m}$ (2.28 % difference) and $W = 70 \mu\text{m}$ (2.66 % difference), respectively. This observation shows that selection of channel width is very important in the simplified 2-D simulation approach. The channel width equivalent to the width of rectangular cross section having the same height and cross sectional area as the 3-D cross section produces more accurate average concentration distributions.

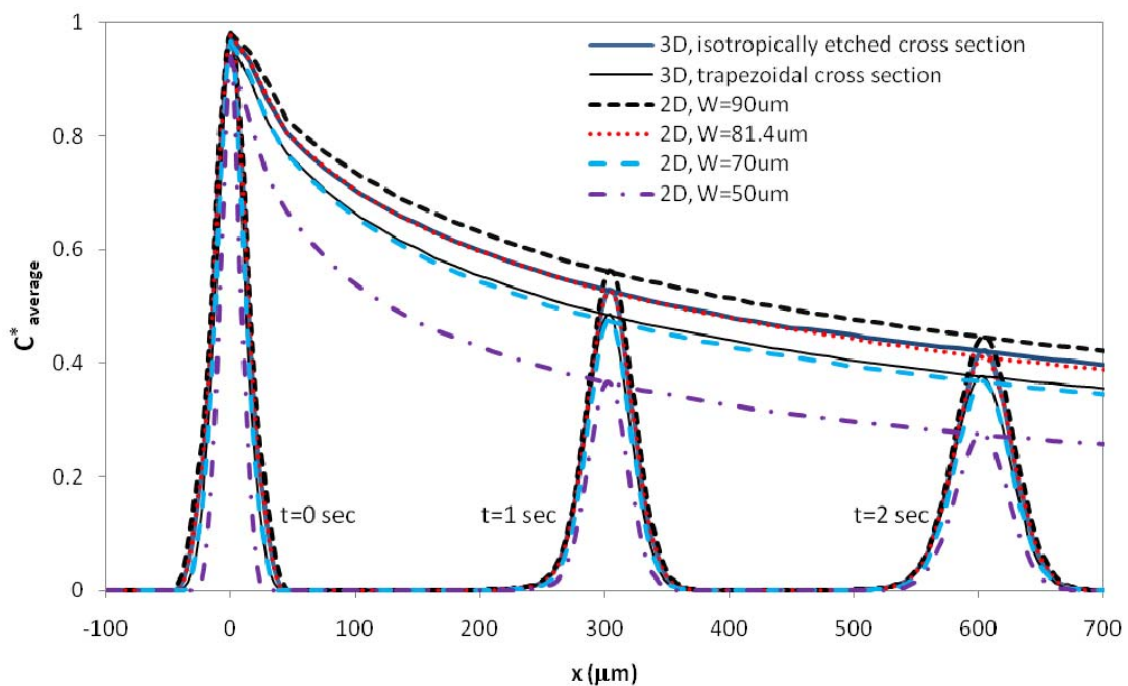


Figure 5-9. The averaged sample concentration distribution at different traveling times ($t = 0, 1,$ and 2 sec) and the variation of peak value with traveling distance (x) calculated from 3-D and 2-D simulation data. A narrow sample loading was used. Sample concentration was normalized by the initial sample concentration value.

A normalized injected sample amount can be represented by the area under the averaged concentration curve in Figure 5-9. Eq. (5-9) shows how the normalized injected sample amount

is calculated for 2-D and 3-D simulation data. Since the injected sample amount was normalized by the cross sectional area (for 3-D) or width (for 2-D), this parameter has a unit of the length, instead of the volume. This definition is used for a proper comparison between 2-D and 3-D simulation data.

$$\begin{aligned}
 \text{Normalized injected sample amount} &= \int C_{average}^*(x)dx = \frac{\iiint C(x, y, z)dydzdx}{C_0 A} && \text{for 3-D and} \\
 &= \frac{\text{Injected sample volume}}{A} \\
 \int C_{average}^*(x)dx &= \frac{\iint C(x, y)dydx}{C_0 W} = \frac{\text{Injected sample area}}{W} && \text{for 2-D} \quad (5-9)
 \end{aligned}$$

Figure 5-10 shows that the injected sample amount is also dependent on the cross sectional shape as well. The sample amount present in the migration channel (a virtual straight channel from the buffer end to the collect end, shown in Figure 5-2) varies initially (up to 0.5 sec) after the injection starts and reaches a constant value, indicating that the sample injection is completed at around 0.5 sec.

The normalized injected sample amounts in 3-D simulation for the cases of the isotropically-etched cross section and the trapezoidal cross section were 24.2 μm and 21.7 μm , respectively. The values in 2-D simulation for the cases of $W = 90 \mu\text{m}$, 81.4 μm , 70 μm and 50 μm were 26.6 μm , 24.1 μm , 20.7 μm , and 14.7 μm , respectively. Considering that there is no significant difference in the sample band width between 2-D and 3-D simulation data, the difference in peak values shown in Figure 5-9 can be attributed to the different injected sample amount between 2-D and 3-D cases. Again, the injected sample amount for 3-D geometry with isotropically-etched cross section is similar to the 2-D case with $W = 81.4 \mu\text{m}$. The percent

differences of 2-D simulation injected amounts for the cases of $W = 90 \mu\text{m}$, $81.4 \mu\text{m}$, $70 \mu\text{m}$ and $50 \mu\text{m}$ from the 3-D value are 9.77 %, -0.78 %, -14.77 % and -39.27 %, respectively.

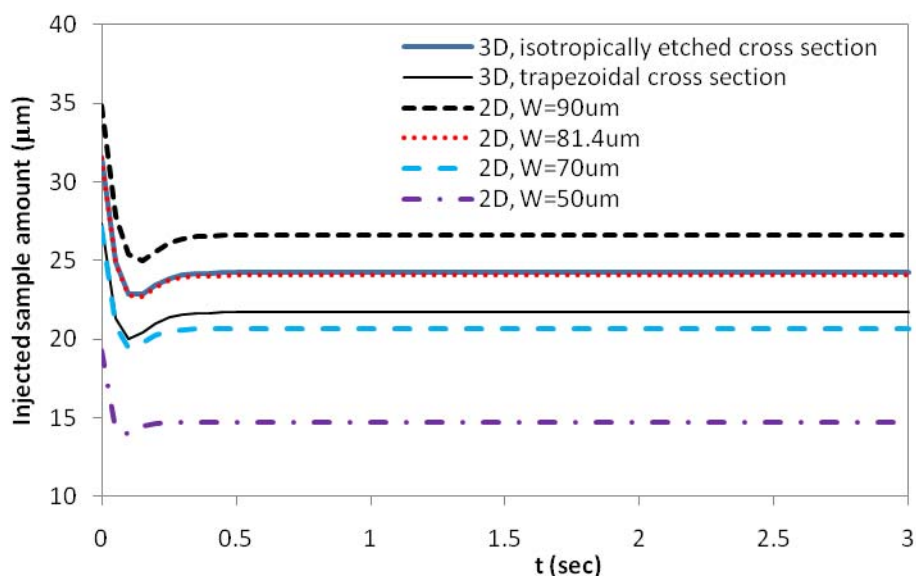


Figure 5-10. Injected sample amount variation with time for six different geometry cases. Loading method 1 was used.

The author has also calculated the injection characteristic of a pinched injection system [59], C_{peak}/σ where C_{peak} is the peak value of a sample concentration distribution and σ is

the spatial standard deviation along the x coordinate defined by $\sigma = \sqrt{\frac{\int C(x)(x-X)^2 dx}{\int C(x)dx}}$ and

$X = \frac{\int C(x)x dx}{\int C(x)dx}$. Figure 5-11 shows C_{peak}/σ with time for the pinched injection systems with

loading method 1. Considering that one of the biggest advantages in the microchip capillary electrophoresis is a fast analysis speed up to a few seconds per assay, the range of traveling time

(~3 sec) in this discussion may cover an entire assay time with a high electric field. The results also show that injection efficiency is highly affected by the cross-sectional shape, and the 3-D results are similar to that of the 2-D case with the width of rectangular cross section with the same cross sectional area. Up to 40% differences were observed between 2-D and 3-D simulation results but 2-D simulation with the channel width equivalent to the width of rectangular cross section having the same height and cross sectional area as the 3-D cross section showed only 2% difference from 3-D data.

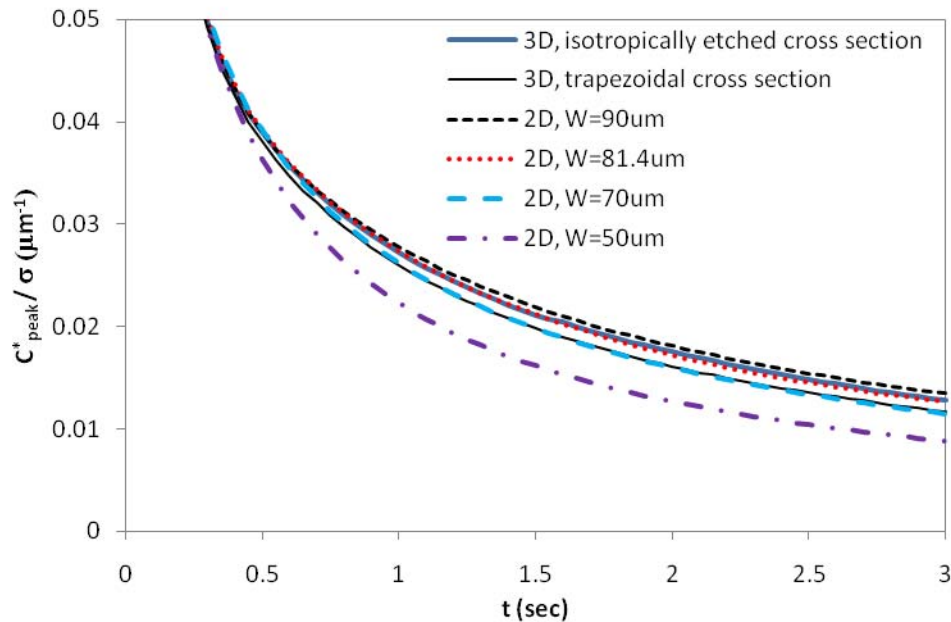


Figure 5-11. Variation of injection efficiency, C_{peak}^*/σ , with time for six different geometry cases with loading method 1.

One further question is how the effect of 3-D geometry (isotropically-etched profile) of a microchannel on injection qualities will change as the channel aspect ratio (H/W_b) is varied. Figure 5-12 shows the effect of channel height on the 3-D simulation results for the isotropically-

etched cross section case, compared with the large width 2-D case. For the isotropically-etched cross sectional channel, the radius of the curved area is equal to the height and the bottom channel width is fixed to $90\ \mu\text{m}$. Thus, as the channel height decreases, the region of curved top surface decreases. With decreasing channel height, the 3-D characteristics also decrease and the 3-D results approach the 2-D results.

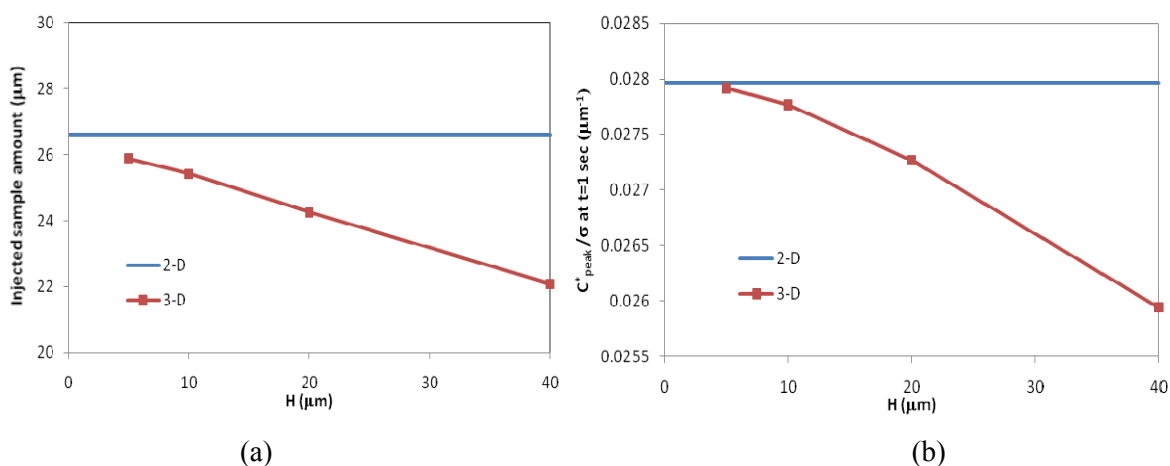


Figure 5-12. The effect of channel height on the 3-D injection performances compared to 2-D results. (a) Sample injection amount and (b) injection characteristic. 2-D channel width = $90\ \mu\text{m}$ (blue line). For the isotropically-etched cross-sectional channel, the radius of the curved area is equal to the height of the channel. The bottom channel width was fixed at $90\ \mu\text{m}$ while the height (H) was varied. With decreasing channel height, the 3-D characteristics also decrease and the 3-D results approach to the 2-D results.

5.6.3. 3-D Characteristics of Sample Dispersion during migration in a Straight Migration Channel

The 3-D characteristics of a sample dispersion during migration were investigated by simulating the molecular diffusion of an initially triangular sample plug in a straight channel. Figure 5-13 shows the variation of the averaged sample concentration distribution in a 2-D

channel with $W = 90 \mu\text{m}$ and in a 3-D isotropically-etched channel as the sample travels with the speed of $200 \mu\text{m/s}$ (The traveling velocity is arbitrarily specified. Note that this speed does not affect the dispersion of sample). The averaged concentration distribution is dispersed, and the peak value decreases with time due to molecular diffusion. The difference between 2-D and 3-D simulation data here is attributed to the difference of the cross sectional shape. Such a difference does not exist if the cross section is rectangular because the uniformity of sample species distribution in the z coordinate will not be perturbed in the rectangular geometry. However, with a non-rectangular cross section, like the isotropically-etched one, the non-uniform channel depth breaks the uniformity of the sample distribution in the z coordinate, resulting in the lateral diffusion pattern of the 3-D case deviating from the 2-D case. The variation of the lateral diffusion pattern further changes the dispersion of a sample plug in the longitudinal direction. The initial distribution of sample concentration of the 3-D case is close to that of the 2-D case but, as the dispersion proceeds, the 3-D peak value deviates from the 2-D peak value. The biggest difference (the 2-D value was 3.9 % lower) between these two values occurs within 1 sec. As the time passes, the 3-D sample distribution gets closer to that of the 2-D case. In other words, the 3-D geometry effect becomes less significant as the sample plug becomes more uniform in the lateral direction and the sample band increases with time. The result shows that the dispersion of sample plug during electroosmotic migration in a straight channel is influenced by the geometry when the initial sample plug has laterally non-uniform distribution. A question can be raised about why the 3-D isotropically-etched channel case doesn't approach the 2-D $90 \mu\text{m}$ width case in Figure 5-9 while it does in Figure 5-13. There are two main differences between these two cases. First, the initial sample distributions are different. Figure 5-13 case is a triangular initial distribution while Figure 5-9 case has a more complicated initial distribution formed by electroosmotic flow combination. Second, the injection behavior (Figure 5-9 case) is complicated

situation than simple migration case due to the sudden change of flow, electric field and sample concentration fields.

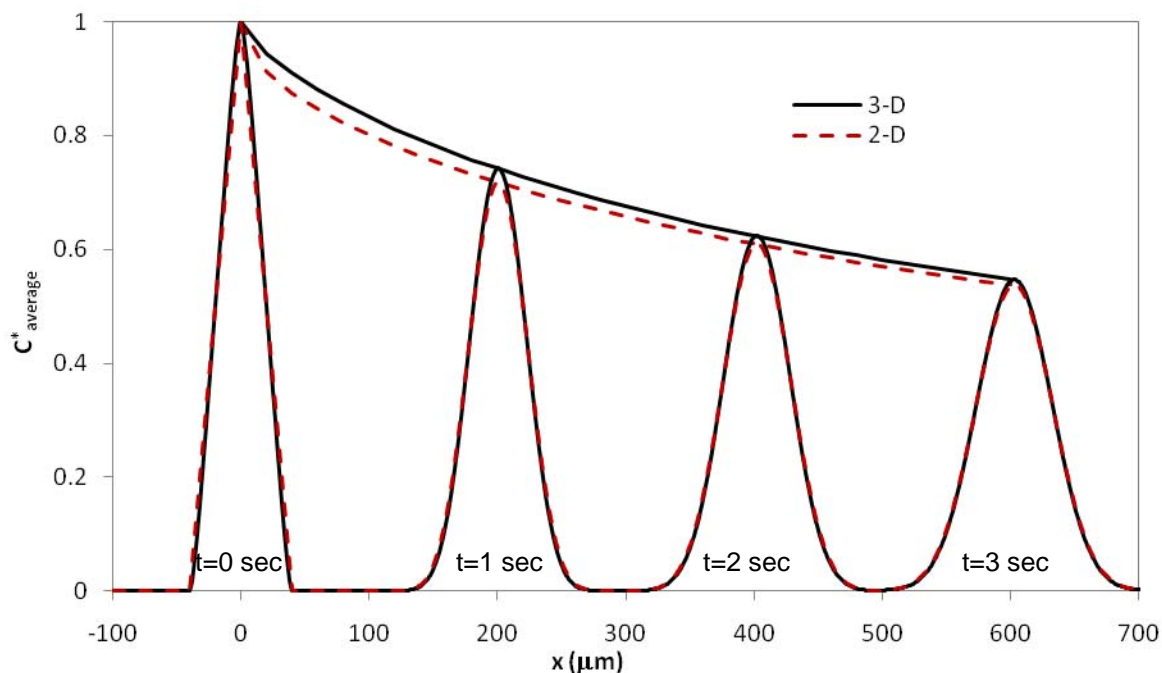


Figure 5-13. The averaged sample concentration distribution at different traveling times ($t = 0, 1, 2,$ and 3 sec) and the variation of peak value with traveling distance (x) calculated from 3-D and 2-D simulation data for sample migration case. The shape of the initial sample plug is triangular. The migration speed is $200 \mu\text{m}/\text{sec}$.

5.6.4. Numerical Inaccuracy due to Sharp Corners at the Intersection

Previous simulations [30, 58, 59] have often used geometries containing sharp corners at the intersection probably due to the convenience of generating structured meshes. In traditional fluid dynamics problems with a no-slip boundary condition, a sharp corner does not cause a problem in obtaining the solution because the zero velocity at the wall prevents discontinuous variation of flow velocity. However, since Helmholtz-Smoluchowski slip flow velocity is adopted

for the boundary condition, discontinuous variation of flow velocity at the sharp corner can arise. This discontinuous variation of flow velocity brings an infinite velocity gradient term in the Navier-Stokes equation. This singularity issue does not occur if no-slip boundary condition is adopted as in references [61, 68, 69]. However, in the current application where a slip boundary condition is adopted, the singularity at the sharp corners may bring numerical inaccuracy. The numerical inaccuracy induced by the sharp edges was investigated by looking at the effect of mesh size near the sharp corners. The simulation case was a 2-D channel with $W = 90 \mu\text{m}$ and a narrow loading method. Figure 5-14 (a) shows that the size of meshes near the sharp corner significantly affects the injected sample amount. As the size decreases even down to 20 nm, the injection volume keeps on varying, indicating that the mesh independence is not achieved even with such a small mesh size. The variation in the injection volume becomes even more significant at small mesh sizes. For the filleted case, the parameter remains constant with the mesh size below $0.5 \mu\text{m}$, indicating the mesh independence. As the mesh size is reduced in the sharp corner geometry, the injected sample amount for the sharp corner case approaches the value for the filleted case. This implies that the solution of the filleted geometry case is more accurate. The effect of fillet radius on the injected sample amount is shown in Figure 5-14 (b). Injected sample volume increases with the fillet radius. However, as the fillet size decreases below $1 \mu\text{m}$, the injected sample amount approaches a constant value. The present study shows that small radius fillet at the corners does not significantly change the performance of the device while it relieves the numerical inaccuracy otherwise developed by singularity related with sharp corners.

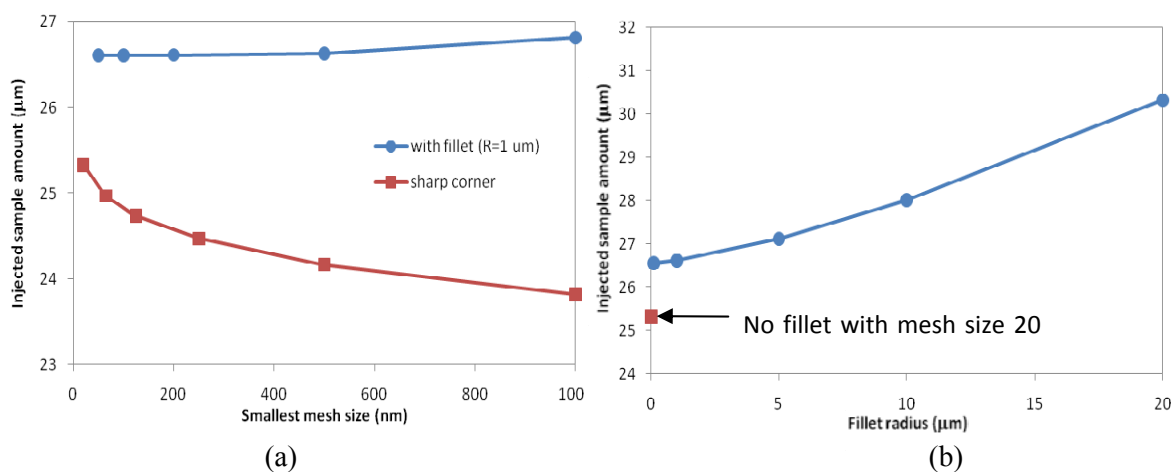


Figure 5-14. The effect of (a) mesh size and (b) fillet radius on injection amount.

5.7. CONCLUSIONS

The 3-D characteristics of the loading and dispensing of sample species during electroosmotic pinched injection in microchip capillary electrophoresis systems that have non-rectangular cross sections was investigated. An isotropically-etched channel resulted in a vertically non-uniform sample plug in the loading stage. The cross-sectional sample profile is distorted like a “V” shape or a “A” shape depending on the sample loading mode (narrow or wide sample) due to the 3-D non-rectangular geometry of the channel. In the sample injection simulation, the 3-D simulation data showed a clear difference from 2-D simulation data. 2-D simulations employing the top and bottom widths resulted in 3~10 % and 28~40 % errors in injection quantities, respectively. Instead, it was observed that the 2-D simulation data using the width calculated from the equivalent cross-sectional area of the 3-D channel show good agreement with the 3-D simulation data (less than 3 % error). This observation gives a guideline as to what width should be selected for a simulation on a pinched injection system when the

computer capability limits only to 2-D simulation. As the channel height decreases while the channel width remains fixed, it was found that the 3-D effects decrease and the 3-D results approach the 2-D results. The dispersion of a sample plug during electroosmotic migration in a straight channel is also influenced by the geometry when the initial sample plug has laterally non-uniform distribution. Thus, for an accurate simulation of injection and migration of a sample in a pinched injection device, 3-D simulations provide added insights to the flow field and sample dispersion.

CHAPTER 6. 3-D SIMULATION OF ELECTROSMOTIC SAMPLE MIGRATION IN MICROCHANNELS: EFFECTS OF SURFACE AND SOLUTION PROPERTY VARIATIONS

6.1 . INTRODUCTION

The commonly observed uniform velocity profile in electroosmotic flows, is attractive in the field of separation science because dynamic dispersion and band broadening effect can be minimized, in comparison to the parabolic velocity profile of pressure-driven flows. The uniform velocity profile approximation in electroosmotic flows has served as the basis for many previous studies employing 2-D [30, 61, 68, 69] or even 1-D [70-72] approximations for the numerical simulations. Such lower dimensional simulations were preferentially adopted for most microchip capillary electrophoresis simulations due to the limitation of computational power in the past. Chapter 3 investigated 3-D characteristics of the loading and dispensing of sample species during electroosmotic pinched injection in microchip capillary electrophoresis systems that have non-rectangular cross-sections. This chapter presents a numerical study that investigates 3-D characteristics of sample dispersion (broadening due to the combined effect of molecular diffusion and convective shear motion) in microchannels during electroosmotic migration when there is variation in microchannel surface or solution properties.

3-D simulations are essential when different zeta potentials are considered at the top and bottom substrates - a situation commonly found in microchannels made of two different materials. There have been efforts to use plastic channels or plastic-glass hybrid channels for microchip capillary electrophoresis systems, mainly because of their easy manufacturing process

and reduced cost. One of the common examples is the ‘polydimethylsiloxane (PDMS)-glass’ hybrid channel [173, 191]. The electroosmotic velocity difference between top and bottom substrates in a hybrid channel, however, generates a shear motion of sample plug and consequently degrades the separation efficiency. The deterioration of separation efficiency in hybrid channels was experimentally demonstrated by Kim et al. [173]. Surface roughness change during a microfabrication process such as wet etching can also result in different zeta potentials for the top and the bottom surfaces. Hu et al. [184] and Qiao [192] reported that surface roughness can significantly reduce the electroosmotic mobility of the glass channels. However, the effect of different zeta potentials for the top and the bottom surfaces of a channel on sample plug dispersion in microchip capillary electrophoresis systems has not been thoroughly investigated. Such investigation requires full 3-D simulations in order to include the effect of every wall of the microchannel. Datta et al. [187] simulated an electroosmotic flow with zeta potential variation on the walls of a rectangular channel and compared their computational results with results obtained from the asymptotic theory. Xuan and Li [193] developed general solutions for arbitrary cross-section and arbitrary distribution of zeta potential. However, none of the previous studies have reported how the 3-D aspects affect the separation efficiency of capillary electrophoresis.

3-D simulations are also essential when internal pressure gradients due to surface or solution property variation are present. While electroosmotic flows produce a uniform flow profile, unintentional local pressure gradient can be developed when electric conductivity or zeta potential variation is induced by ionic concentration gradient or surface adsorption to the channel wall. Protein adsorption at the channel wall and the subsequent change in zeta potential have been reported in the literature [171, 194].

The development of a local pressure gradient can be explained with the breakage of similitude [195] between electric current and fluid flows under variation of conductivity or zeta potential. The electric current conservation equation without internal electric charge (assuming the thickness of Debye layer is neglected) is expressed as

$$\oint \vec{J} \cdot d\vec{A} = \oint \lambda \vec{E} \cdot d\vec{A} = 0 \quad (6-1)$$

where J is electric current density, \vec{E} is the electric field, λ is the electrical conductivity and A is surface area of a control volume. \vec{E} can usually be equated to \vec{V} / μ_{eo} (velocity / electroosmotic mobility) if similitude is satisfied and there is no pressure gradient. By replacing \vec{E} with \vec{V} / μ_{eo} , the following equation is obtained.

$$\oint \frac{\lambda}{\mu_{eo}} \vec{V} \cdot d\vec{A} = 0 \quad (6-2)$$

If the electrical conductivity and electroosmotic mobility of the media are both constant, Eq. (6-2) simply becomes the continuity equation of incompressible steady state flow and thus both flow and electric current conservations are satisfied. In contrast, if there are variations in electrical conductivity or electroosmotic mobility, the flow continuity equation, $\oint \vec{V} \cdot d\vec{A} = 0$, is not guaranteed because the assumption, $\vec{E} = \vec{V} / \mu_{eof}$, is not valid and local pressure gradient has to be adjusted for satisfying the conservation equations. In this chapter, I investigated how the

electrical conductivity and electroosmotic mobility variation builds up internal pressure gradient and affects sample dispersion.

Herr et al. [196] reported an experimental work on how the characteristics of electroosmotic flow and the separation efficiency were affected by having two different zeta potentials along the channel. They also showed pressure gradient could be induced by non-uniform zeta potential along the channel. Ren and Li [197] performed a numerical simulation to investigate how the electroosmotic flow is affected by non-uniform zeta potential along a cylindrical microchannel. The local pressure gradient causes a parabolic velocity effect to the originally uniform electroosmotic flow. The partially parabolic flow profile due to pressure gradient not only degrades the separation efficiency of devices but also invalidates the lower dimensional simplification of sample band dispersion due to the wall effect of pressure driven flows.

Past studies [72, 198] often employed the 1-D Taylor dispersion model [199, 200] to compensate for the pressure driven shear dispersion effect. The Taylor dispersion model transforms the transverse diffusion effect into an additional longitudinal dispersion in a diffusion-like formula by employing the effective diffusion coefficient as follows:

$$D_{eff} = D \left(1 + \beta (UH/D)^2 \right) \quad (6-3)$$

where D is the molecular diffusion coefficient of the sample species, U is the average velocity of a pressure driven flow, H is the characteristic dimension of the channel cross-section, and β is a constant calculated from the cross-sectional shape. The derivation of the Taylor dispersion model involves several approximations. The main approximation is that the convective mixing time scale (σ / U) is much longer than the lateral diffusion time scale (H^2/D) where σ is the sample

bandwidth. This condition is, however, not guaranteed for microchip capillary electrophoresis systems since the sample bandwidths are usually small in those microsystems (e.g. a pinched injection system) and the flow speed (U) is higher than flow speeds in traditional capillary electrophoresis systems. Employment of Taylor dispersion approximation (1-D) in the past was attributed to the computational limitation. In this chapter, the accuracy of Taylor dispersion model is also evaluated by taking microchip operation conditions.

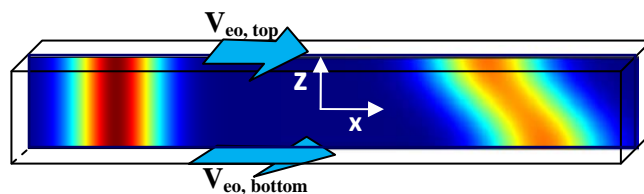
Ren and Li [197] reported a numerical study on how an electric conductivity gradient affects a sample plug during electroosmotic transport using 2-D computational domain. Their study showed that the conductivity differences have significant effects on the sample transport compared with the uniform conductivity case.

This chapter investigates the multi-dimensional characteristics of sample dispersion during electroosmotic migration when there is variation in electrical conductivity due to the presence of sample species. Along with Chapter 5 which focuses on the effect of 3-D geometry (non-rectangular cross-section) on the performance of microchip capillary electrophoresis systems, this study provides a quantitative basis for judging the accuracy of the conventional 1-D or 2-D simulation of sample plug distribution during electroosmotic injection and migration compared to the complete 3-D simulation.

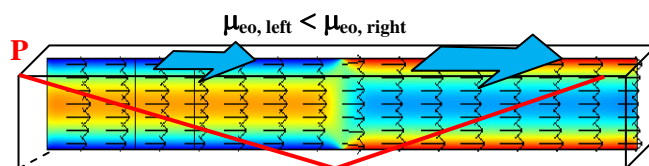
6.2 . PROBLEMS CONSIDERED

Numerical simulations of electroosmotic sample migration in 2-D and 3-D microchannels were considered. For 3-D geometries, both the rectangular and the isotropically etched cross-sections were considered. Four specific cases are explored in this study. The first three cases are for investigating how sample dispersion is affected when there is surface or solution property

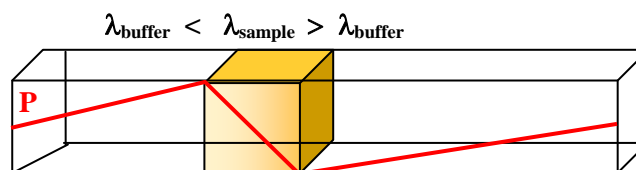
variation. The last case examines whether the Taylor dispersion modeling is appropriate for modeling microchip capillary electrophoresis.



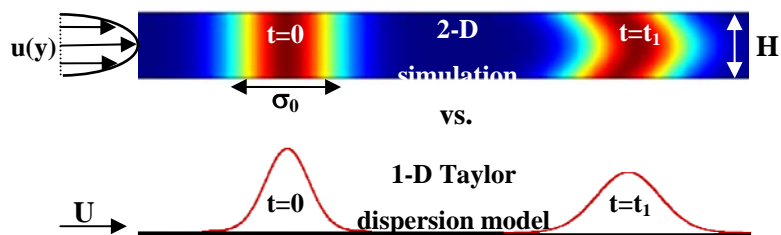
(a) Zeta potential difference between top and bottom substrates



(b) Zeta potential variation along the channel



(c) Conductivity variation due to sample plug



(d) Validity of Taylor dispersion model in microchannels

Figure 6-1. Schematics of the problems considered in Chapter 4.

Case 1. Zeta potential variations among the microchannel walls

The 3-D characteristics of the sample band dispersion in a microchannel due to the shear motion of the two different electroosmotic mobilities are investigated, as illustrated in Figure 6-1(a). The geometries used are an infinitely wide channel (2-D), a 3-D channel with rectangular cross-section, and a 3-D channel with isotropically-etched cross-section (Figure 6-2). The channel with isotropically-etched cross-section represents a glass microchannel made by wet etching that results in different surface roughness for the top/sides and bottom substrates. The 3-D channel with rectangular cross-section represents a PDMS-glass hybrid channel (channel defined in PDMS). The height of the channel (H) was 20 μm for all the geometries. The bottom width of isotropically-etched cross-section was 60 μm . The width of the rectangular cross-section was 20 μm .

The bottom surface of the channel was given an electroosmotic mobility, $\mu_{eo,bottom}$, and the remaining walls (top and sides for the rectangular cross-section and the curved wall for the isotropically etched microchannel) as shown in Figure 6-2 were given another value, $\mu_{eo,top}$. This boundary condition properly represents the situation resulting from the microchannel fabrication where a substrate containing the channel is bonded with a flat substrate (the bottom one). The typical electroosmotic mobility of glass or PDMS is $\mu_{eo} = 4 \times 10^{-8} \text{ m}^2/\text{Vs}$ according to references [30, 76]. For the present simulations, selected was 10% difference for bottom and top electroosmotic mobilities (i.e. $\mu_{eo,bottom} - \mu_{eo,top} = 4 \times 10^{-9} \text{ m}^2/\text{Vs}$). This variation in electroosmotic mobility is plausible for surface roughness change or hybrid material usage [173, 184, 192]. Qiao in his numerical study [192] showed 36% decrease in zeta potential on a rough surface and Spehar et al. in their experimental study [76] showed the electroosmotic mobility difference between fused silica and PDMS was about $2 \times 10^{-8} \text{ m}^2/\text{Vs}$.

A sample plug is considered which has an initial spatial Gaussian distribution with a standard deviation $\sigma_0 = 50 \mu\text{m}$. By applying a constant electric field (1 kV/cm), a steady velocity field is established, satisfying the electroosmotic flow boundary condition on each material surface. Since the entire bulk fluid moves with the slip boundary flow, the diffusion of sample species can be captured by observing the relative movement of species with respect to the average migration velocity (denoted by V_{travel}) of sample plug which is the summation of electrophoretic velocity ($V_{ep} = \mu_{ep}E$) and the average of top and bottom electroosmotic velocities ($(V_{eo,1} + V_{eo,2})/2$). The velocity field is subtracted by the observation velocity, V_{travel} . This approach allows for a shorter channel length (2 mm) as a computational domain instead of a long, real channel and thus the computation time for band broadening analysis is significantly reduced.

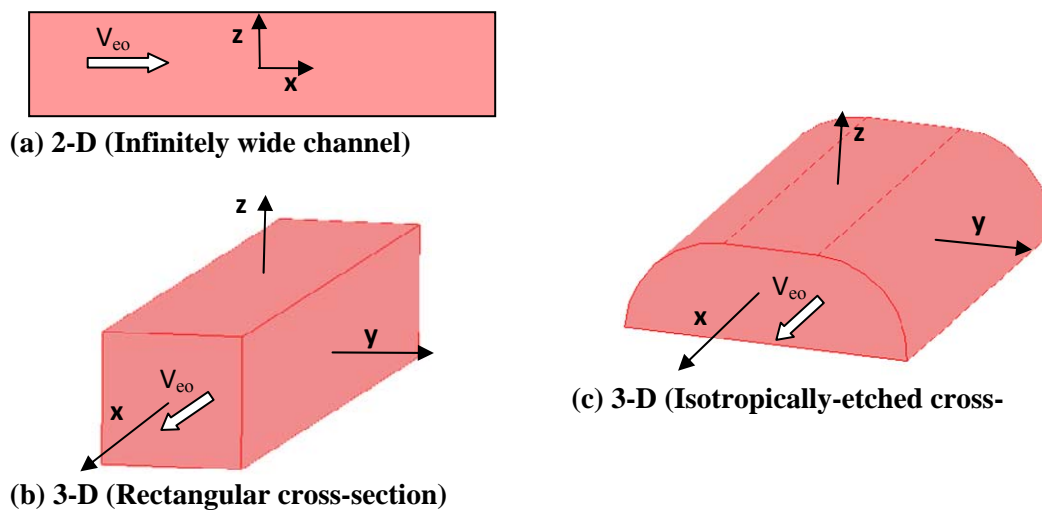


Figure 6-2. Model geometries used in the simulation. Electroosmotic flow is in positive x direction.

Case 2. Zeta potential variation along the channel

For the study of zeta potential variation effect, a step variation of electroosmotic mobility was imposed along the channel; the left half of the channel has a lower zeta potential while the right half has a higher zeta potential (Figure 6-1(b)).

The geometries used in this investigation were also an infinitely wide channel (2-D) with 20 μm height, 3-D channels with isotropically-etched (bottom width = 90 μm) and square cross-sections ($H = W = 20 \mu\text{m}$). The channel length was 1 mm. The sample plug was initially located at 200 μm from the left end with a Gaussian distribution ($\sigma_0 = 50 \mu\text{m}$) and was driven towards the cathode by the electroosmotic flow.

Case 3. Electric conductivity (λ) variation due to the presence of a sample plug

The geometries and initial conditions used for this case are the same as Case 2. The electric conductivity variation due to the presence of ions in a sample plug was implemented by using the relationship between conductivity and ion concentration, Eq. (6-4).

$$\lambda_{ion} = \sum FC_i \mu_{ep,i} z_i \quad (6-4)$$

where F is the Faraday constant, and C_i , $\mu_{ep,i}$, and z_i are the concentration, electrophoretic mobility and valence of species i (Figure 6-1(c)). In this study one sample species with $z = 1$ was considered in addition to the buffer solution so the total conductivity is given as

$$\lambda = \lambda_{buffer} + C \mu_{ep} F \quad (6-5)$$

where λ_{buffer} is the conductivity of buffer and C is sample species concentration. Therefore, the conductivity and electric field distribution vary as the sample plug travels. The selected properties for the simulation are listed in Table 1.

Table 1. Parameter values for cases 1, 2, and 3.

Case 1		Case 2		Case 3	
μ_{eo} variation on walls		μ_{eo} variation in x-axis		conductivity variation	
$\mu_{eo,bottom}$	$4.2 \times 10^{-8} \text{ m}^2/\text{Vs}$	$\mu_{eo,left}$	$3 \times 10^{-8} \text{ m}^2/\text{Vs}$	λ_{buffer}	48 mS/m
$\mu_{eo,top}$	$3.8 \times 10^{-8} \text{ m}^2/\text{Vs}$	$\mu_{eo,right}$	$4 \times 10^{-8} \text{ m}^2/\text{Vs}$	μ_{eo}	$4 \times 10^{-8} \text{ m}^2/\text{Vs}$
				C_{sample}	10 mM
Common parameter values					
μ_{ep}	$-1 \times 10^{-8} \text{ m}^2/\text{Vs}$	D	$1 \times 10^{-10} \text{ m}^2/\text{s}$	$E_{boundary}$	1kV/cm
ρ	1000 kg/m^3	η	0.001 kg/m s		

Case 4. Applicability of 1-D Taylor dispersion model in 3-D microchannel flow

The appropriateness of the 1-D Taylor dispersion model for a rectangular microfluidic channel is investigated by comparing the result of full-dimension simulation with the result of 1-D simplified simulation via the Taylor dispersion model (Figure 6-1(d)).

6.3 . NUMERICAL METHODS & GOVERNING EQUATIONS

The general governing equations for electroosmotic sample dispersion problems considered here are as follows:

$$\text{Flow continuity equation: } \nabla \cdot \vec{V} = 0 \quad (6-6)$$

$$\text{Flow momentum equation: } \rho \frac{D\vec{V}}{Dt} = -\nabla p + \eta \nabla^2 \vec{V} \quad (6-7)$$

$$\text{Electric potential governing equation: } \nabla \cdot (\lambda \nabla \Phi) = 0 \quad (6-8)$$

$$\text{Chemical species conservation: } \frac{\partial C}{\partial t} + \nabla \cdot ((\vec{V} + \mu_{ep} \vec{E})C) = D \nabla^2 C \quad (6-9)$$

$$\text{Energy equation: } \rho c_p \frac{DT}{Dt} = \nabla \cdot (k \nabla T) + \lambda |\vec{E}|^2 \quad (6-10)$$

where \vec{V} is flow velocity, ρ is the density, η is the dynamic viscosity, \vec{E} is the applied electric field, λ is the total electric conductivity, C is sample species concentration, D is the diffusivity of sample species, μ_{eo} is electroosmotic mobility, μ_{ep} are electrophoretic mobility, c_p is constant pressure specific heat capacity and T is temperature. Eq. (6-8) is based on the assumption that the buffer ions are constant everywhere. In general, all the parameters are functions of temperature which is also variable due to the Joule heating [201].

Initial and boundary conditions

At the walls, insulation boundary conditions ($\partial \Phi / \partial n = 0$, $\partial C / \partial n = 0$) were imposed for the electric potential and chemical species while Helmholtz-Smoluchowski slip velocity ($\vec{V}_{eo} = \mu_{eo} \vec{E}$) was imposed on the walls for the flow variables. Detailed validation and explanation of the Helmholtz-Smoluchowski electroosmotic slip velocity is described in references [30, 181]. A spatial Gaussian distribution with a standard deviation (σ_0) was imposed for the initial condition for sample species concentration as described in section 6.2 PROBLEMS CONSIDERED.

COMSOL Multiphysics software version 3.5a was used for the simulations in this chapter. The detailed method is described in section 6.4.

A double Quad-core workstation (Dell Precision T7400, 2.5 GHz) was used for simulation. The computational time for every case except the conductivity variation case (Case 3) ranged from a half hour to 3 hours. The simulation for Case 3 took about a day.

6.4 . RESULTS AND DISCUSSION

In this section, first I present results for the validation of the numerical methods and the effects of Joule heating (if any) on the cases presented in the chapter. Then I present results for the four specific cases (as mentioned earlier in Section 2). The first three cases are for investigating how sample dispersion is affected when there is surface or solution property variation. Table 1 lists the parameter values for cases 1, 2 and 3. The last case (case 4) examines whether the Taylor dispersion formulation is appropriate for modeling microchip capillary electrophoresis.

Validation of present numerical model

The numerical model validation was previously reported in [202] by comparing the current numerical simulation results with the previous numerical [30] and experimental results [143] for a pinched injection system. In addition to that validation, the current numerical simulation result was compared with an analytical solution for constant zeta potential and electrical conductivity with $\mu_{eo} = 4 \times 10^{-8} \text{ m}^2/\text{Vs}$ with a Gaussian initial concentration distribution ($\sigma_0 = 50 \text{ }\mu\text{m}$). 2-D computational domain was selected with the same dimensions as given in Case 2. All the other conditions are the same as listed in Table 1. The analytical solution of this problem is known to be [203]

$$C(x,t) = C_0 \frac{\sigma_0}{\sqrt{\sigma_0^2 + 2Dt}} \exp\left(-\frac{(x - (\mu_{eo} + \mu_{ep})E_{boundary}t)^2}{2(\sigma_0^2 + 2Dt)}\right).$$

The simulation results at the mid-section of the channel, as shown in Figure 6-3, had a good agreement with the analytical solution with less than 0.2 % error.

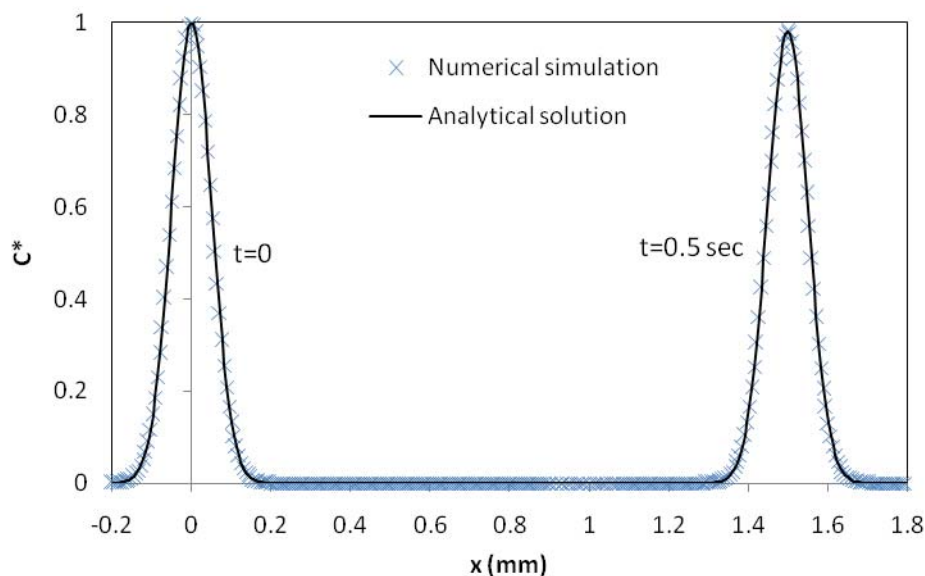


Figure 6-3. Comparison of normalized concentration prediction along the length of a microchannel with an analytical solution for constant zeta potential and conductivity.

Energy equation and temperature effects

Numerical simulations for obtaining temperature distribution for case 1 geometries with a conductivity value of 48 mS/m. Isothermal boundary condition was used for the simulations were performed. It was found that the temperature variation is less than 0.5 K for 3-D case and less than 5.0 K for 2-D infinitely wide channel case. Since the temperature variation for 3-D simulation case was negligible, isothermal condition was assumed and the energy equation was not considered further for the simulations reported in this chapter.

Case 1. Zeta potential variations among the microchannel walls

For the different zeta potential cases, a constant electroosmotic mobility difference ($\mu_{eo,bottom} - \mu_{eo,top} = 4 \times 10^{-9} \text{ m}^2/\text{Vs}$) was imposed between the top (top and side surfaces) and bottom substrates. In the case of the same zeta potential ($\mu_{eo,bottom} = \mu_{eo,top}$), the sample was broadened only via molecular diffusion. However, in the cases of the different (top/sides and bottom) zeta potentials ($\mu_{eo,bottom} \neq \mu_{eo,top}$), the dispersion of sample band was significantly increased by the shear motion of the two different electroosmotic velocities. Figure 6-4 shows the dispersion (broadening) of a sample band at the mid-plane (x-z plane) of a rectangular cross-section 3-D channel after 0.5 second traveling down the channel for (a) the same zeta potential channel case and (b - d) for different zeta potential cases. Figure 6-4(b) shows the results for an infinitely wide channel. The sample concentration profile in the infinitely wide channel (Figure 6-4(b)) is symmetrically deformed whereas the concentration profiles for 3-D cases (Figure 6-4(c and d)) are distorted in an asymmetric way. This is because of the presence of the side walls in 3-D geometries. The side walls are part of the top substrate and were given the same electroosmotic velocity as the top surface. Because the side wall effect is the largest in the rectangular cross-section case, the asymmetry is also largest in that case as shown Figure 6-4(d).

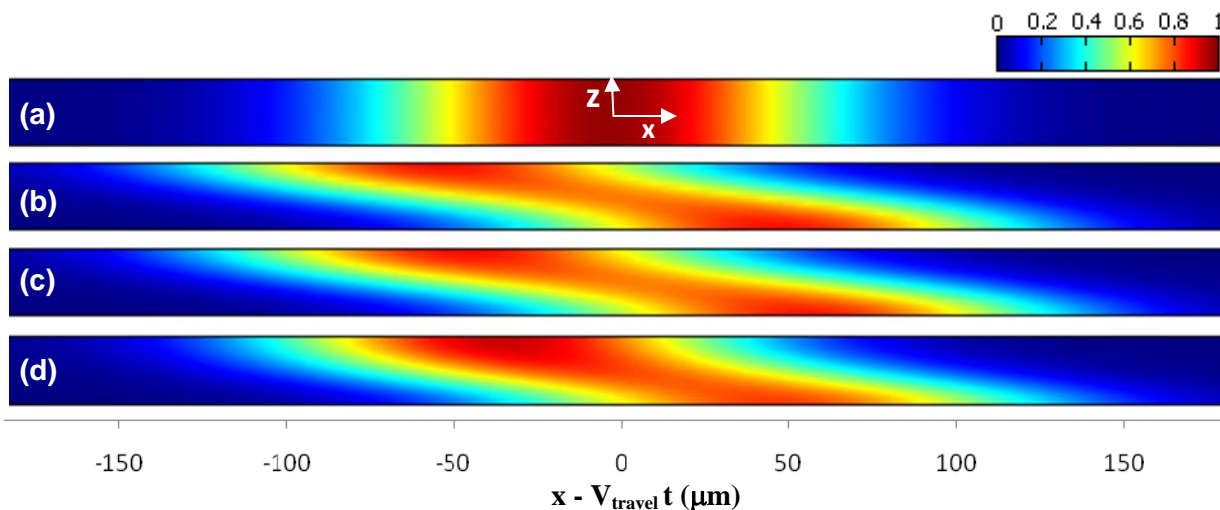


Figure 6-4. The cross sectional view (at the mid-plane; x-z plane) of dispersion of a sample concentration band after 0.5 sec (a) for uniform electroosmotic mobility and (b – d) different top and bottom electroosmotic mobilities ($\mu_{eo,bottom} - \mu_{eo,top} = 4 \times 10^{-9} \text{ m}^2/\text{Vs}$); (b) infinitely wide channel (2-D), (c) 3-D isotropically-etched channel and (d) 3-D square cross sectional channel.

Figure 6-5 shows the cross-sectional average of sample concentration along the transformed x axis ($x - V_{\text{travel}} t$) at $t = 0.5$ sec (for the cases shown in Figure 6-4) where V_{travel} is the traveling velocity of sample plug. The sample concentration is normalized by the sample initial peak concentration, denoted by C^* . It is clearly shown that the different zeta potential case has more sample band broadening (lower separation efficiency) than the same zeta potential case. Also, the distribution is slightly deviated from the Gaussian distribution for the 3-D channel case with different zeta potential. That is because the sample dispersion is not only due to the molecular diffusion but also due to convection (shear motion) induced by the electroosmotic mobility difference. The increase of sample broadening is higher in 2-D case than 3-D cases because the 2-D shear motion more effectively breaks apart the sample distribution. In 2-D case, the top and bottom walls equally pull away the sample plug while, in 3-D case, top and side walls (larger area) pull in one direction and bottom wall (smaller area) pulls in the opposite direction.

Since the rectangular cross-section has higher 3-D characteristics (or higher ratio of top and bottom substrate areas), the sample broadening of that case (rectangular cross-section) is smaller than that of isotropically-etched case.

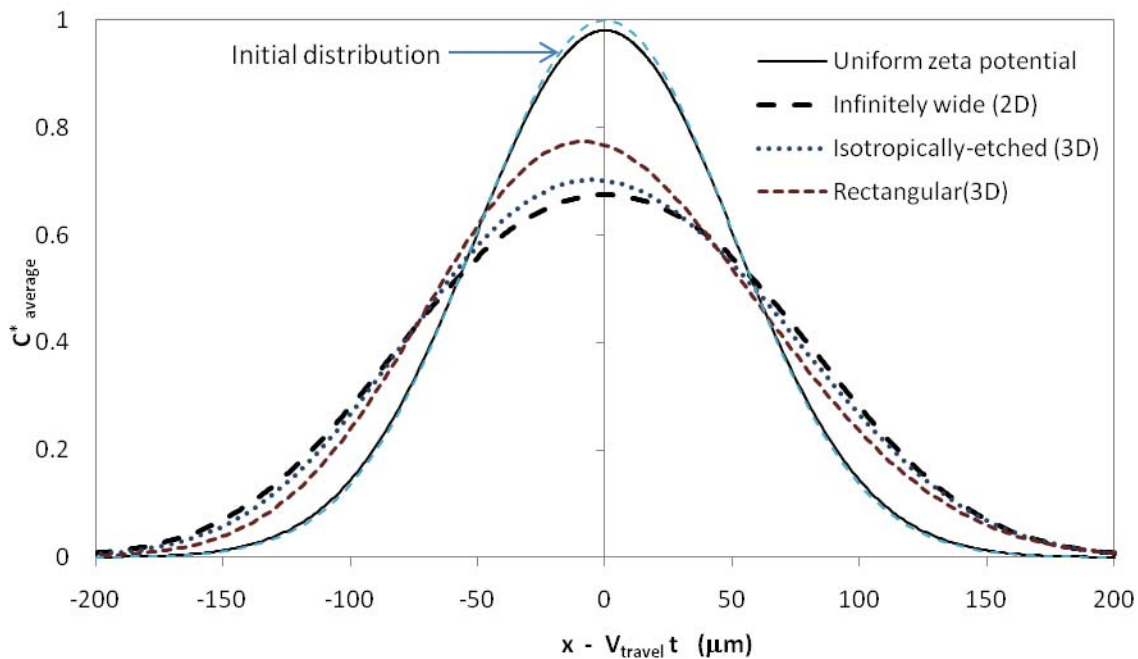


Figure 6-5. Cross-section averaged sample concentration at $t = 0.5$ sec for the case of different zeta potentials for top and bottom substrates (Case 1) for four different channel geometries. The concentration is normalized by the peak of initial sample concentration.

Plate height (h) is often used in the field of separation science as an indicator for the separation efficiency of a system. The plate height is expressed by

$$h = \frac{\sigma^2}{\ell} \quad (6-11)$$

where σ^2 is the spatial variance of sample concentration and ℓ ($V_{travel} \cdot t$) is the distance between the detection point and initial location of the sample. Plate height indicates how much a sample band is dispersed per unit length of the separation channel. The variance of sample distribution for a uniform zeta potential case increases with time in a linear relationship as follows:

$$\sigma^2 = \sigma_0^2 + 2Dt \quad (6-12)$$

where σ_0^2 is the initial variance of sample distribution, t is the traveling time and D is the diffusivity of species. For the calculation of plate height in a small traveling distance, the concept of initial traveling length (ℓ_0) is introduced to compensate the initial variance as follows:

$$\ell_0 = V_{travel} \cdot t_0 = V_{travel} \cdot \left(\frac{\sigma_0^2}{2D} \right), \quad \text{and } h = \frac{\sigma^2}{\ell_0 + \ell} \quad (6-13)$$

where t_0 is initial travel time.

The plate height for the same zeta potential case is expressed as

$$h = \frac{\sigma^2}{\ell_0 + \ell} = \frac{\sigma_0^2 + 2Dt}{V_{travel}(\sigma_0^2/2D) + V_{travel}t} = \frac{2D}{V_{travel}} \quad (6-14)$$

In this study, the selected electroosmotic and electrophoretic mobilities are 4×10^{-8} $\text{m}^2/(\text{Vs})$ and -1×10^{-8} $\text{m}^2/(\text{Vs})$ respectively and the electric field is 1.0 kV/cm. Based on these values, the theoretical plate height for the same zeta potential channel is calculated to be 0.0667 μm .

Figure 6-6 shows the plate heights calculated for 1-D (uniform), 2-D (infinitely wide) and 3-D cases. The plate height for the same zeta potential case remains constant with the traveling distance and the simulated value agrees well with the theoretical value. The plate height for the different zeta potential channel does not remain constant but keeps increasing with traveling distance. The sample dispersion of the different zeta potential cases is the result of combined effects of shear motion due to the difference of electroosmotic mobilities and molecular diffusion. The sample dispersion (σ) by a shear motion is linearly related to the shear length scale, $\Delta V_{eo}t$, ($\Delta V_{eo} = V_{eo,bottom} - V_{eo,top}$) if the molecular diffusion can be neglected. To the contrary, if the lateral molecular diffusion is much faster than the convective dispersion, the concept of the Taylor dispersion model can be applied to this case to transform the effect of shear motion on sample dispersion into a diffusion-like formula. Separating two extreme regimes where either one of these two dispersion mechanism dominates, the following dispersion model is proposed:

$$\sigma^2 = \sigma_0^2 + S(\Delta V_{eo}t)^2 \quad \text{if } (\sigma / \Delta V_{eo}) \ll (H^2 / D) \quad (6-15)$$

$$\sigma^2 = \sigma_0^2 + 2D_{eff}t \quad \text{if } (\sigma / \Delta V_{eo}) \gg (H^2 / D) \quad (6-16)$$

where D_{eff} is an apparent diffusion parameter which includes shear motion interaction with molecular diffusion in the same concept as in Eq. (6-3), S is a proportionality constant and $\Delta V_{eo} = V_{eo,bottom} - V_{eo,top}$. When the effect of convective dispersion is dominant, Eq. (6-15) applies. By neglecting the initial band width, the plate height becomes proportional to traveling time (t) and shear velocity squared (ΔV_{eo}^2). The linear increase of the plate height with traveling distance (or time) at small traveling distance is clearly observed in Figure 6-6. The slope of

curves in Figure 6-6 corresponds to $S\Delta V_{eo}^2/V_{eo}^2$. The proportionality, S , is dependent on the channel cross-sectional shape for the same reason as discussed earlier for Figure 6-5, where 2-D case has higher band broadening than 3-D case; the equal top and bottom substrate areas in 2-D case break apart the sample distribution more effectively. This trend is also clearly shown in Figure 6-6 ($S_{2-D} > S_{\text{isotropically-etched}} > S_{\text{rectangular}}$). If the convective dispersion becomes negligible compared to the lateral diffusion, Eq. (6-16) applies, and the plate height approaches a constant value.

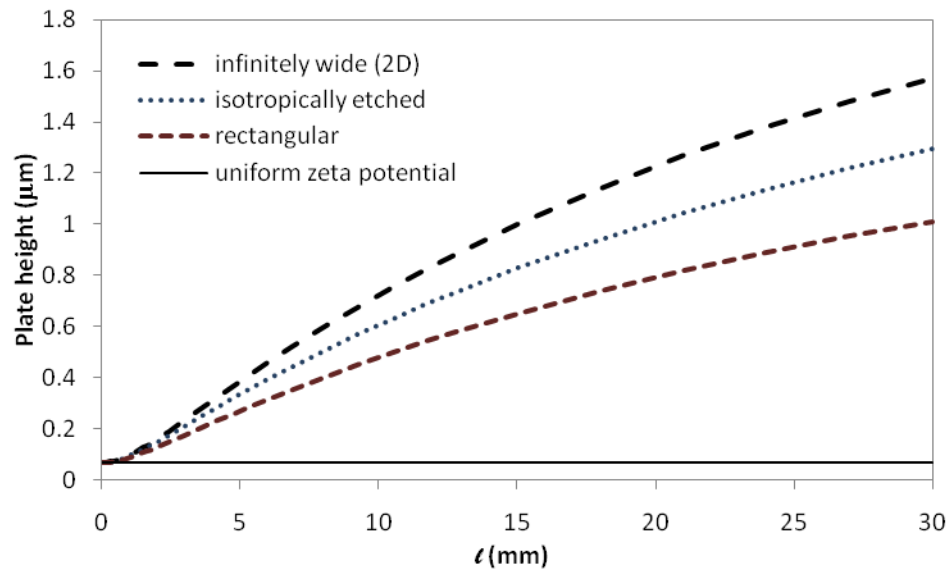


Figure 6-6. Variation of plate heights, $\sigma^2/(\ell_0 + \ell)$, for the case of different zeta potentials for top and bottom substrates (Case 1) vs. traveling distance. $V_{\text{travel}}=3\text{mm/s}$.

Figure 6-7 shows the plate height variation for a long traveling distance for the infinitely wide channel case. The graph shows the effect of the channel height, shear velocity (ΔV_{eo}), and the initial sample band width (σ_0) on plate heights while keeping the Peclet number ($\Delta V_{eo}H/D$)

constant. The plate heights in Figure 6-7 are divergent at a short traveling distance and they approach a constant value as the traveling distance increases. With the analogy to Taylor dispersion, $D_{eff} = D(1 + \beta(UH/D)^2)$, the increased amount of plate height by electroosmotic shear motion at a long traveling distance is expected to increase with shear velocity, ΔV_{eo} , and channel height, H , but decrease with the molecular diffusion coefficient, D . For both cases of convection domination (Eq. (6-15)) and fast lateral diffusion (Eq. (6-16)), the increase of plate height is linearly related with ΔV_{eo}^2 . In microchip capillary electrophoresis, the short distance mechanism is more relevant since the traveling distance is relatively short.

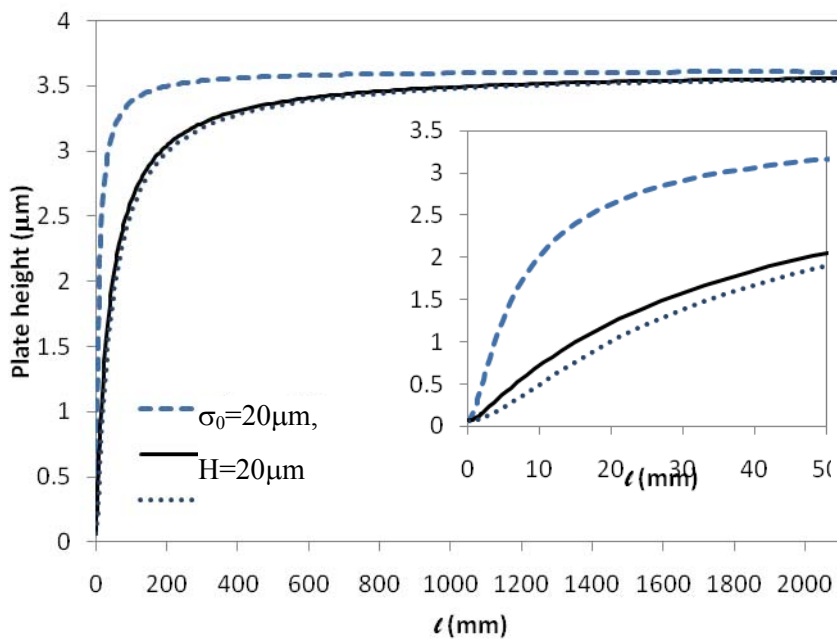


Figure 6-7. Variation of plate heights as a sample plug travels in infinitely wide channels (2-D) for the cases of various sample widths (σ_0) and channel heights (Case 1). Peclet number $(\Delta V_{eo}H/D) = 80$, and $\Delta V_{eo} = 0.4$ mm/s.

Case 2. Zeta potential variation along the channel

The 3-D characteristics of the sample band dispersion in a microchannel due to the zeta potential variation along the channel are considered in Case 2. A lower electroosmotic mobility was imposed on the left half side of the channel than the right half side (Figure 6-1(b)). The different electroosmotic slip velocities induce an internal pressure gradient in order to satisfy the flow continuity. The total volumetric flow rate is maintained constant throughout the channel by the induced pressure gradient. Except for the slip boundary condition of the electroosmotic velocity at the walls, the flow field is similar to a Poiseuille flow. The pressure gradient induces the parabolic velocity profile in addition to electroosmotic velocity on the walls. Assuming a fully developed flow throughout each half channel, the flow continuity is satisfied in the following formula:

$$Q = V_{eo,l} \cdot A - \alpha \frac{\Delta p_l}{L_l} = V_{eo,r} \cdot A - \alpha \frac{\Delta p_r}{L_r} \quad (6-17)$$

where α is a proportionality between pressure gradient and volume flow rate, depending on the channel shape, L is the channel length in a section, Δp is pressure gradient and the subscripts, l and r denote the left and right sides of channel. Since the pressure at both ends is set to be zero (ambient pressure), the pressure at the interface between two different zeta potential regions, $p_i = \Delta p_l = -\Delta p_r$, is expressed as

$$p_i = \frac{A}{\alpha} (V_{eo,l} - V_{eo,r}) \left(\frac{L_l L_r}{L_l + L_r} \right) \quad (6-18)$$

The simulation results showed the pressure distribution is very close to the analytical value obtained by Eq. (6-16) (*the difference is less than 1 % of the total internal pressure change*). This indicates that as the flow passes the interface of two regions the flow is fully developed with the new pressure gradient within a very short distance.

The average velocity is obtained by substituting Eq. (6-18) into Eq. (6-17) in the following form:

$$\overline{V_{eo}} = \frac{Q}{A} = \frac{L_l}{L_l + L_r} V_{eo,l} + \frac{L_r}{L_l + L_r} V_{eo,r} \quad (6-19)$$

Figure 6-8 shows that the computational result of pressure distribution is very close to the analytical value obtained by Eq. (6-13). This indicates that as the flow passes the interface of two regions the flow is fully developed with the new pressure gradient within a very short distance.

Figure 6-9 shows the dispersion of a sample band with time as it travels downstream under internal pressure gradient induced by the zeta potential variation along the channel. As the sample plug migrates in the left half channel, it is bent toward the front due to the convex flow profile generated by the negative pressure gradient. As the sample plug enters into the right half channel, it starts being bent backward of the flow direction due to the concave flow profile generated by the positive pressure gradient. This detailed pattern of a sample plug distortion cannot be captured in the 1-D simplified Taylor dispersion modeling.

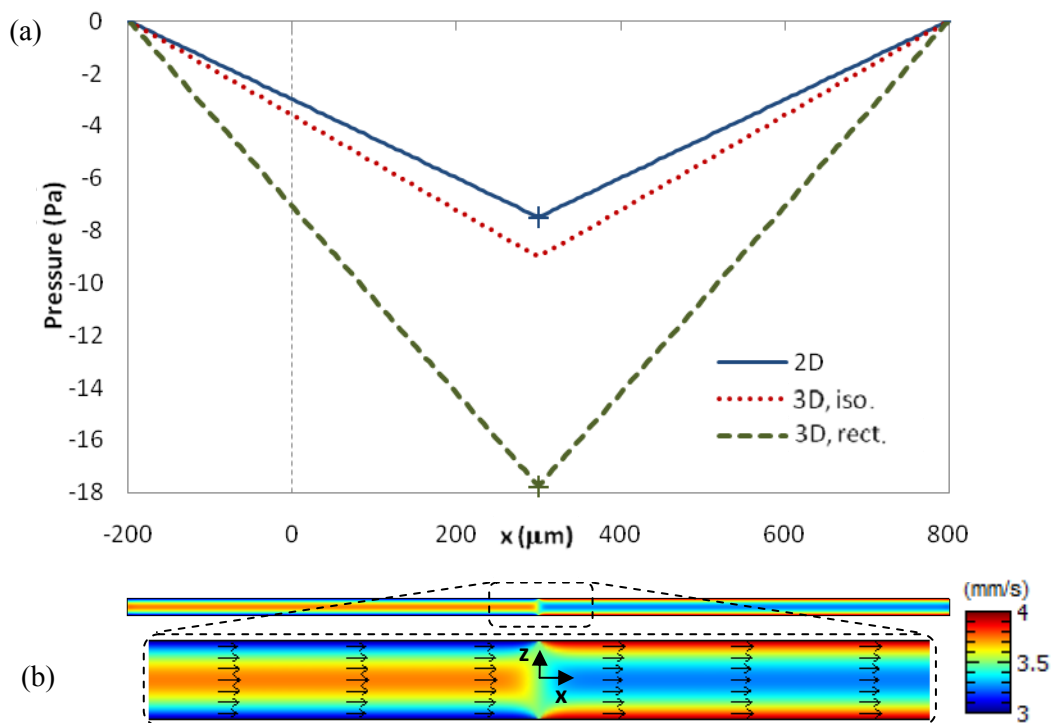


Figure 6-8. Results of Case 2. (a) Pressure distribution along the center line of the channel in the axial (x) direction for 2-D and 3-D cases and (b) the surface plot of x -directional velocity component with velocity vectors for 2-D case. Analytical values of pressure ('+') are calculated via Eq. (13). “3-D, iso.” is for the isotropically-etched channel case and “3-D, rect.” is for the rectangular channel case.

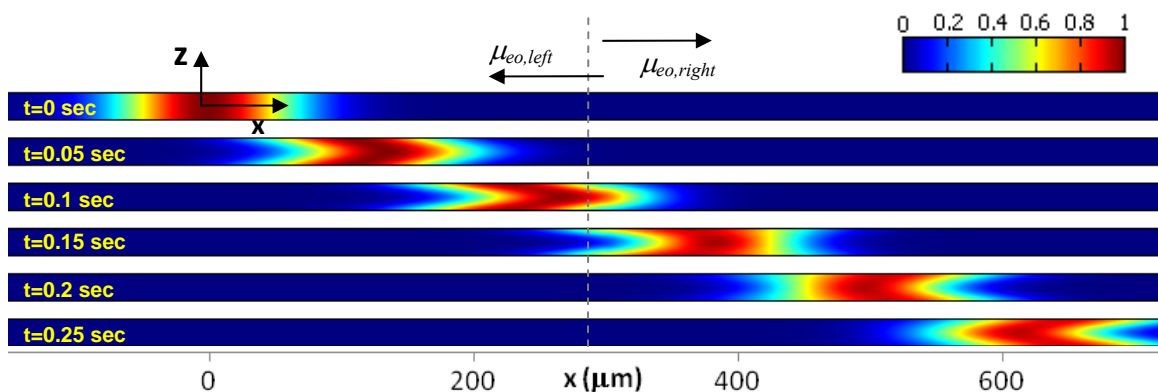


Figure 6-9. Spatial variation of sample concentration at various times for the cases having zeta potential variation in the flow direction (Case 2), infinitely wide channel geometry (2-D).

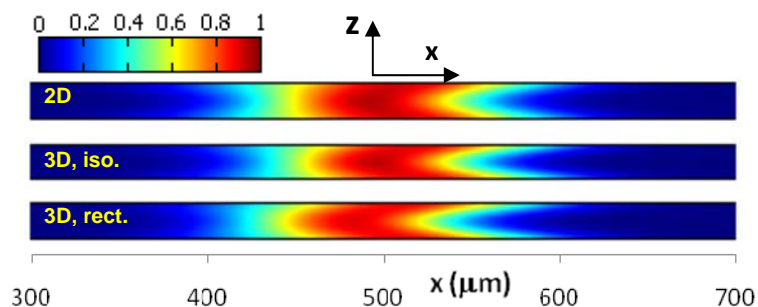


Figure 6-10. The cross sectional view of sample concentration profile at the mid-plane (x-z plane) after 0.2 sec for the case of step change of zeta potential in 2-D and 3-D channels (Case 2). “3-D, iso.” is for the isotropically-etched channel case and “3-D, rect.” is for the rectangular channel case.

Figure 6-10 shows the cross-sectional view of sample concentration profile at the mid-plane (x-z plane) at 0.2 sec for various channel cross sections. There is slight difference between different cross-sectional channels. The difference is more quantitatively demonstrated by taking cross sectional average in Figure 6-11 which shows the cross-sectional (y-z plane) average of sample concentration profile at $t = 0.0, 0.1$ and 0.2 sec for various channel cross-sections. The simulation results (2-D and 3-D) show that the dispersion rate is the highest for the rectangular cross-section case. (The difference between the peak concentrations of rectangular and 2-D cases at 0.2 sec is up to 6 %.) This tendency is because the additional wall effect (side walls) emerged in the transition from 2-D to 3-D increases as the width decreases. The comparison between the 2-D simulations and the 1-D simplified modeling results (D_{eff} was based on the 2-D cross-section and $\left| \overline{V_{eo}} - V_{eo} \right|$ was used for U in Eq. (6-3)) shows that the dispersion rate in the 1-D modeling is higher than the 2-D results. The difference in peak value is up to 24 % at 0.2 sec. This significant difference is because the Taylor modeling assumes that the shear distortion of a sample plug is very quickly diffused in the lateral direction, forming 1-D sample concentration

profile (or uniform in a cross-section) although, in reality, the lateral diffusion is not that fast. This over-diffusion in the Taylor dispersion modeling results in higher dispersion of sample than the actual data via full-dimensional simulation.

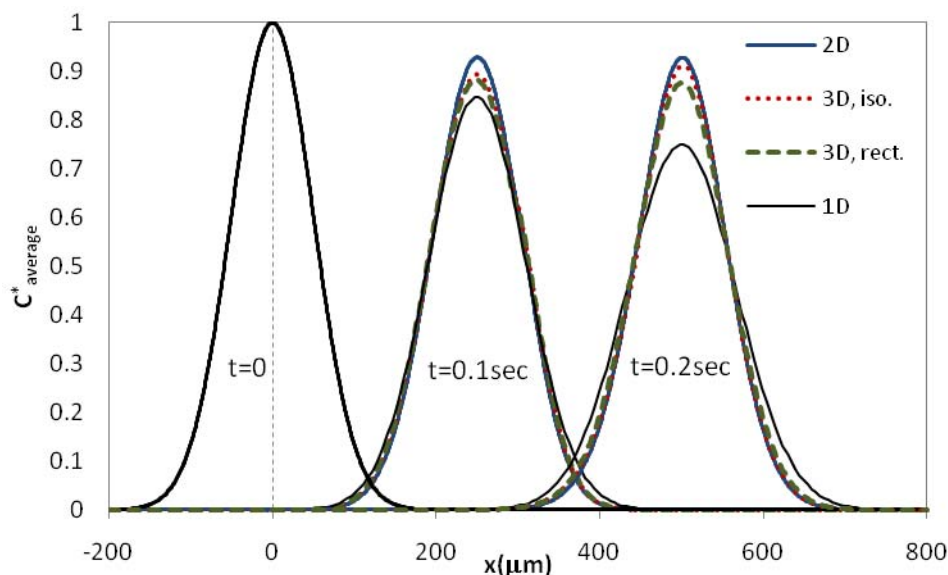


Figure 6-11. Cross-section averaged sample concentration distribution, C^* , at $t = 0, 0.1$ and 0.2 sec for 1-D, 2-D and 3-D channel cases with zeta potential variation in the flow direction (Case 2). ‘3-D, iso.’ is for the isotropically-etched channel case and ‘3-D, rect.’ is for the rectangular channel case.

Case 3. Electric conductivity (λ) variation due to the presence of a sample plug

A common case in which an internal pressure gradient is induced in microchip capillary electrophoresis is the conductivity variation across the sample band due to the presence of ionic species. Figure 6-12 shows the variation of three operating parameters, electric conductivity, electric field and pressure, along the middle line of the channel in the axial direction for the case of conductivity variation. These graphs show how those variables are correlated. The electric conductivity rises where the sample is located. The region of increased conductivity moves as the sample plug migrates as shown in Figure 6-12(a). The increase of conductivity at the sample site

lowers the local electric field and hence reduces electroosmotic velocity (slip velocity) at that location as shown in Figure 6-12(b). The decrease of local electroosmotic velocity in turn induces a favorable pressure gradient to maintain the flow rate constant through the channel as shown in Figure 6-12(c). Here, the species migration speed is affected not only by the electroosmotic flow variation but also by the electric field change. At the sample site, the lowered electric field slows down the electrophoretic migration speed of the sample. Because of the gradient of electrophoretic migration velocity, the sample is concentrated at the front of sample plug as the time passes. The conductivity profile sharply changes at the highly concentrated regions.

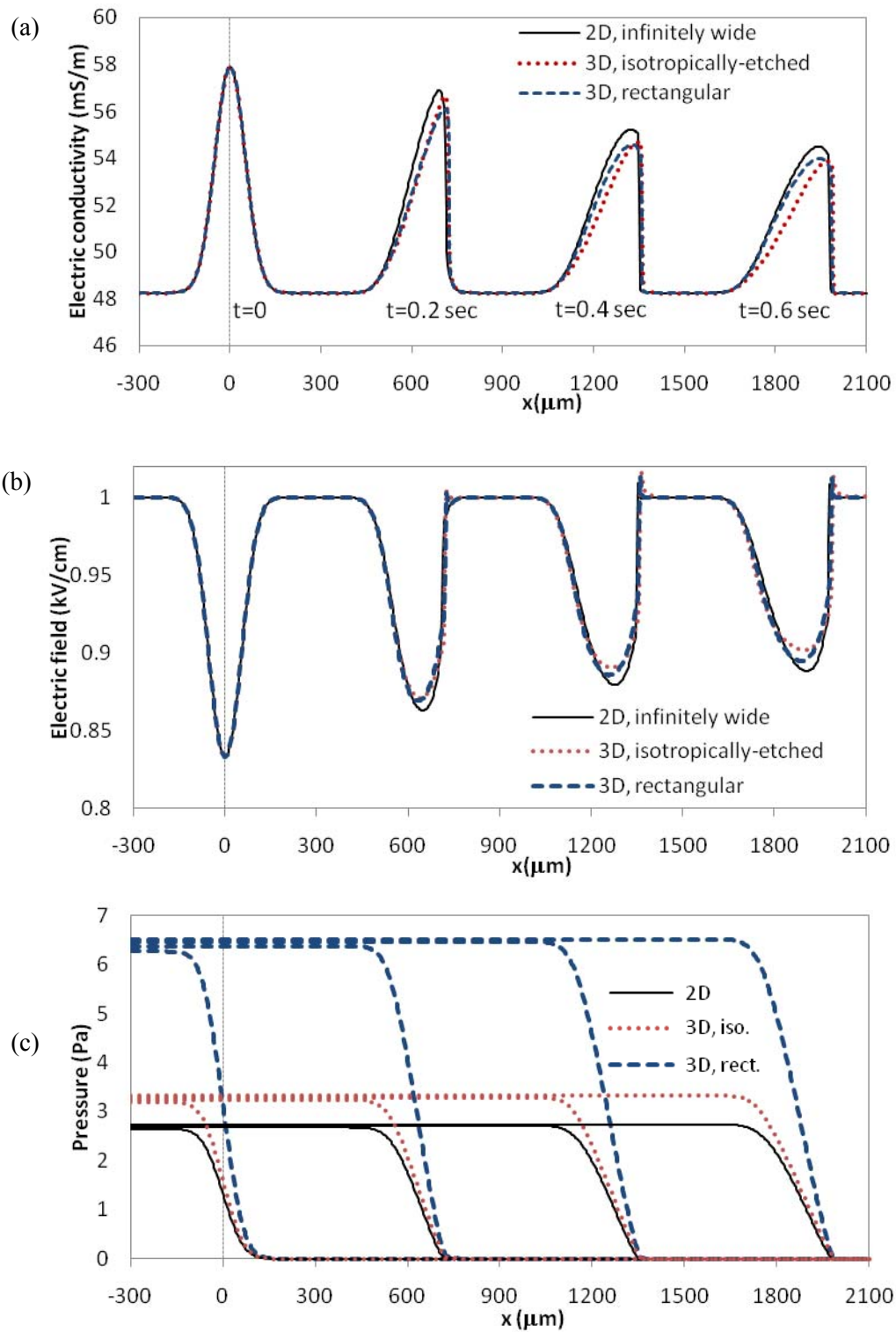


Figure 6-12. Variation of (a) electric conductivity, λ_{total} , (b) electric field and (c) pressure along the middle line ($y = z = 0$) of the channel in the axial direction with various times ($t = 0, 0.2\text{sec}, 0.4\text{sec}$ and 0.6sec) for Case 3.

Figure 6-13 shows the variation of sample concentration field with time. Figure 6-13(a) is the initial sample distribution and Figures 6-13(b) are sample distribution at $t = 0.3$ sec. Figure 6-13(b1) is for the 2-D channel case, Figure 6-13(b2) is for the rectangular channel case and Figures 6-13(b3-4) are for the isotropically-etched channel case. The figures show a clear distortion of sample plug due to the pressure gradient and the non-uniform electric field. It is noticeable that the distortion of sample appears more complicated than the distortion by a parabolic flow profile of pressure driven flow occurred in the case of zeta potential variation along the channel. This is because, in this case, the electric field variation also affects the motion of sample, resulting in more complicated correlation between three governing parameters (concentration, electric field and flow velocity). The arrows in Figure 6-13(b4) indicate relative flow velocity vectors ($\vec{V} - \vec{V}_{eo}$). The relative flow velocity vectors become significant only at the sample site. The relative velocity is negative near the wall whereas it is positive at the center. This velocity distribution elongates further the sample plug.

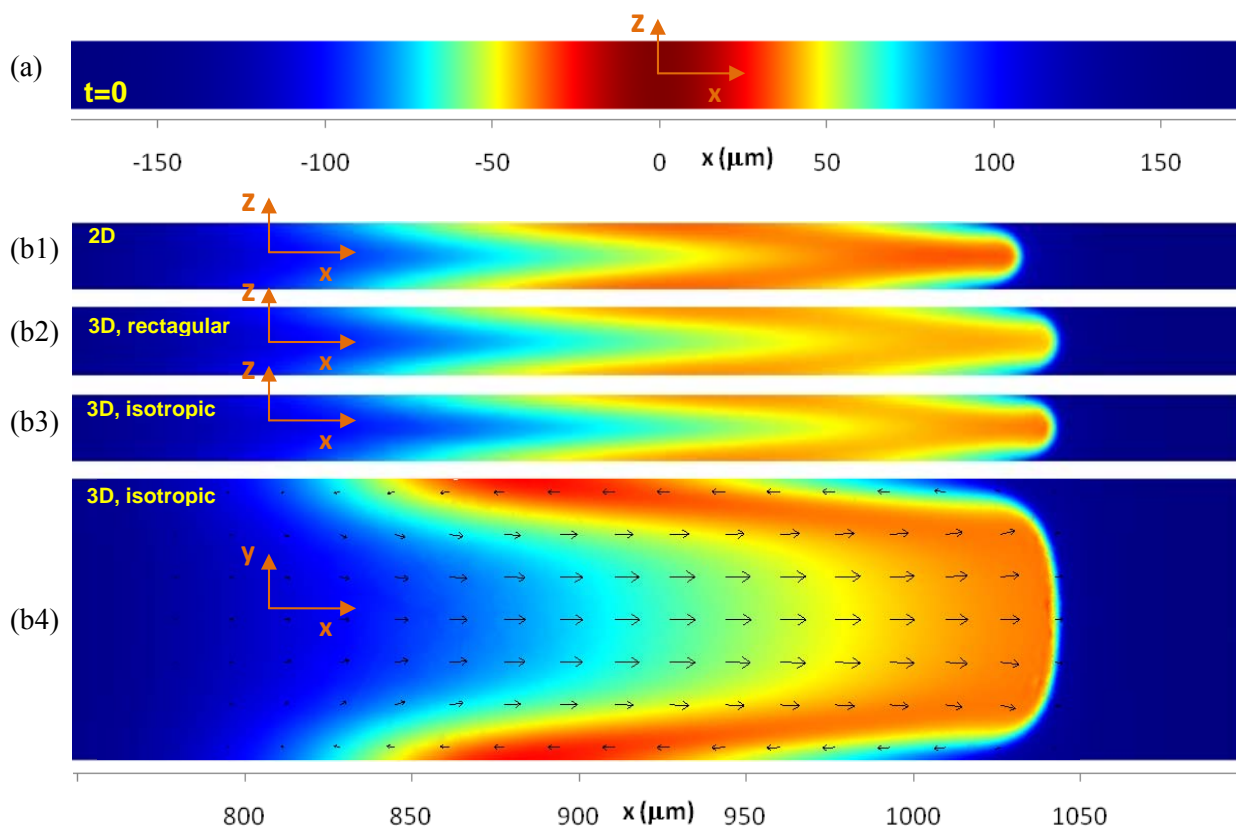


Figure 6-13. Variation of sample concentration with time (a: $t=0$) for Case 3. (b1) $t=0.3$ sec for 2D channel; (b2) $t=0.3$ sec for 3D rectangular channel; (b3) $t=0.3$ sec for 3D isotropically-etched channel, x-z plane; (b4) $t=0.3$ sec for 3D isotropically-etched channel, x-y plane. Arrows indicate relative flow velocity vectors ($\vec{V} - \vec{V}_{eo}$).

The above-mentioned simulation results clearly show that the dispersion of a sample plug under variation of zeta potential or conductivity contains highly multi-dimensional features. Therefore the full dimensional modeling is required for the accurate simulation of a microchip separation system rather than using simplified 1-D model. Because of the complete correlation between three operating parameters and highly time-dependent characteristics of the parameters,

it might not be even possible to develop a simplified 1-D dispersion model like the Taylor dispersion model for the case of conductivity variation.

Case 4. Applicability of 1-D Taylor dispersion model in 3-D microchannel flow

The Taylor dispersion modeling approximates the chemical species conservation equation in 1-D form as follows:

$$\frac{\partial C}{\partial t} + (V_{average} + \mu_{ep} E_x) \frac{\partial C}{\partial x} = D_{eff} \frac{\partial^2 C}{\partial x^2} \quad (6-20)$$

where $V_{average}$ is average flow velocity, E_x is x directional electric field and D_{eff} is apparent diffusion coefficient defined in Eq. (6-3).

The appropriateness of the 1-D Taylor dispersion model for a typical rectangular microfluidic channel was investigated by comparing the result of multi-dimension simulations with the result of 1-D simplified simulation via the Taylor dispersion model. A sample plug was initially distributed in a rectangular channel in a Gaussian formula with a certain standard deviation (σ_0), and it was dispersed with time under the shear motion of pressure driven flow. The key parameters determining the appropriateness of the Taylor dispersion model are the sample band width (σ), the average flow velocity (U), the diffusion coefficient (D) and the dimension of channel cross-section (H). Especially the ratio of the convective time scale (σ/U) to the transversal diffusion time scale (H^2/D) (denoted by $r = (\sigma_0/U)/(H^2/D)$) mainly determines the accuracy of the Taylor dispersion model for a microfluidic channel system. The selected channel geometry was a rectangular channel case for which β value in the Taylor dispersion model (Eq. (6-3)) is calculated to be 0.00837. The diffusion coefficient was fixed as a constant, $1 \times 10^{-10} \text{ m}^2/\text{s}$,

while other parameters were varied. The default case was $U = 1000 \mu\text{m/s}$, $\sigma_0 = 100 \mu\text{m}$ and H (channel width and height) = $20 \mu\text{m}$. The selected sets of parameters are listed in Table 2. These selections of parameters represent typical microfluidic flow environments. The sample plug was dispersed by the combination of molecular diffusion and shear motion of pressure driven flow.

Figure 6-14 shows the percentage difference of the sample band width (σ) between the 1-D simplified simulation with the Taylor dispersion model and the 3-D simulation (a rectangular channel case) as a function of traveling time. It is clearly shown that the difference becomes larger as the ratio (r) of the convective time scale to the lateral diffusion time scale decreases. In other words, the Taylor dispersion modeling loses accuracy as the initial sample band width (σ_0) decreases or the average flow velocity (U) increases or the lateral dimension of channel cross-section (H) increases. For the same reason, the percentage difference between 1-D and 3-D simulation data decreases with traveling time because the sample band width grows with traveling time. The highest error exists at the early stage of the injection. Considering that the behavior of early stage injection is important for fast assay microchip systems, the Taylor dispersion model does not properly capture the shear dispersion that arises in microchip device environment although the Taylor dispersion model may be appropriate for traditional non-microchip capillary devices that have much larger sample band and smaller electric field than the microchip cases.

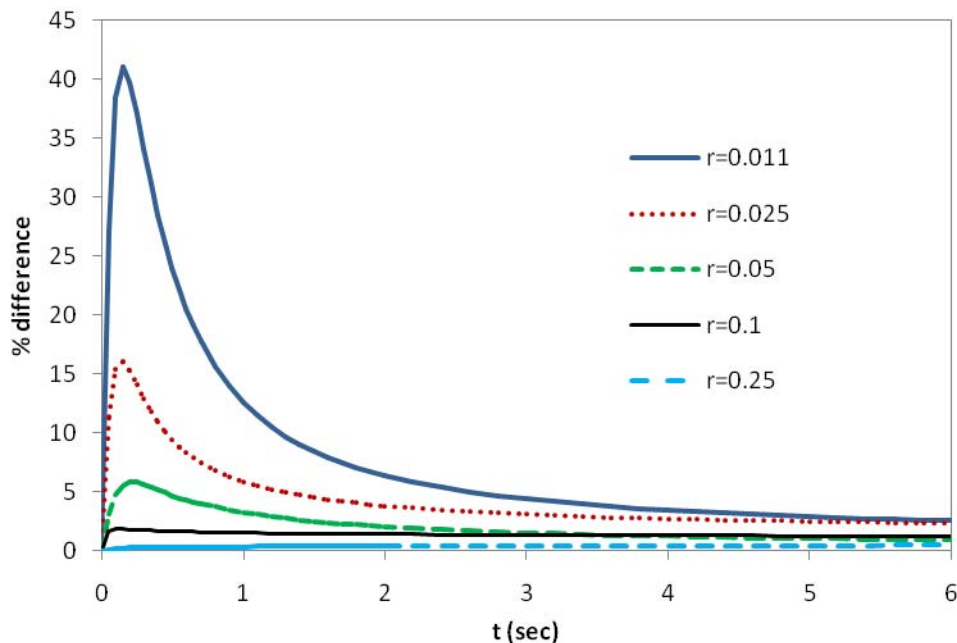


Figure 7-14. Percent difference, $\frac{(\sigma_{1D} - \sigma_{3D})}{\sigma_{3D}} \times 100$, of sample band width, σ , between 1-D and 3-D simulations for various ratios (r) of convection to lateral-diffusion time scales as a sample travels (Case 4).

6.5 . CONCLUSIONS

3-D characteristics of sample dispersion during electroosmotic migration when there is variation in surface or solution properties was investigated. Considering the fast growing computational power, the implementation of complex 3-D simulation is not unrealistic any longer. Most of the 3-D simulations carried out in this chapter required less than a day with a double Quad-core workstation.

A sample band was found to rapidly broaden when there is variation in surface or solution properties as the shear motion accelerates the dispersion. The sample plug under

different zeta potentials for top/sides and bottom substrates was dispersed by either one of the two mechanisms: shear motion dominated dispersion or a combined effect of shear motion and lateral diffusion. At a short traveling distance the shear motion dominates, while at larger traveling distances the combined effect of shear motion and lateral diffusion are important. The plate height (h) increased linearly with the traveling distance initially, indicating that the dispersion is proportional to the shear length, $\Delta V_{eo} t$, while, at a long traveling distance, the plate height plateaus to a value purely determined by the Peclet number. In microchip capillary electrophoresis, the shear motion dominated dispersion is more relevant since the traveling distance is relatively short. The band broadening rate increases linearly with the difference between the zeta potentials of the two substrates. When there is zeta potential variation in the longitudinal direction, the sample plug is bent due to pressure gradient induced by the zeta potential difference. The 1-D simulation with the Taylor dispersion modeling does not properly simulate the shear dispersion of a confined sample having a fast assay speed which is frequently encountered in a typical microchip device environment. The dispersion rate in the 1-D simplified model is higher than the 3-dimensional simulation result due to excessive diffusion in the Taylor dispersion model. Careful attention is required when the 1-D Taylor dispersion model is applied for microchip electrophoresis simulation. The complete correlation between operating parameters and time-dependent characteristics of all the parameters in conductivity variation cases make the Taylor dispersion ineligible for those cases. Three-dimensional modeling is required for accurate simulation of a microchip separation system when there are solution or surface property variations.

CHAPTER 7. CELL LYSIS AND SINGLE CELL ANALYSIS

7.1. INTRODUCTION

Single cell analysis indicates that the constituents of each single cell are examined. Thus, a cell must be lysed before analysis of cell ingredients. The lysis of cells is generally accomplished either chemically with detergents or physically (mechanical or electrical methods) by membrane rupture. Depending on assay requirements, different methods of on-chip cell lysis have been utilized. For protein extraction from a cell, detergents such as sodium dodecyl sulfate (SDS) and Triton X-100 have been successfully used for lysis. However, this method needs complex devices including injection channels and mixing to homogenize samples. In addition, detergents will often interfere with downstream assays and sometimes are not strong enough to activate lysis.

Lysis caused by irreversible electroporation has also been reported and successfully shown at the single cell level. The use of electric lysis as an alternative to chemical or other mechanical lyses has been motivated by its ability to achieve high local fields using integrated microelectrodes. External electric fields disrupt the transmembrane potential, generating micro-pores on the cell membrane. The micro-pores are resealable in a moment if the electric excitation is small. Electrical lysis devices use extreme conditions where the stability of the cell membranes is permanently disrupted, holes on the cell membranes are sustained, and intracellular materials are released. Electrical lysis is the most widely used in microfluidic cell lysis due to its simple structure and rapidity. It can greatly reduce purification steps for preparing bio-samples required in the chemical lysis method. The disruption time is as low as 33ms which is about eight times faster than lysis by SDS. A proper intensity of electric field may need to be applied in order to selectively disrupt the cell membrane while keeping the transorganelle membrane safe. A

numerical analysis shows that the most obvious choice for selective electroporation is by a DC electric field. However, the high DC electric field required for cell lysis also results in water electrolysis, creating hydrogen and oxygen gas bubbles and causing extreme pH conditions near the electrodes. The water electrolysis can be suppressed by adopting a high frequency AC electric field [116].

Electrical cell lysis by applying an electric field through a channel [144] requires a high operational voltage between a pair of external electrodes for acquiring sufficient electric field (1.2 kV/cm) strength to disrupt cells. Some other electrical lysis methods [112, 116] used saw shape electrodes to generate a local high electric field. However, it is difficult to control cell delivery and increase the throughput of assay with the local electric lysis method. Instead, a continuous cell lysis method with a converging and diverging channel geometry was adopted to provide potential of a high throughput assay as illustrated in Figure 2-22 [118]. The serial geometry will be suitable for continual high-throughput CE system by placing a separation channel downstream. From electric current conservation, the following electric field is obtained.

$$I = J_c A_c = \sigma E_c A_c = J_t A_t = \sigma E_t A_t$$

where subscripts c and t denote ‘channel’ and ‘throat’ regions, respectively. For a uniform height channel geometry, this equation becomes

$$E_c W_c = E_t W_t$$

where W is the channel width at a local position. In other words, the local electric field is inversely proportional to the local channel width. One advantage of this geometry is that the severe Joule

heating at the throat region can be effectively discharged because that region is small. Lee and Cho [118] reported that 100% red blood cells were lysed in their device with $E_t=1.2$ kV/cm. But this cell lysis method contains some problems. Firstly, the diverging part may disturb or dilute the sample plug (intracellular material released from single cells). Secondly, if this lysis component is continuously connected to the electrophoretic separation part, it is difficult to maintain the sufficient electric field. This will be discussed with numerical simulation results in Section 7.4.

Osmotic lysis occurs when a cell bursts due to an osmotic imbalance that has caused excess water to move into the cell. It occurs in a hypotonic environment, where water diffuses into the cell and causes its volume to increase. If the volume of water exceeds the cell membrane's capacity, the cell will burst. Lillard et al.[74] used the osmotic lysis method for red blood cell single-cell electrophoresis. They introduced single cells to 50mM H_3PO_4 solution, which has a lower ionic strength than the isotonic condition. Thus the osmotic pressure inside the cell caused cell lysis when the buffer solution was drawn over the cell.

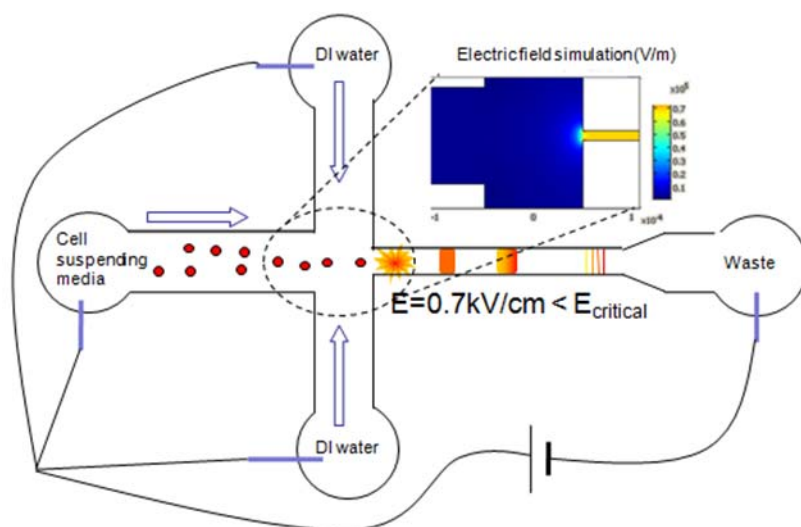


Figure 7-1. Combination of electric and osmotic cell lysis method to achieve longer separation channel and high throughput continuous cell lysis.

Combinations of different cell lysis methods also have been used to improve the cell lysis success rate. Gao et al. used a combination of shear force, basic buffer conditions (pH=9.2) and an electric field to effectively lyse cells even with a relatively low electric field (280V/cm) [144]. Mellors et al.[170] used a combination of electric field and osmotic pressure. Xu and Ying [28] used a combination of electric field and chemical lysis. The currently proposed idea is a combination of electric field, osmotic pressure and mechanical stress by having a very narrow region as illustrated in Figure 7-1.

7.2 . MICROFABRICATION METHOD: GLASS MICROCHIP FABRICATION

The microchannel devices used in this study were made of borosilicate (pyrex) glass or soda lime glass. 3x3” borosilicate glass plates (or 4x4” soda lime glass) with chrome and AZ photoresist coating that were purchased from Telic. A photomask with a certain channel design was placed on top of a chrome glass substrate, and this substrate was exposed to UV light (365 nm) with a dose of 200 mJ/cm². The AZ PR pattern was developed in a mixture of AZ400 and DI water with the volume ratio of 1 to 7. The development time was about 34 sec. After developing, the substrate was immersed in chrome etchant, which was manufactured by Transene. The substrate was then hard-baked on a hot plate at 100 °C for 30 min. The hard baked plate was cut by a diamond pen if needed. The next step was wet etching to form engraved shapes on the glass substrate. Before wet etching, kapton tape was attached on the backside of the glass substrate in order to prevent etching on the backside; backside etching may be non-uniform because of insufficient etchant supply underneath a substrate. The etching solution is a mixture of 79 ml DI water, 17ml nitric acid and 20ml 49% HF. The etch rate with this solution is 0.5 μm/min for borosilicate glass and 5 μm/min for soda lime glass. The 15 μm depth engraved patterns were

fabricated. After wet etching, holes were made by a diamond drill bit (1.5 mm diameter) to form inlets and outlets. The diamond drill bit was operated at a high speed (54000 rpm at 90 psi) spindle by compressed air (65 psi). Before drilling, a glass piece was attached on the backside of the substrate to prevent creating faulty chips, and a thermal glue gun was used for attaching the backing glass. The glass substrate was then cleaned by sonication (30 min) to remove glass dust from drilling and residual from the wet etching process, and PR was removed by either organic solvent or Piranha solution (a mixture of sulfuric acid and hydrogen peroxide (3:1) at 85 °C). The chrome layer on the substrate was then removed by chrome etchant. The substrate with engraved patterns and another piece of the same type of glass were then cleaned in Piranha solution for 30 min and RCA solution (DI water, NH₄OH, H₂O₂; volume ratio of 5:1:1) at 80 °C for 20 min. After carefully rinsing with DI water, the two glass plates were placed on top of each other and placed in a furnace. A slight press can be achieved by placing a Macor plate on top of the glass plates. The thermal bonding was taken slightly above the glass transition temperature of the material for 4 hr (borosilicate: 610 °C, soda lime: 570 °C). The temperature ramping rate was 10 °C/min. If any non-bonding areas were found, further thermal bonding was performed by placing another weight (a Macor plate) on that area. After bonding was complete, pipette tips (cutting off the sharp part) were glued with 30 min-epoxy to serve as reservoirs.

7.3 . MICROCHIP ELECTROPHORESIS: PINCHED INJECTION

One of the most popular applications of microchip CE is the analysis of biochemical molecule mixtures with a pinched injection method. The microchip - LIF system was tested by performing pinched injection and separation prior to single cell analysis.

The pinched injection can be performed in cross or double-T channels as illustrated in Figure 2-29. The pinched injection is usually completed in two modes; “sample loading” mode

and “dispensing” mode. In the sample loading mode, the sample is introduced into the cross region by electroosmotic flow from Sample to Waste reservoir. The pinching action by electroosmotic flows from Collect and Buffer reservoirs to Waste reservoir, which confines the sample to adequate separation in the subsequent step. In the dispensing mode, the applied potential is changed to have electroosmotic flow direction from Buffer reservoir to all the other reservoirs. In this flow direction, the field behind an injected sample plug can be kept clean and the signals from separated analytes are not disturbed. Further discussions on sample loading and injection methods can be found in [59, 141, 143].

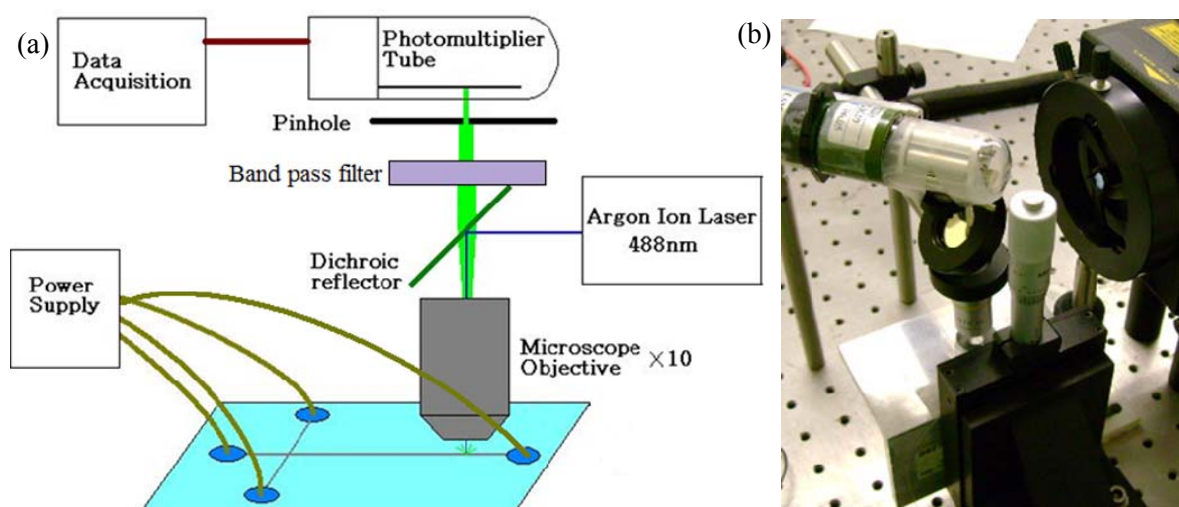


Figure 7-2. (a) Schematic of microchip CE-LIF system and (b) the actual experimental setup used in this study

Figure 7-2 shows the schematic diagram of the experimental setup used for the current study which is a typical microchip CE-LIF system. The LIF setup consists of a laser system (488nm Argon ion laser), optical filters (dichroic filter: Omega, QMAX_DI500LP, band pass filter:) and a photomultiplier tube (Hamamatsu R9220). Platinum wire electrodes were inserted

into the reservoir holes and DC electric voltage was applied through the wires by a high voltage power supply (Labsmith HVS448).

Figure 7-3 shows dimensions of the channel design. The sample was 0.5X PBS, containing a small amount of fluorescein sodium and dichlorofluorescein. For the sample loading step, the electric potential set of $\Phi_S = 400V$, $\Phi_B = 300V$, $\Phi_W = 0V$ and $\Phi_C = 800V$ was applied on the reservoirs. This electric potential set made the electric field set of $E_S = 300V/cm$, $E_B = 100V/cm$, $E_W = -500V/cm$ and $E_C = 100V/cm$. For the dispensing step, the electric potential set of $\Phi_B = 1500V$, $\Phi_S = \Phi_W = 900V$ and $\Phi_C = -1500V$ was applied on the reservoirs. This electric potential set made the electric field set of $E_B = 953V/cm$, $E_S = E_W = -247V/cm$ and $E_C = -459V/cm$. Figure 7-3b shows an image captured with a CCD camera through fluorescence microscope (Nikon Eclipse ME600) for pinched injection of the sample. The CCD image clearly shows a sample plug was injected after switching the potential set from the loading stage to the dispensing stage. Figure 7-4 is the electropherogram using the pinched injection conditions. It shows successful separation of two mixed chemicals by capillary electrophoresis. It was reported that both fluorescein and dichlorofluorescein are negatively charged at $pH > 4$ and the apparent mobility ($\mu_{eo} + \mu_{ep}$) of fluorescein is higher than that of dichlorofluorescein for any ionic strength and pH values [204]. According to that report, the firstly arrived peak should represents fluorescein and the last peak represents dichlorofluorescein. Another interesting aspect is that there is a small peak between the two large signals.

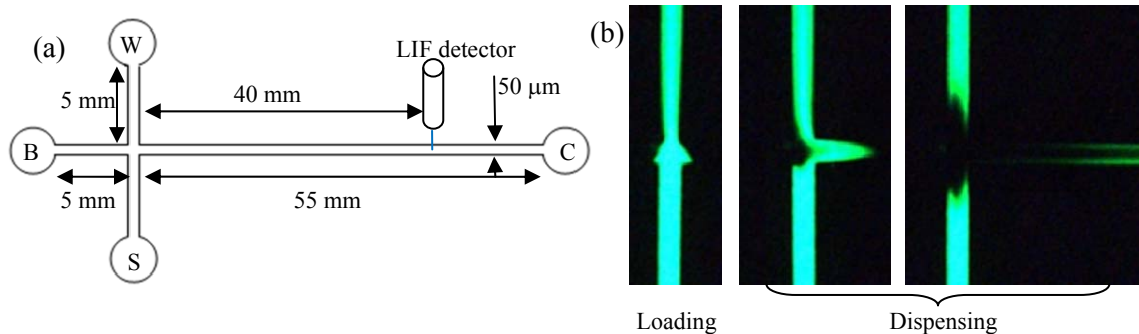


Figure 7-3. (a) Dimensions of the cross-channel design and (b) pinched injection.

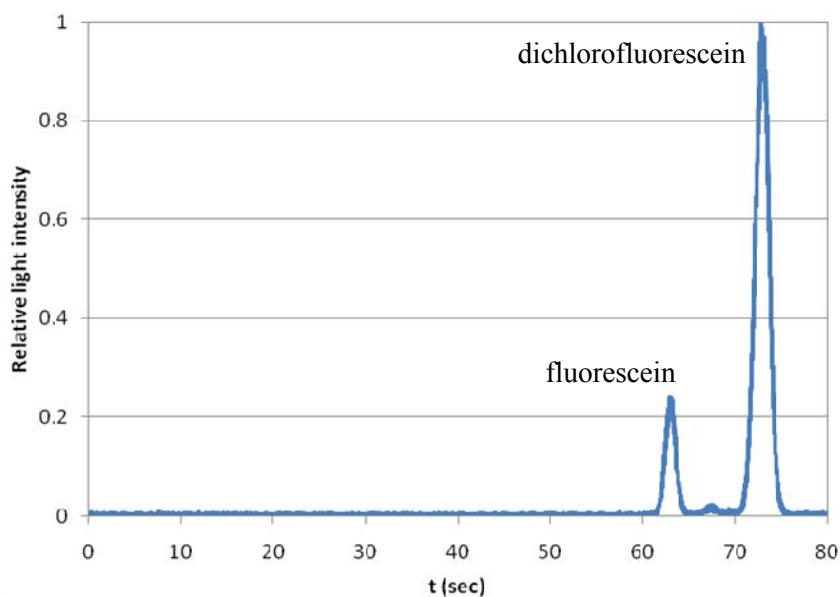


Figure 7-4. Electropherogram of pinched injection of sample containing fluorescein sodium and dichlorofluorescein.

7.4. CONTINUOUS CELL LYSIS

Human red blood cells were used to verify the performance of the current micro chip device. The running buffer was phosphate buffered saline (PBS) 1X. Platinum electrodes were inserted into the reservoirs, and a DC electric field was applied while RBC lysis was observed under a microscope. In order to have the osmotic lysis effect in addition to electric lysis effect, ‘North’

and ‘South’ reservoirs were filled with DI water while the channel and other reservoirs were filled with the running buffer. 3000 V was applied at ‘East’ reservoir while all the other reservoirs were grounded. The electric field was solved with COMSOL multiphysics. The simulation result shows the maximum electric field is 0.7 kV/cm at the narrow channel region (20 μm) as seen in Figure 7-5b. This electric field is not sufficient to lyse cells according to a reference [118] (the critical electric field for red blood cell lysis is about 1 kV/cm). However, with the help of the osmotic lysis effect, cells were lysed when they entered the narrow channel region as shown in Figure 7-6. Another suggested cell lysis method is a combination of electric field and mechanical shear stress by having a shallow region in the narrow channel. The shallow region can be fabricated by properly controlling the glass etch time.

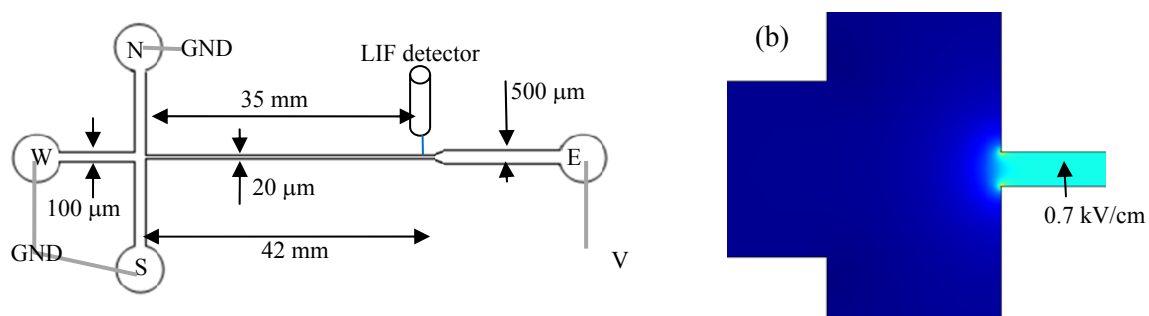


Figure 7-5. (a) Dimensions of the continuous cell lysis device and (b) electric field simulation results at the cross region.

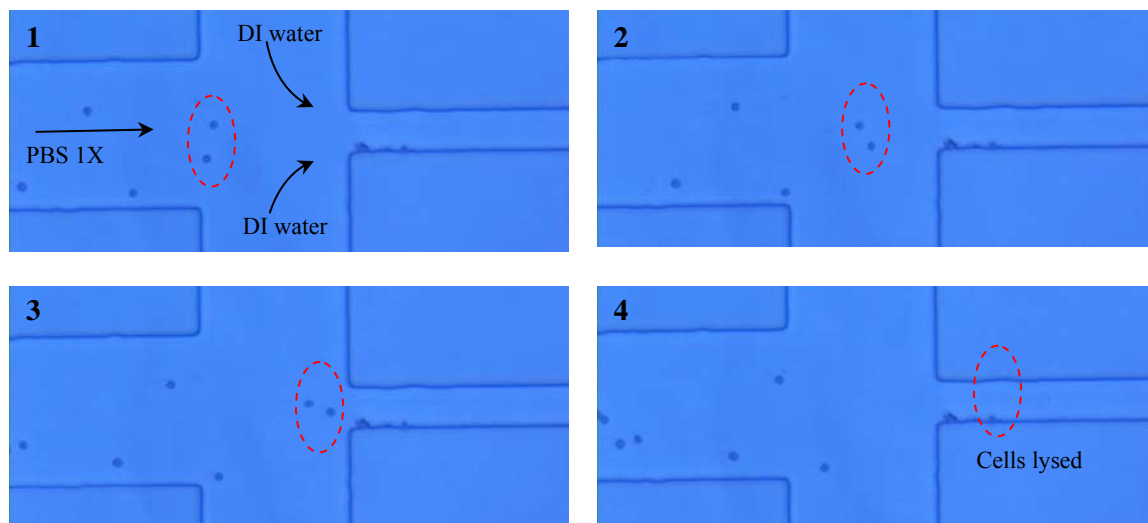


Figure 7-6. Sequential images of continuous cell lysis with combination of electrical and osmotic cell lysis methods. The time interval is 0.2 sec. At stage 4, cells were lysed.

7.5 . SINGLE RED BLOOD CELL ANALYSIS

In this work, labeling was tried with two different labeling agents; fluorescein isothiocyanate (FITC) and 2,3-naphthalenedicarboxaldehyde (NDA). After checking the fluorescence, it was found that FITC-labeled cells emit much brighter fluorescent light as shown in Figure 7-7. Thus, FITC was selected as a labeling agent for this fundamental cell analysis, although FITC is not able to penetrate cellular membranes. FITC cell labeling was done in an incubator for more than 2 hours, following the protocol from [205]. After cell labeling was finished, the remaining fluorescent agent was removed by centrifuge. The CE recordings of FITC-labeled cells following cell-lysis resulted in an electropherogram as shown in Figure 7-8. It shows three peaks. It is not clear whether the signals are from different membrane proteins or from the whole single cells.

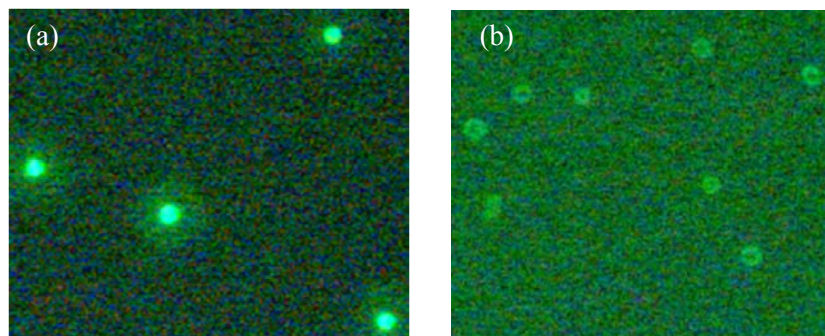


Figure 7-7. Fluorescence image of red blood cells labeled by (a) fluorescein isothiocyanate (FITC) and (b) 2,3-naphthalenedicarboxaldehyde (NDA).

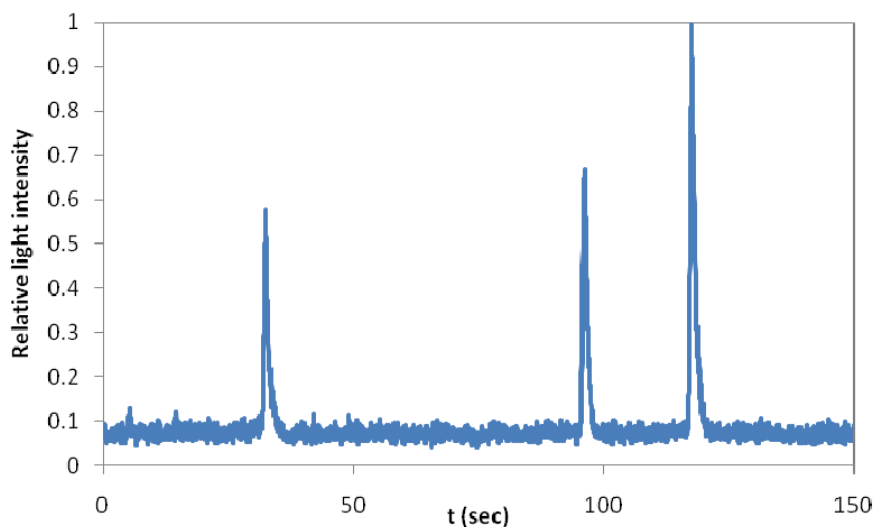


Figure 7-8. Electropherogram after lysing red blood cells. Before this experiment, cells were labeled with (a) fluorescein isothiocyanate (FITC).

7.6 . CONCLUSIONS

The analysis of intracellular constituents through a separation method requires cell lysis. The microchip CE-LIF system developed successfully demonstrated sample separation via a pinched injection. Two fluorescent dyes in a mixture were separated while running capillary zone electrophoresis. The proposed design of cross-channel microchip had osmotic and electrical cell

lysis functions in it. The effective cell lysis was demonstrated with human red blood cells. The single cell analysis using human red blood cells also demonstrated the successful cell lysis. Combination of electric field and mechanical shear stress for cell lysis is also suggested. Mechanical shear stress can be imposed by having a shallow region near the entrance of the narrow channel, which can be made by controlling glass etch time.

CHAPTER 8. CONCLUSIONS & FUTURE WORK

AC and DC electrokinetic phenomena are very useful tools for particle or fluid manipulation for micro total analysis systems. In this thesis, AC and DC electrokinetic phenomena were investigated to better understand them for the realization of microchip capillary electrophoresis for single cell analysis. AC-DC electroosmotic flow interaction was studied by observing the motions of polystyrene microbeads suspended in deionized water in a microchannel as the main AC and DC electrokinetics parameters were varied. Numerical simulations of the flow field were also performed using COMSOL Multiphysics software. Particle-particle interactive DEP force under AC electroosmosis and electrothermal flow conditions was studied by performing experiments on a microchannel - microelectrode system containing polystyrene beads and comparing the experimental results with numerical simulation results using the Maxwell stress tensor calculation. The Maxwell stress tensor analysis demonstrated how the DEP force on a particle was affected when neighboring particles were closer. Accurate numerical studies were performed for understanding 3-D characteristics of the dispersion of sample species that is injected and carried by electroosmotic flow in microchip capillary electrophoresis devices. The following three cases were investigated; 1) non-rectangular cross section of microchannels, 2) different zeta potential for the top and bottom microchannel substrates, and 3) development of internal pressure gradient by variation of electric or electrokinetic properties along the channel direction. The results of the numerical study for the above-mentioned 3 cases clearly show that 3-D modeling is crucial for accurate predictions of sample injection and migration in microchip electrophoresis system. More specifically, the non-rectangular cross section of microchannel affected the shape of the injected sample plug in the pinched-injection system while either the zeta potential variation or local pressure gradient developed shear motion during the migration of sample. The cell lysis is also very important because the release of intracellular components

determines the initial sample band and thus, separation efficiency. Also in order to realize high-throughput single-cell analysis, a reliable continuous cell lysis method was developed.

8.1 . ACHIEVEMENT OF AIMS

Aim 1. To perform experimental and numerical studies on AC electrokinetic particle manipulation in a microchannel.

The effect of DC electroosmotic flow on AC electrokinetic phenomena has been investigated through experimental studies and numerical simulations. The motions of polystyrene microbeads suspended in deionized water in a microchannel were observed as major AC and DC electrokinetics parameters were varied. Numerical simulations of flow field were performed using Comsol Multiphysics. At low frequencies where AC electroosmosis becomes dominant and particles are collected in the middle of the electrodes, shifts of the collected particles were observed due to the force balance between AC electroosmosis and DC electroosmosis. The particle shift increased as DC electroosmosis increased. Flow field were calculated by numerical simulation. The distortion of the circulating flow pattern typical for AC electroosmosis was clearly observed as the DC electroosmosis increased. The flow velocity was plotted and the zero velocity location in the numerical simulation showed good agreement with experimental results. At higher frequencies where dielectrophoresis was dominant, particles were almost immediately swept away by DC electroosmotic flows, indicating that dielectrophoresis (both positive and negative DEP) was significantly deteriorated by DC electroosmotic flows.

Diverse behaviors of microbead particles subject to AC electroosmosis and electrothermal flow conditions through experimental and numerical studies were also investigated. Typical particle behaviors were monitored as the main parameters, such as media conductivity and the frequency of the applied voltage, were varied, and the experimental

observations were compared with numerical simulation results. Since the conventional dipole method for DEP calculation does not consider the effect of neighboring particles and other solid surfaces, we used Maxwell stress tensor method in our numerical study to understand the dielectrophoretic particle-particle interactions. Distinct particle behaviors under ACEO and ETF conditions and diverse particle-particle interactions, such as particle clustering, interval between particles, chain formation, and disc formation, have been analyzed and explained based on the numerical simulation results. For instance, ACEO flow conditions at low media conductivity ($\sigma \sim 2 \mu\text{S/cm}$) resulted in repulsive DEP among particles collected in the middle of electrodes while a higher conductivity ($\sigma \sim 20 \mu\text{S/cm}$) caused particle aggregation. The numerical simulation results showed that the repulsive DEP particle-particle interaction is significant at $2 \mu\text{S/cm}$ but diminishes at $20 \mu\text{S/cm}$. ETF conditions induced particle chain and disc formation $15 \mu\text{m}$ above the electrode edge, and they remained in rotational motion. The calculation of the attractive and repulsive DEP particle-particle interaction was performed for this case, and the unique particle behaviors were explained.

Aim 2. To perform 3-D accurate numerical studies on electroosmotic sample injection and migration to optimize the channel design and operational parameters for effective separation.

The 3-D characteristics of the loading and dispensing of sample species during electroosmotic pinched injection in microchip capillary electrophoresis systems with non-rectangular cross sections were investigated. An isotropically-etched channel resulted in a vertically non-uniform sample plug in the loading stage. The cross-sectional sample profile is distorted like a “V” shape or a “Λ” shape depending on the sample loading mode (narrow or wide sample) due to the 3-D non-rectangular geometry of the channel. In the sample injection simulation, the 3-D simulation data showed a clear difference from 2-D simulation data. 2-D

simulations employing the top and bottom widths resulted in 3~10 % and 28~40 % errors in injection qualities, respectively. Instead, it was observed that the 2-D simulation data using the width calculated from the equivalent cross-sectional area of the 3-D channel shows good agreement with the 3-D simulation data (less than 3 % error). This observation gives a guideline as to what width should be selected for a simulation on a pinched injection system when the computer capability limits one to a 2-D simulation. As the channel height decreases while the channel width remains fixed, it was found that the 3-D effects decrease and the 3-D results approach the 2-D results. The dispersion of a sample plug during electroosmotic migration in a straight channel is also influenced by the geometry when the initial sample plug has laterally non-uniform distribution. Thus, for an accurate simulation of injection and migration of a sample in a pinched injection device, 3-D simulations provide added insights to the flow field and sample dispersion.

3-D characteristics of sample dispersion during electroosmotic migration when there is variation in surface or solution properties was investigated. Considering the rapidly expanding computational power, the implementation of complex 3-D simulations is not unrealistic any longer. Most of the 3-D simulations carried out in this paper required less than a day with a double Quad-core workstation.

A sample band was found to rapidly broaden when there is variation in surface or solution properties as the shear motion accelerates the dispersion. The sample plug under different zeta potentials for top/sides and bottom substrates was dispersed by one of two mechanisms: shear motion-dominated dispersion or a combined effect of shear motion and lateral diffusion. At a short traveling distance, the shear motion dominates, while at larger traveling distances, the combined effect of shear motion and lateral diffusion are important. The plate height (h) increased linearly with the traveling distance initially, indicating that the dispersion is

proportional to the shear length, $\Delta V_{eo} t$, while, at a long traveling distance, the plate height plateaus to a value purely determined by the Peclet number. In microchip capillary electrophoresis, the shear motion dominated dispersion is more relevant since the traveling distance is relatively short. The band broadening rate increases linearly with the difference between the zeta potentials of the two substrates. When there is zeta potential variation in the longitudinal direction, the sample plug is bent due to pressure gradient induced by the zeta potential difference. The 1-D simulation with the Taylor dispersion modeling does not properly simulate the shear dispersion of a confined sample having a fast assay speed, which is frequently encountered in a typical microchip environment. The dispersion rate in the 1-D simplified model is higher than the 3-dimensional simulation result due to excessive diffusion in the Taylor dispersion model. Careful attention is required when the 1-D Taylor dispersion model is applied for microchip electrophoresis simulations. The complete correlation between operating parameters and time-dependent characteristics of all the parameters in conductivity variation cases make the Taylor dispersion ineligible for those cases. Three-dimensional modeling is required for accurate simulation of a microchip separation system when there are solution or surface property variations.

Aim 3. To perform experimental investigation of cell lysis methods and to identify optimal design and operational parameters for a rapid and effective cell lysis.

The analysis of intracellular constituents through a separation method necessitates cell lysis. Initial sample injection is a key element that determines the separation efficiency of capillary electrophoresis. Therefore, the cell lysis must be done in such way that the released intracellular components may have a very narrow initial band. The intracellular biochemical reaction due to external stimuli should also be minimized through a rapid cell lysis. Combination

of electrical and osmotic cell lysis methods was developed for a continuous and high-throughput single-cell analysis and for rapid and effective cell lysis. Red blood cells were considered the first target objects since blood can be taken easily from patients and it contains a massive amount of information about the functioning of all tissues and organs in the body [73].

The microchip CE-LIF system demonstrated sample separation via a pinched injection. Two fluorescent dyes in a mixture were separated while running capillary zone electrophoresis. The proposed design of cross-channel microchip had osmotic and electrical cell lysis functions in it. The effective cell lysis was demonstrated with human red blood cells. The single cell analysis using human red blood cells also demonstrated successful cell lysis.

8.2 . FUTURE WORK

Several future tasks are suggested in this section. Those tasks can expand upon the achievements made through this thesis work, in order to fully complete the objective of developing high-throughput single cell analysis lab-on-a-chips.

(1) Complete analysis of interaction between AC & DC Electrokinetic phenomena

The complete interaction between the flow field, the electric field and the ion concentration may need to be solved for an accurate solution. In the convectional analysis of electroosmosis, several assumptions were involved as follows,

DC electroosmosis

- 1) Thermodynamic equilibrium; the ion concentration in electrolyte follows the Boltzmann distribution
- 2) Neutral net charge and symmetric electrolyte

3) Debye-Huckel approximation; small value of

4) Small Debye thickness

AC electroosmosis

In addition to the above assumptions used for DC electroosmosis, the following additional assumptions were adopted,

5) Every variable oscillates in a harmonic way (linear approximation)

6) Circuit model for electric double layer

7) Simplified geometry; infinitely wide electrodes and infinitesimally narrow gap between electrodes

Particularly, assumption 7) limits the usage of the equation for 2-D interdigitated electrodes. To understand the interaction between the flow field, the electric field and the ion concentration, all above assumptions should be relieved. After relieving all or parts of the above assumptions, the complete analysis can be done by either transient analysis of AC oscillation effect while finding proper boundary condition on the Stern layer on electrodes (this is more rigorous analysis) or stationary electric circuit analysis while finding a proper capacitance model for the Stern layer. The complete analysis will give better agreement with the experimental observations than Chapter 3.

(2) Complete analysis of particle behavior under AC electrokinetic phenomena

Particles under AC electric field experience various forces. Other than electrokinetic forces acting on particles, there are two more interactive forces between two solid bodies (particle-particle or particle-surface) that need to be considered. One is the van der Waals force, which is an attractive force generated by dipole-dipole interactions and electron fluctuation in two

particles. This force is magnified when particles are near each other and can be of the same order as the DEP force [35]. The other force is the double layer interaction. The double layer force between the same type of particles is repulsive because the particles must form the same polarity EDL and, as the two particles approach each other, squashing double layers into a smaller space induces an osmotic pressure [177]. The repulsive double layer force is proportional to $e^{-\kappa y}$ while the attractive van der Waals force is proportional to y^{-2} , where y is the distance between two spherical surfaces [177]. The combined force graph in DLVO analysis [177] shows that the van der Waals attraction dominates over the repulsive double layer interaction at very small or very large distances (y). In other words, two particles at a long distance from each other experience a weak attractive force and if two particles happen to get very close, they will experience a strong attractive van der Waals force and form a group. An attractive double layer force can be also generated between asymmetric surfaces, such as an electrode surface and a particle. The complete force analysis on AC electrokinetically driven particles requires calculation of the van der Waals force and the double layer interaction. Along with complete ACEO analysis, the complete analysis of particle-surface interaction will explain the complicated behaviors observed in Chapter 4.

(3) Application of AC and DC electrokinetics for cell manipulation

AC and DC electrokinetic phenomena such as electrophoresis, electroosmosis, dielectrophoresis, AC electroosmosis, and electrothermal force have drawn much attention in the microfluidics and lab-on-a-chip communities since those techniques have a great potential for effective manipulation of small particles and fluids in microchannel environments. However, there are some limitations in those techniques. Firstly, some phenomena occur only in extreme conditions. For example, ACEO occurs with very low conductivity where biological cells cannot

survive due to osmotic stress. Secondly, particle manipulation is often effective near electrodes. Thirdly, particle trapping is often irreversible or a strong electric field near electrodes damages particles. Chemical release due to a strong electric field may increase Joule heating and damage electrodes. Fourthly, multiple electrokinetic phenomena can occur at the same time as discussed in Chapter 4. Because of these issues, direct application of electrokinetic phenomena to single-cell analysis microchip may require more rigorous research along with the fundamental studies performed in this thesis and other suggested works mentioned in this section.

(4) *High-throughput single cell analysis*

One of the final goals of a vast amount of research on lab-on-a-chip is to develop high-throughput single cell analysis microchip. To achieve this goal, much further research on each component of lab-on-a-chip still needs to be done. The components include cell manipulation, cell lysis, preconcentration, separation and detection as mentioned in Chapter 2.

REFERENCES

1. Bodey, B., *Expert Opin. Biol. Ther.*, 2002. **2**: p. 371.
2. Fink, L., et al., *Exp. Toxicol. Pathol.*, 2006. **57**: p. 25.
3. Trumper, L., et al., *Single-cell analysis of Hodgkin and Reed-Sternberg cells: molecular heterogeneity of gene expression and p53 mutations*. *Blood*, 1993. **81**: p. 3097-3115.
4. Pop, S.M., et al., *Single cell analysis shows decreasing FoxP3 and TGFβ1 coexpressing CD4+CD25+ regulatory T cells during autoimmune diabetes*. *Journal of Experimental Medicine*, 2005. **201**: p. 1333-1346
5. SATOSHI, I., *Surveillance study of autoimmune disease. Single-cell level analysis of T cell cytokine infiltrating kidney of patients with lupus nephritis*. 2004: p. 118-120.
6. Ferrell, J.E.J. and E.M. Machleder, *The biochemical basis of an all-or-none cell fate switch in Xenopus oocytes*. *Science*, 1998. **280**: p. 895.
7. Huang, T.-Y., et al., *Heterogeneity of [Ca²⁺]_i signaling in intact rat aortic endothelium* *FASEB Journal*, 2000. **14**: p. 797.
8. Marcus, J.S., W.F. Anderson, and S.R. Quake, *Parallel Picoliter RT-PCR Assays Using Microfluidics*. *Analytical Chemistry* 2006. **78**: p. 956.
9. Negulescu, P.A., N. Shastri, and M.D. Cahalan, *Intracellular calcium dependence of gene expression in single T lymphocytes* *Proceedings of the National Academy of Sciences of the United States of America*, 1994. **91**: p. 2873.
10. Teruel, M.N. and T. Meyer, *Parallel single-cell monitoring of receptor-triggered membrane translocation of a calcium-sensing protein module*. *Science*, 2002. **295**(1910).
11. Levsky, J., et al., *Single-cell gene expression profiling*. *Science*, 2002. **297**: p. 836-840.
12. Raj, A., et al., *Stochastic mRNA synthesis in mammalian cells*. *PLoS Biol.*, 2006. **4**: p. 1707-1719.
13. Chang, H., et al., *Transcriptome-wide noise controls lineage choice in mammalian progenitor cells*. *Nature*, 2008. **453**: p. 544-547.
14. Dolmetsch, R.E., K. Xu, and R.S. Lewis, *Nature*, 1998. **392**: p. 933-936.
15. Meredith, G.D., et al., *Nat. Biotechnol.*, 2000. **18**: p. 309-312.
16. Mاتيoli, G.T. and H.B. Niewisch, *Electrophoresis of Hemoglobin in Single Erythrocytes*. *Science*, 1965. **150**.
17. Zhang, Z., et al., *One-dimensional protein analysis of an HT29 human colon adenocarcinoma cell*. *Anal. Chem.*, 2000. **72**: p. 318-322.
18. Lodish, H., et al., *Molecular Cell Biology*. 6th edn ed. 2007, New York.
19. Green, R.J., et al., *Competitive protein adsorption as observed by surface plasmon resonance*. *Biomaterials*, 1999. **20**: p. 385-391.
20. Malmsten, M., *Ellipsometry and tirf studies of adsorption processes in parenteral drug delivery*. *Interface Science*, 1997. **5**: p. 159-167.
21. Reddig, P.J. and R.L. Juliano, *Clinging to life: cell to matrix adhesion and cell survival*. *Cancer Metastasis Rev.*, 2005. **24**: p. 425-439.
22. Li, H., et al., *Spatial Control of Cellular Measurements with the Laser Micropipet*. *Anal. Chem.*, 2001. **73**: p. 4625-4631.
23. *Medical Encyclopedia: RBC count*. 2007.
24. McClain, M.A., et al., *Microfluidic Devices for the High-Throughput Chemical Analysis of Cells*. *Anal. Chem.*, 2003. **75**: p. 5646-5655.

25. Rasmussen, T., R.B. Jensen, and O. Skovgaard, *The two chromosomes of Vibrio cholerae are initiated at different time points in the cell cycle*. The EMBO Journal, 2007. **26**: p. 3124–3131.
26. Landers, J.P., *Handbook of Capillary Electrophoresis*. 2nd ed. 1997, Boca Raton: CRC Press.
27. Kennedy, R.T., et al., Science, 1989. **246**: p. 57–63.
28. Xu, C.-X. and X.-F. Yin, *Continuous cell introduction and rapid dynamic lysis for high-throughput single-cell analysis on microfluidic chips with hydrodynamic focusing*. Journal of Chromatography A, 2011. **1218**: p. 726–732.
29. Kaigala, G.V., et al., *An inexpensive and portable microchip-based platform for integrated RT-PCR and capillary electrophoresis*. Analyst, 2008. **133**: p. 331-338.
30. Ermakov, S.V., S.C. Jacobson, and J.M. Ramsey, *Computer Simulations of Electrokinetic Transport in Microfabricated Channel Structures* Anal. Chem., 1998. **70**: p. 4494-4504.
31. Wong, P.K., et al., *Electrokinetic Bioprocessor for Concentrating Cells and Molecules*. Anal. Chem., 2004. **76**: p. 6908-6914.
32. Ramos, A., et al., *Ac electrokinetics: a review of forces in microelectrode structures*. Journal of Physics D: Applied Physics, 1998. **31**: p. 2338-2353.
33. Green, N.G. and H. Morgan, *Separation of submicrometre particles using a combination of dielectrophoretic and electrohydrodynamic forces*. Journal of Physics D: Applied Physics, 1998. **31**: p. L25-30.
34. Green, N.G. and H. Morgan, *Dielectrophoretic separation of nano-particles*. Journal of Physics D: Applied Physics, 1997. **30**: p. L41-L84.
35. Morgan, H. and N.G. Green, *AC Electrokinetics: colloids and nanoparticles*. 2002, England: SRP Ltd.
36. Peter, R.C., Gascoyne, and J. Vykoukal, *Particle separation by dielectrophoresis*. Electrophoresis, 2002. **23**: p. 1973-1983.
37. Green, N.G. and H. Morgan, *Dielectrophoretic investigations of sub-micrometre latex spheres*. Journal of Physics D: Applied Physics, 1997. **30**: p. 2626.
38. Rosenthal, A., B.M. Taff, and J. Voldman, *Quantitative modeling of dielectrophoretic traps*. Lab Chip, 2006. **6**: p. 508-515.
39. Rosenthal, A. and J. Voldman, *Dielectrophoretic Traps for Single-particle Patterning*. Biophysical Journal, 2005. **88**: p. 2193-2205.
40. Wanichapichart, P. and S. Bunthawin, *Determination of Cell Dielectric Properties Using Dielectrophoretic Technique*. ScienceAsia, 2002. **28**: p. 113-119.
41. Riegelman, M., H. Liu, and H.H. Bau, *Controlled Nanoassembly and Construction of Nanofluidic Devices*. Journal of Fluids Engineering, 2006. **128**: p. 6-13.
42. Jones, T.B., *Electromechanics of Particles*. 1995, New York: Cambridge University Press.
43. Liu, Y., et al., *Dielectrophoretic Assembly of Nanowires*. Journal of Physical Chemistry B, 2006. **110**: p. 14098-14106.
44. Oh, J., et al., *A novel technique for fabrication of micro- and nanofluidic device with embedded single carbon nanotube*. Sensors and Actuators B: Chemical, 2009. **in press**.
45. Green, N.G., et al., *Fluid flow induced by nonuniform ac electric fields in electrolytes in microelectrodes. I. Experimental measurements*. Physical Review E, 2000. **61**: p. 4011-4018.
46. Castellanos, A., et al., *Electrohydrodynamics and dielectrophoresis in Microsystems: scaling laws*. Journal of Physics D: Applied Physics, 2003. **36**: p. 2584-2597.

47. Belisle, A., et al., *Microelectrode arrays for two-dimensional polar movement of microparticles in water*. Journal of Vacuum Science and Technology A, 2006. **24**: p. 737-741.
48. Huang, S., et al., *AC electroosmotic generated in-plane microvortices for stationary or continuous fluid mixing*. Sensors and Actuators B, 2007. **125**: p. 326-336.
49. Jacobson, S., T. McKnight, and J. Ramsey, *Microfluidic devices for electrokinetically driven parallel and serial mixing*. Analytical Chemistry, 1999. **71**: p. 4455-4459.
50. Sigurdson, M., D. Wang, and C.D. Meinhart, *Electrothermal stirring for heterogeneous immunoassays*. Lab Chip, 2005. **5**: p. 1366 - 1373.
51. Wang, D., M. Sigurdson, and C.D. Meinhart, *Experimental analysis of particle and fluid motion in ac electrokinetics*. Experiments in Fluids, 2005. **38**: p. 1-10.
52. Li, P., K. Shi, and Z. Liu, *Manipulation and spectroscopy of a single particle by use of white-light optical tweezers*. Optics Letters, 2005. **30**(2): p. 156-158.
53. Ashkin, A., *History of optical trapping and manipulation of small-neutral particle, atoms, and molecules*. IEEE Journal of Quantum Electronics, 2000. **6**(6): p. 841-856.
54. Blideran, M.M., et al., *Mechanically actuated silicon microgripper for handling micro- and nanoparticles*. Microelectronic Engineering, 2006. **83**: p. 1382-1385.
55. Thelander, C. and L. Samuelson, *AFM manipulation of carbon nanotubes: Realization of ultra-fine nanoelectrodes*. Nanotechnology, 2002. **13**(1): p. 108-113.
56. Ramachandran, T.R., et al., *Direct and controlled manipulation of nanometer-sized particles using the non-contact atomic force microscope*. Nanotechnology, 1998. **9**(3): p. 237-245.
57. Takekawa, T., K. Nakagawa, and G. Hashiguchi, *The AFM tweezers: Integration of a tweezers function with an AFM probe*, in *TRANSDUCERS*. 2005.
58. Patankar, N.A. and H.H. Hu, *Numerical Simulation of Electroosmotic Flow*. Anal. Chem., 1998. **70**: p. 1870-1881.
59. Ermakov, S.V., S.C. Jacobson, and J.M. Ramsey, *Computer simulations of electrokinetic injection techniques in microfluidic devices*. Anal. Chem., 2000. **72**(15): p. 3512-3517.
60. Ghosal, S., *Lubrication theory for electro-osmotic flow in microfluidic channel of slowly varying cross-section and wall charge*. J. Fluid Mech., 2002. **459**: p. 103.
61. Fu, L.M., et al., *Electrokinetic injection techniques in microfluidic chips*. Anal. Chem., 2002. **74**: p. 5084-5091.
62. Fu, L.-M., J.-Y. Lin, and R.-J. Yang, *Analysis of electroosmotic flow with step change in zeta potential*. Journal of Colloid and Interface Science, 2003. **258**: p. 266-275.
63. Fu, L.-M., R.-J. Yang, and G.-B. Lee, *Electrokinetic focusing injection methods on microfluidic devices*. Analytical Chemistry, 2003. **75**: p. 1905-1910.
64. Fu, L.-M., et al., *Electrokinetically driven micro flow cytometers with integrated fiber optics for on-line cell/particle detection*. Analytica Chimica Acta, 2004. **507**: p. 163-169.
65. Yang, R.-J., et al., *A new focusing model and switching approach for electrokinetic flow inside microchannels*. Journal of Micromechanics and Microengineering, 2005. **15**: p. 2141-2148.
66. Yang, R.-J., L.-M. Fu, and C.-C. Hwang, *Electroosmotic entry flow in a microchannel*. Journal of Colloid and Interface Science, 2001. **244**: p. 173-179.
67. Yang, R.-J., L.-M. Fu, and G.-B. Lee, *Variable-volume-injection methods using electrokinetic focusing on microfluidic chips*. Journal of Separation Science, 2002. **25**: p. 996-1010.
68. Tsai, C.-H., et al., *Numerical simulation of electrokinetic injection techniques in capillary electrophoresis microchips*. Electrophoresis, 2005. **26**: p. 674-686.

69. Fu, L.-M. and C.-H. Lin, *Numerical Analysis and Experimental Estimation of a Low-Leakage Injection Technique for Capillary Electrophoresis*. Anal. Chem., 2003. **75**: p. 5790-5796.
70. Jorgenson, J.W. and K.D. Lukacs, *Capillary Zone Electrophoresis*. Science, 1983. **222**: p. 266-272.
71. Dose, E.V. and G.A. Guiochon, *High-Resolution Modeling of Capillary Zone Electrophoresis and Isotachopheresis*. Anal. Chem., 1991. **63**: p. 1063-1072.
72. Bercovici, M., S.K. Lele, and J.G. Santiago, *Open source simulation tool for electrophoretic stacking, focusing, and separation*. J. of Chromatography A, 2009. **1216**: p. 1008-1018.
73. Toner, M. and D. Irimia, *Blood-on-a-chip*. Annual Review of Biomedical Engineering, 2005. **7**: p. 77-103.
74. Lillard, S.J., et al., *Separation of hemoglobin variants in single human erythrocytes by capillary electrophoresis with laser-induced native fluorescence detection*. Journal of Chromatography A, 1995. **718**: p. 397-404.
75. El-Ali, J., P.K. Sorger, and K.F. Jensen, *Cells on chips*. Nature, 2006. **442**: p. 403.
76. Spehar, A.-M., et al., *Electrokinetic characterization of poly(dimethylsiloxane) microchannels*. Electrophoresis, 2003. **24**: p. 3674-3678.
77. Pohl, H.A., *Dielectrophoresis*. 1978, Cambridge: Cambridge University Press.
78. Benselama, A.M., P. Pham, and É. Canot, *Modeling of the dielectrophoretic forces acting upon biological cells: A numerical comparison between Finite Element/Boundary Element Maxwell stress tensor methods and point-dipole approach*, in *NSTI-Nanotech*. 2004. p. 188-191.
79. Lide, D.R., *CRC Handbook of Chemistry and Physics*. 81st edn ed. 2000, New York: CRC Press.
80. Poulsen, C., et al., Anal Chem, 2005. **77**: p. 667-672.
81. Balagadde, F., et al., Science, 2005. **309**: p. 137-140.
82. Gu Han Kwon, Y.Y.C., Joong Yull Park, Dong Hun Woo, Kyu Back Lee, Jong Hoon Kim and Sang-Hoon Lee, *Electrically-driven hydrogel actuators in microfluidic channels: fabrication, characterization, and biological application*. Lab Chip, 2010. **10**: p. 1604-1610.
83. He, M., et al., *Selective Encapsulation of Single Cells and Subcellular Organelles into Picoliter- and Femtoliter-Volume Droplets*. Anal Chem, 2005. **77**: p. 1539-1544.
84. Radko, S.P. and A. Chrambach, *Separation and characterization of sub- μm - and μm -sized particles by capillary zone electrophoresis*. ELECTROPHORESIS, 2002. **23**: p. 1957-1972.
85. Park, J.-S. and H.-I. Jung, *Multiorifice Flow Fractionation: Continuous Size-Based Separation of Microspheres Using a Series of Contraction/Expansion Microchannels*. Anal. Chem. , 2009. **81**: p. 8280-8288.
86. Kuntaegowdanahalli, S.S., et al., *Inertial microfluidics for continuous particle separation in spiral microchannels*. Lab Chip, 2009. **9**: p. 2973-2980.
87. Segre, G. and A. Silberberg, *Radial particle displacements in poiseuille flow of suspensions*. Nature, 1961. **189**: p. 209-210.
88. Carlo, D.D., et al., *Continuous inertial focusing, ordering, and separation of particles in microchannels*. PNAS, 2007. **104**: p. 18892-18897
89. Park, J.-S., S.-H. Song, and H.-I. Jung, *Continuous focusing of microparticles using inertial lift force and vorticity via multi-orifice microfluidic channels*. Lab Chip, 2009. **9**: p. 939-948.

90. Yang, L., P. Banada, and M. Chatni, *A multifunctional micro-fluidic system for dielectrophoretic concentration coupled with immuno-capture of low numbers of Listeria monocytogenes*. Lab Chip, 2006. **6**: p. 896–905.
91. Rousselet, J., G. Markx, and R. Pethig, *Separation of erythrocytes and latex beads by dielectrophoretic levitation and hyperlayer field-flow fractionation*. Colloid Surf. A, 1998. **140**: p. 209–216.
92. Yang, J., Y. Huang, and X. Wang, *Differential analysis of human leukocytes by dielectrophoretic field-flow fractionation*. Biophys. J., 2000. **78**: p. 2680–2689.
93. Choi, S. and J. Park, *Microfluidic system for dielectrophoretic separation based on a trapezoidal electrode array*. Lab Chip, 2005. **5**: p. 1161–1167.
94. Li, Y. and K. Kaler, *Dielectrophoretic fluidic cell fractionation system*. Anal. Chim. Acta, 2004. **507**: p. 151–161.
95. Leu, T., H. Chen, and F. Hsiao, *Studies of particle holding, separating, and focusing using convergent electrodes in microsorters*. Microfluid Nanofluid, 2005. **1**: p. 328–335.
96. Pamme, N. and C. Wilhelm, *Continuous sorting of magnetic cells via on-chip free-flow magnetophoresis*. Lab Chip, 2006. **6**: p. 974–980.
97. INGLIS, D., R. RIEHN, and R. AUSTIN, *Continuous microfluidic immunomagnetic cell separation*. Appl. Phys. Letter, 2004. **85**: p. 5093–5095.
98. Kim, U. and H.T. Soh, *Simultaneous sorting of multiple bacterial targets using integrated Dielectrophoretic–Magnetic Activated Cell Sorter*. Lab Chip, 2009. **9**: p. 2313–2318.
99. Neuman, K.C. and A. Nagy, *Single-molecule force spectroscopy: optical tweezers, magnetic tweezers and atomic force microscopy*. NATURE METHODS, 2008. **5**: p. 491–505.
100. Moffitt, J.R., et al., *Recent Advances in Optical Tweezers*. Annual Review of Biochemistry, 2008. **77**: p. 205–228.
101. MacDonald, M., S. Neale, and L. Paterson, *Cell cytometry with a light touch: sorting microscopic matter with an optical lattice*. J. Biol. Regul. Homeost., 2004. **18**: p. 200–205.
102. Roman, G.T., et al., *Single-cell manipulation and analysis using microfluidic devices*. Anal Bioanal Chem, 2007. **387**: p. 9–12.
103. Wheeler, A.R., et al., *Microfluidic Device for Single-Cell Analysis*. Anal Chem, 2003. **75**: p. 3581–3586.
104. Peng, X.Y.L. and P.C.H. Li, *A Three-Dimensional Flow Control Concept for Single-Cell Experiments on a Microchip. I. Cell Selection, Cell Retention, Cell Culture, Cell Balancing, and Cell Scanning*. Anal. Chem., 2004. **76**: p. Anal. Chem. 2004, 76, 5273–5281.
105. Sethu, P., et al., *Continuous Flow Microfluidic Device for Rapid Erythrocyte Lysis*. Anal. Chem., 2004. **76**: p. 6247–6253.
106. Irimia, D., R.G. Tompkins, and M. Toner, *Single-Cell Chemical Lysis in Picoliter-Scale Closed Volumes Using a Microfabricated Device*. Anal. Chem., 2004. **76**: p. 6137–6143.
107. Zeringue, H.C., M.B. Wheeler, and D.J. Beebe, *A microfluidic method for removal of the zona pellucida from mammalian embryos*. Lab Chip, 2005. **5**: p. 108–110.
108. Zhang, L.Y., et al., *Determination of dopamine in single rat pheochromocytoma cell by capillary electrophoresis with amperometric detection*. J. Chromatogr. B, 2003. **792**.
109. Kim, J., et al., *Cell lysis on a microfluidic CD (compact disc)*. Lab Chip, 2004. **4** p. 516–522.

110. Carlo, D.D., K.-H. Jeong, and L.P. Lee, *Reagentless mechanical cell lysis by nanoscale barbs in microchannels for sample preparation*. Lab Chip, 2003. **3**: p. 287-291.
111. Taylor, M.T., et al., *Lysing Bacterial Spores by Sonication through a Flexible Interface in a Microfluidic System*. Anal. Chem., 2001. **73**: p. 492-496.
112. Lu, H., M.A. Schmidt, and K.F. Jensen, *A microfluidic electroporation device for cell lysis*. Lab Chip, 2005. **5**: p. 23-29.
113. Neumann, E., A.E. Sowers, and C.A.E. Jordan, *Electroporation and Electrofusion in Cell Biology*. 1989, New York: Plenum Press.
114. Zimmermann, U., *Electrical breakdown, electropermeabilization and electrofusion*. Rev. Physiol. Biochem. Pharmacol., 1986. **105**: p. 175-256.
115. Grahl, T. and H. Markl, *Killing of microorganisms by pulsed electric fields*. Appl. Microbiol. Biotechnol., 1996. **45**: p. 148-157.
116. Lee, S.-W. and Y.-C. Tai, *A micro cell lysis device*. Sensors and Actuators, 1999. **73**: p. 74-79.
117. Lu, K.-Y., et al., *Three dimensional electrode array for cell lysis via electroporation*. Biosensors and Bioelectronics, 2006. **22**: p. 568-574.
118. Lee, D.W. and Y.-H. Cho, *A continuous electrical cell lysis device using a low DC voltage for a cell transport and rupture*. Sensors and Actuators B, 2007. **124**: p. 84-89.
119. Prinz, C., et al., *Bacterial chromosome extraction and isolation*. Lab Chip, 2002. **2**.
120. Waters, L.C., et al., *Multiple sample PCR amplification and electrophoretic analysis on a microchip*. Analytical Chemistry, 1998. **70**(24): p. 5172-5176.
121. Xue, Q. and E.S. Yeung, *Determination of lactate dehydrogenase isoenzymes in single lymphocytes from normal and leukemia cell lines*. J. Chromatogr. B: Biomed. Appl., 1996. **677**: p. 233-240.
122. Zhang, H. and W. Jin, *Determination of different forms of human interferon-gamma in single natural killer cells by capillary electrophoresis with on-capillary immunoreaction and laser-induced fluorescence detection*. . Electrophoresis, 2004. **25**: p. 1090-1095.
123. Zhang, H. and W. Jin, *Single-cell analysis by intracellular immuno-reaction and capillary electrophoresis with laserinduced fluorescence detection*. J. Chromatogr. A, 2006. **1104**: p. 346-351.
124. Rau, K.R., et al., *Investigation of laser-induced cell lysis using time-resolved imaging*. Appl. Phys. Lett., 2004. **84**: p. 2940-2942.
125. Rau, K.R., et al., *Pulsed laser microbeam-induced cell lysis: timeresolved imaging and analysis of hydrodynamic effects*. Biophys. J., 2006. **91**: p. 317-329.
126. Lichtenberg, J., E. Verpoorte, and N.F.d. Rooij, *Sample preconcentration by field amplification stacking for microchip-based capillary electrophoresis*. Electrophoresis, 2001. **22**: p. 258-271.
127. Gong, M., et al., *On-Line Sample Preconcentration Using Field-amplified Stacking Injection in Microchip Capillary Electrophoresis*. Anal. Chem., 2006. **78**: p. 3730-3737.
128. Jung, B., R. Bharadwaj, and J.G. Santiago, *Thousandfold signal increase using field-amplified sample stacking for on-chip electrophoresis*. Electrophoresis, 2003. **24**: p. 3476-3483.
129. Wainright, A., et al., *Sample pre-concentration by isotachopheresis in microfluidic devices*. Journal of Chromatography A, 979 (2002) 2002. **979**: p. 69-80.
130. Liu, D., et al., *Simplified transient isotachopheresis/capillary gel electrophoresis method for highly sensitive analysis of polymerase chain reaction samples on a microchip with laser-induced fluorescence detection*. Journal of Chromatography A, 2008. **1214**: p. 165-170.

131. Park, C.C., et al., *Controlling Data Quality and Reproducibility of a High-Sensitivity Immunoassay Using Isotachophoresis in a Microchip*. Anal. Chem., 2008. **80**: p. 808-814.
132. Lin, C.-C., B.-K. Hsu, and S.-H. Chen, *Integrated isotachophoretic stacking and gel electrophoresis on a plastic substrate and variations in detection dynamic range*. Electrophoresis, 2008. **29**: p. 1228–1236.
133. Cui, H., et al., *Isoelectric Focusing in a Poly(dimethylsiloxane) Microfluidic Chip*. Anal. Chem., 2005. **77**: p. 1303-1309.
134. Raisi, F., et al., *Microchip isoelectric focusing using a miniature scanning detection system*. Electrophoresis, 2001. **22**: p. 2291–2295.
135. Wen, J., et al., *Microfabricated isoelectric focusing device for direct electrospray ionization-mass spectrometry*. Electrophoresis, 2000. **21**: p. 191-197.
136. Wen, J., et al., *Microfluidic Preparative Free-Flow Isoelectric Focusing: System Optimization for Protein Complex Separation*. Anal. Chem., 2010. **82**: p. 1253–1260.
137. Ge, Z., W. Wang, and C. Yang, *Towards high concentration enhancement of microfluidic temperature gradient focusing of sample solutes using combined AC and DC field induced Joule heating*. Lab Chip, 2011.
138. Shackman, J.G., M.S. Munson, and D. Ross, *Temperature gradient focusing for microchannel separations*. Anal Bioanal Chem, 2007. **387**: p. 155–158.
139. Becker, M., et al., *Temperature gradient focusing in miniaturized free-flow electrophoresis devices*. Electrophoresis, 2009. **30**: p. 4206–4212.
140. Jacobson, S.C., et al., *Microchip structures for submillisecond electrophoresis*. Analytical Chemistry, 1998. **70**(16): p. 3476-3480.
141. Jacobson, S.C., et al., *Effects of Injection Schemes and Column Geometry on the Performance of Microchip Electrophoresis Devices*. Anal. Chem., 1994. **66**(7): p. 1107-1113.
142. Jacobson, S.C., et al., *Microchip Capillary Electrophoresis with an Integrated Postcolumn Reactor*. Analytical Chemistry, 1994. **66**(20): p. 3472-3476.
143. Jacobson, S.C. and J.M. Ramsey, *Electrokinetic Focusing in Microfabricated Channel Structures*. Anal. Chem., 1997. **69**: p. 3212-3217.
144. Gao, J., X.-F. Yin, and Z.-L. Fang, *Integration of single cell injection, cell lysis, separation and detection of intracellular constituents on a microfluidic chip*. Lab Chip, 2004. **4**: p. 47-52.
145. Liu, C.C. and D.F. Cui, *Design and fabrication of poly(dimethylsiloxane) electrophoresis microchip with integrated electrodes*. Microsyst Technol, 2005. **11**: p. 1262–1266.
146. Vickers, J.A., M.M. Caulum, and C.S. Henry, *Generation of Hydrophilic Poly(dimethylsiloxane) for High-Performance Microchip Electrophoresis*. Anal. Chem., 2006. **78**: p. 7446-7452.
147. Burns, M.A., et al., *An Integrated Nanoliter DNA Analysis Device*. Science, 1998. **282**: p. 484.
148. Kim, D.-K. and S.H. Kang, *On-channel base stacking in microchip capillary gel electrophoresis for high-sensitivity DNA fragment analysis*. Journal of Chromatography A, 2005. **1064**: p. 121–127.
149. Kim, Y.-J., et al., *Microchip capillary gel electrophoresis using programmed field strength gradients for the ultra-fast analysis of genetically modified organisms in soybeans*. Journal of Chromatography A, 2005. **1083**: p. 179–184.
150. Effenhauser, C.S., G.J.M. Bruin, and A. Paulus, *Integrated chip-based capillary electrophoresis*. Electrophoresis, 1997. **18**: p. 2203-2213.

151. Chang, T.L., et al., *Diagnostic Validation of Capillary Electrophoresis Analysis of T-Cell Receptor Gamma-Chain Gene Rearrangements: Prediction of Malignant Transformation of Cutaneous T-Cell Lymphoproliferative Disorders*. Clin. Chem. , 2003. **49**: p. 513.
152. Jeon, S.S., et al., *Fast molecular diagnostics of canine T-cell lymphoma by PCR and capillary gel electrophoresis with laser-induced fluorescence detector*. J. Chromatogr. B, 2007. **854**: p. 268-272.
153. Pal, R., et al., *An integrated microfluidic device for influenza and other genetic analyses*. Lab Chip, 2005. **5**: p. 1024-1032.
154. Wu, H.Y., A.R. Wheeler, and R.N. Zare, in *Proc. Natl. Acad. Sci. U. S. A.* 2004. p. 12809–12813.
155. Ros, A., et al., *Electrophoresis*, 2006. **27**: p. 2651–2658.
156. Munce, N.R., et al., *Anal. Chem.*, 2004. **76**: p. 4083–4989.
157. Uchiyama, K., H. Nakajima, and T. Hobo, *Detection methods for microchip separations*. Anal Bioanal Chem, 2004. **379**: p. 375–382.
158. Yeung, E.S., *Study of single cells by using capillary electrophoresis and native fluorescence detection*. Journal of Chromatography A, 1999. **830**: p. 243–262.
159. Vandaveer IV, W.R., et al., *Recent developments in electrochemical detection for microchip capillary electrophoresis*. Electrophoresis, 2004. **25**: p. 3528–3549.
160. Hulvey, M.K., C.N. Frankenfeld, and S.M. Lunte, *Separation and Detection of Peroxynitrite Using Microchip Electrophoresis with Amperometric Detection*. Anal. Chem., 2010. **82**.
161. Tsukagoshi, K., N. Jinno, and R. Nakajima, *Development of a Micro Total Analysis System Incorporating Chemiluminescence Detection and Application to Detection of Cancer Markers*. Anal. Chem., 2005. **77**: p. 1684-1688.
162. Zhao, S., X. Li, and Y.-M. Liu, *Integrated Microfluidic System with Chemiluminescence Detection for Single Cell Analysis after Intracellular Labeling*. Anal. Chem., 2009. **81**.
163. Cao, P. and M.J. Moini, *Am. Soc. Mass Spectrom.*, 1999. **10**: p. 184–186.
164. Hofstadler, S.A., et al., *Rapid Commun. Mass Spectrom.*, 1996. **10**: p. 919–922.
165. Rubakhin, S.S., et al., *Anal. Chem.*, 2006. **78**: p. 7267–7272.
166. Ramsey, R. and J. Ramsey, *Anal Chem* 1997. **69**: p. 1174–1178.
167. Rohner, T., J. Rossier, and H. Girault, *Anal Chem*, 2001. **73**: p. 5353–5357.
168. Tang, K., et al., *Anal Chem*, 2001. **73**: p. 1658–1663.
169. Kameoka, J., et al., *Anal Chem*, 2001. **73**: p. 1935–1941.
170. Mellors, J.S., et al., *Integrated Microfluidic Device for Automated Single Cell Analysis Using Electrophoretic Separation and Electrospray Ionization Mass Spectrometry*. Anal. Chem., 2010. **82**: p. 967–973.
171. Locascio, L.E., C.E. Perso, and C.S. Lee, *Measurement of electroosmotic flow in plastic imprinted microfluid devices and the effect of protein adsorption on flow rate*. J. of Chromatography A, 1999. **857**: p. 275-284.
172. Kirby, B.J. and E.F. Hasselbrink, *Zeta potential of microfluidic substrates: 1. Theory, experimental techniques, and effects on separations*. Electrophoresis, 2004. **25**: p. 187-202.
173. Kim, M.-S., et al., *Fabrication of microchip electrophoresis devices and effects of channel surface properties on separation efficiency*. Sensors and Actuators B, 2005. **107**: p. 818-824.
174. Hart, R., R. Lec, and H.M. Noh, *Enhancement of heterogeneous immunoassays using AC electroosmosis* Sensors and Actuators B: Chemical, 2010. **147**: p. 366-375.

175. Hart, R., et al., *Improved Protein Detection on an AC Electrokinetic Quartz Crystal Microbalance (EKQCM)*. Biosensors and Bioelectronics, 2011. **in press**.
176. Giner, V., et al., *Transverse dipolar chaining in binary suspensions induced by rf fields*. J. Phy. D: Appl. Phys., 1999. **32**: p. 1182-1186.
177. Israelachvili, J., *Intermolecular and Surface Forces*. 1992: Academic Press.
178. Oh, J., et al., *Comprehensive analysis of particle motion under non-uniform AC electric fields in a microchannel*. Lab Chip, 2009. **9**: p. 62–78.
179. Sjostrom, L. and T. Akesson, *The Stability of Charged Colloids—Attractive Double Layer Forces Due to Asymmetric Charge Distribution*. Journal of Colloid and Interface Science, 1996. **181**: p. 645-653.
180. Popa, I., et al., *Importance of Charge Regulation in Attractive Double-Layer Forces between Dissimilar Surfaces*. Physical Review Letter, 2010. **104**: p. 228301.
181. Probstein, *Physicochemical Hydrodynamics: An Introduction*. 2nd ed. 1994: Wiley-Interscience.
182. Ghosal, S., *Fluid mechanics of electroosmotic flow and its effect on band broadening in capillary electrophoresis*. Electrophoresis, 2004. **25**: p. 214-228.
183. Dill, K.A. and S. Bromberg, *Molecular Driving Forces: Statistical Thermodynamics in Chemistry & Biology*. 2, ed. 1. Vol. 4. 2002: Garland Science. 7.
184. Hu, Y., C. Werner, and D. Li, *Electrokinetic Transport through Rough Microchannels*. Anal. Chem., 2003. **75**: p. 5747-5758.
185. Young, M.E., P.A. Carroad, and R.L. Bell, *Estimation of diffusion coefficients of proteins* Biotechnology and Bioengineering, 1980. **22**: p. 947-955.
186. Chae, K.S. and A.M. Lenhoff, *Computation of the Electrophoretic Mobility of Proteins*. Biophysical Journal, 1995. **68**: p. 1120-1127.
187. Datta, S., S. Ghosal, and N. Patankar, *Electroosmotic flow in a rectangular channel with variable wall zeta-potential: comparison of numerical simulation with asymptotic theory*. Electrophoresis, 2006. **27**: p. 611-619.
188. Yang, R.-J., L.-M. Fu, and Y.-C. Lin, *Electroosmotic Flow in Microchannels*. J. Colloid Interface Sci., 2001. **239**: p. 98-105.
189. Chang, C.-C. and R.-J. Yang, *Computational analysis of electrokinetically driven flow mixing in microchannels with patterned blocks*. J. Micromech. Microeng., 2004. **14**: p. 550-558.
190. Fu, L.-M., et al., *A novel microfluidic mixer utilizing electrokinetic driving forces under low switching frequency*. Electrophoresis, 2005. **5**: p. 1814–1824.
191. Mourzina, Y., et al., *Capillary zone electrophoresis of amino acids on a hybrid poly(dimethylsiloxane)-glass chip*. Electrophoresis, 2005. **26**: p. 1849 - 1860.
192. Qiao, R., *Effects of molecular level surface roughness on electroosmotic flow*. Microfluidics and Nanofluidics, 2007. **3**: p. 33-38.
193. Xuan, X. and D. Li, *Electroosmotic flow in microchannels with arbitrary geometry and arbitrary distribution of wall charge*. Journal of Colloid and Interface Science, 2005. **289**: p. 291-303
194. Ghosal, S., *Effect of Analyte Adsorption on the Electroosmotic Flow in Microfluidic Channels*. Anal. Chem., 2002. **74**: p. 771-775.
195. Cummings, E.B., et al., *Conditions for similitude between the fluid velocity and electric field in electroosmotic flow*. Anal. Chem., 2000. **72**: p. 2526-2532.
196. Herr, A.E., et al., *Electroosmotic Capillary Flow with Nonuniform Zeta Potential*. Anal. Chem., 2000. **72**: p. 1053-1057.

197. Ren, C.L. and D. Li, *Electrokinetic sample transport in a microchannel with spatial electrical conductivity gradients*. J. Colloid Interface Sci., 2006. **294**: p. 482-491.
198. Huber, D.E. and J.G. Santiago, *Taylor-Aris dispersion in temperature gradient focusing*. Electrophoresis, 2007. **28**: p. 2333-2344.
199. Taylor, G.I., *Dispersion of soluble matter in solvent flowing slowly through a tube*. Proc. Roy. Soc. A, 1953. **219**: p. 186-203.
200. Aris, R., *On the Dispersion of a Solute in a Fluid Flowing through a Tube*. Proc. R. Soc. Lond. A, 1956. **235**: p. 67-77.
201. Cetin, B. and D. Li, *Effects of Joule Heating on electrokinetic transport*. Electrophoresis, 2008. **29**: p. 994-1005.
202. Lee, D.-H., B. Farouk, and H.M. Noh, *3-D Simulation of Electroosmotic Injection and Migration in Microchannels: Effects of Non-rectangular Cross Section*. Separation Science and Technology, 2011. **46**: p. 195-204.
203. Virtanen, R., *The Variance and the quantity $2Dt$ in capillary zone electrophoresis*. Electrophoresis, 1993. **14**: p. 1266-1470.
204. Perez-Ruiz, T., et al., *Separation of Fluorescein Dyes by Capillary Electrophoresis Using β -Cyclodextrin*. Chromatographia, 1998. **48**: p. 263-267.
205. Butcher, E.C. and I.L. Weissman, *Direct fluorescent labeling of cells with fluorescein or rhodamine isothiocyanate. I. Technical aspects*. Journal of Immunological Methods, 1980. **37**: p. 97-108

APPENDIX I APPENDIX – PROTOCOLS

1. FABRICATION OF PDMS MICROCHANNELS

A. Materials:

Mold master : SU-8 2000 series, developer, isopropyl alcohol.

PDMS : Dow Corning Sylgard 184 Elastomer kit

Spin coater, UV exposer, vacuum desiccator, oxygen plasma machine

B. SU-8 mold master fabrication

1. Prepare a Si wafer without oxide layer.
2. If the Si wafer has stains on it, clean with Piranha solution (mixture is 3:1, sulfuric acid to 30% hydrogen peroxide) at 85 °C for 5 minutes.
3. Remove natural oxide layer on the Si wafer in 1% HF for 5 minutes
4. Dehydrate for 5 minutes at 150 °C and cool down for 2 minutes
5. (Optional) To improve the adhesion of SU-8 mold to Si wafer, spin coat Microprime HP Primer (Spin at 4000 rpm and bake 150 °C for 5 min)
6. Select an SU-8 grade, depending on a channel depth. For example, SU-8 2035 is proper for 40 μm height. Slowly warm up SU-8 to the room temperature condition.
7. Place the Si wafer on a spin coating chuck and pour SU-8 on the Si wafer and spin coat with a proper speed. For example, for 40 μm height, spin at 500 rpm for 7 sec with acceleration of 100 rpm/sec and spin at 3000 rpm for 30 sec with acceleration of 300 rpm/sec.
8. Soft bake the SU-8 coating on a hot plate. Ramp temp to 95 °C and stay there for 6 min then turn off and let cool down to 30 °C

9. Place a desired photomask on the SU-8 coating with good contact and expose under UV light (365 nm) for 9 sec (dose of 160 mJ/cm²)
10. To finish cross-link, post-exposure bake following the same as step 8
11. Develop in SU-8 developer for 5 minutes.
12. Rinse the substrate with isopropyl alcohol (NOT WATER)

C. Silanization

1. Place a vacuum chamber inside a fume hood. The silanizing agent produces a HCl gas which is harmful.
2. Place the mold master and a blank glass slide in the chamber
3. Place 2-3 drops of Silanizing agent (Tridecafluoro-1,1,2,2-tetrahydro-octyl-1-trichlorosilane) on the glass slide. Note: Do not place drops on your master. The agent does not evaporate completely and leaves behind a sticky residue
4. Apply vacuum for 2 minutes, then close the valve and leave the chamber under vacuum for 30 minutes.

D. PDMS replica molding

1. Mix PDMS and curing agent in 10:1 mass ratio.
2. Stir the mixture well with a glass bar.
3. Apply vacuum for 30 minutes or until all the bubbles burst.
4. Pour the mixture over the mold master.
5. Place the PDMS material in an oven at 70 °C for 2 hours for curing.
6. Cut with a razor blade and peel off the PDMS channel.

2. FABRICATION OF MICRO ELECTRODES

A. Metal deposition

1. Prepare a glass substrate and clean it with Piranha solution.
2. Put the glass substrate in a metal-evaporator (thermal or e-beam).
3. Deposit a chrome layer first (20 nm) and then a gold layer (200nm).

B. Shipley (positive PR) photolithography

1. Place the glass substrate with metal deposition on a spin coating chuck, pour SC 1827 on the substrate and spin at 3000 rpm for 30 sec with acceleration of 1000 rpm/sec.
2. Soft bake at 100 °C for 6 min.
3. Develop with MF351:water (1:3)

3. FABRICATION OF GLASS MICROCHANNELS

A. Glass etching

1. Prepare a chrome deposited glass plate with AZ1500 PR coating.
2. Expose UV 7 sec.
3. Develop for 34sec with AZ400(1) : DI(7)
4. Chrome etch with agitation until the pattern is clearly seen.
5. Hard bake at 100 °C for 30 min.
6. Attach kapton tape on the backside of the substrate to prevent non-uniform etching.
7. Glass etch with mixture of 79 ml DI, 17 ml nitric acid solution and 20 ml 49% HF.
The etch rate with this solution is 0.5 $\mu\text{m}/\text{min}$ for borosilicate glass and 5 $\mu\text{m}/\text{min}$ for soda lime glass.
6. Dice glass chips and drill holes for inlets.

7. Remove PR with acetone (or Piranha solution) and chrome with chrome etchant.

B. Glass bonding

1. Sonicate a glass chip for 1 hr to remove debris from wet etching or drilling
2. Clean the glass chip and another blank glass plate with piranha at 85 °C for 30 min.
The glass plate must be the same type as the glass chip
3. Surface treat with RCA (100ml DI, 20ml NH₄OH, 20ml H₂O₂) at 80 °C for 20min.
4. Rinse with DI water on spin machine at 500 rpm 10 sec (shot DI water) and 2000 rpm 30 sec.
5. Align well and press top and bottom glasses and check the fringes. If fringes are found, it means there are particles between plates.
6. Put the glass chip in a furnace. Place the sandwiched glass plates between two macor plates. Raise the temperature with ramp of 10 °C /min to 570 °C for soda lime glass, or 610 °C for borofloat glass.
7. After cooling down furnace temperature to the room temperature, inspect the chip bonding state. If there is non-bond area, try with higher bonding temperature by 5 °C increase or place more weight and repeat the bonding procedure.

4. AC ELECTROKINETICS EXPERIMENT

A. Materials:

AC Electrokinetics Chip with electrical connections

Glass coverslips

200 µl pipettor

Low conductivity 2 µm microsphere solution

High conductivity 2 μm microsphere solution

Function generator

Microscope with camera

B. Procedure

1. Place a 50 μl drop of the low conductivity microsphere solution on the surface of one of the interdigitated electrodes and cover with a coverslip
2. Place the device on the microscope stage and observe the particles
3. Attach the function generator to the device
4. Fill out the chart below by setting the appropriate frequency and voltage settings for each line of the chart and writing observations
5. When the first chart is filled, repeat the procedure with the high conductivity solution.
6. Clean the device with isopropyl alcohol
7. Dry the device under compressed air
8. Apply the high conductivity solution and fill out the second chart

5. EOF MEASUREMENT

High electric power is used in this process. Special care should be taken to avoid touching a high voltage electrode with bare hands.

A. Device and Solution preparation

1. Fabricate a microcapillary channel made of the material on which you want to obtain EOF information.

2. Make reservoirs at the ends of the channel in order to minimize the perturbation due to electroosmotic flow (such as a significant level difference generating a pressure gradient or ion depletion).
3. Prepare two buffer solutions with slightly different concentrations (e.g. 10 mM PBS and 8 mM PBS). *Electroosmotic mobility (or zeta potential) is dependent upon both ionic concentration and pH of the solution. Buffer solution is used for keeping a constant pH. We can neglect the electroosmotic mobility variation due to slight variation of ionic concentration. Refer to the appendix for the dependence of EOF on ionic strength and pH.*
4. Rinse channels with 100 mM NaOH for 15 minutes, then 15 minutes with filtered deionized water (DI). After this, introduce your buffer of choice, flush it for another 15 min, stop the flow for 2 minutes and then resume flushing with buffer for 10 minutes.
5. Mark the inlet and outlet reservoirs with a label.

B. Electroosmotic mobility measurement

1. Measure the length of channel, L , on which EOF is run.
2. Insert platinum electrodes into the reservoirs. The ground electrode will be at the inlet reservoir and the high voltage electrode will be at the outlet reservoir.
3. Apply a negative high electric potential (e.g. -400V to make $E=100\text{V/cm}$ in 4cm channel). *The direction of electroosmotic flow is the same as that of electric current for normal glass or polymer channels (having negative zeta potential). We want to have the inlet reservoir to be grounded in order not to disturb the electric power*

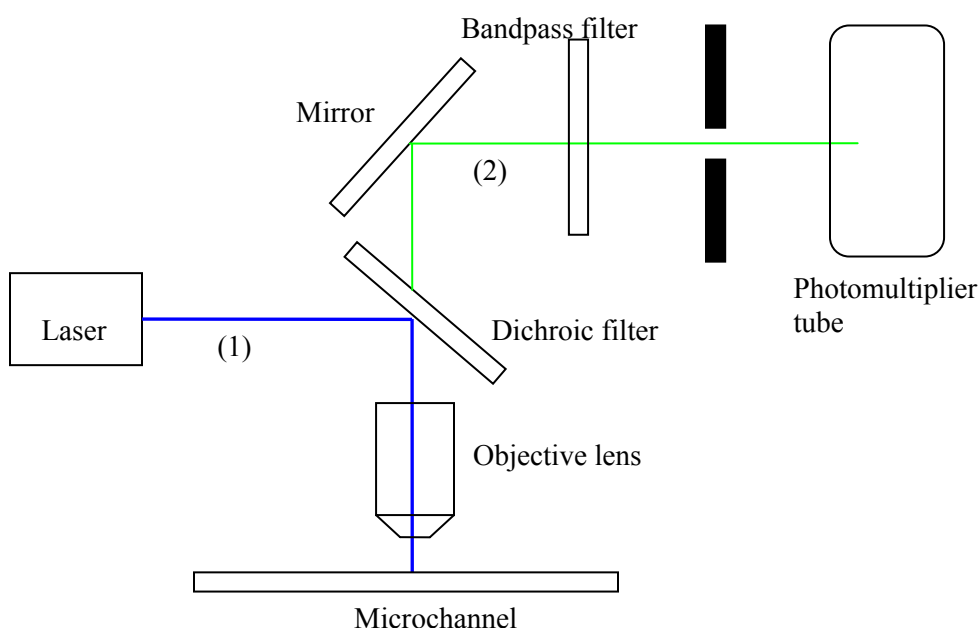
while replacing the buffer solution and to minimize the possibility of accidentally touching high voltage.

4. Read the electric current and check any issues. *If the signal is below 10 μA , the connectivity of conductive media needs to be checked. This means the channel may be blocked by particles or bubbles trapped in the channel. Generally, you can try to push the liquid in the reservoir to clear the clog with pressure. If the signal is above 100 μA , there is a high chance to have bubble generation due to the electric heating (Joule heating). Lower the electric field.*
5. Wait until the current signal stabilizes.
6. Start tracing the measurement in Sequencer software.
7. Completely remove the solution in the inlet reservoir and quickly fill with the other type of solution. (e.g. if 10mM PBS was initially in the reservoir, replace it with 8mM PBS)
8. Observe the variation of current. Wait until the signal remains constant for more than 1 minute.
9. Stop tracing.
10. Open the data file with Excel and create a current vs. time graph and check if the data is what you expected.
11. Analyze the graph to obtain the flow traveling time through the channel.
12. If the signal is not linear this means a problem occurred, disregard the data or take the sharpest slope and make a linear variation curve.
13. Calculate the electroosmotic mobility and then calculate the zeta potential with assuming the ambient water viscosity and permittivity.

- Repeat the steps 3-13 to get multiple data for electroosmotic mobility and calculate the average value.

6. PINCHED INJECTION EXPERIMENT

- Fabricate a cross or double-T channel (glass microchannel refer to section 3).
- Prepare dye sample and buffer solution. Semi-soluble dye can be dissolved with sonication.
- Measure conductivity of solutions. Make sure that the conductivity should be constant for all the solutions used, to avoid internal pressure gradient.
- Align optical system. First align the laser path (1), then place a fluorescent plate and check the fluorescent path (2). Laser path can be checked by inserting a paper. The fluorescent pass can be checked by an eye with safety goggles. Turn off the laser after aligning optical system.



5. Fill the channel with buffer solution and fill the reservoirs with proper solutions. Cleaning with 0.1 M NaOH solution may be needed before filling with buffer solution. Insert electrodes into reservoirs.
6. Put a microchip on the X-Y-Z stage.
7. Remove mirror and look through objective lens with a bare eye. Laser should be off at this stage. Adjust Z knob to locate the channel at the focal plane. When you clearly see the channel, the chip is on the focal plane.
8. Turn on the laser. Wear the safety goggles. Adjust X-Y knobs to make the focused laser shine the target point.
9. Place back the mirror and enclose the optical system by placing the top lid.
10. Apply power 15V to activate photomultiplier tube. Turn on the high voltage power supply.
11. Open Labsmith Sequence software and Labview software (LIF).
12. Control reservoir power via Sequence and record the output data via LIF.

7. SINGLE CELL ANALYSIS

A. Prepare red blood cells.

1. Centrifuge blood samples at 1000 rpm for 5 min to separate the erythrocytes.
2. Discard the supernatant and wash erythrocytes with PBS 3-4 times by centrifuging until a clear supernatant was obtained.

B. Label red blood cells with FITC.

1. Prepare fluorescein isothiocyanate (FITC) in PBS by shaking an excess of FITC crystals in PBS for 1~3 hour at room temperature and removing the undissolved

crystals by centrifugation (1500 X g, 15 min) and filtration through filters (0.22 μm pore size).

2. Store the stock solutions in aliquots at -35°C until use.
3. Label cells with FITC at 37°C in PBS (pH7.4) for 10~20 min.
4. After incubation, wash cells with medium for three times to fully remove the extracellular FITC.

C. Cell analysis

1. Prepare experimental setup as described in Section 7 (pinched injection).
2. Fill the microchannel with PBS 1X medium and align the channel, following the method described in Section 7.
3. Inject red blood cells into the inlet reservoir.
4. Insert platinum electrodes into all the reservoirs.
5. Apply high voltage electric field satisfying the cell lysis condition.
6. Record electropherogram and analyze the data.

8. COMSOL SIMULATION OF PINCHED INJECTION

Electroosmotic sample injection and migration can be simulated by employing three application modes in COMSOL multiphysics: 1. Flow field, 2. DC electric field, 3. Chemical species. The governing equations corresponding to three application modes are as follows.

$$\text{Flow governing equation: } \rho \frac{D\vec{V}}{Dt} = -\nabla p + \eta \nabla^2 \vec{V} \quad \nabla \cdot \vec{V} = 0$$

$$\text{Electric potential governing equation: } \nabla^2 \Phi = 0$$



Chemical species conservation:
$$\frac{\partial C}{\partial t} + \nabla \cdot ((\vec{V} + \mu_{ep} \vec{E})C) = D\nabla^2 C$$



Electroosmotic flow is treated as a slip flow by adopting thin electric double layer. The slip electroosmotic velocity is obtained by $\vec{V}_{eo} = \mu_{eo} \vec{E}$.

A. Select application modes in Model Navigator

1. In the Model Navigator, select 2D (select 3D for 3D simulation) from the Space dimension list.
2. In the Application Modes tree, select MEMS Module>Microfluidics> Incompressible Navier-Sokes. Click Add.
3. In the Application Modes tree, select MEMS Module>Electrostatics>Conductive Media DC. Click Add.
4. In the Application Modes tree, select MEMS Module>Microfluidics>Electrokinetic Flow>Transient analysis. Click Add. Click OK.

B. Geometry Modeling

1. Shift-click the Rectangle/Square button  on the Draw toolbar
2. In the Width edit field, type 5e-4, and in the Height edit field, type 2e-5. Change the base to the center. Click OK.
3. Click the Zoom Extents button  on the Main toolbar.
4. Shift-click the Rectangle/Square button on the Draw toolbar
5. In the Width edit field, type 2e-5, and in the Height edit field, type 5e-4. Change the base to the center. Click OK.

6. Select the two rectangles you created and click the Create Composite Object button  on the Draw toolbar. Uncheck Keep interior boundaries and click OK.
7. Click Fillet/Chamfer button  on the Draw toolbar and apply 1e-6 fillet to the four corner points.

C. Physics Settings

1. From the Options menu, choose Constants. In the Constants dialog box, define constants with names, expressions, and (optionally) descriptions; when done, click OK.
2. In the Multiphysics menu, select Incompressible Navier-Sokes (mmglf). From Physics menu, select Subdomain Settings, then set the properties: density and viscosity.
3. In the Multiphysics menu, select Electrokinetic Flow (chekf). From Physics menu, select Subdomain Settings, then set the parameters: diffusivity and electrophoretic mobility.

D. Boundary Conditions

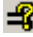

1. In the Multiphysics menu, select Conductive Media DC (emdc). From the Physics menu, open the Boundary Settings dialog box. Set the parameters: Electric potential boundary conditions for inlets and outlets and Electric insulation for walls.
2. In the Multiphysics menu, select Incompressible Navier-Sokes (mmglf). From the Physics menu, open the Boundary Settings dialog box. Set the parameters: Outlet for inlets and outlets and Wall/ Electroosmotic velocity for walls (Ex: Ex_emdc, Ey: Ey_emdc, μ_{eo} : electroosmotic mobility)

3. In the Multiphysics menu, select Electrokinetic Flow (chekf). From the Physics menu, open the Boundary Settings dialog box. Set the parameters: $C=1$ for the sample reservoir, $C=0$ for buffer reservoir, Convective flux for outlets and Insulation/Symmetry for walls.


E. Mesh Generation

From the Mesh menu, choose Free Mesh Parameters. On the Global page, click the Custom mesh size button, then set the Maximum element size to $1e-5$. Click Remesh. When the mesher has finished, click OK.

F. Computing the Solution

1. Click the Solver Parameters button  on the Main toolbar and make sure the Solver setting is Stationary. Click OK.
2. Click the Solver Manager button  on the Main toolbar
3. On the Initial Value page, select Current solution for Initial value
4. On the Solve For page, select Conductive Media DC (emdc). Click Solve.
5. Select Incompressible Navier-Sokes (mmglf). Click Solve.
6. Select Electrokinetic Flow (chekf). Click Solve.

E. Postprocessing

1. Click the Plot Parameters button  on the Main toolbar.
2. Click the Surface tab. From the Predefined quantities list on the Surface Data page, select Electrokinetic Flow (chekf)>concentration. Click OK.